UNIVERSITÉ DU LUXEMBOURG

PhD-FSTM-2025-08
The Faculty of Science, Technology and Medicine

DISSERTATION

Defence held on 06/10/2025 in Luxembourg

to obtain the degree of

DOCTEUR DE L'UNIVERSITÉ DU LUXEMBOURG

EN *Sciences de l'ingénieur*

by

Guanchen LIU
Born on 01 October 1993 in China

TITLE OF THE DISSERTATION

Lattice Boltzmann numerical and experimental studies of bubble dynamics

Dissertation defence committee

Dr. Stephan Leyer, dissertation supervisor
Professor, Université du Luxembourg

Dr. Horst-Michael Prasser
Professor Emeritus, ETH ZÜRICH, Switzerland

Dr. Stefan MAAS, Chairman
Professor, Université du Luxembourg

Dr. -Ing. habil. Dr. h. c. Uwe Hampel
Professor, Director, Institute of Fluid Dynamics (HZDR), Germany

Dr. Nikolaos Prasianakis
Scientist, Paul Scherrer Institute, Switzerland

Affidavit

I hereby confirm that the PhD thesis entitled “Lattice Boltzmann numerical and experimental studies of bubble dynamics” has been written independently and without any other sources than cited.

Luxembourg, _____ _____

Guanchen LIU

Abstract

Boiling heat transfer is fundamentally governed by the dynamics of vapor bubbles, whose nucleation, growth, and departure control both local heat transfer and macroscopic performance. This dissertation presents a comprehensive investigation of single-bubble boiling dynamics through an integrated numerical–experimental framework.

On the numerical side, an advanced thermal multiphase lattice Boltzmann method (LBM) is developed and implemented. The framework is based on the Huang–MRT pseudopotential formulation, combined with a virtual-density wetting scheme and Peng–Robinson equation of state, enabling stable and tunable control of surface tension, density ratio, and contact angle. The model is validated through a series of benchmark tests, including thermodynamic consistency, Laplace law, droplet and thin-film evaporation, and contact-angle calibration, thereby establishing its reliability for phase-change simulations.

On the experimental side, a dedicated single-bubble boiling facility is constructed using a laser-patterned indium–tin–oxide (ITO) heater. High-speed visualization combined with automated image processing provides quantitative measurements of bubble departure diameter, frequency, and growth characteristics. These experiments serve as a direct validation platform for the numerical predictions.

Systematic comparisons between LBM simulations, experimental data, and classical theoretical correlations reveal clear limitations of static, quasi-equilibrium models such as those of Fritz and Cole, which perform reasonably at low Jakob numbers but fail under stronger superheating or hydrophobic conditions. By incorporating both the Jakob number and surface wettability, a refined semi-empirical correlation is proposed, achieving improved agreement with both simulations and experiments. Furthermore, force-balance analyses clarify the transition of dominant detachment mechanisms across different regimes, highlighting the interplay between buoyancy, surface tension, and unsteady drag forces.

Beyond the detailed analysis of single-bubble dynamics, the validated LBM framework is extended to investigate pool boiling, structured surfaces, and selected three-dimensional configurations. These studies demonstrate the model's capability to address complex boiling scenarios and provide insights into surface–fluid interactions and heat transfer enhancement strategies.

Overall, this dissertation establishes a state-of-the-art LBM-based framework, supported by targeted experimental validation, for predictive investigation of nucleate boiling. The findings advance the fundamental understanding of bubble departure mechanisms, refine the applicability of classical boiling models, and lay a foundation for future multiscale modeling and engineering-scale thermal management applications.

Acknowledgements

The completion of this dissertation has only been possible thanks to the generous support, guidance, and encouragement of many individuals and institutions. I would like to take this opportunity to express my sincere gratitude to all those who have contributed to this work.

First and foremost, I am deeply indebted to my supervisor, Prof. Stephan Leyer, for his continuous guidance, patience, and support throughout my doctoral journey. Even during my initial adaptation when language barriers were a challenge, his encouragement and constructive advice proved invaluable. His detailed feedback on every research problem, combined with his academic rigor and generosity, has profoundly shaped my development as a researcher. I am equally grateful to Prof. Stefan Maas and Dr. Nikolaos Prasianakis, members of my CET committee. Dr. Prasianakis, as an expert in lattice Boltzmann methods, has provided highly professional advice that helped me quickly identify the essence of complex problems and avoid many detours.

This research was conducted within the framework of the Thermal Engineering Group led by Prof. Leyer, whose support I gratefully acknowledge. Financial support from the China Scholarship Council (CSC) through a Public Welfare Scholarship is also sincerely appreciated, as it provided the opportunity to pursue this doctoral research abroad.

The experimental part of this work would not have been possible without the assistance of the technical staff at DOE laboratories. I am particularly grateful to Grace Ligbado for project coordination and management, to Daniel Warnimont for equipment installation, sample preparation, and system debugging, and to Vicente Reis Adonis, Claude Colle, and Ralph Reiter for their contributions to machining and component fabrication. Their efforts were fundamental to the success of the experiments. I also warmly acknowledge the support of the administrative staff, whose assistance facilitated many aspects of this work.

Special thanks go to Prof. em. Dr. Horst-Michael Prasser (ETH Zürich), who generously provided image-processing algorithms tailored to my experiments, thereby establishing a direct link between the experimental measurements and numerical simulations. I am also grateful to Dr. Iurii Dolganov and Dr. Dionysios Stefanitsis for their valuable suggestions on experimental design. In addition, I would like to

thank Dr. Tobias Jäger for his kind guidance during my learning process of numerical coding, which helped me gain a deeper understanding of the computational framework.

I am thankful as well to all members of the Thermal Engineering Group for their support, collaboration, and collegial atmosphere, which made the research process both productive and enjoyable.

Finally, I owe my deepest gratitude to my family and friends for their unconditional love, patience, and encouragement. Their unwavering support has been a constant source of strength, and this dissertation is dedicated to them.

Guanchen LIU
Luxembourg, August, 2025

Contents

List of Figures

List of Tables

Abbreviations

LBM	Lattice Boltzmann Method
CFD	Computational Fluid Dynamics
N-S equation	Navier-Stokes equations
D2Q9, D3Q19	Velocity discrete model in LBM
SRT (BGK)	Single-Relaxation Time model
MRT	Multiple-Relaxation Time model
TRT	Two-Relaxation Time model
LBGK	Lattice BGK model
CHF	Critical Heat Flux
ONB	Onset of Nucleate Boiling
Ja	Jakob number
Bo	Bond number
We	Weber number
Re	Reynolds number
Nu	Nusselt number
Pr	Prandtl number
Pe	Peclet number
q"	Local heat flux (W/m^2)
$\underline{q}$	Average heat flux (W/m^2)
$\mathbf{d_b}$	Bubble departure diameter (m)
$\mathbf{f_d}$	Bubble departure frequency (Hz)
LU (or l.u.)	Lattice unit
SC model	Shan–Chen pseudopotential model
EOS	Equation of State
VLE	vapor–liquid equilibrium
vdW EOS	van der Waals Equation of State
PR EOS	Peng–Robinson Equation of State
RK EOS	Redlich–Kwong Equation of State
VCM	Velocity Correction Method

FDM	Finite Difference Method
EDM	Exact Difference Method
DFM	Discrete Force Method
RK4	Runge–Kutta 4th-order method
AD	Absolute deviation
RE	Relative error (%)
TV	Temperature variation
LH	Local Heat flux distribution
LHV	Local Heat flux Variation

Greek Symbols

τ	Relaxation time
Δt	Time step
c_s	Speed of sound in lattice units
T	Temperature (K)
ΔT	Superheat or temperature difference (K)
ε	Thermal diffusivity (m^2/s)
σ	Surface tension (N/m)
μ	Dynamic viscosity ($Pa \cdot s$)
λ	Thermal conductivity ($W/(m \cdot K)$)
λ_s	Thermal conductivity of solid ($W/(m \cdot K)$)
ρ	Density (kg/m^3)
ω	Acentric factor (dimensionless)
χ	Scaling factor for heat flux
β	Weight factor in MRT or force models
ν	Kinematic viscosity (m^2/s)
α	Direction index or thermal diffusivity
θ	Contact angle (°)
ϕ	Contact angle control parameter

ψ	Pseudopotential function
$\Delta\rho$	Density difference between phases

Subscripts

c	Critical state or property
eq	Equilibrium value
x, y, z	Cartesian coordinates
l	Liquid phase
v	Vapor phase
s	Saturation value
r	Reference or unit conversion
e	Discrete velocity direction
ave	Averaged quantity
max	Maximum value
min	Minimum value
ps	Physical unit
lb	Lattice unit
b	Bubble
d	Departure (used in f_d, d_b)
w	Wetting/contact line (e.g., d_w)

Chapter 1

Introduction And Motivation

Boiling heat transfer, characterized by the formation and evolution of vapor bubbles, plays a critical role in numerous industrial and engineering applications, including thermal energy conversion, electronics cooling, and microfluidic systems. At the core of this complex phase-change process lies the behavior of individual bubbles, which significantly influences the efficiency of heat transfer and the stability of the system. The ability to accurately simulate and experimentally capture the dynamics of a single bubble is essential to developing a comprehensive understanding of boiling phenomena and improving the design of advanced thermal systems. This chapter provides a detailed overview of the relevant background, boiling mechanisms, research challenges, and recent developments in the field. In addition, it introduces the motivation for the research, outlines the objectives and scope of the study, and highlights the primary contributions and structure of the thesis.

1.1 Background and Research Significance

Bubble dynamics represents a fundamental topic in multiphase fluid mechanics, holding significant relevance across a wide range of engineering and natural systems. Bubble formation occurs through various mechanisms, primarily influenced by factors such as gas solubility in the liquid, variations in temperature and pressure, the presence of impurities, and interfacial properties. The evolution of a bubble - from nucleation to growth, motion, and eventual collapse or departure - plays a critical role in determining the efficiency and stability of heat and mass

transfer processes. In particular, during boiling, the behavior of single bubbles directly influences the local heat flux, surface temperature distribution, and the overall thermal performance of the system.

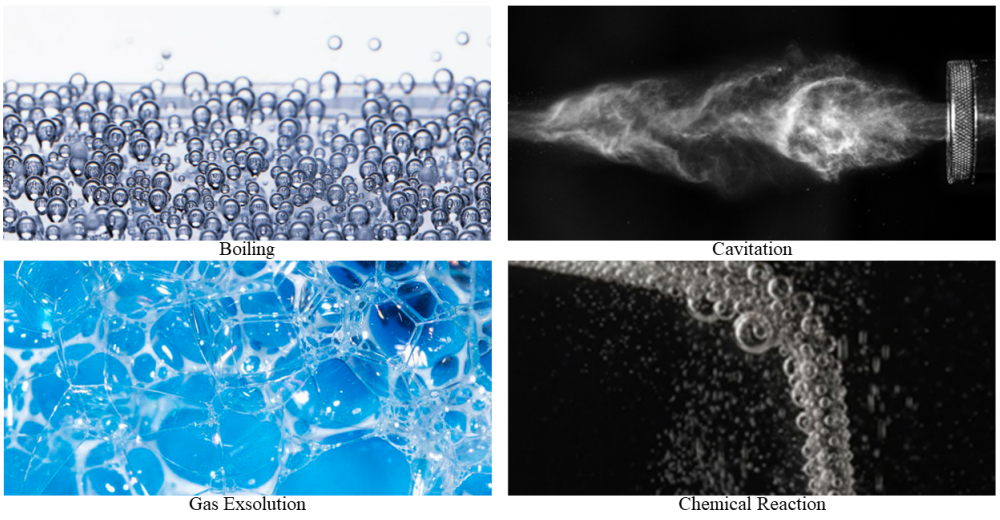

FIG. 1.1: Bubble phenomena

In recent years, the rapid advancement of electronics, energy systems, and microfluidic technologies has drastically increased the demand for efficient thermal management solutions. Boiling heat transfer, characterized by the phase change from liquid to vapor accompanied by bubble formation, offers superior heat transfer coefficients due to the absorption of latent heat. This makes it a highly attractive mechanism in high-flux thermal systems. However, inherently complex interfacial dynamics, strong coupling between thermal and hydrodynamic effects, and the stochastic nature of bubble nucleation events pose substantial challenges for both researchers and engineers. Therefore, a deep understanding of single-bubble behavior is of paramount importance, as it not only constitutes the fundamental building block of boiling phenomena but also exerts a direct influence on local thermal responses and system-level performance. Accurate modeling and experimental observation of single-bubble dynamics enable researchers to better interpret complex multibubble interactions and provide a robust theoretical foundation for the optimization and prediction of boiling heat transfer in practical systems. In summary, the study of single-bubble dynamics serves as a critical pathway toward revealing the microscopic mechanisms of boiling heat transfer and acts as a vital bridge between fundamental theory and engineering applications.

1.2 Boiling Phenomena and Research Approaches

Boiling phenomena involve complex bubble dynamics that are governed by interfacial forces, thermal gradients, and hydrodynamic conditions. In order to better understand and model this multiphase phenomenon effectively, it is very important to examine both the fundamental mechanisms of bubble dynamics and their specific mainfestations in boiling systems. The following subsections provide a conceptual overview of the classical boiling regimes and boiling curve, followed by a discussion of the experimental and numerical methods widely used in boiling research.

1.2.1 Boiling applications

The vapor-liquid phase transition [7] is widely utilized in both daily life and industrial engineering, with evaporation and boiling being two representative examples. Compared with evaporation, boiling is a more complex and intense phase-transition process, characterized by the generation of discrete vapor bubbles within superheated liquid near or on heated surfaces. This process involves not only dynamic interfacial behavior, but also the nucleation and evolution of phase boundaries [8]. From the perspective of heat transfer [9], boiling [10] exhibits an inherent advantage over single-phase convection, thanks to the latent heat associated with phase transition. This enables boiling to achieve significantly higher heat transfer coefficients under relatively small temperature differences.

In recent years,the growing demand for efficient thermal management in microelectronics and photonics has highlighted the importance of boiling heat transfer. For example, heat flux densities in integrated circuits have already exceeded 1000 W/cm^2 [11], and are projected to increase further. As chip performance is highly sensitive to temperature, excessive heat can result in degraded function or catastrophic failure. Therefore, improving boiling performance is critical for ensuring the reliability and efficiency of high-density heat-generating devices [12]. Boiling heat transfer is also essential in nuclear reactors, where it plays a central role in steam generation and reactor cooling. In chemical processing and power generation, boiling contributes to phase-change heat exchangers, distillation units, and thermal energy storage systems. In aerospace and biomedical devices, boiling is employed in compact heat removal systems, particularly under reduced gravity or

confined space conditions. Depending on the characteristics of the fluid motion [13], the boiling can be classified as pool boiling and flow boiling. Pool boiling occurs under natural convection, while flow boiling includes external and internal forced convection cases [14]. Pool boiling, which is free of external pumping, is widely used for fundamental research.

The enhancement and control of boiling are of major interest in engineering design. This includes controlling bubble departure, suppressing dry-out, delaying transition to film boiling, and maximizing critical heat flux. Therefore, understanding bubble dynamics is not just a matter of academic interest—it is a practical necessity for improving the safety, efficiency, and compactness of thermal systems.

1.2.2 Mechanisms and Boiling Curve

As the liquid temperature rises to or above its saturation point, the vapor bubbles begin to nucleate, grow, and depart, driven by thermal and mechanical interactions within the fluid. This dynamic process is influenced by multiple parameters, including surface wettability, microstructure geometry, local subcooling, and superheat levels, which make modeling and control of boiling challenging and essential for high-performance heat transfer systems. The boiling process can be classified into pool boiling and flow boiling, depending on whether the liquid motion is driven by natural convection or external flow. In pool boiling, which is more relevant to fundamental studies, the liquid remains largely stationary except for motion induced by bubble activity. The heat transfer behavior during pool boiling is traditionally described using the classical boiling curve, which relates heat flux to surface superheat (the temperature difference between the heated surface and the liquid's saturation temperature).

The classical boiling curve, first established through systematic experiments by Shiro Nukiyama in 1934 [1], his pool boiling experiments received high recognition in the international heat transfer community and were the first to elucidate the physical principles of boiling phenomena.

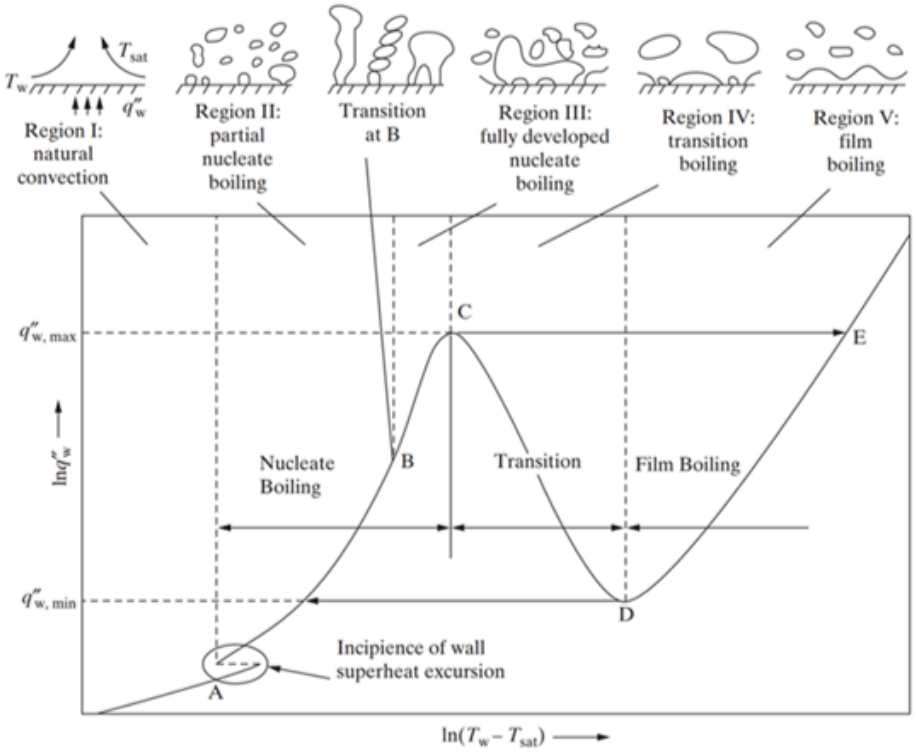

FIG. 1.2: Boiling curve from Shiro Nukiyama's pool boiling experiment [1]

In his experiments, water was used as the working fluid, and a horizontal heating wire served as the heated surface. The surface temperature of the heating wire was determined by measuring the resistance variation with temperature, while the heat flux was controlled by adjusting the electrical power input. As shown in Fig. 1.2, four major boiling regimes were defined: the boiling process sequentially passes through the natural convection [15] (O-A), nucleate boiling [16] (A-B-C), transition boiling [17] (C-D) and film boiling [18] (D-E).

1. Natural Convection (Region O–A) :
   At small surface superheat, heat transfer occurs mainly through natural convection. No bubbles have formed yet, the heat transfer coefficient remains low, and the relationship between surface superheat and heat flux is approximately linear.

2. Nucleate boiling (Region A–C):
   With increased superheat, vapor bubbles begin to nucleate at discrete sites on the heating surface, with point A known as the onset point of nucleate boiling (ONB). In the early stage (A–B), both natural convection and bubble-induced convection contribute to heat transfer. As nucleation becomes more

intense, the system enters the fully developed nucleate boiling regime (B–C), characterized by frequent bubble formation, coalescence, and detachment. The heat flux reaches a peak at point C, known as the Critical Heat Flux (CHF). At this point, the liquid can no longer completely wet the surface between successive bubble departures.

3. Transition Boiling (Region C–D):
   Beyond the CHF point, the liquid begins to lose contact with the portion of the surface, forming intermittent patches of vapor. Heat transfer becomes unstable and heat flux drops despite increasing surface temperature. Point D marks the Leidenfrost point [19], where the minimum heat flux occurs.

4. Film Boiling (Region D–E):
   At high superheat, a continuous vapor film insulates the heating surface from the liquid. Heat transfer in this regime is dominated by conduction and radiation through the vapor layer, resulting in significantly reduced thermal performance and a possible risk of thermal failure.

Each regime of the boiling curve is associated with distinct bubble dynamics. In nucleate boiling, for instance, the interaction between bubbles and the heating surface strongly enhances heat transfer. Conversely, in film boiling, the absence of direct liquid–surface contact leads to thermal resistance buildup and reduced efficiency. Therefore, understanding and controlling the nucleate boiling stage is crucial for optimizing heat transfer while avoiding undesirable transition to film boiling.

To analyze and predict boiling behavior, especially in engineering applications, numerous empirical and semi-theoretical correlations have been proposed. Among them, Rohsenow's correlation [20] is one of the most representative for estimating the heat flux in nucleate boiling, relating it to fluid properties, wall superheat, and a surface–liquid interaction coefficient [21]. However, this formulation is applicable primarily to nucleate boiling heat flux prediction and its validity is limited when extended to other boiling regimes or complex surface conditions. The equation is typically expressed as:

$$q'' = \mu_l h_{fg} \left[\frac{g(\rho_l - \rho_v)}{\sigma} \right]^{1/2} \left(\frac{c_p(T_w - T_{sat})}{C_{sf} h_{fg} Pr^n} \right)^3 \tag{1.1}$$

where:
- q'': heat flux
- μ_l: liquid viscosity
- h_{fg}: latent heat of vaporization
- ρ_l, ρ_v: densities of liquid and vapor
- σ: surface tension
- $T_w - T_{sat}$: wall superheat
- c_p: specific heat
- Pr: Prandtl number
- C_{sf}: surface-fluid interaction coefficient

In addition, among the many empirical and semi-theoretical correlations developed for critical heat flux (CHF) prediction, the Zuber [22] and Kutateladze [23] models are two of the most representative examples. Both are derived from hydrodynamic instability theory and incorporate the effects of surface tension, density difference between liquid and vapor, and gravitational acceleration.

Zuber's model:

$$q''_{\text{CHF, Zuber}} = \frac{\pi}{24}\rho_v h_{fg}\left[\frac{\sigma g(\rho_l - \rho_v)}{\rho_v^2}\right]^{1/4} \tag{1.2}$$

Kutateladze's model:

$$q''_{\text{CHF, Kutateladze}} = C_K \rho_v^{1/2} h_{fg}\left[\sigma g(\rho_l - \rho_v)\right]^{1/4} \tag{1.3}$$

While these correlations are widely used and provide valuable first-order estimates of CHF, they are based on simplified assumptions and are primarily validated for pool boiling on smooth, horizontal surfaces under normal gravity. Their predictive accuracy diminishes for structured or micro-scale surfaces, non-uniform heating, reduced gravity, or complex geometries. Consequently, in advanced applications, these models often require empirical correction factors or coupling with high-fidelity numerical simulations.

In summary, the classical boiling curve and the above-mentioned correlations represent only a small subset of the many empirical and semi-theoretical approaches developed over decades of boiling research. While these methods provide valuable

insight into regime classification and offer practical estimates of heat flux or critical heat flux, their applicability is inherently limited by simplified assumptions, restricted operating conditions, and sensitivity to surface and fluid properties. In particular, they often fail to capture the complex coupling between interfacial dynamics, transient thermal transport, and microscale surface characteristics that governs boiling heat transfer in modern engineered systems.

These limitations underscore the need for more physics-informed and versatile modeling approaches capable of resolving boiling phenomena from the bubble scale upward. By integrating high-resolution experiments with advanced numerical simulations, such as the lattice Boltzmann method, it becomes possible to bridge the gap between macroscopic correlations and the underlying microscale mechanisms, enabling more accurate prediction and control of boiling processes in both fundamental studies and engineering applications.

1.2.3 Experimental and Numerical Investigation Method

To investigate boiling phenomena comprehensively, both experimental observation and numerical simulation have been extensively employed. Each approach offers unique advantages and limitations in revealing bubble-scale mechanisms and quantifying thermal performance. From an experimental perspective, boiling processes can be investigated through a combination of visualization, thermal measurement, and flow diagnostics. Among them, high-speed imaging is one of the most common tools, enabling real-time capture of bubble nucleation, growth, coalescence, and departure. Infrared thermography is particularly effective for capturing transient temperature distributions on heated surfaces during phase change. Furthermore, advanced optical techniques such as Particle Image Velocimetry (PIV) and Laser-Induced Fluorescence (LIF) allow for the analysis of velocity fields and temperature distributions [24–26]. In addition to these methods, microfabricated heater-sensor arrays and MEMS-based platforms provide high spatial and temporal resolution measurements of localized heat flux and temperature, making them ideal for studying microscale boiling phenomena [27, 28]. In recent years, non-invasive imaging methods such as X-ray radiography and neutron imaging have also been increasingly employed to visualize internal flow structures and bubble dynamics in opaque fluids or confined geometries [29, 30].

Although these experimental techniques have significantly advanced the understanding of boiling heat transfer, they still face several inherent limitations. Practical challenges include high equipment costs, complex calibration procedures, and restricted optical access in geometrically confined environments. In particular, resolving transient interfacial phenomena at the microscale remains a formidable task.

Moreover, most experimental investigations rely on macroscopic observations, which inevitably introduces measurement uncertainties and limits overall precision. For instance, McHale et al. reported that measurement uncertainties in length and time dimensions in nucleate boiling experiments are approximately 2.9 % and 2.5 %, respectively [31]. Moreover, when boiling on microstructured surfaces is studied, it is difficult to achieve precise control over surface morphology and wettability [32]. Furthermore, accurately measuring localized thermal parameters, such as surface temperature, heat flux, and interfacial velocity, poses substantial technical challenges that can hinder the reliability and resolution of the experimental results [33]; for instance, measurement uncertainties in wall temperature and local heat flux can reach 2.8 K and 6.3%, respectively, even under controlled experimental conditions [34].

In contract, numerical simulation offers a powerful and flexible tool for investigating boiling dynamics within a highly controlled virtual environment. For studies involving boiling or phase separation, traditional computational fluid dynamics (CFD) approaches typically solve the Navier–Stokes equations coupled with energy conservation equations. To achieve model closure, phase change is typically incorporated through the introduction of energy source terms or empirical correlations. For example, nucleation sites, interfacial heat transfer rates, and vapor generation rates are often predefined or artificially prescribed based on assumed physical models. In addition, various interface capture or tracking techniques are required to resolve the liquid–vapor separation and accurately describe interfacial dynamics. Among the widely used methods are:

Volume of Fluid (VOF): tracks the volume fraction of each phase within grid cells; suitable for large interface deformation, but may suffer from numerical diffusion.

Level Set Method: defines a signed distance function to capture the interface location with high smoothness but requires reinitialization and may lose mass conservation.

Front Tracking Method: explicitly tracks the moving interface using marker points; accurate but complex to implement.

Phase Field Method: introduces a diffuse interface governed by Cahn–Hilliard equations, suitable for modeling interface thermodynamics and topological changes.

These modeling dependencies make simulation results highly sensitive to underlying assumptions and parameter tuning. Without appropriate simplifications or calibrations, significant discrepancies often arise between numerical predictions and experimental observations. In response to these limitations, mesoscale modeling techniques have emerged as promising alternatives. Among them, the Lattice Boltzmann Method (LBM) offers distinct advantages in simulating interfacial dynamics and multiphase flows. The subsequent chapters will elaborate on the LBM framework, its implementation for bubble dynamics, and its validation against experimental observations.

1.3 Research Motivation and Scientific Challenge

Despite decades of research, the microscopic mechanisms governing boiling heat transfer—particularly the dynamics of individual vapor bubbles—remain incompletely understood. This knowledge gap arises from the intrinsic complexity of interfacial phenomena, which involve coupled interactions among microscale capillary forces, unsteady thermal conduction, and stochastic nucleation processes. Conventional experimental and numerical approaches each face limitations in resolving these dynamics with sufficient spatial–temporal fidelity.

From an experimental perspective, capturing single-bubble behavior such as departure diameter, frequency, and nucleation site activity demands extremely high temporal and spatial resolution. Achieving repeatable nucleation events under well-controlled surface and thermal conditions is technically challenging, which complicates the reproducibility and accuracy of measured local heat transfer parameters.

From a numerical standpoint, traditional CFD-based boiling simulations typically rely on empirical closure laws or semi-empirical correlations to approximate phase-change processes. Such models require assumptions about nucleation site distribution, vapor generation rate, and interfacial heat transfer, which can limit their predictive capability and cause deviations from experimental reality—especially for structured surfaces or microscale boiling conditions.

These challenges motivated the implementation of a dedicated Lattice Boltzmann Method (LBM) framework for boiling simulation, driven by the following considerations:

1. **Integration of state-of-the-art sub-models** – The framework incorporates advanced multiphase and thermal models, including improved formulations such as the virtual density approach for accurate contact angle control, enhanced force discretization schemes (Huang-MRT), and a fourth-order Runge–Kutta method (RK4) for robust and accurate thermal coupling in the heat solver.

2. **Lack of openly accessible high-fidelity boiling codes** - While there are partial implementations of LBM in the literature, there is no publicly available code that integrates all advanced models required for accurate and robust boiling simulations in one framework.

3. **Comprehensive coverage of boiling-relevant physics** – The model accounts for all key physical mechanisms in boiling, including nucleation, bubble growth, coalescence, detachment, phase-change heat transfer, and wettability effects.

4. **Direct validation with controlled experiments** – The availability of well-designed single-bubble boiling experiments allows direct, quantitative validation of the simulation results, strengthening the link between numerical predictions and physical reality.

5. **Capability to study both simple and complex configurations** – The code enables simulation of canonical single-bubble problems as well as realistic structured surfaces and complex geometries, supporting both fundamental research and design optimization.

6. **Evaluation of closure laws for continuum-scale CFD** – The framework serves as a numerical laboratory for testing and refining boiling-related closure models, such as correlations for bubble departure diameter and frequency, which are critical for larger-scale CFD applications.

1.4 Research Objectives and Main Content of This Study

Building upon the challenges outlined in Section 1.2.2 and the motivation discussed above, the primary objective of this work is to implement and validate a high-fidelity, state-of-the-art lattice Boltzmann method (LBM) framework for boiling heat transfer. The framework integrates advanced multiphase and thermal sub-models, covers all key physical mechanisms relevant to single-bubble boiling, and is directly validated against controlled experiments. By combining numerical simulation and experimental measurement, this study aims to bridge the gap between simplified empirical correlations and the underlying microscale physics, thereby enabling more accurate prediction and control of boiling phenomena. The specific objectives are:

1. **Implement an advanced LBM framework for boiling simulation**
   Implement a two- and three-dimensional Shan–Chen pseudopotential LBM model, incorporating state-of-the-art sub-models such as the virtual density approach for accurate contact angle control, the Huang–MRT collision operator for improved stability, and a fourth-order Runge–Kutta (RK4) scheme for robust thermal coupling.

2. **Validate the model through benchmark tests and controlled experiments**
   Conduct comprehensive numerical verifications, including thermodynamic consistency, Laplace law, D^2-law, pressure tensor evaluation, and evaporation benchmarks. Design and perform single-bubble boiling experiments with precise control of nucleation sites, enabling quantitative validation of bubble departure diameter, frequency, and growth dynamics.

3. **Investigate bubble dynamics on various surface configurations**
   Study the effects of surface morphology (flat, rectangular, and V-grooved)

and wettability (hydrophilic to hydrophobic) on bubble nucleation, growth, and departure, providing physical insight into boiling enhancement mechanisms.

4. **Compare with theoretical models and propose refined correlations** Systematically compare LBM predictions with experimental measurements and classical empirical correlations (e.g., Fritz, Cole). Develop new predictive relations for bubble departure diameter as a function of the Jacob number and contact angle.

5. **Extend the LBM framework to complex boiling phenomena** Apply the model to pool boiling over planar and structured surfaces to demonstrate its versatility and potential for optimizing heat transfer designs in engineering applications.

The insights gained from this research are expected to contribute to the development of predictive, experimentally validated simulation tools for microscale boiling phenomena, with applications in electronics cooling, energy systems, and other thermal management technologies.

1.5 Contributions and Innovations

The main contributions and innovations of this study can be summarized as follows:

1. **Development of a customized LBM framework for single bubble boiling simulations** Unlike conventional CFD tools (e.g. Ansys Fluent) that rely on standardized commercial platforms, LBM requires user-developed implementations. Due to the lack of publicly available LBM code, in this study, which I built entirely from scratch, the code integrates advanced multiphase and thermal models, including the virtual density approach for precise contact angle control, the Huang–MRT collision operator for enhanced numerical stability, and a fourth-order Runge–Kutta (RK4) scheme for accurate thermal coupling. This combination enables robust simulation of nucleation, growth, coalescence, and departure of vapor bubbles in both 2D and 3D.

2. **Comprehensive physical coverage for boiling-relevant phenomena** The framework captures all key mechanisms in boiling heat transfer, nucleation, phase change, surface tension effects, wettability, and bubble-surface interaction, allowing a detailed analysis of both fundamental single-bubble dynamics and complex surface boiling configurations.

3. **Experimental design for direct model validation** A controlled single-bubble boiling experiment was developed using ITO-coated glass in laser pattern to trigger repeatable nucleation events. High-speed imaging and automated image analysis were used to extract quantitative bubble parameters (departure diameter, growth rate, frequency), allowing direct validation of the LBM model.

4. **Quantitative comparison and refinement of closure models** Simulation results were compared with experimental measurements and classical empirical correlations (e.g., Fritz, Cole). Based on the LBM–experiment agreement, a new semi-empirical correlation for bubble departure diameter was proposed as a function of Jacob number and contact angle, offering improved predictive accuracy for CFD closure laws.

5. **Extension to complex boiling simulations for engineering applications** The validated LBM framework was applied to pool boiling over planar and structured surfaces, demonstrating its versatility for studying heat transfer enhancement strategies and its potential as a numerical testbed for surface design optimization.

1.6 Thesis organization

This dissertation is organized into eight chapters that progress from motivation and background, through model development and validation, to comparative analysis, numerical extensions, and final perspectives. The structure is designed to move from fundamentals to applications while maintaining a consistent thread between numerical modeling, experimental observation, and theoretical interpretation.

Chapter 1 sets the stage with the background and significance of boiling heat transfer, introduces the research motivation and scientific challenges, and outlines

the objectives, scope, and contributions of the study. It also surveys classical boiling regimes and representative correlations, and positions the lattice Boltzmann method (LBM) as a mesoscale framework capable of bridging empirical practice and microscale physics.

Chapter 2 formulates the LBM framework adopted in this work. It reviews force incorporation in LBM, details the Huang–MRT pseudopotential formulation and its implementation, and describes the coupling to the energy equation. The computational setup and unit–conversion strategies are specified. The chapter then conducts a suite of benchmark validations, including thermodynamic consistency and vapor–liquid coexistence, Laplace's law and pressure–tensor evaluation, thin-film evaporation and the droplet D^2–law, as well as wettability and contact–angle calibration, establishing both numerical stability and thermodynamic consistency.

Chapter 3 turns to single-bubble simulations and defines the numerical scenarios used to interrogate bubble dynamics. It discusses the evolution of density, temperature, and flow fields throughout nucleation, growth, departure, and collapse; introduces and compares fixed-temperature and constant-heat-flux boundary conditions; and clarifies how wettability and heating mode shape cycle evolution and local heat–flux response.

Chapter 4 presents the experimental framework for controlled single-bubble boiling. It describes the laser-patterned ITO microheater, the integrated apparatus and diagnostics, and the assessment of measurement uncertainties. Methods for surface–temperature measurement and calibration are provided, together with an image–processing pipeline (background modeling, flood–fill segmentation, feature extraction) that delivers quantitative bubble metrics for comparison with simulations.

Chapter 5 reports experimental results and performs quantitative validation of the LBM predictions. It compares departure diameter, growth behavior, and frequency across operating conditions, analyzes agreements and discrepancies, and examines unified scalings linking simulation and experiment. The outcome is an evidence–based assessment of the framework's predictive capability for single–bubble dynamics.

Chapter 6 systematically contrasts LBM predictions with state-of-the-art correlations and theoretical models for key bubble parameters. Beyond classical empirical

relations (e.g., Fritz, Cole), the chapter employs a force–balance analysis to diagnose departures between models and simulations, identifies regime-dependent error sources, and develops a refined correlation that incorporates both Jakob number and contact angle. Sensitivity to contact diameter modeling and contact angle is discussed in the context of closure development.

Chapter 7 extends the validated framework to more complex configurations. It demonstrates single–bubble nucleation on structured heaters (rectangular and V–shaped), explores pool boiling under alternative boundary conditions, investigates structured and mixed-wettability surfaces, and constructs preliminary boiling curves, illustrating how the model can interrogate heat–transfer enhancement mechanisms and surface–fluid interactions.

Chapter 8 concludes the dissertation. It synthesizes the principal findings, highlights the contributions of the integrated numerical–experimental approach, and outlines future directions, including higher physical fidelity (e.g., increased density ratios, temperature–dependent properties, Marangoni effects), three–dimensional simulations, flow and subcooled boiling, closure–model development and multiscale coupling, and upgrades to the experimental platform. A brief closing remarks section discusses how the proposed LBM framework can serve as a bridge between microscale mechanisms and engineering-scale thermal management applications.

1.7 Support

This work was carried out within the framework of a collaborative project between the Thermal Engineering Group at the University of Luxembourg and the DOE Thermodynamics Group, whose support is gratefully acknowledged. The author also acknowledges support from the China Scholarship Council (Public Welfare Scholarship).

Chapter 2

LBM Model and Benchmark Tests

This chapter unifies the numerical methodology and its benchmark validation into a single, coherent narrative. To keep the main text focused, detailed descriptions of the four mainstream LBM phase-separation models (e.g., color-gradient [35], free-energy [36], pseudopotential [2], and phase-field [37]) as well as forcing variants (e.g., the classical Shan–Chen construction [2], weighted-gradient formulations [38], and discrete forcing schemes such as Guo [39]) are deferred to the appendix.

In this chapter, I first introduce the LBM framework: pseudopotential formulation, Huang–MRT collision operator, contact-angle control via the virtual-density scheme, thermal coupling, and boundary conditions. And then validate the implementation against canonical tests (Laplace law, D^2-law, pressure-tensor consistency, thin-film evaporation, and contact-angle calibration), thereby establishing the model's accuracy and robustness for the application studies that follow.

2.1 Review of LBM Principle

The mesoscopic and particle characteristics of the lattice Boltzmann method (LBM) give it a unique advantage in solving problems related to interface dynamics, such as multiphase flows. Among the different phase separation models, the pseudopotential model is particularly notable because of its simple and straightforward approach. Shan and Chen introduced it in their pioneering work, where it was

applied to simulate multiphase and multicomponent flows using LBM [2][40]. For this reason, the pseudopotential model is often referred to as the "Shan-Chen model" (SC model).

In LBM, fluid behavior is described by the evolution of distribution functions associated with discrete particle velocities. The governing equation varies depending on the presence of external sources (e.g., body forces or heat sources). In the absence of such terms, and using the single-relaxation-time (BGK/SRT) collision operator [41], the evolution equation is expressed as:

$$f_i(\mathbf{x} + \mathbf{e}_i \Delta t, t + \Delta t) = f_i(\mathbf{x}, t) - \frac{1}{\tau}\left(f_i(\mathbf{x}, t) - f_i^{\mathrm{eq}}(\mathbf{x}, t)\right) \tag{2.1}$$

Here, $f_i(\mathbf{x}, t)$ denotes the distribution function of particles moving in the i-th lattice direction with velocity $\mathbf{e}_i$, at position $\mathbf{x}$ and time t. The relaxation time τ governs the rate of return to equilibrium and is related to the kinematic viscosity ν by:

$$\nu = c_s^2(\tau - 0.5)\Delta t,$$

where c_s is the lattice speed of sound and Δt is the time step. The equilibrium distribution function f_i^{eq} is defined as:

$$f_i^{\mathrm{eq}} = \omega_i \rho \left[1 + \frac{\mathbf{e}_i \cdot \mathbf{u}}{c_s^2} + \frac{(\mathbf{e}_i \cdot \mathbf{u})^2}{2c_s^4} - \frac{\mathbf{u}^2}{2c_s^2}\right] \tag{2.2}$$

where ω_i is the lattice weight associated with the i-th direction, ρ is the fluid density, and $\mathbf{u}$ is the macroscopic velocity at position $\mathbf{x}$. The lattice sound speed c_s is related to the lattice velocity c by:

$$c_s = \frac{c}{\sqrt{3}}$$

In the D2Q9 velocity model, the distribution functions f_i correspond to discrete velocity directions. As shown in the Fig. 2.1, their physical meanings are categorized as follows:

- f_0: rest particle (zero velocity direction)
- f_1, f_3: particles moving along the horizontal (x) direction

- f_2, f_4: particles moving along the vertical (y) direction
- f_5, f_6, f_7, f_8: particles moving along the diagonal directions

These directional indices form the basis for streaming and collision operations in the LBM algorithm and are essential for constructing appropriate boundary conditions.

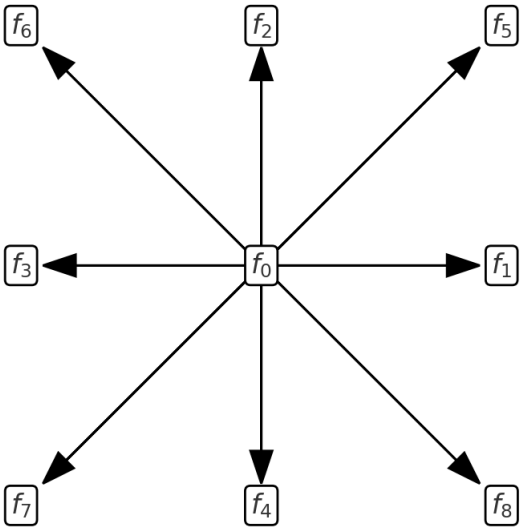

FIG. 2.1: Schematic of the computational domain

The most commonly used discrete velocity sets for 2D and 3D are D2Q9 and D3Q19, respectively, as illustrated in Fig. 2.2.

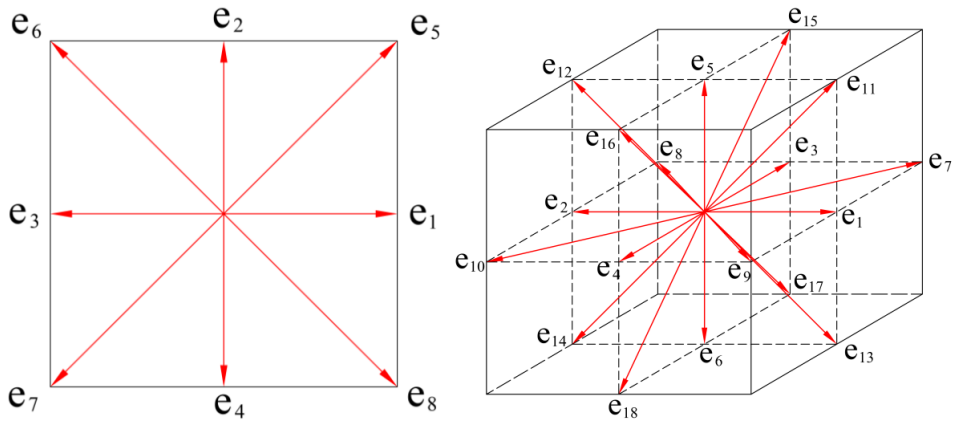

FIG. 2.2: Discrete velocity in D2Q9 lattice (left) and D3Q19 lattice (right). See ref. [2]

For the D2Q9 model, the lattice weights ω_i are defined as:

$$w_i = \begin{cases} 4/9 & i = 0 \\ 1/9 & i = 1 - 4 \\ 1/36 & i = 5 - 9 \end{cases} \tag{2.3}$$

and the corresponding discrete velocities $\mathbf{e}_i$ are given by:

$$\mathbf{e}_i = \begin{cases} (0,0), & i = 0 \\ (\pm 1, 0)c, (0, \pm 1)c, & i = 1 \sim 4 \\ (\pm 1, \pm 1)c, & i = 5 \sim 8 \end{cases} \tag{2.4}$$

Here, $c = \frac{\Delta x}{\Delta t}$ denotes the lattice velocity, where Δx is the lattice spacing and Δt is the time step. In most LBM implementations, both Δx and Δt are typically set to unity [42], yielding a normalized lattice velocity of $c = 1$.

For the D3Q19 model, the lattice weights ω_i and discrete velocities $\mathbf{e}_i$ are defined as:

$$w_i = \begin{cases} 1/3 & i = 0 \\ 1/18 & i = 1 - 6 \\ 1/36 & i = 7 - 18 \end{cases} \tag{2.5}$$

$$\mathbf{e}_i = \begin{cases} (0,0,0) & i = 0 \\ (\pm 1,0,0)c,\ (0,\pm 1,0)c,\ (0,0,\pm 1)c & i = 1-6 \\ (\pm 1,\pm 1,0)c,\ (\pm 1,0,\pm 1)c,\ (0,\pm 1,\pm 1)c & i = 7-18 \end{cases} \tag{2.6}$$

The macroscopic fluid density and velocity are computed from the distribution functions:

$$\rho = \sum_i f_i, \quad \rho\mathbf{u} = \sum_i \mathbf{e}_i f_i \tag{2.7}$$

By applying the Chapman–Enskog expansion [43], it can be shown that the LBM recovers the Navier–Stokes equations in the incompressible limit.

In summary, the evolution equation (2.1) describes two fundamental processes in LBM: the left-hand side represents particle propagation (streaming), while the right-hand side corresponds to local particle collisions. The distribution function f_i relaxes towards its equilibrium f_i^{eq} over a characteristic time scale τ. It should be noted that Eq. (2.1) applies to systems without external sources. To simulate more complex flows involving external forces (e.g. gravity, electromagnetic fields), a source term Ω_i must be incorporated into the evolution equation [44]:

$$f_i(\mathbf{x} + \mathbf{e}_i\Delta t, t + \Delta t) = f_i(\mathbf{x}, t) - \frac{1}{\tau}\left(f_i(\mathbf{x}, t) - f_i^{\mathrm{eq}}(\mathbf{x}, t)\right) + \Delta t\,\Omega_i. \tag{2.8}$$

Here, Ω_i accounts for the body forces acting on the fluid. In the present study, this includes gravity, interparticle interaction forces, and fluid–solid interactions. These force formulations and their implementation strategies will be discussed in detail in subsequent sections. Furthermore, the multiple-relaxation-time (MRT) collision model [45] used in this study will be introduced in the next subsection.

2.2 Force Incorporation in LBM

2.2.1 General Force Incorporation Methods

In order to correctly recover the macroscopic hydrodynamic governing equations, certain techniques are required to introduce forces into the LBM framework. Different methods of force incorporation affect both the numerical accuracy and stability of simulations [46]. Most existing schemes are formulated under the BGK (single-relaxation-time) collision model. It can be categorized into the following three types: velocity correction method (VCM) [47], discrete force method (DFM) [48], and exact difference method (EDM) [49]. The equilibrium distribution function in LBM is given by

The velocity correction method was first proposed by Shan and Chen [2]. This method modifies the fluid velocity in the equilibrium function using:

$$\mathbf{u}^{eq} = \mathbf{u} + \frac{\tau \mathbf{F}}{\rho}, \tag{2.9}$$

and the macroscopic velocity is updated as:

$$\rho \mathbf{U} = \rho \mathbf{u} + \frac{\delta_t}{2} \mathbf{F}. \tag{2.10}$$

This approach is straightforward and widely used in early pseudopotential models (e.g., SC [2] and Yuan-Schaefer models [50]), but it introduces truncation errors and lacks moment consistency in nonuniform force fields. Building on this approach, Guo et al. [39] further extended the LBM framework to handle external forces (e.g., gravity and electromagnetic forces) by applying the Shan-Chen velocity correction method, leading to the development of the Guo forcing scheme.

The second method is DFM, which directly adds a discretized force term F_i to the evolution equation. A commonly used discretization is the Guo forcing scheme [51]:

$$F_i = \left(1 - \frac{1}{2\tau}\right) \omega_i \left[\frac{\mathbf{e}_i - \mathbf{u}}{c_s^2} + \frac{(\mathbf{e}_i \cdot \mathbf{u})\mathbf{e}_i}{c_s^4}\right] \cdot \mathbf{F}, \tag{2.11}$$

which is known for improved accuracy and Galilean invariance.

In addition to the two aforementioned force incorporation methods, EDM [52] computes the effect of the force as the exact difference between two equilibrium distributions:

$$\Delta f_i = f_i^{eq}(\rho, \mathbf{u} + \Delta\mathbf{u}) - f_i^{eq}(\rho, \mathbf{u}), \tag{2.12}$$

where $\Delta\mathbf{u} = \mathbf{F}\delta_t/\rho$. Through this processing, EDM avoids force discretization and achieves better numerical consistency, especially in nonuniform fields. Table 2.1 summarizes the main features of these methods.

TABLE 2.1: Comparison of force incorporation methods under BGK operator

Method	**Advantages**	**Limitations**
VCM (e.g., Shan-Chen)	Compatible with classic pseudopotential models;	Implicit force treatment; lacks moment consistency;
DFM (e.g., Guo)	Explicit forcing; Galilean invariant	Requires discretization; sensitive to force formulation
EDM (e.g., Kupershtokh)	No discretization error; highly accurate in nonuniform fields	Less used in MRT framework; complex with thermal/multiphysics extensions

Among the commonly used force incorporation strategies, the VCM is simple but prone to numerical errors in non-uniform force fields; the DFM is more flexible but relies on empirical coefficients; while the EDM offers better theoretical consistency, it is primarily restricted to implementations based on the BGK collision operator. However, the BGK (single-relaxation-time) scheme itself imposes inherent limitations on numerical stability and accuracy, especially under conditions of strong phase change and high density ratios.

In this study, the interparticle force in the pseudopotential model is incorporated into the LBM evolution equation using the Guo forcing scheme [39], in conjunction with an EOS-based pseudopotential to model boiling flows. To overcome

the limitations of the BGK operator, a multi-relaxation-time (MRT) formulation is adopted, which enables independent relaxation of kinetic moments, suppresses spurious currents, and enhances the stability of multiphase simulations. The section below presents the MRT-based pseudopotential LBM framework employed in this study.

2.2.2 MRT-based Force Incorporation Framework

As previously discussed, the BGK operator exhibits limitations in stability and accuracy. To address these challenges, the multi-relaxation-time (MRT) model has been widely adopted due to its ability to relax different kinetic moments independently, thereby improving numerical stability and accuracy.

As illustrated in Fig. 2.3, while the evolution of the distribution function still a two-step process of collision and streaming, it involves transformations between velocity space and moment space via a collision matrix $\mathbf{M}$ and its inverse. This matrix-based procedure enables selective relaxation of physical moments, which enhances the control over numerical dissipation and reduces spurious currents.

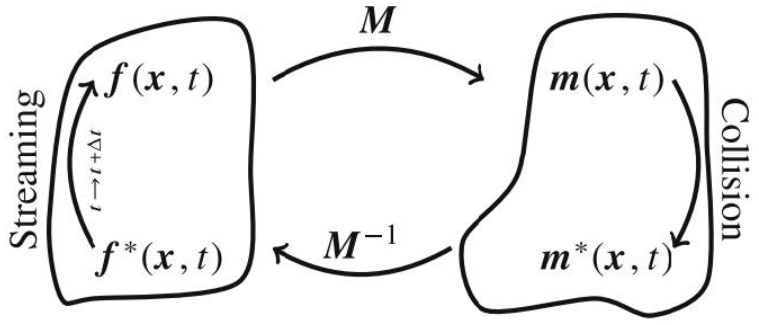

FIG. 2.3: MRT-based collision and streaming process.[2]

The MRT evolution loop can be summarized as:

$$\mathbf{f}(\mathbf{x},t) \xrightarrow{M} \mathbf{m}(\mathbf{x},t) \xrightarrow{\text{Collision}} \mathbf{m}^*(\mathbf{x},t) \xrightarrow{M^{-1}} \mathbf{f}^*(\mathbf{x},t) \xrightarrow{\text{Streaming}} \mathbf{f}(\mathbf{x}+\mathbf{e}_i\Delta t, t+\Delta t)$$

Here, $\mathbf{f}$ is the vector of the distribution function in velocity space; $\mathbf{m}$ is the moment vector; $\mathbf{m}^{\text{eq}}$ is equilibrium moment vector constructed from macroscopic quantities;

$\mathbf{f}^*, \mathbf{m}^*$ stands for the post-collision states; M, M^{-1} are transformation and inverse transformation matrices.

Specifically, $\mathbf{f}(\mathbf{x}, t)$ is first mapped to the moment space using the transformation matrix M:

$$\mathbf{m}(\mathbf{x}, t) = M \cdot \mathbf{f}(\mathbf{x}, t)$$

Then the post-collision moments are calculated using:

$$\mathbf{m}^*(\mathbf{x}, t) = \mathbf{m}(\mathbf{x}, t) - \mathbf{S}\left[\mathbf{m}(\mathbf{x}, t) - \mathbf{m}^{\mathrm{eq}}(\mathbf{x}, t)\right] \tag{2.13}$$

where $\mathbf{S}$ is a diagonal relaxation matrix. The post-collision distribution function is then recovered by:

$$\mathbf{f}^*(\mathbf{x}, t) = M^{-1} \cdot \mathbf{m}^*(\mathbf{x}, t) \tag{2.14}$$

After the collision step, the distribution functions are propagated to neighboring nodes according to the lattice velocities $\mathbf{e}_i$:

$$f_i(\mathbf{x} + \mathbf{e}_i \Delta t, t + \Delta t) = f_i^*(\mathbf{x}, t) \tag{2.15}$$

When an external force $\mathbf{F}$ is present, the LB equation in the MRT framework must be extended to incorporate the force term, among the commonly used force incorporation methods introduced in the above section, VCM is not recommended here, as the fluid velocity in MRT is coupled to multiple moments. A simple correction of velocity can alter the accuracy of moment relaxation, introducing significant numerical errors. At this time, the widely used approach is DFM, such as the Guo forcing scheme, which can be adapted to the MRT model by transforming the discretized force term F_i into moment space prior to collision operations. The F_i projected into moment space can be expressed as:

$$\mathbf{S}_F = M \cdot \mathbf{F}_i \tag{2.16}$$

Then followed by a post-collision and streaming step, the moment update equation becomes:

$$\mathbf{m}^*(\mathbf{x},t) = \mathbf{m}(\mathbf{x},t) - \mathbf{S}\left[\mathbf{m}(\mathbf{x},t) - \mathbf{m}^{\mathrm{eq}}(\mathbf{x},t)\right] + \left(\mathbf{I} - \frac{1}{2}\mathbf{S}\right) \cdot \mathbf{S}_F \tag{2.17}$$

In fact, the EDM is also mathematically compatible with MRT, as it modifies the distribution function by computing the difference between two equilibrium states. However, EDM requires two evaluations of the equilibrium function and corresponding moment transformations, significantly increasing computational cost and potentially reducing model stability in MRT-based implementations. Table 2.2 presents the improvements of the MRT model over the BGK model. Table 2.3 shows a comparison between EDM and DFM within the MRT framework.

Table 2.2: Comparison Between BGK and MRT Collision Operator

Issue	BGK	MRT Improvement
Numerical Stability	Unstable at high Reynolds numbers, prone to numerical oscillations	Improved stability through different relaxation times
Viscosity Control	Large errors at low viscosity	Allows independent viscosity adjustment, improving accuracy
Anisotropy Error	Inaccurate modeling of shear flow and vortices	Reduces anisotropy errors, enhancing modeling precision
Boundary Conditions	Large errors in complex boundaries	Enables more accurate boundary layer calculations
High Mach Number Adaptability	Only applicable for low Mach numbers (Ma < 0.3)	Suitable for higher Mach numbers (Ma > 0.3)

In summary, while both DFM and EDM can be used in MRT frameworks, DFM is more efficient and numerically stable. In this study, the DFM based on Guo's scheme is adopted within the MRT framework to achieve a balance between precision, stability, and computational efficiency. The following section introduces the complete MRT-based pseudopotential LBM model implemented in this work for dynamic boiling simulations.

Table 2.3: Comparison Between EDM and DFM

Comparison Item	Exact Difference Method (EDM)	Discrete Force Method (DFM)
Computation Method	Computes f_i^{eq} twice and takes the difference	Directly adds the discrete force term to the LBM equation
Moment Space Processing	Requires additional moment transformations	Directly implemented within the MRT structure
Computational Cost	Higher (extra calculations of f_i^{eq} and moment transformations)	Lower (only requires one moment transformation)
Stability	Suitable for high-density ratio and multiphase flows, but moment control is more complex	Suitable for high Reynolds number and high-precision flows, more stable
Applicable Scenarios	Multiphase flow, low surface tension, high-density ratio	High Reynolds number flows, optimized for MRT structures
Common Applications	Shan-Chen pseudo-potential method	External force processing in MRT-LBM

2.3 Numerical Model Implementation in This Study

As introduced above, the MRT collision operator offers higher accuracy and stronger numerical stability [53][54] compared to the BGK collision operator. Considering that, we adopt the DFM to force incorporation scheme and implement a more advanced Huang-MRT [55] framework based on the pseudopotential model for numerical modeling. This section will elaborate on the model we employed.

2.3.1 Huang-MRT Framework

I numerically implemented the MRT-based pseudopotential model with third-order correction as analyzed by Huang *et al.* [55]. This model offers the following two main advantages:

Third-order consistency: The inclusion of the third-order correction term $\mathbf{Q}_m$ eliminates the truncation error at the third order in the Chapman–Enskog expansion, whereas commonly MRT schemes guarantee accuracy only up to the second order.

Independently tunable surface tension: The parameters k_1 and k_2 allow a precise adjustment of the interfacial tension without modifying the relaxation rates or the interaction strength.

Specifically, we first introduce the collision in the moment space, define the equilibrium moments, the force moments, and the third-order correction moments, and then give the transformation matrix and the streaming step.

Let $\mathbf{f} = (f_0, \ldots, f_8)^T$ be the D2Q9 distribution vector and define

$$\mathbf{m} = M\,\mathbf{f},$$

where $M \in \mathbb{R}^{9\times 9}$ is the D'Humière transformation matrix (Eq. 2.3.1). The post-collision moments are

$$\mathbf{m}^* = \mathbf{m} - S\big(\mathbf{m} - \mathbf{m}^{\mathrm{eq}}\big) + \Delta t\big(I - \tfrac{1}{2}\mathbf{S}\big)\,\mathbf{F}_m + \mathbf{S}\,\mathbf{Q}_m, \tag{2.18}$$

with $\mathbf{S} = \mathrm{diag}(s_0, s_e, s_\varepsilon, s_j, s_q, s_j, s_q, s_p, s_p)$, where $\mathbf{S}$ is the relaxation rate matrix [53], and $\Delta t = 1$. Then, the post-collision distributions can be recovered by:

$$\mathbf{f}^* \;=\; M^{-1}\,\mathbf{m}^*$$

followed by streaming:

$$f_i(\mathbf{x} + \mathbf{e}_i\,\Delta_t,\; t + \Delta_t) = \; f_i^*(\mathbf{x}, t)\,, \quad i = 0, \ldots, 8.$$

The macroscopic density and momentum are obtained directly from the distribution functions as

$$\rho(\mathbf{x}, t) = \sum_{i=0}^{8} f_i(\mathbf{x}, t), \qquad \rho\,\mathbf{u}(\mathbf{x}, t) = \sum_{i=0}^{8} \mathbf{e}_i\, f_i(\mathbf{x}, t) \;+\; \frac{\Delta t}{2}\,\mathbf{F}_m(\mathbf{x}, t),$$

where the last term accounts for the half-step contribution [51] [56] of the pseudopotential force $\mathbf{F}_m$, ensuring the exact recovery of the Navier–Stokes equations [57][58].

The equilibrium moment vector is:

$$\mathbf{m}^{\mathrm{eq}} = \begin{bmatrix} \rho \\ -2\rho + 3\rho\,|\mathbf{u}|^2/c^2 \\ \rho - 3\rho\,|\mathbf{u}|^2/c^2 \\ \rho\,u_x/c \\ -\rho\,u_x/c \\ \rho\,u_y/c \\ -\rho\,u_y/c \\ \rho\,(u_x^2 - u_y^2)/c^2 \\ \rho\,u_x u_y/c^2 \end{bmatrix}.$$

where ρ is density, $\mathbf{u} = (u_x, u_y)^T$ is velocity, satisfying $|\mathbf{u}| = \sqrt{\mathbf{u_x}^2 + \mathbf{u_y}^2}$, lattice speed $c = \Delta x/\Delta t$ and lattice sound speed $c_s^2 = c^2/3$. Then, for an intermolecular force $\mathbf{F}_m = (F_x, F_y)^T$ (interaction strength $G = -1$), the discrete force moment vector is the following:

$$\mathbf{F}_m = \begin{bmatrix} 0 \\ 6\,\dfrac{\mathbf{F}\cdot\mathbf{u}}{c^2} \\ -6\,\dfrac{\mathbf{F}\cdot\mathbf{u}}{c^2} \\ F_x/c \\ -F_x/c \\ F_y/c \\ -F_y/c \\ 2\,\dfrac{F_x u_x - F_y u_y}{c^2} \\ \dfrac{F_x u_y + F_y u_x}{c^2} \end{bmatrix}.$$

For a detailed derivation of the Taylor series expansion of this interaction force, see [59] and [60]. Under the MRT framework, the components of the forcing term in the moment space are defined as Q_i, to achieve third-order accuracy and allow surface tension tuning, non-zero corrections are added in moments 1, 2, 7, and 8, these terms can be expressed as:

$$Q_1 = 3\,(k_1 + 2\,k_2)\,\frac{|\mathbf{F}|^2}{G\,\psi^2\,c^2}, \qquad Q_2 = -\,Q_1,$$

$$Q_7 = k_1\,\frac{F_x^2 - F_y^2}{G\,\psi^2\,c^2}, \qquad Q_8 = k_1\,\frac{F_x F_y}{G\,\psi^2\,c^2},$$

with all other $Q_i = 0$. The parameters satisfy the relation [55]:

$$\epsilon = -8\,(k_1 + k_2).$$

Hence, the expression for Q_m can be written as:

$$\mathbf{Q}_m = \begin{bmatrix} Q_0 \\ Q_1 \\ Q_2 \\ Q_3 \\ Q_4 \\ Q_5 \\ Q_6 \\ Q_7 \\ Q_8 \end{bmatrix} = \begin{bmatrix} 0 \\ 3\,(k_1 + 2\,k_2)\,\dfrac{|\mathbf{F}|^2}{g\,\psi^2\,c^2} \\ -3\,(k_1 + 2\,k_2)\,\dfrac{|\mathbf{F}|^2}{g\,\psi^2\,c^2} \\ 0 \\ 0 \\ 0 \\ 0 \\ k_1\,\dfrac{F_x^2 - F_y^2}{g\,\psi^2\,c^2} \\ k_1\,\dfrac{F_x F_y}{g\,\psi^2\,c^2} \end{bmatrix},$$

Here, $|F|^2 = F_x^2 + F_y^2$, and $\psi(\rho)$ is the pseudopotential function.

The moment space basis is given by the D'Humière transformation matrix [61]:

$$M = \begin{bmatrix} 1 & 1 & 1 & 1 & 1 & 1 & 1 & 1 & 1 \\ -4 & -1 & -1 & -1 & -1 & 2 & 2 & 2 & 2 \\ 4 & -2 & -2 & -2 & -2 & 1 & 1 & 1 & 1 \\ 0 & 1 & 0 & -1 & 0 & 1 & -1 & -1 & 1 \\ 0 & -2 & 0 & 2 & 0 & 1 & -1 & -1 & 1 \\ 0 & 0 & 1 & 0 & -1 & 1 & 1 & -1 & -1 \\ 0 & 0 & -2 & 0 & 2 & 1 & 1 & -1 & -1 \\ 0 & 1 & -1 & 1 & -1 & 0 & 0 & 0 & 0 \\ 0 & 0 & 0 & 0 & 0 & 1 & -1 & 1 & -1 \end{bmatrix}.$$

and its inverse M^{-1} is used to map post-collision moments back to the distribution space, which is given by:

$$M^{-1} = \frac{1}{36} \begin{bmatrix} 4 & -4 & 4 & 0 & 0 & 0 & 0 & 0 & 0 \\ 4 & -1 & -2 & 6 & -6 & 0 & 0 & 9 & 0 \\ 4 & -1 & -2 & 0 & 0 & 6 & -6 & -9 & 0 \\ 4 & -1 & -2 & -6 & 6 & 0 & 0 & 9 & 0 \\ 4 & -1 & -2 & 0 & 0 & -6 & 6 & -9 & 0 \\ 4 & 2 & 1 & 6 & 3 & 6 & 3 & 0 & 9 \\ 4 & 2 & 1 & -6 & -3 & 6 & 3 & 0 & -9 \\ 4 & 2 & 1 & -6 & -3 & -6 & -3 & 0 & 9 \\ 4 & 2 & 1 & 6 & 3 & -6 & -3 & 0 & -9 \end{bmatrix}.$$

In the M matrix, each row corresponds to a specific moment, as explained in the following table 2.4.

In addition, we choose the diagonal relaxation rates as:

$$s_0 = s_j = 1, \quad s_e = s_\varepsilon = s_p, \quad s_p = \frac{1}{\nu/(c_s^2\,\Delta t) + \frac{1}{2}}, \quad s_q = \frac{1}{\frac{1}{2} + \frac{1}{12\left(1/s_p - \frac{1}{2}\right)}},$$

TABLE 2.4: Row Moment (m_k) Physical meaning

Row	Moment (m_k)	Physical meaning
1	$m_0 = \rho$	Density
2	$m_1 = e$	Energy mode (trace of stress tensor)
3	$m_2 = \varepsilon$	Energy-square mode (deviatoric part)
4	$m_3 = j_x$	x-momentum
5	$m_4 = q_x$	x-component of energy (heat) flux
6	$m_5 = j_y$	y-momentum
7	$m_6 = q_y$	y-component of energy (heat) flux
8	$m_7 = p_{xx}$	Normal stress difference $\Pi_{xx} - \Pi_{yy}$
9	$m_8 = p_{xy}$	Shear stress Π_{xy}

so that $s_0 = 1$ enforces mass conservation; $s_j = 1$ enforces momentum conservation; s_p recovers the desired kinematic viscosity ν via $\nu = c_s^2\,(1/s_p - 1/2)\,\Delta t$; s_q tunes the higher order moments for interface stability (surface tension control).

The general form of MRT $\mathbf{S} = \mathrm{diag}(s_i)$ originates from d'Humières (1992, 2002) [61, 62], and the impact of different s_i on numerical dissipation and stability is discussed in detail by Lallemand & Luo (2000) [63]. Equations (2.18), together with the definitions of $\mathbf{m}^{\mathrm{eq}}$, $\mathbf{F}_m$, $\mathbf{Q}_m$, the transformation matrix M, the relaxation matrix $\mathbf{S}$, and the streaming step, fully specify the Huang–MRT numerical model used throughout this study.

2.3.2 Force Term and Fluid-Solid Coupling

In the standard pseudopotential LBM, the total force can be written as:

$$\mathbf{F} = \underbrace{\mathbf{F}_{\mathrm{int}}}_{\substack{\text{fluid–fluid}\\ \text{(pseudopotential)}}} + \underbrace{\mathbf{F}_{\mathrm{ads}}}_{\substack{\text{fluid–solid}\\ \text{(adhesion)}}} + \underbrace{\mathbf{F}_g}_{\text{buoyancy}},$$

with

$$\mathbf{F}_{\mathrm{ads}} = -\,G_w \sum_{\alpha} \omega(|\mathbf{e}_\alpha|^2)\, x_\alpha\, S(\mathbf{x} + \mathbf{e}_\alpha)\, \mathbf{e}_\alpha,$$

where $\mathbf{F}_{\mathrm{int}}$ is the standard Shan-Chen pseudopotential force (denoted by Huang's improved $\mathbf{F}_m$ in the above section), $\mathbf{F}_{\mathrm{ads}}$ is the adhesion force commonly used to describe the fluid-solid interaction proposed by Gong [64], and $\mathbf{F}_g$ is the buoyancy (gravity) term. In $\mathbf{F}_{\mathrm{ads}}$, G_w are the strength of the fluid-solid interaction, $\omega(|\mathbf{e}_\alpha|^2)$

are the directional weights; $x_\alpha = \omega_\alpha/3$ is a correction coefficient; and $S(\mathbf{x}+\mathbf{e}_\alpha)$ is the wall indicator function, defined by:

$$S(\mathbf{x}+\mathbf{e}_\alpha) = \begin{cases} 1, & \text{if } \mathbf{x}+\mathbf{e}_\alpha \text{ is solid,} \\ 0, & \text{if } \mathbf{x}+\mathbf{e}_\alpha \text{ is fluid.} \end{cases}$$

In this study, to avoid separate $\mathbf{F}_{\text{ads}}$ and eliminate non-physical density jumps on the wall, we adopt the improved virtual-density scheme of Li & Luo [65]. Concretely, for each node adjacent to the solid boundary we compute a local virtual density ρ_w (Eq. 2.3.2), convert it to a 'ghost' pseudopotential ψ_{ghost} through the chosen EOS (Eq. 2.19), and then use ψ_{ghost} in place of the usual ψ whenever a neighbor lies within the solid.

In this improved formulation, both fluid-fluid and fluid-solid interactions are incorporated into a unified pseudopotential force $\mathbf{F}_{\text{int}}$, which is constructed from the following components.

Local virtual density: To impose the desired wettability, a virtual density $\rho_w(\mathbf{x})$ is assigned to solid nodes based on the average density of neighboring fluid nodes:

$$\rho_w(\mathbf{x}) = \begin{cases} \varphi\, \rho_{\text{ave}}(\mathbf{x}), & \varphi \geq 1 \quad \text{(decrease } \theta\text{)}, \\ \rho_{\text{ave}}(\mathbf{x}) - \Delta\rho, & \Delta\rho \geq 0 \quad \text{(increase } \theta\text{)}, \end{cases}$$

where φ and $\Delta\rho$ are scaling factors for adjusting the wettability. The average density of solid–adjacent fluid nodes is given by:

$$\rho_{\text{ave}}(\mathbf{x}) = \frac{\sum_{k=1}^{8} w_k\, \rho(\mathbf{x}+\mathbf{e}_k)\, s_w(\mathbf{x}+\mathbf{e}_k)}{\sum_{k=1}^{8} w_k\, s_w(\mathbf{x}+\mathbf{e}_k)}, \quad s_w(\mathbf{x}+\mathbf{e}_k) = \begin{cases} 1, & \text{solid}, \\ 0, & \text{fluid}. \end{cases}$$

Ghost pseudopotential:

The virtual density is then converted into a ghost pseudopotential, which is assigned to solid nodes when evaluating the interaction force:

$$\psi_{\text{ghost}} = \sqrt{\frac{2\left[p_{\text{EOS}}(\rho_w) - \rho_w\, c_s^2\right]}{G\, c^2}}. \tag{2.19}$$

Here, p_{EOS} denotes the non-ideal equation of state; in this work, the Peng–Robinson (P–R) EOS is employed, as detailed in the next section.

Unified interaction force:

The fluid–fluid and fluid–solid forces are then evaluated together through the following pseudopotential formulation:

$$\mathbf{F}_{\mathrm{int}}(i,j) = -\,G\,\psi_{i,j}\sum_{k=1}^{8} w_{F,k}\;\psi_{\mathrm{nb}}(i+e_{k,x},\,j+e_{k,y})\;\mathbf{e}_k\;\Delta t,$$

where the neighbor pseudopotential ψ_{nb} is defined as:

$$\psi_{\mathrm{nb}}(i',j') = \begin{cases} \psi_{\mathrm{ghost}}, & j' < 0 \text{ or } j' > NY-1, \\ \psi_{i',j'}, & \text{otherwise.} \end{cases}$$

Here, $G = -1$ is the pseudopotential interaction strength; $\psi_{i,j} = \psi(i,j)$ is the pseudopotential at lattice node (i,j); $w_{F,k} = w_F(|\mathbf{e}_k|^2)$ are the interaction weights ($1/3$ for $|\mathbf{e}_k|^2 = 1$, $1/12$ for $|\mathbf{e}_k|^2 = 2$); $\mathbf{e}_k = (e_{k,x}, e_{k,y})$ are the D2Q9 lattice velocities; and Δt is the lattice time step in lattice units (set to 1).

Total Force: The total forcing term is then expressed as:

$$\mathbf{F} = \mathbf{F}_{\mathrm{int}} + \mathbf{F}_g, \quad \mathbf{F}_g = (\rho - \rho_0)\,\mathbf{g},$$

where $\mathbf{F}_g$ is the body force due to gravity.

This formulation unifies fluid–fluid and fluid–solid interactions within $\mathbf{F}_{\mathrm{int}}$, mitigates non-physical density discontinuities at the fluid–solid interface, and ensures stable contact-angle control over complex geometries. The detailed contact-angle adjustment strategy and validation through benchmark tests are presented in the following section.

2.3.3 Energy Equation Coupling

Thus far we have constructed the MRT pseudopotential LBM for two-phase flow (Eqs. 2.18–2.3.2), including fluid–fluid and fluid–solid forces and the resulting density and velocity fields. We now introduce the temperature field to capture the

phase change. The energy equation is solved by a finite-difference scheme coupled to the LBM [66].

Neglecting viscous dissipation, the temperature T satisfies

$$\rho c_v \frac{DT}{Dt} = \nabla\cdot(\lambda\,\nabla T) - T\Big(\frac{\partial p_{\mathrm{EOS}}}{\partial T}\Big)_{\rho}\nabla\cdot\mathbf{u}, \tag{2.20}$$

where ρ and $\mathbf{u}$ are provided by the LBM, c_v is the specific heat, and λ the thermal conductivity. Applying a finite-difference discretization to the material derivative $\frac{D}{Dt}$ [67] transforms Eq. (2.20) into

$$\partial_t T + \mathbf{u}\cdot\nabla T = \frac{1}{\rho c_v}\nabla\cdot(\lambda\nabla T) - \frac{T}{\rho c_v}\Big(\tfrac{\partial p_{\mathrm{EOS}}}{\partial T}\Big)_{\rho}\nabla\cdot\mathbf{u}. \tag{2.21}$$

We denote the right-hand side by $K(T)$ and integrate in time using a classical fourth-order Runge-Kutta (RK4) [68] scheme:

$$T^{n+1} = T^n + \frac{\Delta t}{6}\big(h_1 + 2h_2 + 2h_3 + h_4\big), \tag{2.22}$$

$$\begin{aligned} h_1 &= K\big(T^n\big),\\ h_2 &= K\big(T^n + \tfrac{\Delta t}{2}h_1\big),\\ h_3 &= K\big(T^n + \tfrac{\Delta t}{2}h_2\big),\\ h_4 &= K\big(T^n + \Delta t\, h_3\big). \end{aligned}$$

The spatial derivatives in $K(T)$ are discretized by the isotropic central difference scheme of Lee & Lin [69]. The choice of RK4 over implicit Crank–Nicolson, ADI, or lower-order explicit methods is motivated by its fourth-order temporal accuracy, and straightforward explicit coupling with the LBM hydrodynamic solver without the need for iterative linear solvers. This is particularly advantageous in high-density-ratio phase-change simulations, where sharp liquid–vapor interfaces require accurate resolution of transient thermal fields while avoiding the numerical damping often introduced by implicit schemes. Moreover, RK4 allows intermediate evaluations (h_1–h_4) to directly incorporate the latest ρ and $\mathbf{u}$ from the LBM, ensuring tight coupling between momentum and energy transport at each time step.

In my code implementation, the RK4 scheme, which advances the temperature field based on the advection–diffusion equation with a thermodynamic source term. The kernel $K(T)$ contains three contributions: (i) the advection term $-\mathbf{u}\cdot\nabla T$, (ii) the variable-coefficient diffusion term $\nabla\cdot(\lambda\nabla T)/(\rho c_v)$, and (iii) a compressibility-related source term $-TR(\nabla\cdot\mathbf{u})/[c_v(1-b\rho)]$. The bottom and top boundaries are treated as Dirichlet conditions, with the bottom wall maintained at the superheated temperature T_b (or T_s outside the heater) and the top wall fixed at $T_{\text{up}} = T_s$. The thermal conductivity λ is not constant but is updated at each time step according to $\lambda = \rho c_v \alpha$, where $\alpha = 0.05/c_v$ is a constant thermal diffusivity coefficient. Consequently, λ varies spatially and temporally with the local density, resulting in a higher conductivity in the liquid phase ($\lambda_l \approx 0.325$) and a lower conductivity in the vapor phase ($\lambda_v \approx 0.019$), which correspond to the typical values computed from the respective phase densities at the initial state. Although λ does not explicitly depend on temperature, it changes indirectly through the phase-dependent density evolution, thereby capturing the contrast in heat transfer capability between the two phases during boiling.

It is crucial to emphasize that the pseudopotential LBM and the thermal solver are intrinsically coupled via the EOS. Specifically, the non-ideal pressure $p_{\text{EOS}}(\rho, T)$ enters both the pseudopotential $\psi(\rho, T)$ (Eq. 2.19) and the source term in the energy equation. In this work, we consistently employ the Peng–Robinson EOS for all simulations [70]:

$$p_{\text{EOS}}(\rho, T) = \frac{\rho RT}{1 - b\,\rho} - \frac{a\,\alpha(T)\,\rho^2}{1 + 2b\,\rho - b^2\,\rho^2}, \tag{2.23}$$

$$\alpha(T) = \Big[1 + (0.37464 + 1.54226\omega - 0.26992\omega^2)\big(1 - \sqrt{T/T_c}\big)\Big]^2,$$

where R is the universal gas constant, T_c and P_c are the critical temperature and pressure of the fluid, and ω is the acentric factor (for water, $\omega = 0.344$ [71]). The PR parameters a and b are then given by

$$a = 0.45724\,\frac{R^2 T_c^2}{P_c}, \quad b = 0.07780\,\frac{R\,T_c}{P_c}.$$

[71]

The interaction strength $G = -1$ ensuring thermodynamic consistency and accurate liquid–vapor coexistence in our simulations.

At each iteration, the sequence is:

1. update $\rho, \mathbf{u}$ via MRT–LBM with $\mathbf{F}_{\text{int}}$ (Eqs. 2.18–2.3.2); 2. compute $K(T)$ from the current $\rho, \mathbf{u}$ and EOS in Eq. (2.20); 3. advance T by RK4 (Eq. 2.22) with central differences. This completes the liquid–vapor phase-change model, fully coupling mass, momentum and energy in a unified MRT framework.

2.3.4 Modelling and Numerical Uncertainties

The present study implements the Huang-type MRT pseudopotential lattice Boltzmann framework for liquid–vapor phase-change simulations using a C++ code. Although this model provides a solid theoretical foundation and ensures good thermodynamic consistency, certain modelling assumptions and numerical constraints remain in the current implementation, which may influence the quantitative accuracy of the boiling predictions. In general, these uncertainties can be classified into two categories: (i) simplifications associated with the physical modelling and (ii) discretisation errors arising from the numerical implementation.

From the modelling viewpoint, the present implementation adopts a two-dimensional (2D) computational domain to simulate boiling phenomena that are inherently three-dimensional (3D). This simplification, which is widely used in the literature, allows for high spatial resolution and manageable computational cost, but it also modifies the geometric relationships among surface tension, buoyancy, and viscous forces, potentially leading to deviations in the absolute values of bubble departure diameter and growth rate. The intermolecular interaction is formulated using the pseudopotential approach coupled with the Peng–Robinson (PR) equation of state, where the coefficients a, b, and ω are fixed according to the critical parameters of the working fluid. Consequently, the local saturation properties are determined by a constant reference temperature T_s, without accounting for pressure-dependent variations in the saturation temperature. The thermal conductivity is modelled as a density-dependent function, $\lambda = \rho c_v \alpha$, where α is a constant thermal diffusivity coefficient. This approach provides a realistic contrast between the liquid and vapor phases but neglects the explicit temperature dependence of thermal conductivity and specific heat. In addition, the top boundary is maintained at the saturation temperature ($T_{\text{up}} = T_s$), which prevents the development of bulk subcooling or condensation in the vapor region. These modelling choices ensure

numerical stability and computational efficiency while still capturing the dominant thermodynamic and interfacial mechanisms of phase change.

From the numerical perspective, additional uncertainties arise from the discretisation scheme, relaxation settings of the MRT collision operator, and boundary condition treatment. The diffuse interface is typically resolved by 3−5 lattice nodes, which may lead to small deviations in the computed curvature and capillary pressure compared with their continuum counterparts. The relaxation matrix parameters (s_p, s_q) control the effective viscosity and numerical stability of the model; minor variations in these coefficients can slightly alter the Reynolds number, momentum diffusion, and the damping of interfacial oscillations. The energy equation is solved explicitly using a fourth-order Runge–Kutta (RK4) integration scheme, which ensures high temporal accuracy but is conditionally stable and sensitive to large velocity or temperature gradients near the phase interface.

The boundary conditions are another source of modelling uncertainty. Both the bottom and top walls are treated with Dirichlet conditions for temperature and density, while the side boundaries are periodic, resulting in a closed pool configuration without external mass or heat flux. This treatment guarantees numerical stability but restricts the representation of open-system effects such as vapor venting or liquid replenishment.

Overall, these numerical constraints define the accuracy limits of the current MRT–LBM implementation. Based on current implementation, several key parameters exhibit strong sensitivity and therefore require careful calibration. The wall–fluid interaction parameters, φ and $\Delta\rho$, directly determine the apparent contact angle and thus strongly influence bubble adhesion, contact-line dynamics, and departure frequency. The interfacial force coefficients k_1, ϵ, and k_2 govern the effective surface tension and interface stability, affecting the curvature of the bubble neck and the timing of detachment. The superheat level $(T_b - T_s)$ or, equivalently, the Jakob number (Ja), controls the rate of phase change and the overall heat flux response, while the gravitational acceleration g determines the balance between buoyancy and surface tension, influencing the bubble departure diameter. In addition, the thermal diffusivity coefficient α defines the relative heat-transfer capability between liquid and vapor phases and thereby affects the growth rate of the bubble.

A consistent and systematic calibration of these parameters is essential to reduce modelling uncertainty and achieve physically meaningful predictions. In the present study, each parameter is validated through a sequence of benchmark tests: the surface tension is verified by the Laplace pressure relation, the equation of state and coexistence densities are checked for thermodynamic consistency, and the phase-change performance is evaluated via an evaporation test under controlled superheat. These validations ensure that the implemented MRT–LBM framework can quantitatively reproduce the fundamental thermodynamic behaviours required for reliable boiling simulations.

The detailed results of these benchmark validations are presented in the following section to demonstrate the reliability and physical consistency of the implemented model.

2.4 Computational Setup

2.4.1 Geometric Configuration and Domain Size

To investigate the dynamics of single bubble boiling on a microheater, a two-dimensional rectangular computational domain of size $L_x \times L_y = 200 \times 400$ lattice units is employed, as illustrated in Fig. 2.4. The domain is initially divided into two regions: the lower half is filled with saturated liquid, while the upper half contains vapor, forming a stable liquid–vapor system under the influence of gravity.

At the center of the bottom wall, a microheater of width 40 (lattice units, l.u.) and height 10 is embedded to provide localized heat input. A constant temperature is imposed on the microheater surface to induce superheating, thus initiating bubble nucleation. The regions adjacent to the heater are modeled as adiabatic to prevent heat leakage, while the entire bottom wall is treated as a no-slip boundary to ensure fluid velocity vanishes at the solid–fluid interface. The top boundary is set as a constant-pressure outlet to accommodate the upward movement of vapor, and periodic boundary conditions are applied to both vertical sides to eliminate artificial wall effects and preserve lateral homogeneity.

This setup ensures that bubble nucleation, growth, and departure are primarily driven by localized thermal gradients, interfacial forces, and buoyancy, all within a

thermodynamically consistent environment. It allows for the natural development of the bubble cycle and facilitates detailed observation of interfacial behavior with minimal boundary interference.

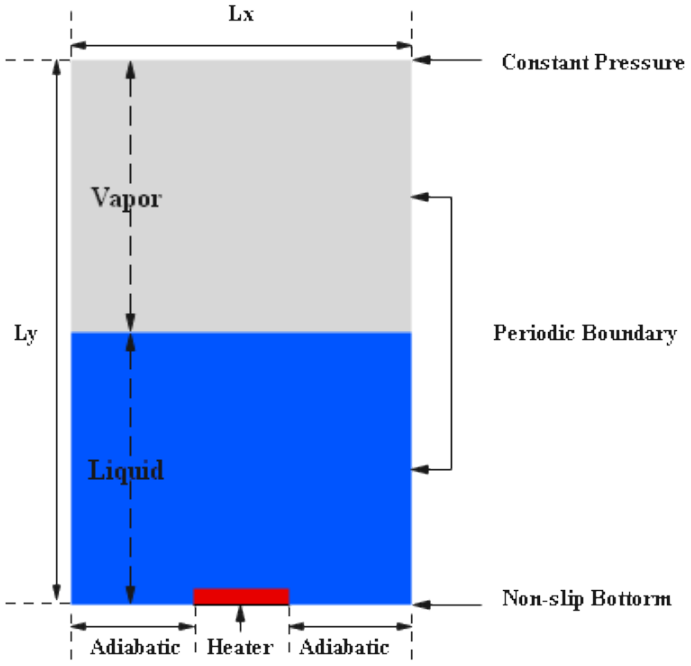

FIG. 2.4: Schematic of the computational domain

2.4.2 Initial and Boundary Conditions Setting

At the beginning of the simulation ($t = 0$), the density field is initialized as a stationary liquid–vapor system with a horizontal interface. A diffuse hyperbolic tangent profile is applied to represent the phase boundary [72]:

$$\rho(x, y) = \frac{\rho_l + \rho_v}{2} - \frac{\rho_l - \rho_v}{2} \tanh\left(\frac{2(y - y_0)}{w_{\text{ini}}}\right)$$

where ρ_l and ρ_v denote the equilibrium densities of the liquid and vapor phases, y_0 is the center of the domain, and $w_{\text{ini}} = 2$ is the initial thickness of the interface. The velocity field is initialized as $\vec{u} = 0$ and the temperature is set to saturation temperature T_{sat} throughout the domain, except at the central heating strip at the bottom ($y = 0$), where a superheated temperature $T_w > T_{\text{sat}}$ is applied over 40 lu. A small random perturbation is also introduced near the wall to promote nucleation.

A no-slip boundary condition is imposed using a modified Zou-He like scheme [73]:

$$
\begin{aligned}
f_2 &= f_4, \\
f_5 &= f_7 - \frac{1}{2}(f_1 - f_3) - \frac{1}{4}(F_x + F_y), \\
f_6 &= f_8 + \frac{1}{2}(f_1 - f_3) + \frac{1}{4}(F_x - F_y),
\end{aligned}
$$

which ensures $u_y = 0$ and accounts for external forces of the pseudopotential model.

For the heater, a constant wall temperature boundary condition is imposed. In this work, the temperature field is not solved by a thermal lattice Boltzmann (LBM) scheme, but rather by the macroscopic Partial Differential Equation (PDE) of heat conduction, which is integrated in time using a fourth-order Runge–Kutta (RK4) method. To ensure consistency at the boundary, the fixed temperature condition $T = T_w$ is expressed in the form of an equilibrium thermal distribution,

$$
g_i(x, 0) = g_i^{\mathrm{eq}}(\rho, T_w, \vec{u} = 0).
$$

which here simply serves as a mathematical representation of the prescribed wall temperature for coupling with the LBM solver. It should be emphasized that the evolution of T is entirely governed by the PDE with RK4 integration, while the above expression only enforces the constant boundary condition at the heater.

Outside the heater, an adiabatic boundary condition is imposed using a bounce-back scheme for the thermal distribution function [74]:

$$
g_i(x, 0) = g_{\underline{i}}(x, 1).
$$

ensuring a zero normal temperature gradient.

For the top, a constant-pressure outlet is implemented by prescribing a fixed density $\rho_{\mathrm{top}} = \rho_v$ and temperature $T_{\mathrm{top}} = T_{\mathrm{sat}}$. To recover unknown distribution functions, a first-order extrapolation scheme is used, following Fei et al. [73]:

$$
u_y = \frac{f_0 + f_1 + f_3 + 2(f_2 + f_5 + f_6)}{\rho_{\mathrm{top}}} - 1 + \frac{F_y \delta t}{2\rho_{\mathrm{top}}},
$$

$$
\begin{aligned}
f_4 &= f_2 - \frac{2}{3}\rho_{\text{top}} u_y - \frac{1}{3} F_y \delta t, \\
f_8 &= \frac{1}{2}\rho_{\text{top}} - \frac{1}{2}(f_0 + f_2 + f_4) - f_1 - f_5 - \frac{1}{4} F_x \delta t, \\
f_7 &= \rho_{\text{top}} - \sum_{i \neq 7} f_i.
\end{aligned}
$$

This approach ensures thermodynamic consistency and stable mass conservation across the top boundary, enabling vapor outlet under natural buoyancy.

In addition, periodic boundary conditions are used for both hydrodynamic and thermal fields:

$$
f_i(0, y) = f_i(N_X - 1, y), \quad g_i(0, y) = g_i(N_X - 1, y).
$$

The wettability of the wall is controlled using the improved virtual pseudopotential scheme [65]. This method is implemented by modifying the virtual pseudopotential ψ_w at wall-adjacent nodes, and is directly incorporated into the interfacial force term $\mathbf{F}_{\text{int}}$ in the pseudopotential model, ensuring consistency with the theoretical formulation presented earlier.

It should be noted that the present numerical setup is particularly effective for investigating saturated pool boiling, as the entire liquid domain is initialized at the saturation temperature T_{sat} and the top boundary is also maintained at $T_{\text{top}} = T_{\text{sat}}$. This configuration ensures a thermodynamically consistent environment for studying bubble nucleation, growth, and departure under well-defined superheated conditions. However, when extending the model to subcooled boiling, several inherent constraints must be considered. Because the top boundary and bulk liquid are both fixed at T_{sat} and no cooling inflow or volumetric heat sink is included, the current setup does not allow the bulk liquid to become subcooled.

To enable subcooled conditions in future studies, the framework could be modified by prescribing a subcooled far-field temperature ($T_{\text{top}} = T_{\text{sat}} - \Delta T_{\text{sub}}$), applying a Robin-type convective boundary condition $-\lambda\, \partial T/\partial n = h\,(T - T_\infty)$ with $T_\infty < T_{\text{sat}}$, or introducing a mild volumetric cooling term into the energy equation. Such extensions would make it possible to investigate the effects of bulk subcooling and condensation within the same pseudopotential LBM framework.

2.5 Unit Conversion and Scaling Strategy

To ensure physical interpretability and comparability of the simulation results, an appropriate unit conversion strategy is essential in the lattice Boltzmann method (LBM). In this work, two complementary conversion approaches are adopted: a traditional non-dimensional mapping based on capillary theory [75] , and a lattice-to-physical unit conversion based on critical properties. These two methods serve different but mutually reinforcing purposes—one emphasizes model universality, while the other enables direct comparison with physical experiments. The details are presented below.

2.5.1 Dimensionless unit conversion

Non-dimensionalization is a widely adopted approach to eliminate the influence of physical scale and unify simulation results under a consistent theoretical framework. Following Gong [76], Son [77], and others, this study adopts a scaling system based on capillary length l_0, defined as:

$$l_0 = \sqrt{\frac{\sigma}{g(\rho_l - \rho_v)}}, \quad u_0 = \sqrt{g l_0}, \quad t_0 = \frac{l_0}{u_0} \tag{2.24}$$

Here, σ is the surface tension, g is gravitational acceleration, and ρ_l, ρ_v are the liquid and vapor densities, respectively. These quantities define the characteristic length, velocity, and time scales for the system.

The corresponding lattice-based values are summarized in Table 2.6. These allow other physical quantities to be expressed in dimensionless form, ensuring that the simulation is governed by a consistent set of non-dimensional groups. In this study, we consider the Jacob number (Ja), Prandtl number (Pr), Eötvös number (Eo), and Nusselt number (Nu), which are defined as:

$$Ja = \frac{c_p(T_w - T_{\text{sat}})}{h_{fg}}, \quad Pr = \frac{\nu}{\alpha}, \quad Eo = \frac{g(\rho_l - \rho_v)D^2}{\sigma}, \quad Nu = \frac{qD}{\lambda(T_w - T_{\text{sat}})}$$

Here, c_p is the specific heat, h_{fg} is the latent heat of vaporization, ν is the kinematic viscosity, α is the thermal diffusivity, q is the local or average heat flux, λ is thermal conductivity, and D is the characteristic bubble diameter. The Nusselt number

quantifies the relative strength of convective versus conductive heat transfer across the liquid–vapor interface, making it particularly relevant for boiling simulations.

TABLE 2.5: Key Dimensionless Numbers Used in This Study

Symbol	**Definition / Physical Meaning**
Ja	Jacob number: thermal driving force for phase change
Pr	Prandtl number: ratio of momentum to thermal diffusivity
Eo	Eötvös number: gravity vs. surface tension effect on bubble shape
Nu	Nusselt number: convective vs. conductive heat transfer ratio

TABLE 2.6: Characteristic Variables in Lattice Units ($l.u.$)

Variable	l_0	u_0	t_0
Value	14.63	0.021	696.67

2.5.2 Lattice unit to physical unit conversion

Although the non-dimensional method is good for comparative studies, it does not directly yield real physical values, which are often required for experimental validation. To address this limitation, a complementary unit conversion method is introduced based on the matching of thermodynamic properties in the pseudopotential LBM model.

Specifically, this approach maps lattice units to physical units by matching critical properties such as the critical temperature T_c, critical pressure P_c, critical density ρ_c, and surface tension σ, which are derived from the PR EOS. Following Wang et al. [78], the ratios of key thermodynamic parameters are first calculated:

$$a_{\mathrm{r}} = \frac{a_{ps}}{a_{lb}}, \quad b_{\mathrm{r}} = \frac{b_{ps}}{b_{lb}}, \quad R_{\mathrm{r}} = \frac{R_{ps}}{R_{lb}}, \quad \sigma_{\mathrm{r}} = \frac{\sigma_{ps}}{\sigma_{lb}} \tag{2.25}$$

Here, the physical values are calculated using the following:

$$a_{ps} = 0.45724 \frac{R_{ps}^2 T_{c,ps}^2}{P_{c,ps}},$$
$$b_{ps} = 0.0778 \frac{R_{ps} T_{c,ps}}{P_{c,ps}},$$
$$R_{ps} = \frac{1}{0.307} \frac{P_{c,ps}}{T_{c,ps}}$$

The surface tension σ is calculated from the pressure tensor according to [53, 55], as described in 3. Finally, the conversion factors for the four fundamental physical units are given by

$$M_{\mathrm{r}} = a_{\mathrm{r}}^{-3} b_{\mathrm{r}}^{5} \sigma_{\mathrm{r}}^{3}, \quad L_{\mathrm{r}} = a_{\mathrm{r}}^{-1} b_{\mathrm{r}}^{2} \sigma_{\mathrm{r}}, \quad t_{\mathrm{r}} = a_{\mathrm{r}}^{-3/2} b_{\mathrm{r}}^{5/2} \sigma_{\mathrm{r}}, \quad \Theta_{\mathrm{r}} = a_{\mathrm{r}} b_{\mathrm{r}}^{-1} R_{\mathrm{r}}^{-1} \tag{2.26}$$

Later, Gong et al. [76] proposed a similar method by directly selecting the critical density, pressure, temperature, and surface tension as four base units. In this formulation, the conversion ratios are as follows:

$$\rho_{\mathrm{r}} = \frac{\rho_{c,ps}}{\rho_{c,lb}}, \quad P_{\mathrm{r}} = \frac{P_{c,ps}}{P_{c,lb}}, \quad \theta_{\mathrm{r}} = \frac{T_{c,ps}}{T_{c,lb}}, \quad \sigma_{\mathrm{r}} = \frac{\sigma_{ps}}{\sigma_{lb}} \tag{2.27}$$

and the derived unit conversion factors are:

$$M_{\mathrm{r}} = \frac{\rho_{\mathrm{r}} \sigma_{\mathrm{r}}^{3}}{P_{\mathrm{r}}^{3}}, \quad L_{\mathrm{r}} = \frac{\sigma_{\mathrm{r}}}{P_{\mathrm{r}}}, \quad t_{\mathrm{r}} = \frac{\rho_{\mathrm{r}}^{1/2} \sigma_{\mathrm{r}}}{P_{\mathrm{r}}^{3/2}}, \quad \Theta_{\mathrm{r}} = \theta_{\mathrm{r}} \tag{2.28}$$

To demonstrate the effect of varying pseudopotential parameters on the physical unit conversion, two representative cases are selected: $a = \frac{3}{49}$ and $a = \frac{1}{49}$, with fixed values of $b = \frac{2}{21}$ and $R = 1$. The conversion is performed under the condition of reduced temperature $T_r = 0.86$, corresponding to typical subcritical boiling conditions for water.

Tables 2.7, 2.8, 2.9, 2.10 summarize the unit conversion results for both cases. The four fundamental units: mass (M_r), length (L_r), time (t_r), and temperature (Θ_r) are first derived from the independent physical parameters ρ_c, P_c, T_c, and σ. These then allow for conversion of derived quantities, including kinematic viscosity

ν, thermal conductivity λ, and specific heat at constant volume c_v, for both liquid and vapor phases.

A comparison between the two cases shows that decreasing the a value (i.e., increasing interface thickness in lattice units) significantly alters the fundamental conversion scales. Notably, the temperature conversion factor Θ_r increases by nearly threefold when a decreases from 3/49 to 1/49, and the time scale t_r becomes much smaller, indicating faster dynamics in physical time.

TABLE 2.7: Unit conversion for water at 0.86 T_c (Independent Parameters), a = 3/49

Independent parameters	Lattice unit (lb/l.u.)	Physical unit (p.s.)	Conversion factors	Reference Value
ρ_c	2.6572 mu/lu^3	322 kg/m^3	M_r	2.3624×10^{-24} kg
P_c	0.0894 mu/(lu ts^2)	2.2064×10^7 kg/(m s^2)	L_r	2.6914×10^{-9} m
T_c	0.1094 tu	647.1 K	t_r	1.8859×10^{-12} s
$\sigma_{0.86Tc}$	0.0274 mu/ts^2	0.0182 kg/s^2	Θ_r	5.9150×10^3 K

TABLE 2.8: Unit conversion for water at 0.86 T_c (Other Parameters), a = 3/49

Parameter	Lattice unit (lb/l.u.)	Physical unit (p.s.)	Reference Value
ν_l	0.0326lu^2/ts	1.2542×10^{-7} m^2/s	$\nu_r = 3.8409 \times 10^{-6}$ m^2/s
ν_v	0.1529lu^2/ts	5.8729×10^{-7} m^2/s	
λ_l	3.6510 mu/(ts^3 tu)	0.5851 kg m/(s^3 K)	$\lambda_r = 0.1603$ kg m/(s^3 K)
λ_v	0.3718mu/(ts^3 tu)	0.05959 kg m/(s^3 K)	
$c_{v,l}$	8.9776 lu^2/(ts^2 tu)	3091.2 m^2/(s^2 K)	$c_{v,r} = 344.3226$ m^2/(s^2 K)
$c_{v,v}$	7.8952 lu^2/(ts^2 tu)	2718.5 m^2/(s^2 K)	

This unit conversion scheme provides a flexible framework for tuning the interface thickness and physical scale simultaneously, allowing the LBM results to be mapped to real fluid systems like water while preserving thermodynamic consistency.

TABLE 2.9: Unit conversion for water at 0.86 T_c (Independent Parameters), a = 1/49

Parameter	Lattice unit (lb/l.u.)	Physical unit (p.s.)	Conversion factors	Reference Value
ρ_c	2.6572 mu/lu^3	322 kg/m^3	M_r	6.0325×10^{-26} kg
P_c	0.0298 mu/(lu ts^2)	2.2064×10^7 kg/(m s^2)	L_r	7.9254×10^{-10} m
T_c	0.0365 tu	647.1 K	t_r	3.2055×10^{-13} s
$\sigma_{0.86Tc}$	0.031 mu/ts^2	0.0182 kg/s^2	Θ_r	1.7748×10^4 K

TABLE 2.10: Unit conversion for water at 0.86 T_c (Other Parameters), a = 1/49

Parameter	Lattice unit (lb/l.u.)	Physical unit (p.s.)	Reference Value
ν_l	0.0640 lu^2/ts	1.2542×10^{-7} m^2/s	$\nu_r = 1.9595 \times 10^{-6}$ m^2/s
ν_v	0.2997 lu^2/ts	5.8729×10^{-7} m^2/s	
λ_l	7.1539 mu/(ts^3 tu)	0.5851 kg m/(s^3 K)	$\lambda_r = 0.0818$ kg m/(s^3 K)
λ_v	0.7286mu/(ts^3 tu)	0.05959 kg m/(s^3 K)	
$c_{v,l}$	8.9745 lu^2/(ts^2 tu)	3091.2 m^2/(s^2 K)	$c_{v,r} = 344.4426$ m^2/(s^2 K)
$c_{v,v}$	7.8925 lu^2/(ts^2 tu)	2718.5 m^2/(s^2 K)	

2.5.3 Validation of Bubble Departure Diameter via Unit Conversion

To further validate the effectiveness of the proposed unit conversion strategy, we perform a direct comparison of bubble departure diameters between LBM simulations and physical experiments. This verification step ensures that the LBM results, when appropriately scaled, fall within the expected physical range observed in real systems.

The conversion process involves two key steps. First, the lattice-to-physical unit conversion factor L_r is derived based on critical thermodynamic properties, as

previously introduced. For the current case at $T = 0.86T_c$, the resulting length scale is:

$$L_r = 2.6914 \times 10^{-9}\,\mathrm{m/lu}.$$

With a computational domain of $N = 120$ lattice nodes, the total physical domain size is calculated as:

$$L_x = N \cdot L_r = 120 \times 2.6914 \times 10^{-9} = 3.22968 \times 10^{-7}\,\mathrm{m}.$$

In the LBM simulation, the departure diameter ranges from $D_{\min} = 23.1$ to $D_{\max} = 40.8$ lu, corresponding to:

$$D_{\mathrm{LBM}} = [62.16\,\mathrm{nm},\ 109.8\,\mathrm{nm}].$$

To allow meaningful comparison with experimental measurements, a scaling factor is introduced based on the ratio of the experimental field of view to the simulated domain:

$$L_s = \frac{L_{\mathrm{phys}}}{L_x} = \frac{0.01}{120 \cdot 2.6914 \times 10^{-9}} \approx 3.096 \times 10^4.$$

Multiplying the LBM results by this factor gives the predicted bubble departure diameter range in physical units:

$$D_{\mathrm{predict}} = L_s \cdot D_{\mathrm{LBM}} = [1.93\,\mathrm{mm},\ 3.40\,\mathrm{mm}].$$

These predictions are in good agreement with the experimentally measured values of:

$$D_{\mathrm{exp}} = [1.8886\,\mathrm{mm},\ 4.2120\,\mathrm{mm}].$$

A visual summary of this unit conversion validation is presented in Fig. 2.5, and the quantitative comparison is listed in Table 2.11. The alignment between simulation and experiment demonstrates the validity of our scaling method and confirms that

the LBM simulation results can be meaningfully interpreted in the context of real physical systems. All physical properties used in this conversion are obtained from the REFPROP [79] database provided by NIST.

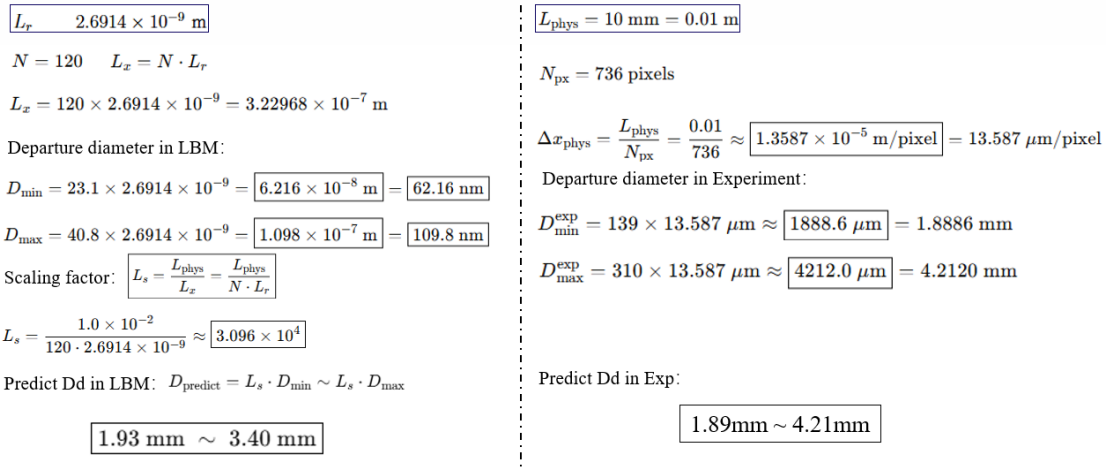

FIG. 2.5: Comparison of bubble departure diameter between LBM simulation and experiment. The left panel shows the LBM results and scaling process, while the right panel presents experimental measurements.

TABLE 2.11: Comparison of Bubble Departure Diameters in Different Units

Quantity	**LBM (Raw)**	**LBM (Scaled)**	**Experiment**
Minimum D_d	23.1 l.u. $\approx$ 62.16 nm	1.93 mm	1.89 mm
Maximum D_d	40.8 l.u. $\approx$ 109.8 nm	3.40 mm	4.21 mm

2.6 Thermodynamic Consistency Validation

In LBM, particularly within the pseudopotential framework, an equation of state (EOS) is essential for computing the local pressure:

$$P = \rho RT + f(\rho, T) \tag{2.29}$$

Where P is the pressure, ρ is the fluid density, R is the gas constant, and T is the temperature. The term $f(\rho, T)$ accounts for non-ideal interactions. Although the ideal gas EOS is sufficient for dilute and high-temperature gases, it does not capture phase transition phenomena. Real-fluid EOSs, such as Peng-Robinson

(PR), Redlich-Kwong (RK), and their variants are widely used for simulating vapor-liquid co-existence and supercritical behavior. To evaluate the applicability of different EOS in phase-change simulations, we analyze their pressure–volume P–v characteristics.

Table 2.12 summarizes several commonly used EOS and their parameters [80]. The performance of each EOS is compared through MATLAB generated P–v diagrams under reduced temperature $T_r = T/T_c$.

TABLE 2.12: Summary of commonly used equations of state (EOS)

EOS	**Expression**	**Parameters**
RK	$p = \frac{\rho RT}{1-b\rho} - \frac{a\rho^2}{\sqrt{T}(1+b\rho)}$	$a = 0.42748\frac{R^2T_c^{2.5}}{p_c}, \quad b = 0.08664\frac{RT_c}{p_c}$
SRK	$p = \frac{\rho RT}{1-b\rho} - \frac{a\alpha(T)\rho^2}{1+b\rho}$	$\alpha(T) = \left[1 + (0.480 + 1.574\omega - 0.176\omega^2)(1 - \sqrt{T/T_c})\right]^2$
		$a = 0.45724\frac{R^2T_c^2}{p_c}, \quad b = 0.0778\frac{RT_c}{p_c}$
PR	$p = \frac{\rho RT}{1-b\rho} - \frac{a\alpha(T)\rho^2}{1+2b\rho-b^2\rho^2}$	$\alpha(T) = \left[1 + (0.37464 + 1.54226\omega - 0.26992\omega^2)(1 - \sqrt{T/T_c})\right]^2$
vdW	$p = \frac{\rho RT}{1-b\rho} - a\rho^2$	Classical EOS; earliest cubic model
CS	$p = \rho RT \cdot f(\rho b) - a\rho^2$	Carnahan–Starling correction for hard-sphere fluids

2.6.1 Different Equations of State

As shown in Fig. 2.6, the van der Waals (vdW) equation of state is the first cubic EOS proposed for real fluids [81]. While it provides reasonable predictions in high-temperature, low-density vapor regions, it exhibits significant inaccuracies in the phase-transition and high-density liquid regions.

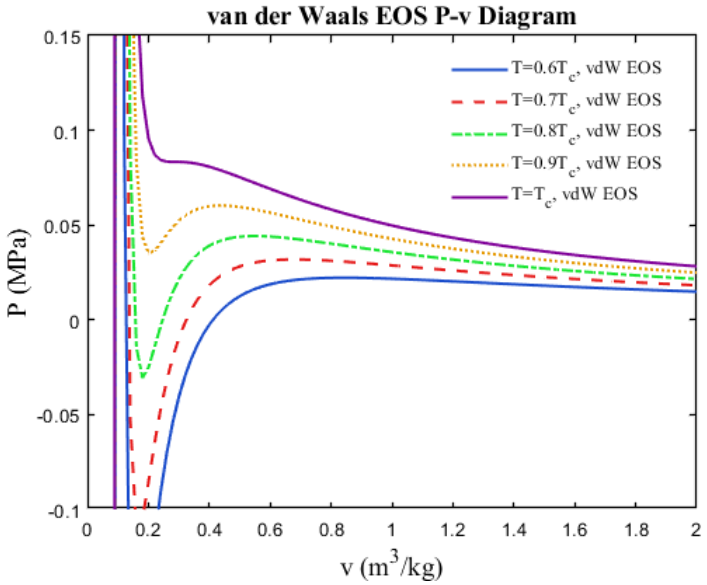

FIG. 2.6: p–v diagram of the van der Waals (vdW) equation of state at different temperatures.

Specifically, the vdW EOS does not accurately reproduce the saturated vapor pressure and the coexistence characteristics of the vapor and liquid. Although it can be used for qualitative fluid behavior, its limited accuracy makes it unsuitable for high-fidelity phase-transition simulations. Therefore, it is generally not recommended for use in pseudopotential LBM-based phase-change modeling.

Fig. 2.7 and 2.8 show the P–v diagrams for the Redlich-Kwong (RK) [82] and Soave-Redlich-Kwong (SRK) EOS [83], respectively. From the figures, it can be observed that both EOS can generally describe vapor–liquid phase transitions. However, studies have indicated [84] that while these equations perform well under moderate temperature and pressure conditions, they exhibit significant errors in the high-density liquid phase. Compared to the PR EOS, their accuracy in phase-transition calculations is slightly lower.

The main advantage of these EOS is their relatively low computational cost, making them suitable for simulations where computational efficiency is a priority. Furthermore, research has shown that these equations are applicable to high-temperature fluid phase-transition simulations. However, at low temperatures, their inherent inaccuracies may cause numerical instability in LBM, making them less suitable for simulating phase transitions with high density ratios.

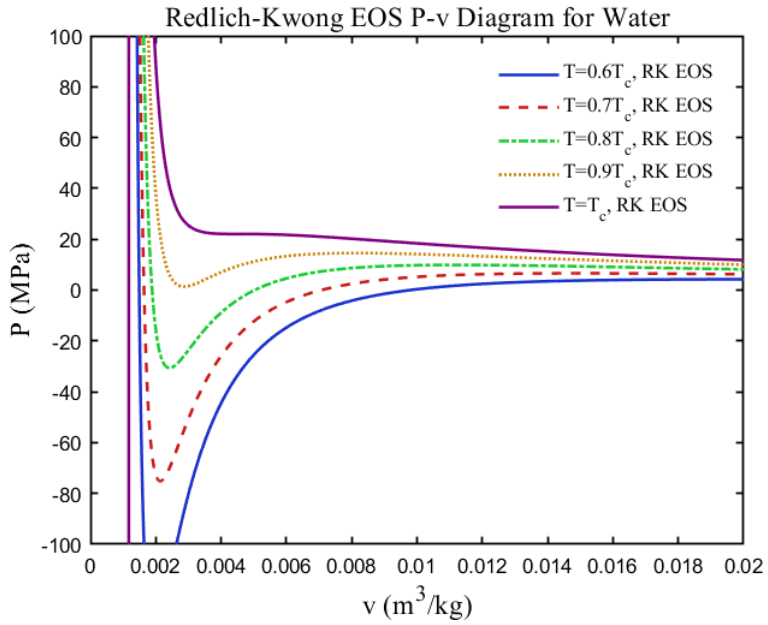

FIG. 2.7: p–v diagram of the Redlich–Kwong (RK) equation of state at different temperatures.

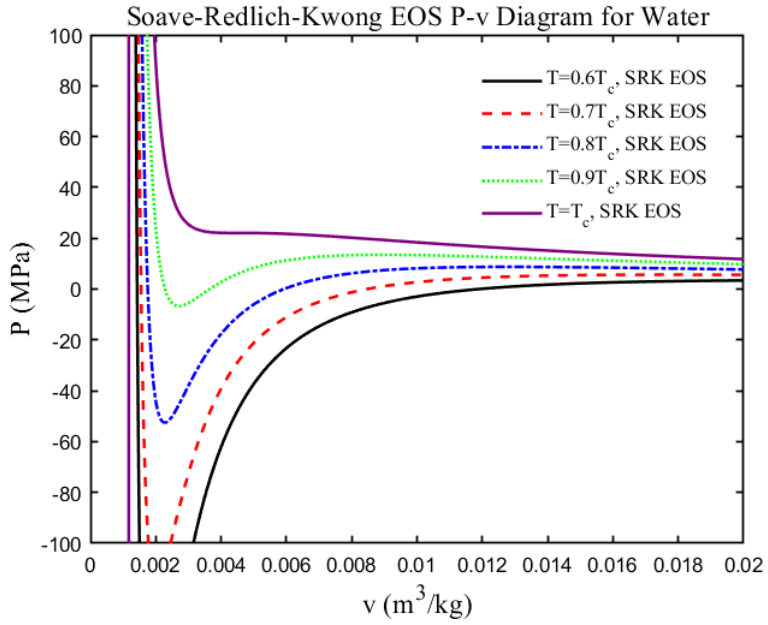

FIG. 2.8: p–v diagram of the Soave–Redlich–Kwong (SRK) equation of state for water at different temperatures

Finally, Fig. 2.9 presents the Peng–Robinson (PR) EOS [85]. As shown in the figure, this model provides accurate predictions of vapor–liquid phase behavior and has been widely adopted in petrochemical and supercritical fluid simulations. The key advantage of the PR EOS lies in its ability to offer a reliable balance

between computational efficiency and thermodynamic accuracy across a broad temperature range. This makes it particularly attractive for LBM simulations, where both stability and computational cost are critical. Among various cubic EOS options, PR has demonstrated superior performance in capturing vapor–liquid coexistence curves, interfacial tension, and critical properties, which are essential in modeling phase-change phenomena. However, it is important to note that when the saturation temperature drops below approximately 0.60 T_c, the accuracy of the PR EOS deteriorates, resulting in an increased error in the prediction of the coexistence properties. This limitation is not unique to PR but is commonly observed in all cubic EOSs due to their fundamental theoretical formulation.

In general, the aforementioned EOSs are all derived from van der Waals nonideal gas theory [86]. Within their applicable ranges, each EOS can effectively capture the inflection behavior associated with vapor–liquid phase transitions, which corresponds to the nonmonotonic regions of the isothermal pressure–volume curves. At lower temperatures, the coexistence of subcooled liquid, vapor, and phase-transition regions is clearly distinguishable. As the temperature increases toward the critical point, the inflection point diminishes, consistent with the disappearance of phase boundaries near the criticality.

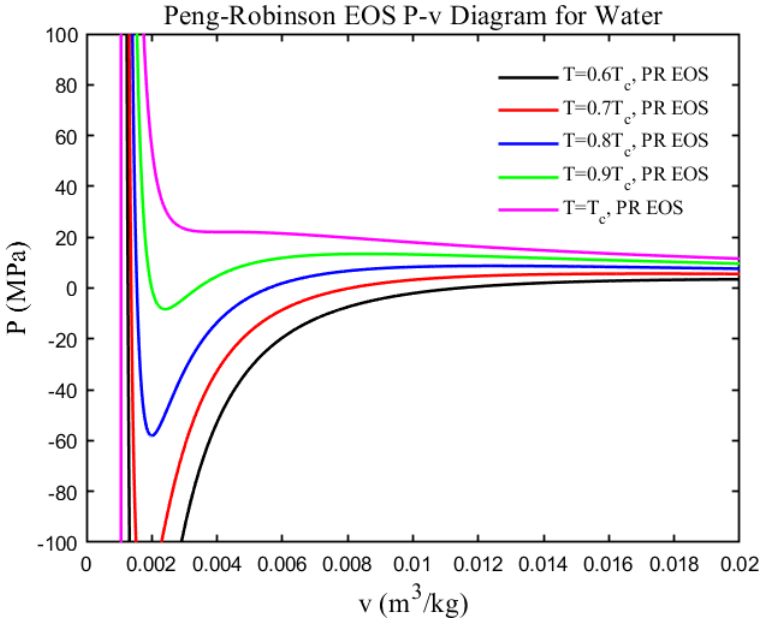

FIG. 2.9: p–v diagram of the Peng–Robinson (PR) equation of state for water at different temperatures

2.6.2 Maxwell Construction and Vapor–Liquid Coexistence

To further validate the thermodynamic consistency of the LBM framework, this section introduces the Maxwell construction theory and compares the vapor–liquid coexistence behavior predicted by various EOSs. The Maxwell construction provides a theoretical benchmark for evaluating the equilibrium properties of two-phase systems by enforcing the equal area rule along the isothermal pressure-volume curve $P - v$. By comparing the predicted coexistence curves of LBM with the Maxwell construction results and the experimental data of IAPWS-IF97 [87], we assess the precision of different EOS formulations. The results highlight the superior thermodynamic consistency of the PR EOS, thereby justifying its adoption in the present study.

2.6.2.1 Maxwell construction

For non-ideal equations of state, the vapor–liquid coexistence is obtained by Maxwell's equal-area construction [88]. Below the critical temperature the subcritical isotherm $P(v)$ develops a non-monotonic S-shaped (van der Waals) loop with a mechanically unstable segment where $(\partial P/\partial v)_T > 0$. (Equivalently, viewed as $v(P)$ the relation becomes multivalued with two metastable branches and one unstable branch.) Maxwell replaces this loop by a horizontal tie line at the coexistence pressure $P_{\mathrm{sat}}(T)$ such that the areas above and below the line are equal, i.e.

$$\int_{v_l}^{v_v} \big[P(v,T) - P_{\mathrm{sat}}(T)\big]\,\mathrm{d}v \;=\; 0, \tag{2.30}$$

which yields the coexistence specific volumes v_l (liquid) and v_v (vapor) and enforces equality of pressure and chemical potential (equivalently, equal Gibbs free energy) in the two phases [89, 90]. Fig. 2.10 illustrates the principle of equal areas A and B under the isothermal curve.

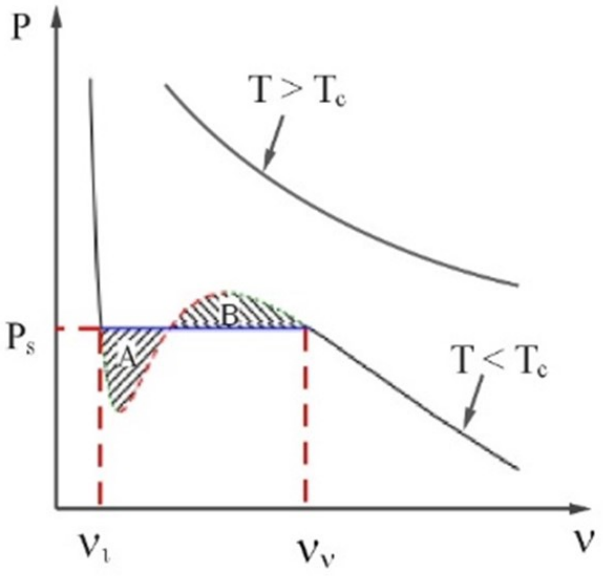

FIG. 2.10: Maxwell equal-area construction on a subcritical isotherm. The S-shaped loop for $T < T_c$ is replaced by a horizontal tie line at P_{sat} (blue) so that the two shaded areas are equal. The dashed vertical lines mark the coexistence volumes v_l and v_v. A supercritical isotherm ($T > T_c$) is shown for reference.

The numerical procedure is that, for a given T, we bracket the two roots v_l and v_v of $P(v,T) = P_{\text{sat}}$, and drive the equal-area residual $R(P_{\text{sat}}) = \int_{v_l}^{v_v} [P(v,T) - P_{\text{sat}}]\, \mathrm{d}v$ to zero (e.g., by bisection or Newton). The resulting $P_{\text{sat}}(T)$, $v_l(T)$, and $v_v(T)$ define the coexistence curve that we use as the thermodynamic baseline for validating LBM results under the chosen EOS.

2.6.2.2 vapor-liquid coexistence

In this subsection I compared vapor–liquid coexistence curves obtained from LBM simulations using several equations of state (vdW, CS, RK, SRK, and PR) against their Maxwell–construction predictions and the IAPWS-IF97 reference data [87]. The simulations follow the droplet–in–vapor setup of Yuan and Schaefer [71] and use the MRT-based hybrid thermal LBM described earlier. Throughout this section, we plot the results in reduced variables, where the reduced temperature and reduced density are defined by the EOS-specific critical properties as

$$T_r \equiv \frac{T}{T_c}, \qquad \rho_r \equiv \frac{\rho}{\rho_c}.$$

(When comparing different EOS, each curve is nondimensionalized by its own T_c and ρ_c unless stated otherwise). Unless stated otherwise: (i) black $\times$ symbols denote the IAPWS–IF97 reference correlation; (ii) the red solid curve is the Maxwell construction liquid branch of the given EOS; (iii) the blue solid curve is the Maxwell construction vapor branch; and (iv) colored markers represent LBM results obtained with that EOS.

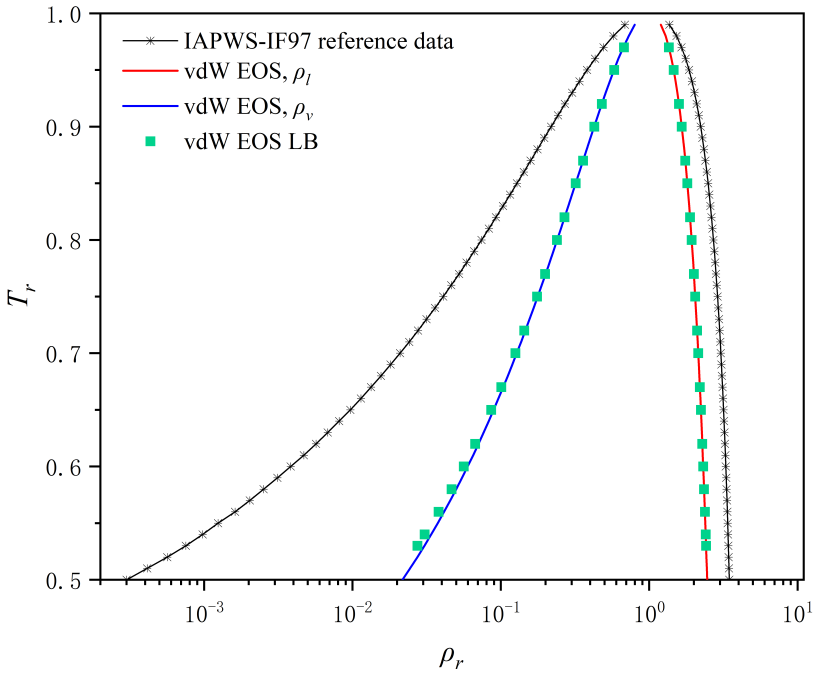

FIG. 2.11: vdW EOS vapor–liquid coexistence in reduced variables (T_r, ρ_r)

Fig. 2.11 compares the van der Waals (vdW) EOS results. The LBM data agree reasonably well with the Maxwell-based coexistence curve, particularly on the liquid branch. Noticeable discrepancies appear on the vapor branch ($\rho_r < 1$), where LBM tends to under-predict the vapor density. Relative to the IAPWS-IF97 reference, both the LBM and the vdW–Maxwell curves deviate considerably in the low-density region, reflecting an inherent limitation of the vdW EOS: while it captures qualitative two-phase behavior, it lacks the accuracy required for real-fluid properties near saturation. Hence, the vdW EOS is not recommended for precise phase-transition simulations within the present pseudopotential LBM framework.

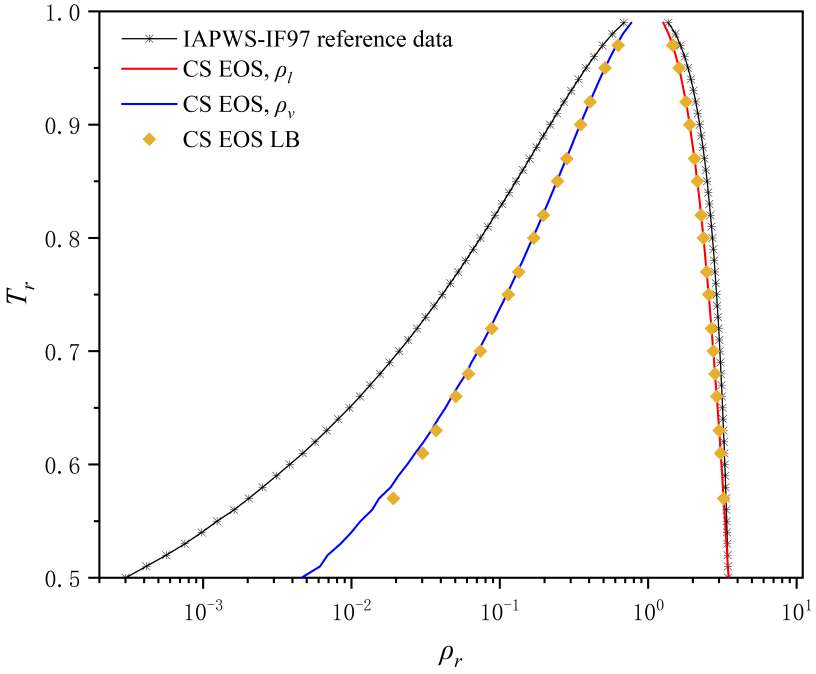

FIG. 2.12: CS EOS vapor–liquid coexistence in reduced variables (T_r, ρ_r)

Fig. 2.12 compares the Carnahan–Starling (CS) EOS against its Maxwell prediction and the IAPWS-IF97 reference curve. The LBM data closely follow the CS–Maxwell coexistence curve over most of the range, confirming the numerical implementation. However, noticeable discrepancies with IAPWS-IF97 remain—most prominently on the vapor branch at low densities—indicating that, while CS improves over simple cubic forms in describing repulsive effects, it still lacks the fidelity required for quantitative vapor–liquid equilibrium of real water. Consequently, the CS EOS is suitable for qualitative two-phase behavior but is not recommended as a high-accuracy reference for phase-transition simulations in the present pseudopotential LBM framework.

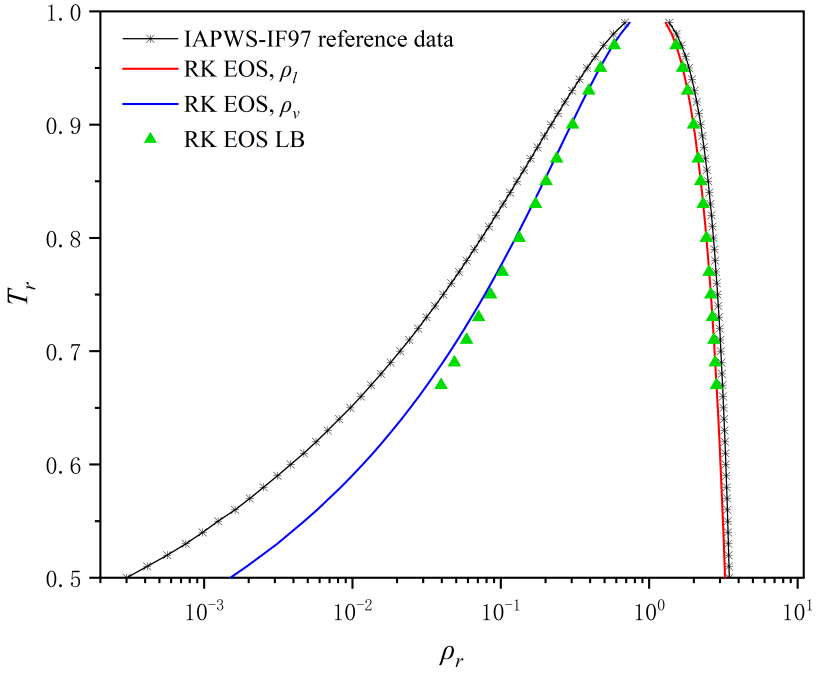

FIG. 2.13: RK EOS vapor–liquid coexistence in reduced variables (T_r, ρ_r)

Fig. 2.13 compares the RK EOS with its Maxwell prediction and the IAPWS-IF97 reference. Among the cubic forms considered, RK shows a clear improvement over vdW and CS—especially on the liquid branch and close to the critical region—and the LBM data collapse onto the RK–Maxwell curve, confirming the numerical implementation. Nevertheless, deviations persist in the low-density vapor-phase region, indicating that the RK EOS still lacks the accuracy required for precise predictions across the full two-phase spectrum.

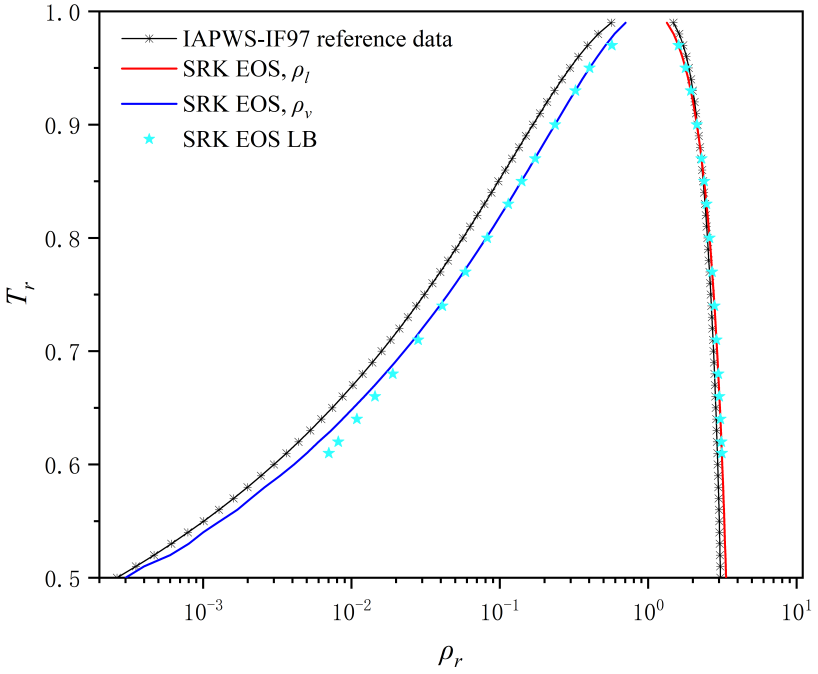

FIG. 2.14: SRK EOS vapor–liquid coexistence in reduced variables (T_r, ρ_r)

Fig. 2.14 presents the vapor–liquid coexistence curves obtained using the SRK EOS [91]. As an improved version of the RK EOS, the SRK model introduces a temperature-dependent correction factor, enhancing its predictive accuracy, particularly in the vapor-phase region. The numerical results exhibit strong agreement with both the theoretical solution and the experimental reference data from IAPWS-IF97. Compared to the RK EOS, the SRK formulation delivers better performance at low densities and across a broader temperature range.

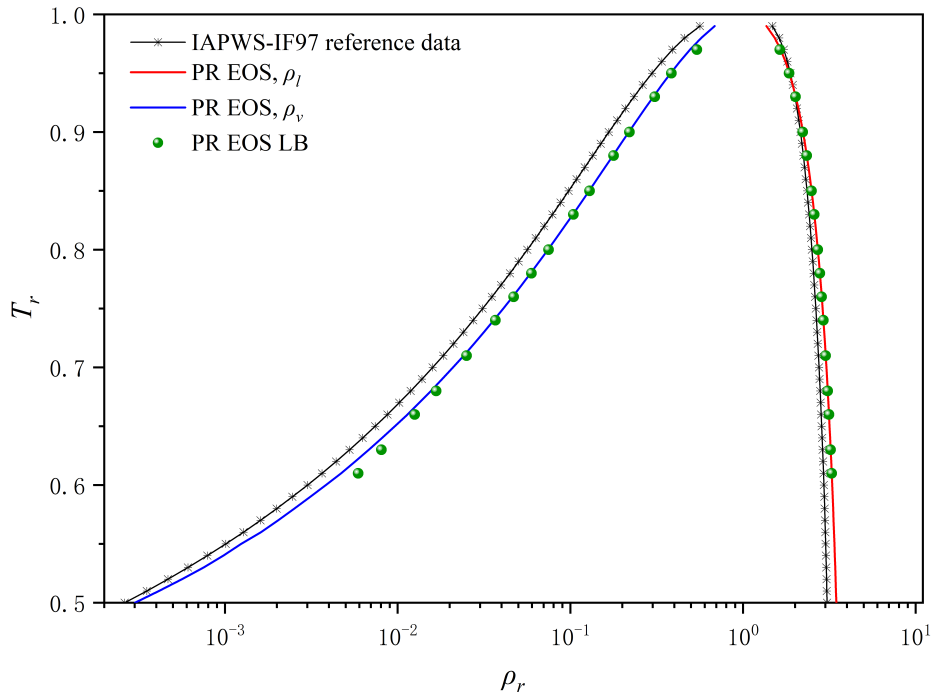

FIG. 2.15: PR EOS vapor–liquid coexistence in reduced variables (T_r, ρ_r)

Fig. 2.15 compares the Peng–Robinson (PR) equation of state with its Maxwell construction and the IAPWS-IF97 reference curve. It shows that, among the cubic EOS tested (vdW, CS, RK, SRK, PR), the LBM data coincide with the PR–Maxwell coexistence curve and match IAPWS-IF97 most closely on both branches. Small deviations remain on the dilute-vapor side. I therefore adopt PR for all subsequent pseudopotential LBM simulations.

2.6.3 Error Comparison Across EOS Models

To quantitatively assess the predictive accuracy of various EOS models, Figure 2.16 presents the mean absolute error (MAE) for both vapor and liquid branches, using IAPWS-IF97 data as reference [87]. The MAE is defined as:

$$\mathrm{MAE} = \frac{1}{N}\sum_{i=1}^{N}\left|\rho_i^{\mathrm{LB}} - \rho_i^{\mathrm{ref}}\right| \tag{2.31}$$

Among all tested EOS models, the PR EOS yields the lowest overall error, particularly excelling in vapor-phase prediction. In contrast, the vdW EOS displays

the highest error, especially in the liquid region, reflecting its limitations in describing real-fluid thermodynamics. The CS EOS also exhibits considerable error in the vapor branch. RK and SRK EOSs show moderate accuracy, with SRK outperforming RK due to its improved alpha function.

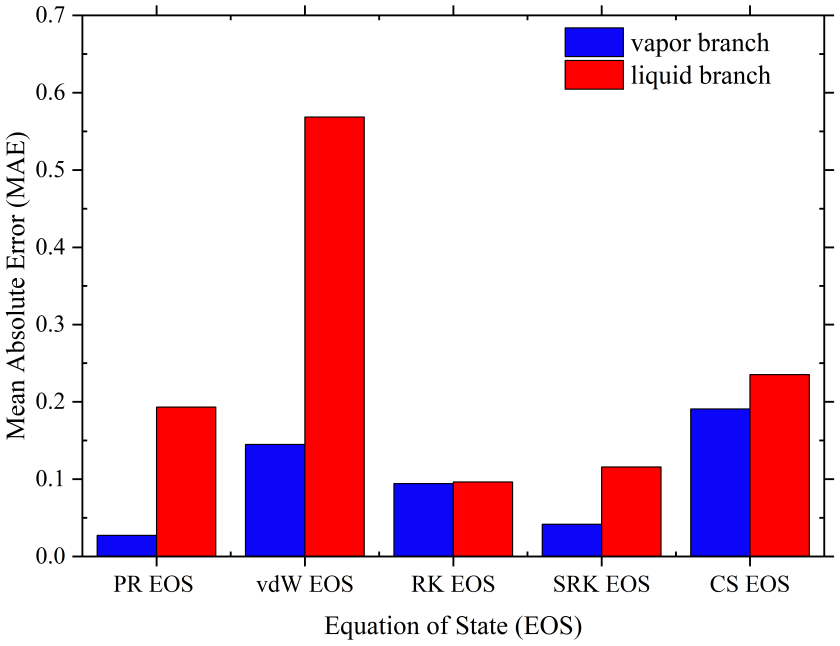

FIG. 2.16: MAE Comparison Across EOS Models

Overall, this comparison confirms the PR EOS stands out for its strong balance of numerical stability, thermodynamic fidelity, and computational efficiency, making it a preferred choice for pseudopotential LBM simulations involving bubble dynamics and phase-change processes. As such, the present study adopts PR EOS as a baseline model for subsequent simulations and validation tests.

2.7 Interface-Level Validation

In multiphase systems, the interface between vapor and liquid is not a mathematically sharp boundary, but a finite-thickness transition zone where the fluid density continuously varies from the vapor density ρ_v to the liquid density ρ_l [92]. This diffuse interface is a key physical feature in the pseudopotential LBM framework, directly influencing surface tension and interfacial forces.

Fig. 2.17 illustrates the schematic structure of a vapor–liquid interface, showing the density profile and the interfacial width δz_i. The shape and stability of this region

are jointly affected by temperature, surface tension, and the choice of equation of state (EOS) [71, 93]. An accurate representation of this region is essential for capturing phenomena such as droplet formation, capillarity, and pressure jumps.

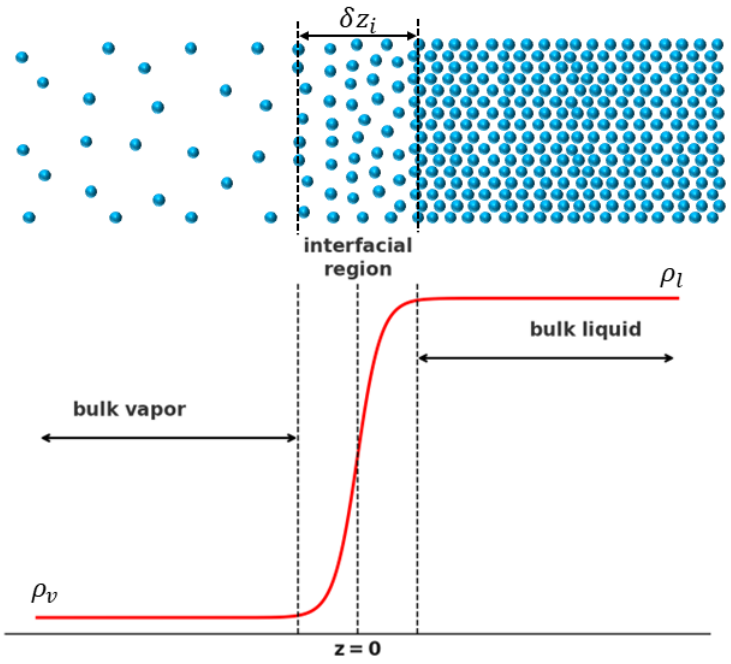

FIG. 2.17: Density evolution of vapor-liquid interface

To verify the model's capability of capturing interfacial effects, the following two tests are conducted in this work: **Laplace Law Validation**: Using the pressure difference across a curved interface to compute surface tension. **Pressure Tensor Consistency**: Evaluating the mechanical definition of surface tension via integration of the pressure tensor across the interface.

2.7.1 Laplace Law

To validate the capability of the model to capture interfacial tension, the Laplace law is examined under both the standard Li-MRT framework [93] and the improved Huang-MRT framework [94]. The Laplace law establishes a linear relationship between the pressure difference across a curved liquid–vapor interface and the droplet curvature [95]:

$$\Delta P = P_{\text{in}} - P_{\text{out}} = \frac{2\sigma}{R}, \tag{2.32}$$

where σ is the surface tension and R the droplet radius. A linear relationship between ΔP and $1/R$ serves as a benchmark for validating interfacial physics.

Static droplets with $R \in [15, 40]$ (lattice units) are initialized in a 200×200 domain. P_1 is sampled at the droplet center, P_2 in the far-field vapor. As shown in Fig. 2.18, the Laplace law is well recovered at different reduced temperatures ($T = 0.78T_c, 0.86T_c, 0.90T_c$), confirming the reliability of the Shan-Chen model based on MRT to resolve interfacial tension.

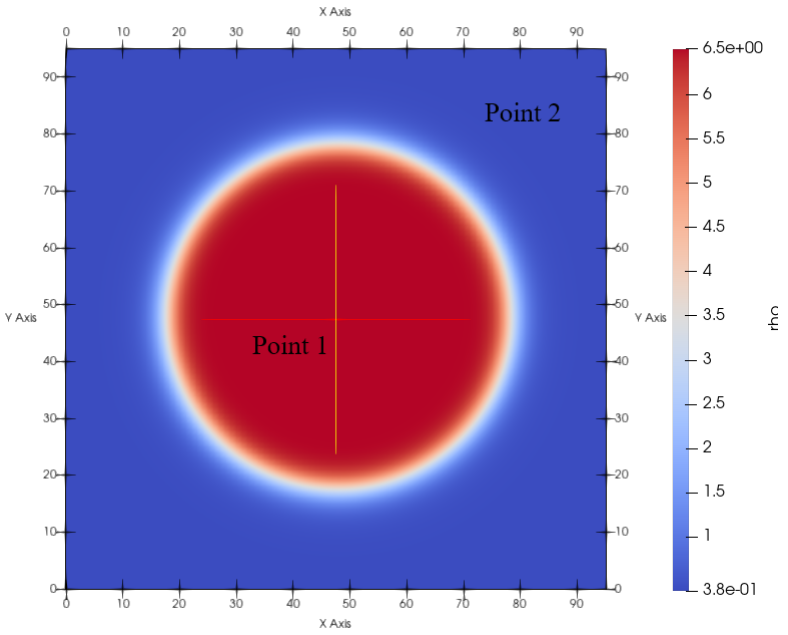

FIG. 2.18: Example of the initialized droplet ($T = 0.86T_c$, $R = 30$)

Fig. 2.19 consolidates the three temperatures ($T = 0.78T_c$, $0.86T_c$, $0.90T_c$) into a single plot of ΔP versus $1/R$. Markers are LBM data; solid lines are least-squares fits. The excellent linearity for all T confirms Eq. (2.32). The fitted slopes yield consistent surface tensions across radii, with small residuals attributable to diffuse interfaces, EOS approximation, and finite-size effects [96, 97].

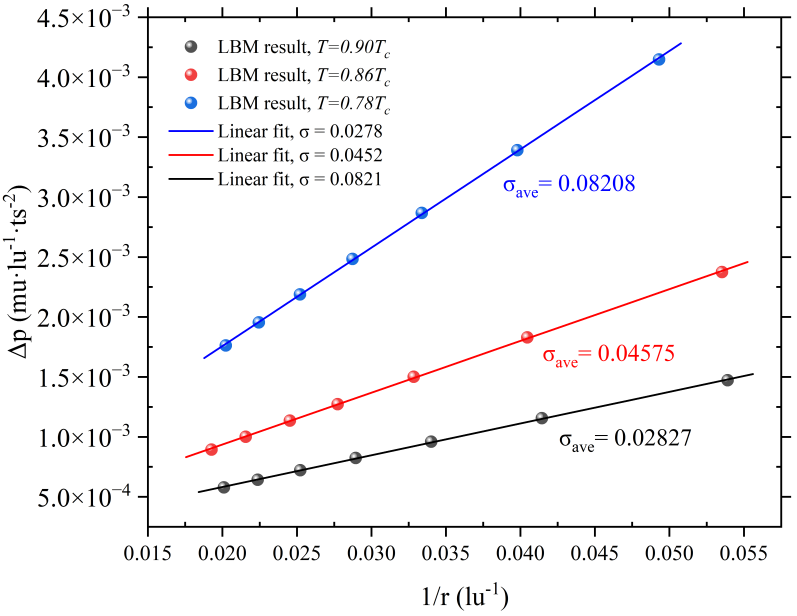

FIG. 2.19: Laplace test consolidated over three temperatures ($T = 0.78T_c$, $0.86T_c$, $0.90T_c$): ΔP vs. $1/R$. Markers: LBM; lines: linear fits

In the pseudopotential LBM, the surface tension σ and the vapor–liquid coexistence densities are usually coupled. The Li–MRT formulation inherits this coupling, whereas the Huang–MRT scheme [94] decouples them by: (i) introducing a thermodynamic-consistency parameter ε to set the bulk/mechanical-stability condition (hence the coexistence curve), and (ii) adding interfacial-stress terms in moment space weighted by two coefficients k_1 and k_2, which primarily control σ with minimal impact on the coexistence densities.

ε **(thermodynamic consistency):** appears in the forcing term and adjusts the isotropic part of the discrete pressure tensor so that the coexistence densities match the Maxwell construction for a chosen EOS. Typical values are $\varepsilon \in [1, 2]$; here we use $\varepsilon = 1.30$ and 1.67.

k_1, k_2 **(interfacial stress):** weight additional gradient contributions to the deviatoric/interfacial pressure tensor. In the Chapman–Enskog limit these are proportional to $|\nabla\psi|^2$, $\nabla\psi\,\nabla\psi$, and $\psi\nabla\nabla\psi$ (with ψ the pseudopotential), hence σ scales approximately linearly with a combination of k_1 and k_2, more detailed description can be found in ref. [55].

To keep the bulk EOS and mechanical stability unchanged while tuning σ, the parameters satisfy:

$$\boxed{\varepsilon = -8\,(k_1 + k_2)}$$

We therefore (1) fix ε to match the Maxwell coexistence; (2) sweep k_1 to reach the target σ; (3) set $k_2 = -\varepsilon/8 - k_1$.

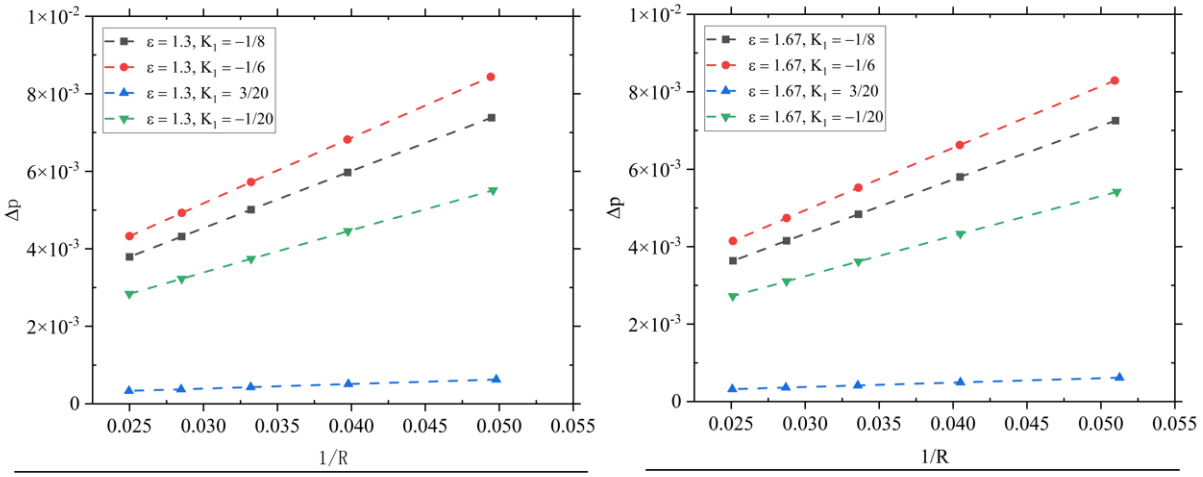

K1	ε = 1.3		
	σ	ρv (r = 40 lu.)	ρl (r = 40 lu.)
- 1/6	0.17304	0.337702	6.50667
- 1/8	0.151673	0.339186	6.50469
- 1/20	0.113483	0.341846	6.50113
3/20	0.0133841	0.348833	6.49173

K1	ε = 1.67		
	σ	ρv (r = 40 lu.)	ρl (r = 40 lu.)
- 1/6	0.165181	0.39042	6.51866
- 1/8	0.144806	0.391743	6.51674
- 1/20	0.108373	0.394115	6.51328
3/20	0.0128032	0.400318	6.50413

FIG. 2.20: Laplace validation with Huang–MRT: linear ΔP–$1/R$ holds for different (ε, K_1); the slope gives the tunable σ. Left: $\varepsilon = 1.3$; Right: $\varepsilon = 1.67$.

Fig. 2.20 shows ΔP versus $1/R$ for two values of ε (1.30 and 1.67) and several k_1 (hence several σ). All datasets exhibit excellent linearity, confirming Laplace's law $\Delta P = 2\sigma/R$; the fitted slopes yield σ. Tables beneath the plots report the corresponding σ together with the equilibrium densities at $R = 40$. For $\varepsilon = 1.67$, σ is tunable from ≈ 0.013 to 0.165; for $\varepsilon = 1.30$, from ≈ 0.013 to 0.173. Across these variations the coexistence densities ρ_v and ρ_l remain nearly invariant, demonstrating that Huang–MRT enables flexible surface-tension control without compromising the density separation.

2.7.2 Pressure Tensor Calculation

Accurate evaluation of the pressure (Cauchy stress) tensor is essential for capillarity in pseudopotential LBM. In continuum mechanics the mechanical state is described by a tensor; the scalar pressure p is only a special case corresponding to an isotropic

stress state (e.g., an inviscid fluid at rest). Whenever anisotropy arises—due to viscosity, confinement, or in particular interfacial (Korteweg) stresses—the normal and tangential components differ and the full tensor must be used. Across a vapor–liquid interface the capillary stress makes the stress anisotropic even at steady equilibrium; thus one typically observes $P_n \neq P_\tau$, and their difference integrates to the surface tension.

In this study we evaluate the pressure tensor using the formulation of Huang [53] (see also [98]). Along a one–dimensional planar interface, the normal and tangential components read

$$P_n = P_{xx} = \frac{\rho c^2}{3} + \frac{G\delta_x^2}{2}\psi^2 + \frac{G\delta_x^4}{6}\left[-\frac{1+12k_d-12k_1-12k_2}{2}\left(\frac{d\psi}{dx}\right)^2 + (1-6k_d)\psi\,\frac{d^2\psi}{dx^2}\right],$$

$$P_\tau = P_{yy} = \frac{\rho c^2}{3} + \frac{G\delta_x^2}{2}\psi^2 + \frac{G\delta_x^4}{6}\left[(a_3-6k_d b_2+6k_2)\left(\frac{d\psi}{dx}\right)^2 + (a_4-6k_d b_2)\,\psi\,\frac{d^2\psi}{dx^2}\right],$$

where G is the interaction strength, $\psi(\rho)$ the pseudopotential, c the lattice speed, δ_x the lattice spacing, and $k_1, k_2, k_d, a_3, a_4, b_2$ are isotropy/gradient coefficients determined by the chosen discrete force/gradient stencils [53, 98]. (Along the interface we take x as the normal direction.) A steady planar interface at $T = 0.80T_c$ is simulated under liquid–vapor coexistence. From the converged fields we extract ρ, ψ and compute the derivatives by centered differences, then assemble P_n and P_τ with the above expressions.

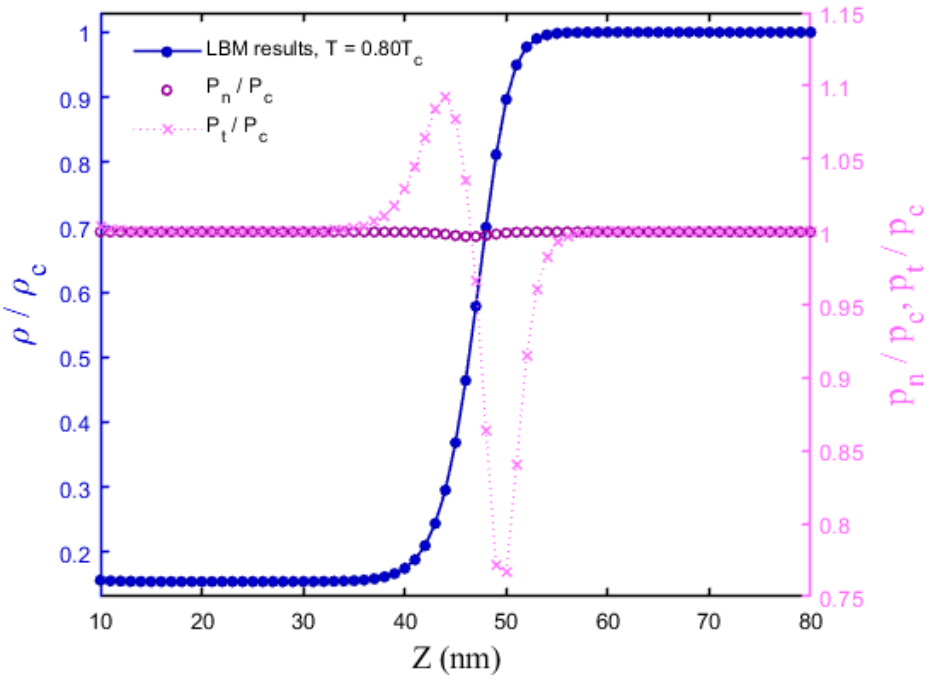

FIG. 2.21: Density and pressure tensor across a planar vapor–liquid interface at $T = 0.80T_c$

Fig. 2.21 confirms the expected anisotropy of the stress tensor near the interface: P_n is flat (mechanical equilibrium), while P_τ exhibits a localized deficit that integrates to the interfacial tension, consistent with thermodynamic theory. This validates the implemented pressure–tensor formulation and provides a reliable route for evaluating σ in diffuse–interface simulations.

2.8 Evaporation Model Validation

This section validates the implemented phase–change model in two canonical settings: (i) steady thin–film evaporation and (ii) transient droplet evaporation.

2.8.1 Steady-State Thin Film Evaporation

I employ PR EOS (shown in Sec. 2.6.2 to agree best with VLE data) and pseudopotential LBM. The computational setup is sketched in Fig. 2.22: a liquid layer (left) is heated by a uniform wall heat flux q (energy per unit area and time); vapor exits at a pressure outlet on the right; top and bottom are periodic.

In steady film evaporation the wall heat flux q is balanced by the latent heat transport at the interface,

$$q \;=\; h_{fg}\, m'', \tag{2.33}$$

where m'' is the interfacial mass flux (evaporation rate per unit area) and h_{fg} is the latent heat of vaporization. Here, m'' is obtained from the global mass balance,

$$m'' \;=\; \frac{1}{A_w}\,\frac{d}{dt}\int_{\Omega_v} \rho\, d\Omega \quad \text{(steady state: constant in time)},$$

with A_w the heated–wall area and Ω_v the vapor region. The latent heat h_{fg} is computed from the PR EOS using:

$$h = u + \frac{p}{\rho} = -\int \frac{1}{\rho^2}\left[T\left(\frac{\partial p}{\partial T}\right)_{\rho} - p\right] d\rho + \frac{p}{\rho}, \tag{2.34}$$

and $h_{fg} = h(\rho_v) - h(\rho_l)$ evaluated between coexistence densities (PR–Maxwell); see [99–102]. For details on the derivation of the latent heat of vaporization of PR EOS, please refer to Appendix D.

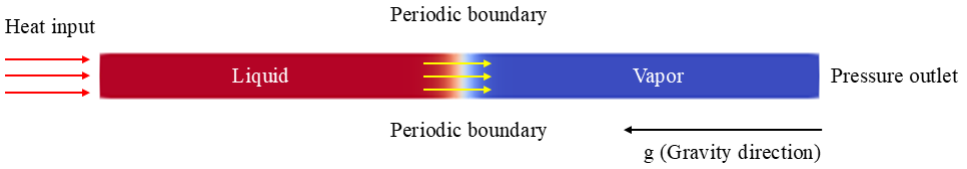

FIG. 2.22: Schematic of the thin–film evaporation configuration: uniform wall heat flux q at the heated wall (left), pressure outlet (right), and periodic boundaries in the transverse direction.

Before quantifying Eq. (2.33), we assess the influence of the computational domain at $T = 0.80T_c$ with fixed $q = 4 \times 10^{-5}$ (lattice units). Fig. 2.23 reports the steady m'' versus domain size ($L_x \times L_y$) at fixed grid spacing. The result quickly plateaus: for domains $\geq 120 \times 20$ lu the variation of m'' is below a few percent, indicating negligible lateral–boundary influence. We therefore use 240×20 lu (and larger) in the following.

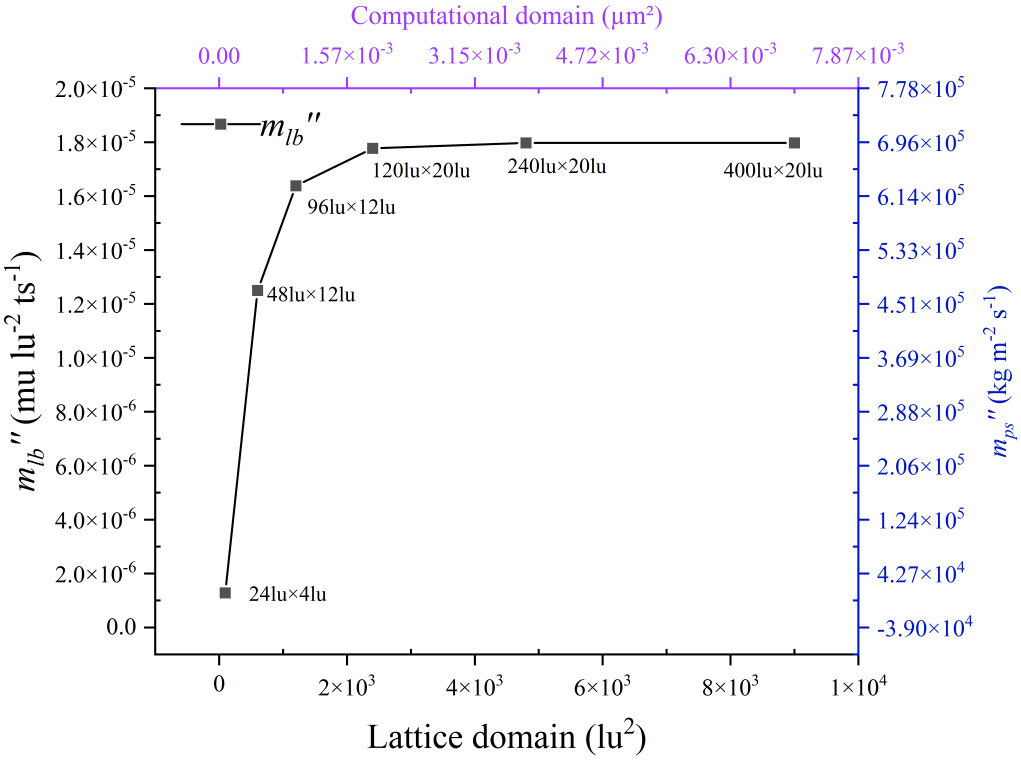

FIG. 2.23: Domain–size sensitivity of the steady interfacial mass flux m'' at $T = 0.80T_c$ and fixed q. Convergence beyond 120×20 lu shows minimal boundary influence

Subsequent simulations analyze the linearity between m'' and q at three temperatures ($T = 0.70T_c$, $0.80T_c$, and $0.90T_c$). Fig. 2.24 shows that q and m'' are linearly related, as predicted by Eq. (2.33). The slopes $k = \partial q/\partial m''$ decrease with temperature (0.291, 0.239, 0.178 in lattice units), consistent with the PR–EOS latent heat $h_{fg}(T)$. The agreement confirms that the model captures steady evaporation quantitatively.

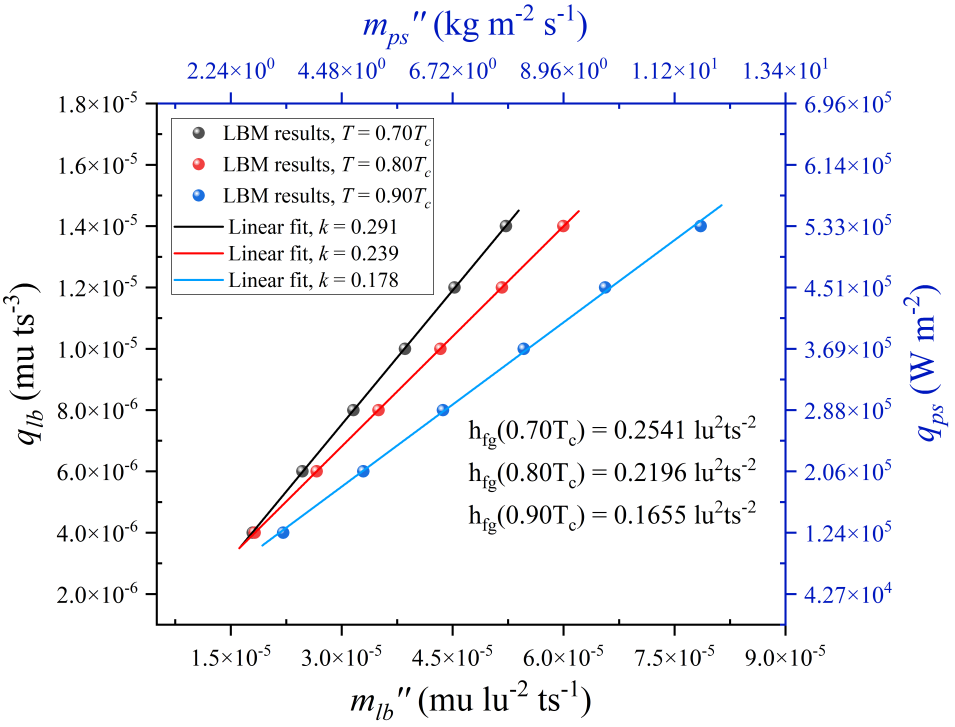

FIG. 2.24: Thin–film evaporation: linear relation $q = h_{fg}\, m''$ at three temperatures
Slopes (k) match the PR–EOS latent heat: $k = 0.291$ at $0.70T_c$, $k = 0.239$ at $0.80T_c$, $k = 0.178$ at $0.90T_c$

Small deviations at $T = 0.90T_c$ reflect the usual deterioration near the critical point (diffuse interfaces and EOS limitations). Overall, the PR–based pseudopotential LBM reproduces the expected q–m'' scaling over a broad range of conditions.

2.8.2 Droplet D^2 – Law

This section assesses the transient evaporation of an isolated droplet against the classical D^2 law,

$$D^2(t) = D_0^2 - K\,t, \qquad K \equiv -\frac{d(D^2)}{dt}, \tag{2.35}$$

which holds under a quasi-steady gas phase, nearly uniform droplet temperature, spherical symmetry, and an inert quiescent ambient [103].

In my verification case, the working fluid is single-component; the ambient is therefore pure vapor of the same fluid (no air or other non-condensables). The initial temperature field is prescribed as a smooth hyperbolic-tangent profile so

that the droplet interior is at T_s while the surrounding vapor is superheated to:

$$T_b \;=\; T_s + \Delta T,$$

i.e. a finite temperature difference exists from the start. The computational domain is periodic in both directions and gravity is neglected. The temperature field is advanced by the energy solver (advection–diffusion plus compressibility work) using a fourth-order Runge–Kutta (RK4) scheme. Consequently, the mid-time evolution approximates the classical assumptions (quasi-steady gas phase), whereas at very late times vapor accumulates in the finite periodic box and the gas-phase quasi-steadiness breaks down.

An initial radius $r_0 = 30$ lu is used. The instantaneous droplet radius r is obtained from the iso-density contour:

$$\rho = \rho_{\text{iso}} \equiv \frac{\rho_l + \rho_v}{2},$$

with (ρ_l, ρ_v) taken from the PR-EOS Maxwell construction at the simulation temperature. The diameter is $D = 2r$. This threshold definition is robust for diffuse interfaces and avoids additional corrections.

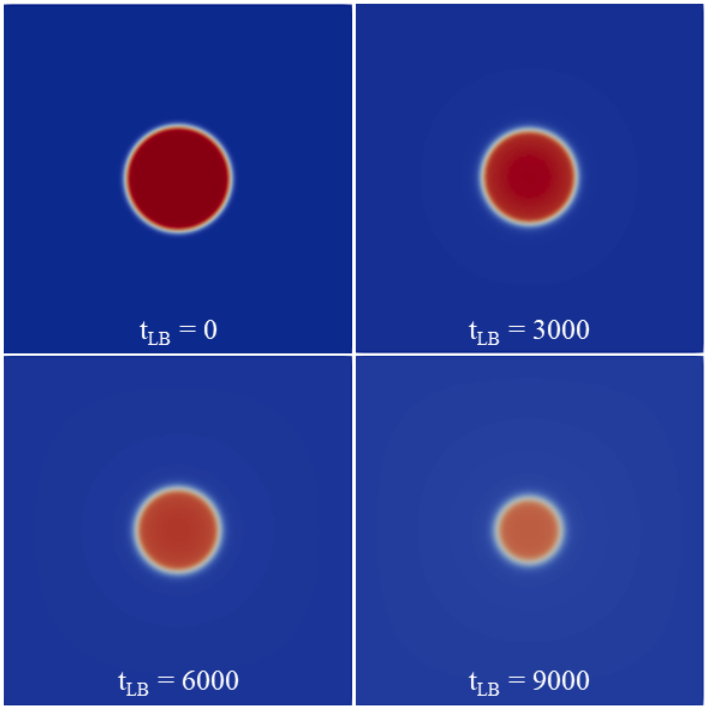

FIG. 2.25: Time sequence of droplet evaporation (color: density; t_{LB} in lattice time).

Fig. 2.25 shows the shrinking droplet. The evolution of D^2 is reported in Fig. 2.26 (lattice time on the lower axis; converted physical time on the upper axis for reference). After a short thermal spin-up, an extended interval exhibits a clear linear decrease of D^2, and the fitted slope gives a constant K in that quasi-steady stage, in agreement with Eq. (2.35). Deviations from linearity appear as the droplet approaches disappearance; these are expected because (i) the periodic domain promotes vapor accumulation so the gas phase is no longer quasi-steady, and (ii) the interfacial thickness becomes non-negligible relative to the droplet size. Similar departures have been reported when vapor residence time is large and convection is weak [103]. Overall, the MRT–LBM reproduces the defining linear D^2 regime with a constant evaporation constant K, while the early/late deviations are consistent with the known limitations of the idealized assumptions, in line with previous LBM studies [73].

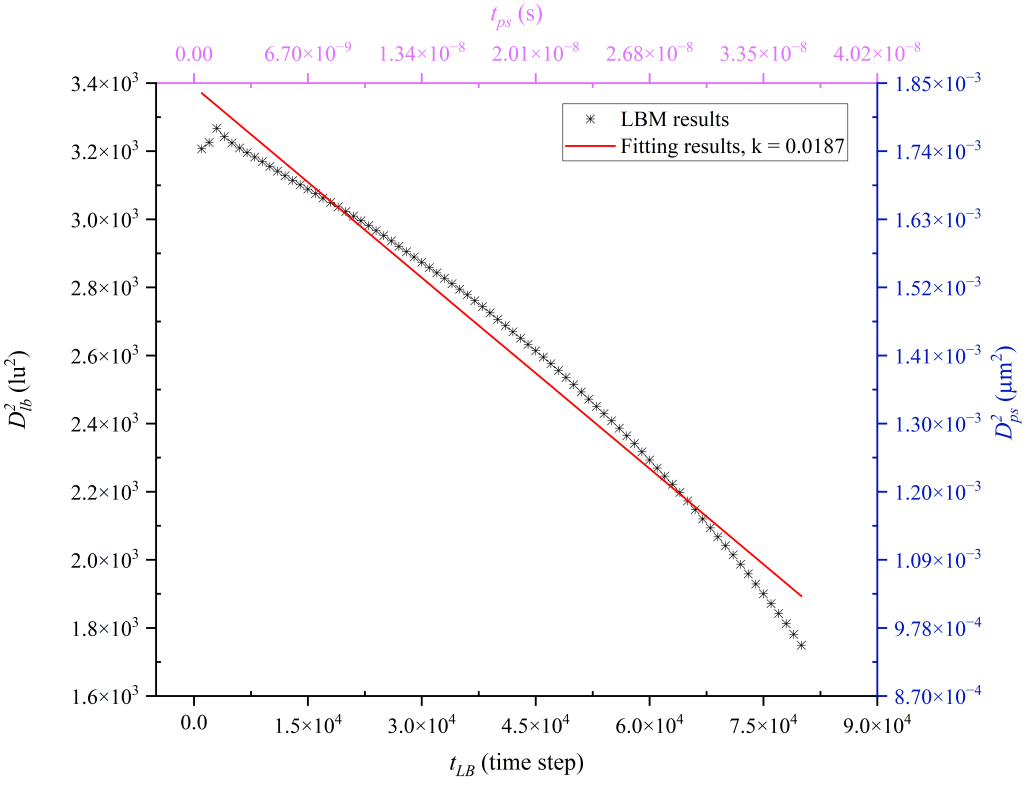

FIG. 2.26: Droplet D^2 in lattice and physical time. The red line is a least-squares fit over the quasi-steady interval; its slope yields $K = -d(D^2)/dt$.

Remarks. (i) Classical analytical correlations express K in terms of λ, c_p, ρ_l and the Spalding number B_T for an *inert* environment; here we *measure* K from the linear stage because the ambient is pure vapor and the domain is periodic. (ii) Introducing a non-condensable carrier gas and/or an open (non-periodic) far-field

temperature boundary would further suppress vapor accumulation and extend the linear D^2 interval, but that is beyond the scope of the present verification.

2.9 Wettability and Contact Angle Validation

Wettability quantifies liquid–solid affinity via the static contact angle θ at the three-phase line. At equilibrium, Young's relation holds:

$$\cos\theta = \frac{\gamma_{SG} - \gamma_{SL}}{\gamma_{LG}}, \tag{2.36}$$

with interfacial tensions $\gamma_{SG}, \gamma_{SL}, \gamma_{LG}$ for solid–gas, solid–liquid and liquid–gas, respectively (Fig. 2.27). Surfaces are termed hydrophilic if $\theta < 90°$ and hydrophobic if $\theta > 90°$.

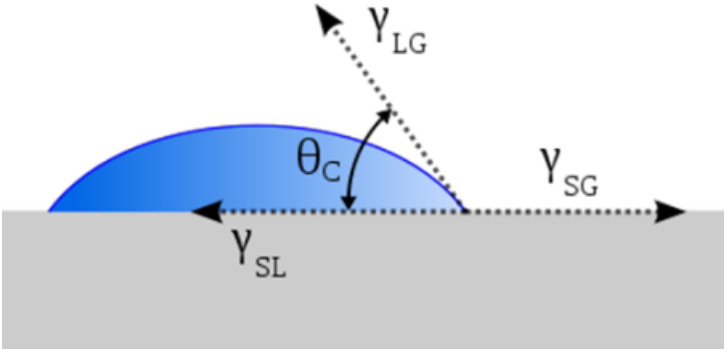

FIG. 2.27: Definition of the contact angle θ.

We impose wettability using the improved virtual-density scheme of Li & Luo [65], which avoids spurious density jumps at the wall and unifies fluid–fluid and fluid–solid interactions in the pseudopotential force (Sec. 2.3.2). For each solid-adjacent lattice node $\mathbf{x}$, a local virtual density $\rho_w(\mathbf{x})$ is assigned from nearby fluid information:

$$\rho_w(\mathbf{x}) = \begin{cases} \varphi\,\rho_{\text{ave}}(\mathbf{x}), & \varphi \geq 1 \quad \text{(more hydrophilic, } \theta\downarrow\text{)}, \\ \rho_{\text{ave}}(\mathbf{x}) - \Delta\rho, & \Delta\rho \geq 0 \quad \text{(more hydrophobic, } \theta\uparrow\text{)}, \end{cases}$$

where the local fluid average is:

$$\rho_{\text{ave}}(\mathbf{x}) = \frac{\sum_\alpha w_\alpha \, \rho(\mathbf{x}+\mathbf{e}_\alpha) \, s_w(\mathbf{x}+\mathbf{e}_\alpha)}{\sum_\alpha w_\alpha \, s_w(\mathbf{x}+\mathbf{e}_\alpha)}, \quad s_w(\mathbf{y}) = \begin{cases} 1, & \mathbf{y} \text{ is solid}, \\ 0, & \mathbf{y} \text{ is fluid}. \end{cases}$$

Here, φ and $\Delta\rho$ are the control parameters: $\varphi > 1$ decreases θ (more hydrophilic); $\Delta\rho > 0$ increases θ (more hydrophobic). The baseline $\varphi = 1$ or $\Delta\rho = 0$ gives $\theta \simeq 90°$. The virtual density is mapped to a ghost pseudopotential ψ_{ghost} through the chosen EOS (Peng–Robinson here) and used whenever a neighbor lies in the solid, so that fluid–fluid and fluid–solid forces are handled consistently within $\mathbf{F}_{\text{int}}$.

2D validation on a flat wall

To keep the main text focused, multi-panel snapshots are moved to Appendix B (Fig. B.1–B.3). We retain one baseline frame and a compact calibration table. In this study, contact angles were measured using ImageJ [104]. Although there may be minor manual errors, the trend confirms an accurate prediction of contact angles on flat surfaces.

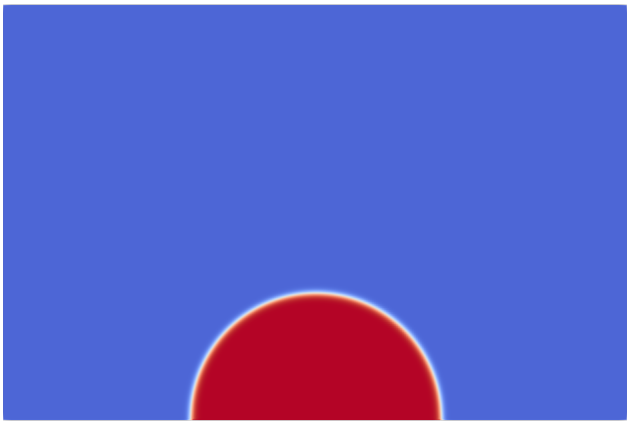

FIG. 2.28: Baseline on a flat wall: $\varphi = 1$ (or $\Delta\rho = 0$) gives $\theta \simeq 90°$.

TABLE 2.13: Flat-wall calibration: examples of $(\varphi, \Delta\rho)$ vs. measured θ.

Mode	Parameter	1.05	1.20	1.30	0.05 / 0.20 / 0.30
Hydrophilic ($\varphi > 1$)	θ	82.5°	63.1°	47.7°	—
Hydrophobic ($\Delta\rho > 0$)	θ	—	—	—	97.3°/123.5°/143.6°

Curved walls and 3D extension

The virtual-density scheme does not require wall normals or explicit contact-line handling; it uses the local fluid average in Eqs. (2.9)–(2.9) and is therefore dimension-agnostic: the very same algorithm applies in 2D and 3D and is robust on complex curvatures.

On a spherical wall (diameter 70 lu) with a droplet of diameter 50 lu, $\varphi = 1$ yields $\theta \simeq 90°$ (Fig. 2.29); varying φ or $\Delta\rho$ changes θ monotonically (Fig. 2.30). Representative 3D results (flat and curved walls) show the same monotone trends; detailed panels are moved to Appendix B (Fig. B.4–A.B). Table 2.14 summarizes a few 3D calibration points.

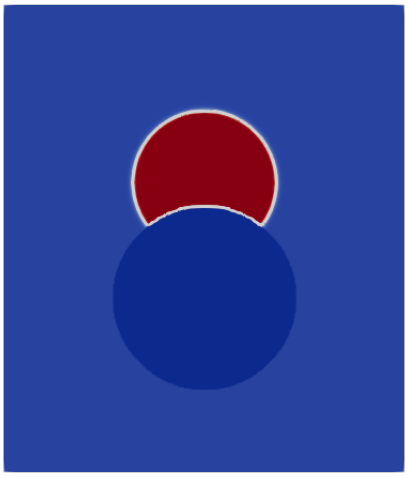

FIG. 2.29: Curved-wall baseline: $\varphi = 1$ gives $\theta \simeq 90°$.

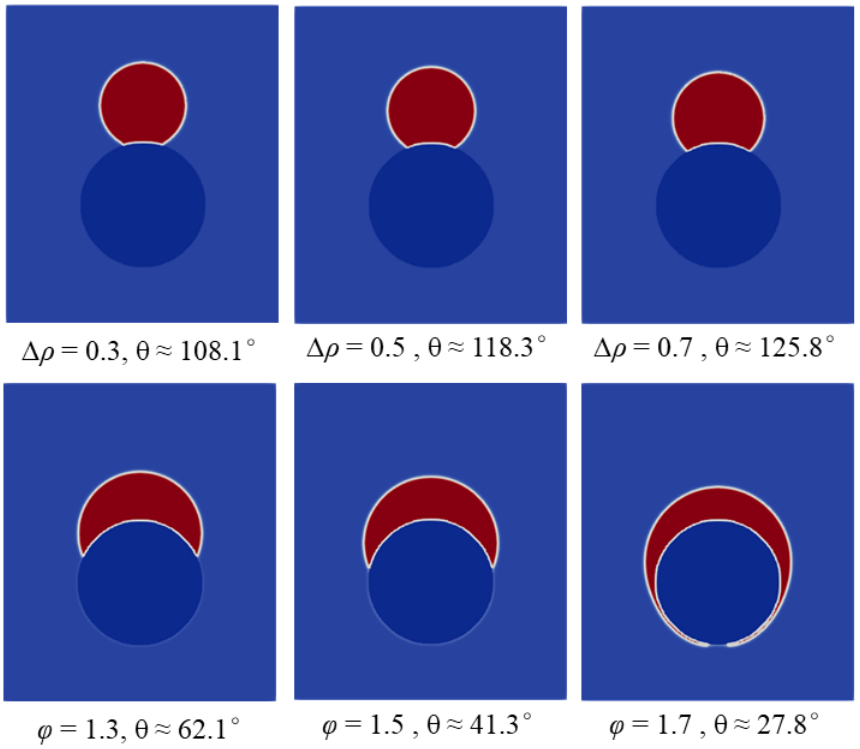

FIG. 2.30: Contact-angle control on a curved wall via the virtual-density scheme.

TABLE 2.14: 3D calibration on flat/curved walls: examples of $(\varphi, \Delta\rho)$ vs. θ.

Case	Parameter	Measured θ	Trend
3D flat (hydrophilic)	$\varphi = 1.1/1.2/1.3$	$72.9^\circ/63.1^\circ/47.7^\circ$	monotone $\downarrow$
3D curved (hydrophilic)	$\varphi = 1.1/1.2/1.3$	$61.8^\circ/41.1^\circ/21.4^\circ$	monotone $\downarrow$
3D flat (hydrophobic)	$\Delta\rho = 0.05/0.20/0.30$	$97.3^\circ/123.5^\circ/143.6^\circ$	monotone $\uparrow$
3D curved (hydrophobic)	$\Delta\rho = 0.1/0.2/0.3$	$102.5^\circ/114.7^\circ/136.7^\circ$	monotone $\uparrow$

Advantages of virtual density format contact angle

(i) φ and $\Delta\rho$ provide monotonic, one-parameter control of θ on both sides of 90°; (ii) a one-time calibration per numerical setup allows prescribing a target θ in applications; (iii) the virtual-density scheme is naturally extensible to curved surfaces and 3D without wall-normal reconstruction, which makes it more robust than Geometric contact-angle (GCA) on rough/curved walls;

2.10 Summary of This Chapter

This chapter built a single, coherent mesoscopic framework for liquid–vapor phase change based on the pseudopotential LBM. The workflow integrates: (i) a Peng–Robinson (PR) equation of state embedded via the $\psi(p, \rho, T)$ formulation; (ii) a momentum solver with the Huang–MRT collision operator, whose parameters (ε, k_1, k_2) decouple and tune interfacial stress (surface tension) without altering coexistence; (iii) Guo's forcing to couple body forces consistently; (iv) a virtual–density fluid–solid coupling that provides stable, precise contact–angle control on flat and curved walls; and (v) a thermal solver (RK4 time stepping) coupled to the EOS for latent–heat effects. Background on alternative phase–separation models and forcing/coupling variants is moved to the Appendix to keep the narrative focused.

Model fidelity was established with canonical tests: Maxwell equal–area coexistence (vdW, CS, RK, SRK, PR; PR chosen for its best overall agreement), Laplace's law with tunable σ, pressure–tensor consistency across a planar interface, steady thin–film evaporation following $q = h_{fg}\, m''$ (with m'' the interfacial mass flux) including grid–independence, and the droplet D^2–law (linear stage). Together these benchmarks demonstrate that the interfacial mechanics, wetting control, and phase–change coupling are accurate and robust for the application studies that follow.

What the model is used for next

The developed model is applied to several objectives:

1. It is used to predict bubble–scale dynamics in pool boiling without imposed cross–flow, including nucleation, growth, and departure, as well as their dependence on wettability and micro/curved geometries.
2. It provides quantitative observables such as departure diameter, frequency, and growth rate, which enable direct comparison with experiments and classical correlations.
3. The framework offers robust and monotonic control of the apparent static contact angle on flat and structured walls in two dimensions, with selected three–dimensional snapshots included only to verify the scalability of the contact–angle control.
4. The pseudopotential LBM framework intrinsically accounts for the key physical

phenomena relevant to boiling heat transfer—such as surface tension, wettability, phase change, and force balance—without relying on additional empirical closure laws. This feature highlights its potential as a predictive tool for investigating bubble dynamics under diverse thermal and geometric conditions.

Assumptions and limitations

The analysis in this chapter is conducted under a number of assumptions that define its range of validity:

1. **Flow regime.** The focus is on pool boiling without any imposed cross–flow; gravity is included, and convection arises solely from buoyancy and bubble dynamics.
2. **Working fluid.** Only a single component (water) is considered, with phase equilibrium at the interface enforced through the equation of state (EOS).
3. **Thermophysical properties.** They are assumed to be temperature independent except where specified by the EOS and latent–heat evaluation, while effects such as Marangoni stresses and viscous heating are neglected.
4. **EOS accuracy.** A cubic Peng–Robinson EOS is employed: it provides reasonable coexistence densities but is subject to known limitations, particularly on the dilute–vapor branch and near critical conditions.
5. **Diffuse interface and resolution.** The interface is treated as diffuse with finite thickness determined by lattice and forcing parameters. Sufficient resolution is required to capture near–wall films and contact–line regions while minimizing spurious currents; dynamic contact–angle hysteresis is not modeled, and an effective static angle is prescribed instead.
6. **Numerical constraints.** Numerical stability is ensured by operating at low Mach numbers and moderate density ratios, meaning that very high Reynolds or Weber numbers and extreme density ratios lie outside the present validation envelope.

In addition to the two-dimensional model described in this thesis, a three-dimensional model based on the D3Q19 lattice has also been implement, incorporating the same physical features as the 2D framework. A description of this 3D extension is provided in the Appendix C. However, due to the high computational cost and the lack of performance optimization, large-scale three-dimensional boiling simulations remain time-consuming and are therefore not included in the main part of this work. The present study is thus restricted to two-dimensional simulations,

which is justified by the fact that the validation strategy relies primarily on single-bubble boiling tests that exhibit a nearly symmetric configuration. It should be noted that subcooled boiling is not included in the present work. Although the framework allows for an extension towards subcooled conditions, the current implementation has not yet been fully validated and therefore no results are presented. This aspect is left for future work.

Chapter 3

LBM Single Bubble Dynamics Calculation

The dynamic behavior of a single vapor bubble serves as a fundamental unit for understanding phase-change boiling heat transfer at the microscale. It involves complex interactions among surface wettability, localized heating, thermal boundary layers, and transient vapor–liquid phase transitions.

Recent advances in high-speed imaging and mesoscale simulation techniques have demonstrated that the evolution of a single bubble, including its nucleation, growth, departure, and post-departure behavior, underpins key boiling characteristics such as heat transfer enhancement, critical heat flux, and dry-out prevention [105–109]. From a modeling perspective, accurately capturing single-bubble evolution requires robust multiphysics coupling among interfacial tension, phase change, natural convection, and solid–fluid heat conduction. In this regard, the LBM offers distinct advantages due to its ability to resolve complex interfaces and thermodynamic coupling with high spatial and temporal fidelity. In particular, the pseudopotential-based MRT LBM model provides a stable and physically consistent framework for simulating bubble–surface interactions and interfacial motion.

This chapter presents a detailed numerical investigation of single-bubble phase-change boiling under various wettability and thermal boundary conditions. Particular emphasis is placed on extracting dynamic parameters such as bubble departure diameter, departure frequency, in addition to bubble growth rate and wall heat flux. These parameters are not only central to describing bubble-scale dynamics, but also serve as closure quantities in widely used macroscopic boiling

models, such as the RPI model, where they determine heat partitioning between microlayer evaporation, transient conduction, and quenching. By providing direct numerical access to these quantities, the present study bridges mesoscale bubble dynamics with continuum-scale CFD models, thereby offering both physical insight and quantitative benchmarks. Moreover, the chapter describes the bubble circulation phase and the evolution of field variables, which together contribute to a systematic understanding of boiling heat transfer at the bubble scale.

3.1 Bubble Evolution and Departure Mechanism

The evolution of a single bubble on a microheater surface typically proceeds through three distinct stages: nucleation, growth, and departure. Fig. 3.1 illustrates this process under moderate superheat conditions ($Ja = 0.3$), based on the present LBM simulations.

At the nucleation stage ($t^* \approx 13.6$–23.1), vapor first emerges at the heated wall due to local superheating and interfacial instability, forming a nearly hemispherical bubble. Surface tension maintains strong adhesion at the heater base, preventing premature detachment. During the growth stage ($t^* \approx 23.1$–42.1), buoyancy and vapor influx promote vertical elongation, while a neck develops near the contact line as surface tension resists upward motion. Finally, at the departure stage ($t^* \approx 44.8$–47.6), the bubble neck thins rapidly as buoyancy and inertia overcome capillary retention, resulting in detachment. A small residual vapor nucleus may remain at the wall, serving as a seed for subsequent cycles. The LBM simulations capture this cycle with smooth and continuous interfaces, in agreement with experimental observations [110–112].

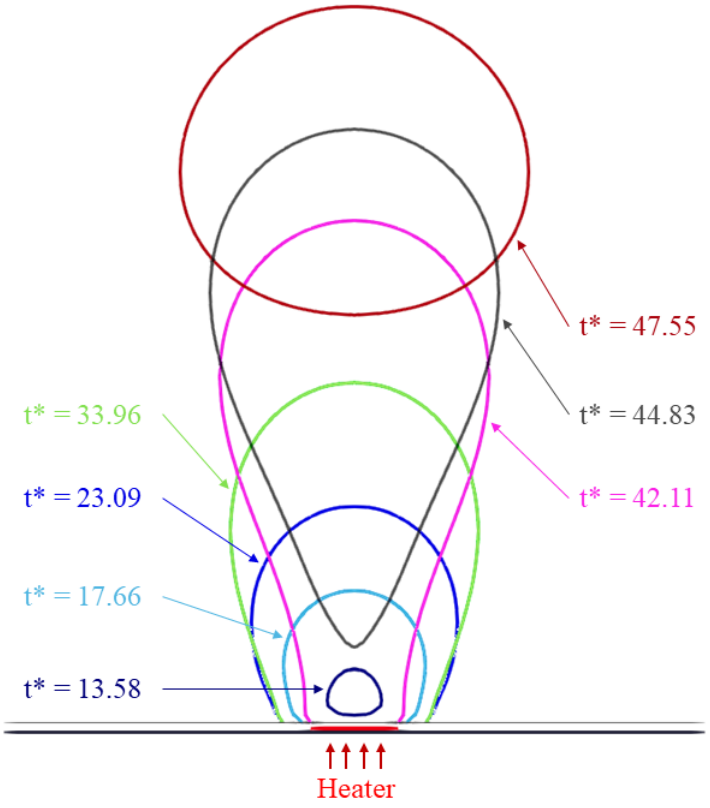

FIG. 3.1: Bubble outline morphology changes over time
$Ja = 0.30, \theta \approx 63.2°$

This morphological transition can be consistently explained by the force balance framework shown in Fig. 3.2. In the early growth stage, the surface tension force F_s dominates over buoyancy F_b, anchoring the bubble to the surface. With continuous vapor generation, F_b and the pressure difference force F_p increase, while inertial effects F_i accelerate vertical elongation. Once the generalized force balance condition is satisfied,

$$F_b + F_p + F_i = F_s + F_d, \tag{3.1}$$

the bubble departs as upward forces exceed capillary and hydrodynamic resistance.

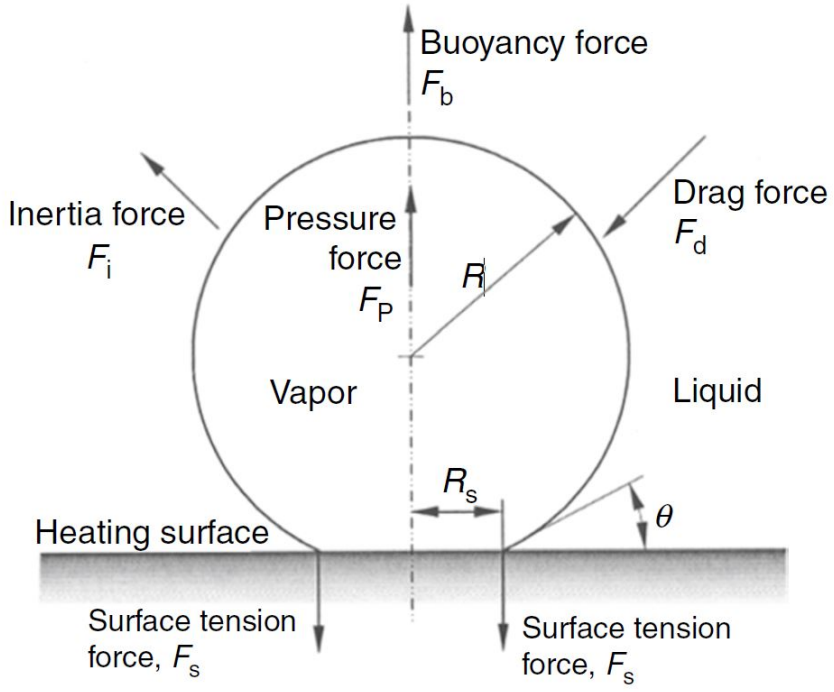

FIG. 3.2: Forces acting on a vapor bubble from a heated surface [113]

As illustrated in Fig. 3.2, the main forces include:

Driving forces (promoting detachment):
Buoyancy force: $F_b = \rho_l g V$
Pressure difference force: $F_p = (p_v - p_l)A$
Inertia force: $F_i \approx C_i \rho_l R^2 \dfrac{d^2 R}{dt^2}$

Resisting forces (retarding detachment):
Surface tension force: $F_s = 2\pi R_s \sigma \sin\theta$
Hydrodynamic drag: $F_d = \frac{1}{2} C_d \rho_l A v^2$

In summary, the LBM framework provides a self-consistent description of bubble evolution and detachment, inherently accounting for interfacial tension, buoyancy, inertia, drag, and heat transfer. A more detailed comparison between force-balance models and empirical departure correlations will be presented in Chapter 6, where the predictive capability of LBM results is systematically evaluated against theoretical approaches.

3.2 Bubble Departure Mechanism

3.2.1 Density field evolution

The density field provides a direct visualization of phase distribution during boiling and thus serves as the primary indicator of bubble cycle dynamics. To examine the effect of surface wettability, simulations were performed under identical heating conditions with $Ja = 0.23$, where the wetting parameters were set as $\phi = 1.3$ for hydrophilic and $\Delta\rho = 0.3$ for hydrophobic surfaces.

As shown in Fig. 3.3(a), the hydrophilic surface exhibits a discernible waiting period between consecutive bubble cycles. After the first bubble detaches at $t^* = 58.41$, the surface is completely rewetted, leading to a quiescent interval ($t^* = 58.41$–63.85) before a new nucleation event occurs. The second bubble appears at $t^* = 72.01$, grows into a nearly spherical shape due to buoyancy-driven expansion, and detaches at $t^* = 100.52$. The repeated sequence of waiting, nucleation, growth, and departure indicates a periodic process regulated by the rewetting dynamics.

In contrast, Fig. 3.3(b) demonstrates the hydrophobic case, where a residual vapor nucleus remains after the first detachment at $t^* = 62.49$. This remnant vapor acts as a preferential site for re-nucleation, so that a new bubble emerges almost immediately at $t^* = 63.85$, without any perceptible waiting period. The subsequent bubble assumes a more elongated, bell-shaped profile at $t^* = 103.24$, develops a neck, and detaches again at $t^* = 120.90$. Compared to the hydrophilic surface, the absence of a waiting stage and the anisotropic bubble morphology clearly reflect enhanced vapor retention and faster activation dynamics, consistent with previous studies [114, 115].

Additional simulations further confirm that the waiting period on hydrophilic surfaces strongly depends on the imposed superheat. At low Ja (< 0.25), vapor generation is insufficient to trigger immediate nucleation, and a temporal gap appears between cycles. With increasing superheat, however, the waiting period diminishes and eventually disappears, as continuous nucleation becomes thermodynamically favorable.

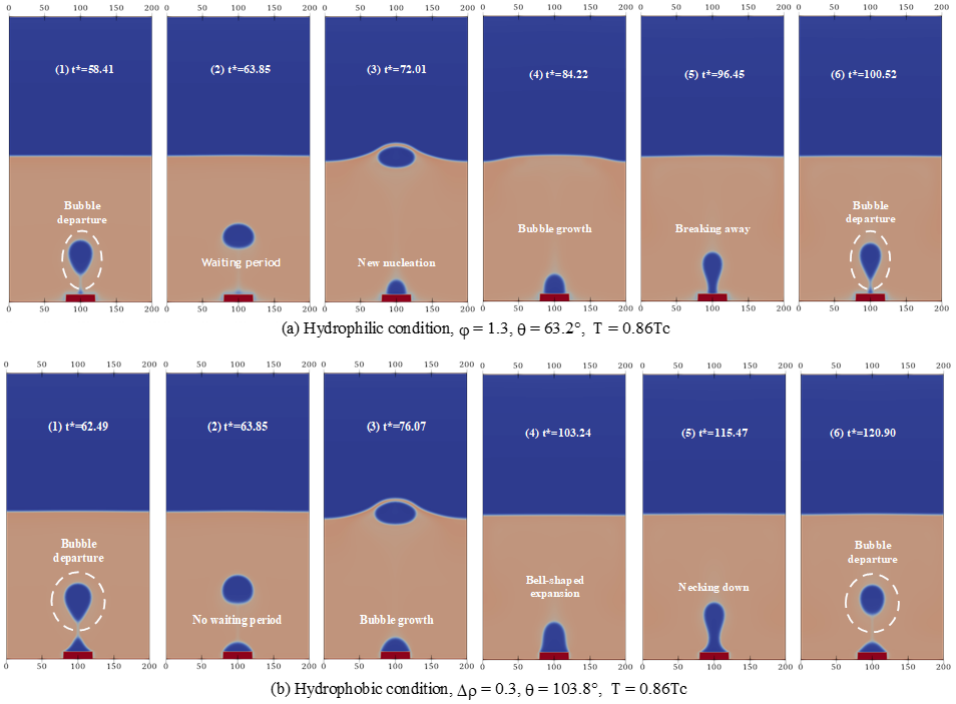

FIG. 3.3: Contact angle for Hydrophobic surface

In summary, the continuity of bubble cycles is jointly controlled by surface wettability and superheat level. Hydrophilic surfaces promote complete rewetting, thereby introducing a waiting period, while hydrophobic surfaces retain vapor nuclei that act as "nucleation memory," sustaining nearly uninterrupted bubble generation. The present results not only highlight the nucleation dynamics differences reported in previous numerical studies (such as Ref. [114, 115]) but also highlight the capability of the pseudopotential LBM to systematically capture the coupled effects of wettability and thermal forcing on boiling cycle evolution.

3.2.2 Temperature field evolution

The evolution of the temperature field provides critical insights into the thermal dynamics during bubble nucleation and departure. Fig. 3.4 and Fig. 3.5 present the spatiotemporal temperature field under hydrophilic and hydrophobic conditions, respectively. All simulations are conducted at the same superheat level (Ja = 0.23) using a Dirichlet boundary condition at the bottom wall. This ensures a consistent thermal input while highlighting the influence of surface wettability.

In the hydrophilic case (Fig. 3.4), following bubble departure at $t^* = 57.05$, the temperature field near the wall becomes relatively uniform, with the vertical temperature gradient significantly weakened. This recovery occurs during the waiting period, when the absence of a bubble allows heat to accumulate in the wall layer. A new bubble nucleates at $t^* = 67.92$ and enters a growth phase at $t^* = 86.94$. The isotherms exhibit a symmetric, concentric pattern around the bubble, reflecting a fully restored and stable thermal environment. Such symmetry supports spherical bubble growth and a periodic cycle of nucleation and departure, consistent with the density field evolution observed in Fig. 3.3(a).

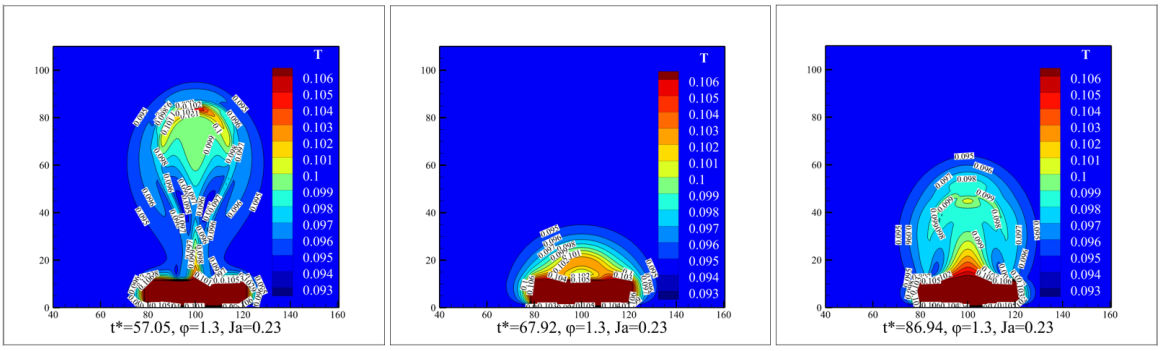

FIG. 3.4: Temperature field evolution on hydrophilic surface $\varphi = 1.3, Ja = 0.23$

By contrast, the hydrophobic case (Fig. 3.5) exhibits pronounced asymmetry in the temperature field. At $t^* = 61.13$, during bubble detachment, a steep vertical temperature gradient persists near the heater surface. Unlike the hydrophilic condition, no waiting period follows detachment because a residual vapor nucleus anchors to the wall. As a result, a new bubble nucleates almost immediately at $t^* = 65.21$, within a thermally disturbed field that has not yet recovered from the previous cycle. Consequently, the bubble grows into a vertically elongated, bell-like structure by $t^* = 105.96$, accompanied by distorted isotherms on the upper and lateral regions. This continuous thermal interaction across overlapping cycles increases the energy barrier for detachment and prolongs the bubble lifetime.

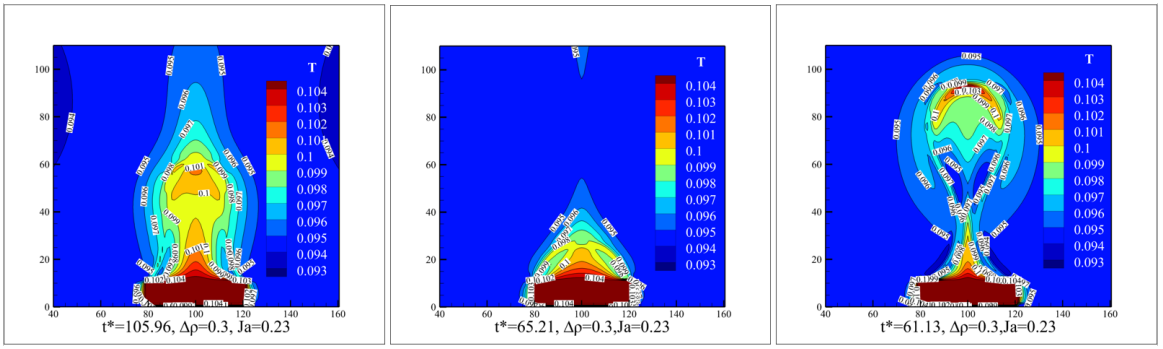

FIG. 3.5: Temperature field evolution hydrophobic surface
$\Delta\rho = 0.3, Ja = 0.23$

In summary, hydrophilic surfaces promote thermal recovery between cycles, yielding symmetric isotherms and repeatable bubble dynamics. Hydrophobic surfaces, in contrast, maintain an unsteady thermal field due to residual vapor, resulting in asymmetric isotherms and extended bubble cycles. These findings align with previous numerical observations that link hydrophilic rewetting to enhanced thermal efficiency [114, 116] and hydrophobic nucleation memory to continuous vapor generation [115]. Thus, the present simulations not only reproduce state-of-the-art trends but also elucidate the underlying thermal field mechanisms governing bubble evolution.

3.2.3 Flow field evolution

The velocity field evolution provides valuable insights into the momentum transport and convection induced by bubble dynamics. Figs. 3.6 and 3.7 illustrate the flow structures on hydrophilic and hydrophobic surfaces under the same superheat condition (Ja = 0.23), enabling a direct comparison of surface wettability effects.

On the hydrophilic surface (Fig. 3.6), bubble detachment at $t^* = 57.05$ induces two symmetric counter-rotating vortices, generated by the upward motion of the bubble and the displacement of surrounding liquid. After detachment ($t^* = 67.92$), the flow field near the heating surface becomes nearly stagnant, with vortices dissipating and streamlines returning to a vertical downward profile. This quiescence corresponds to a distinct waiting period, during which the fluid field relaxes before the initiation of the next nucleation cycle. At $t^* = 86.94$, buoyancy-driven upward jets and small vortices reappear beneath the growing bubble, marking the re-initiation of convection.

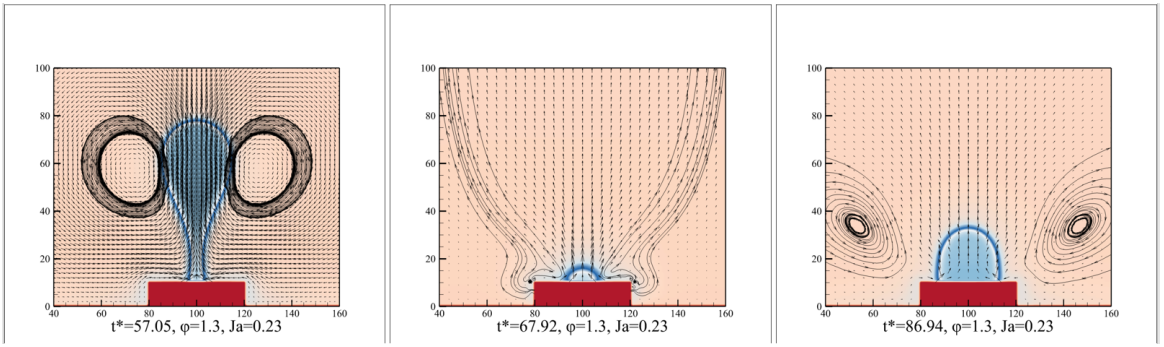

FIG. 3.6: The flow field evolution under hydrophilic surface $\varphi = 1.3, Ja = 0.23$

In contrast, the hydrophobic surface (Fig. 3.7) exhibits a less periodic and more disturbed pattern. At $t^* = 61.13$, bubble detachment also generates twin vortices, but due to the absence of a clear waiting period, a new bubble rapidly nucleates on the residual vapor nucleus. By $t^* = 65.21$, the system already hosts a new bubble while the vortices from the previous cycle are still present, leading to overlapped disturbances. At $t^* = 105.96$, the streamlines above the bubble remain stretched and asymmetric, while the vortices fail to fully reform. The persistence of residual vapor suppresses the recovery of flow symmetry and prolongs bubble attachment, ultimately distorting the bubble shape.

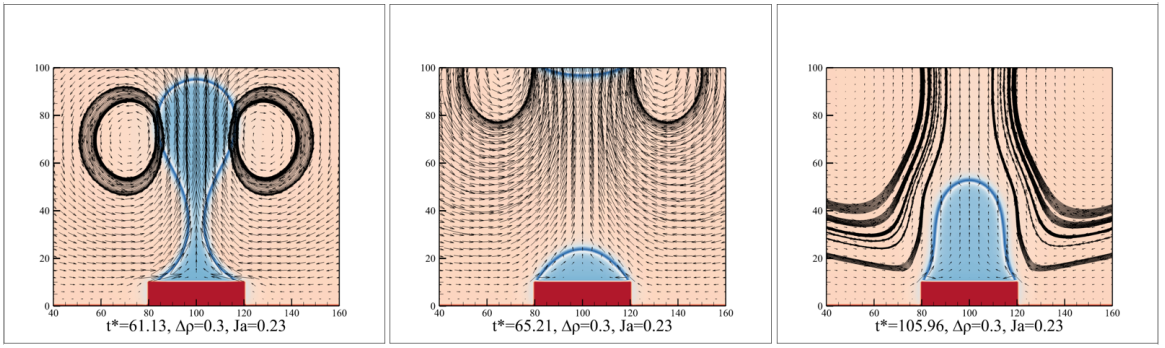

FIG. 3.7: The flow field evolution under hydrophobic surface $\Delta\rho = 0.3, Ja = 0.23$

Overall, the velocity field on hydrophilic surfaces demonstrates a well-defined and cyclic evolution of vortex generation and dissipation, consistent with separated bubble growth and detachment stages. In contrast, hydrophobic surfaces promote cycle overlap due to residual vapor retention, resulting in persistent convective disturbances and unsteady flow structures. These observations are fully consistent with the previously discussed density and temperature fields: the hydrophilic

surface facilitates periodic renewal of the thermal–hydrodynamic environment, whereas the hydrophobic surface promotes overlapping cycles and incomplete relaxation. This confirms that surface wettability governs not only phase distribution and thermal transport but also the momentum transfer mechanisms driving bubble dynamics.

Thus, the role of surface wettability can be regarded as a distinct and critical parameter for further exploration. Its systematic investigation may provide valuable guidance for designing surface modifications aimed at enhancing boiling heat transfer performance.

3.3 Heating Condition Implementation

In boiling experiments and theoretical studies, two types of thermal boundary conditions are commonly employed: fixed wall temperature (Dirichlet) and constant wall heat flux (Neumann). To ensure that our numerical model can be consistently compared with the state of the art, both boundary conditions are implemented and analyzed in the present study.

To evaluate their influence on bubble dynamics, we introduce three diagnostic quantities (all expressed in lattice units unless otherwise stated):

TV (Temperature Variation): temporal evolution of wall temperature at a reference point (center of the heating surface).
LHV (Local Heat Flux Variation): temporal evolution of local heat flux density at the same reference point.
LH (Local Heat Flux Distribution): spatial distribution of wall heat flux density along the entire heating surface.
These parameters allow us to directly compare the thermal response of the heater under different boundary conditions and to link our simulation results with classical boiling experiments.

3.3.1 Fixed temperature condition

The wall temperature is directly prescribed as:

$$T_b = T_s(1 + x), \tag{3.2}$$

where $T_s = 0.86T_c$ is the saturation temperature and x is the relative superheat. This enforces an isothermal heating surface, mimicking low-resistance heaters.

As shown in Fig. 3.8(a), TV remains constant, confirming strict thermal control. The characteristic time instants labeled as a–b–c–d and a'–b'–c'–d' in Fig. 3.8(a) and Fig. 3.9(a) represent successive stages within two complete bubble cycles: (a) waiting period before nucleation, (b) onset of bubble nucleation, (c) bubble growth and expansion, and (d) bubble departure followed by surface rewetting. This labeling helps correlate the temporal evolution of wall temperature (TV) and local heat flux variation (LHV) during repetitive bubble cycles.

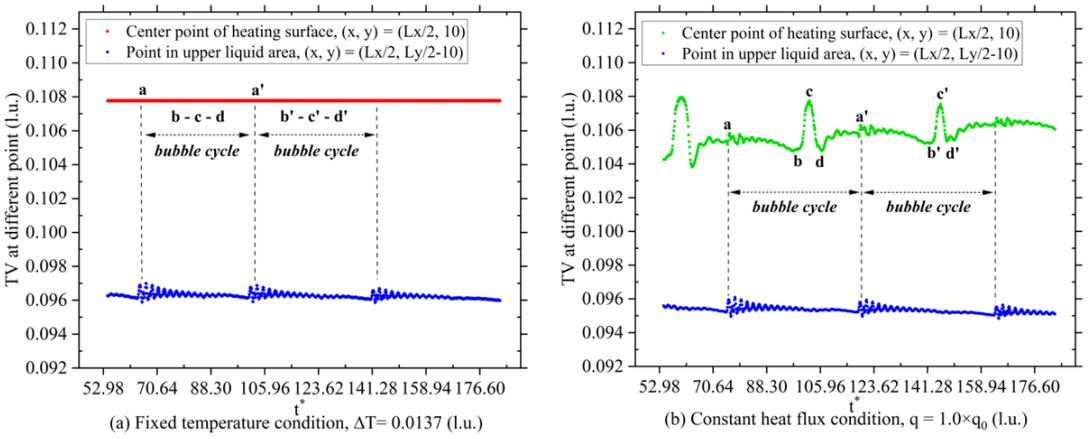

FIG. 3.8: TV for fixed-temperature and constant heat-flux conditions. The labels a–d and a'–d' denote successive stages of the bubble cycle: (a) waiting period, (b) nucleation, (c) bubble growth, and (d) departure.

The dynamic system response under fixed-temperature heating is clearly reflected in the periodic oscillations of LHV (Fig. 3.9(a)) and in the spatial redistribution of local heat flux (LH) along the wall (Fig. 3.10).

Before nucleation, LH remains nearly uniform. During bubble growth, LH decreases at the center due to vapor layer formation and peaks appear near the contact line. After detachment, LH contracts and redistributes.

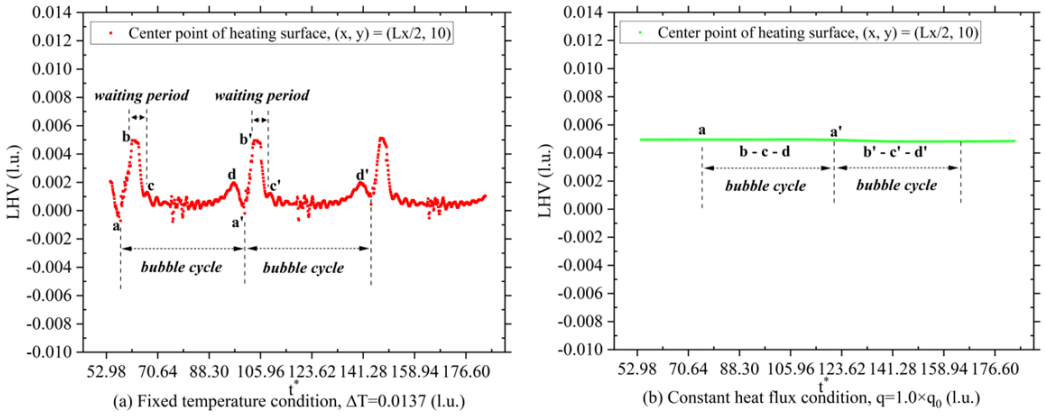

FIG. 3.9: LHV for fixed-temperature and constant heat-flux conditions. The symbols a–d and a'–d' correspond to two representative bubble cycles, including the waiting, nucleation, growth, and departure stages.

This cyclic evolution of TV, LHV, and LH illustrates the energy exchange process between the heating surface and the surrounding liquid, which is characteristic of the nucleate boiling regime and agrees well with previous numerical observations of heat flux concentration near the three-phase contact line [111, 117].

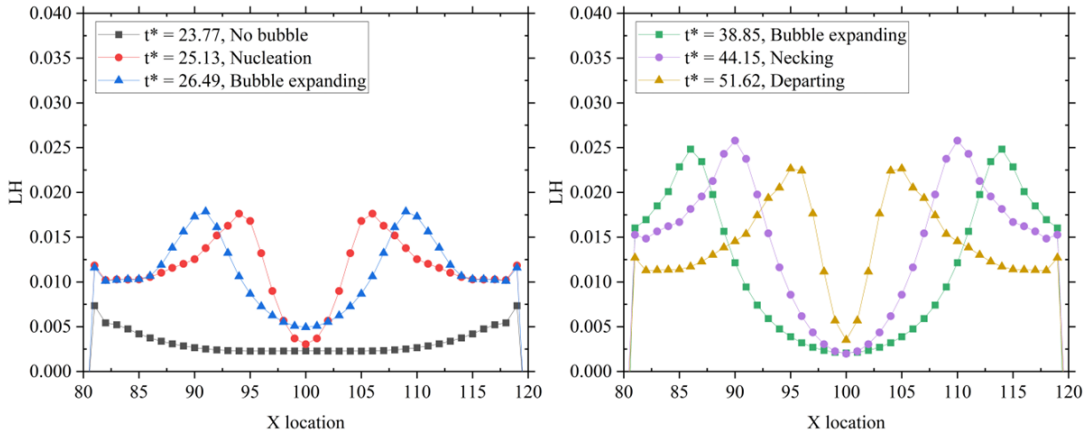

FIG. 3.10: Local heat flux distribution under fixed temperature condition

3.3.2 Constant heat flux condition

In this case, a uniform total heat flux density q is imposed at the bottom wall as the boundary condition for the heat conduction equation. This setup corresponds to a constant-power heating mode, in which the overall energy input to the wall remains fixed while the local wall temperature evolves dynamically in response to

the boiling process. In the simulation, the local wall temperature is obtained by solving the heat conduction equation with the imposed flux as boundary condition.

It should be emphasized that the term "constant heat flux" refers to the globally imposed average heat flux, not to a spatially uniform local value at each surface node. As vapor bubbles nucleate, grow, and depart, the local temperature gradients beneath and around them become highly non-uniform. Consequently, the instantaneous *local* heat flux distribution varies with time, even though the spatially averaged heat flux remains constant. This behavior reflects realistic transient heat redistribution on the heating surface, where portions intermittently covered by bubbles experience reduced heat transfer, while exposed regions undergo enhanced local fluxes.

As shown in Fig. 3.11, the local heat flux exhibits strong spatial modulation correlated with bubble dynamics. During the nucleation and expansion stages, heat is preferentially concentrated near the contact line, whereas during bubble departure and rewetting, the heat flux redistributes across the surface. These oscillations occur under the constraint of constant total heat input, demonstrating that the simulation correctly captures the local heat transfer feedback in a constant-flux boiling scenario.

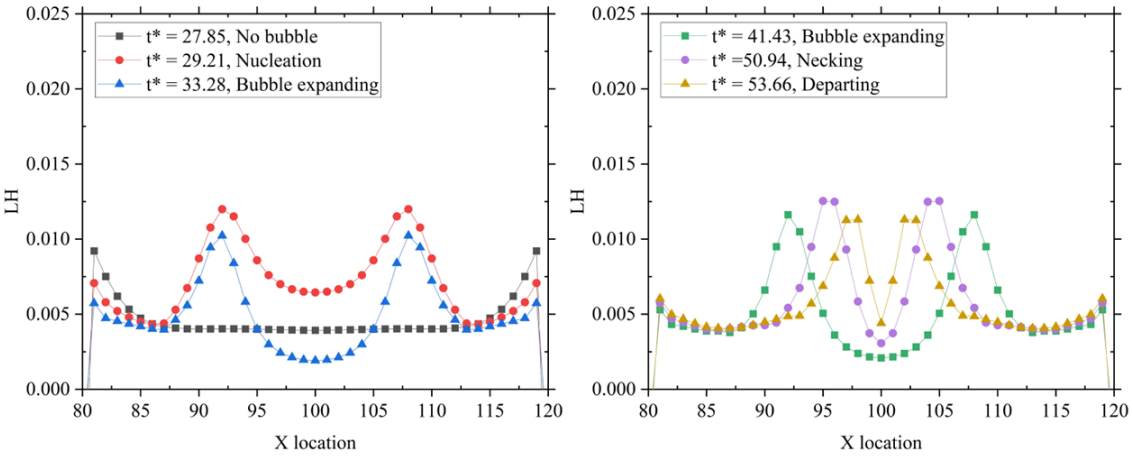

FIG. 3.11: Local redistribution of wall heat flux under constant total heat flux boundary condition.

Comparative Discussion for these two heating condition

Under **fixed temperature**: the wall remains isothermal, but the local heat flux strongly fluctuates with bubble dynamics.

Under **constant heat flux**: the wall temperature itself undergoes cyclic variations, while the heat flux input is fixed.
Thus, both conditions capture different aspects of boiling heat transfer. The Dirichlet boundary provides a reference case with strong temperature control, whereas the Neumann boundary reproduces realistic heater operation where wall superheat is not prescribed but results from the energy balance.

In summary, this section demonstrates the numerical implementation and physical interpretation of two heating conditions. The adopted approaches not only ensure compatibility with existing theoretical models [111] [118] but also allow potential consistency with experimental practice, for instance through constant-power heating implement by controlling the input current in ITO glass heaters.

3.4 Summary of This Chapter

This chapter established a mesoscopic lattice Boltzmann method (LBM) framework for investigating single-bubble boiling dynamics. The bubble life cycle was divided into four stages—nucleation, growth, departure, and rewetting—and the coupled evolution of density, temperature, and flow fields was systematically analyzed. In addition, two heating conditions widely used in the literature were implemented and compared, namely fixed wall temperature (Dirichlet condition) and constant heat flux (Neumann condition). Three diagnostic metrics were introduced to characterize the thermal response during the bubble cycle: (i) TV (temporal variation of a representative wall temperature), (ii) LHV (time evolution of local wall heat flux at a reference point), and (iii) LH (instantaneous spatial distribution of wall heat flux along the heated wall).

Key findings can be summarized as follows:
1. Wall heat transfer is strongly non-uniform over the bubble cycle. During bubble growth, the vapor layer reduces heat transfer at the wall center, while heat flux intensification occurs near the three-phase contact line.
2. Surface wettability significantly influences bubble departure. Hydrophilic surfaces facilitate faster rewetting, whereas hydrophobic surfaces promote larger contact radii and slower rewetting.
3. Increasing superheat alters the balance among buoyancy, capillarity, inertia, and viscous forces, thereby affecting bubble growth rate, departure diameter, and

departure frequency.
4. Unlike quasi-steady classical models, the LBM framework captures inherently unsteady behaviors, resolving transient details in bubble growth and departure.

On the impact of heating conditions:
Under fixed-temperature heating, the wall temperature remains constant, and the system response is mainly reflected in LHV oscillations and LH redistribution. Under constant-flux heating, the wall temperature becomes an outcome of the energy balance and fluctuates cyclically with nucleation, growth, departure, and rewetting. Although the underlying mechanisms differ, both boundary conditions reveal heat-flux concentration near the contact line and vapor-layer shielding during bubble growth. At the same time, the two conditions are complementary in numerical simulations: on the one hand, they are consistent with classical theoretical models; on the other hand, they provide potential links to experimental practice, such as constant-power heating via ITO glass with controlled input current.

Methodological relevance:
The proposed diagnostic metrics (TV, LHV, and LH) offer a unified and physics-informed framework for comparing thermal responses under different heating conditions and parametric settings (wettability, superheat). The implementation of both Dirichlet and Neumann boundaries ensures compatibility with theoretical models and creates an interface for experimental comparison, thus laying the foundation for quantitative validation.

Outlook for subsequent research:
The results of this chapter provide theoretical and methodological support for the following studies. Future work will focus on:

(i) systematically assessing parametric trends under controlled boundary conditions;
(ii) comparing unsteady LBM predictions with classical quasi-steady correlations to identify their discrepancies;
(iii) establishing connections between simulation and experimental data through unit conversion and scaling analysis, thereby constructing a coherent validation pathway.

Chapter 4

Single Bubble Boiling: Experimental Framework

Let's now turn to direct experimentation. The purpose of this chapter is to establish a controllable single-bubble boiling platform that enables a meaningful comparison with the numerical predictions obtained using the LBM framework. Instead of a strict one-to-one correspondence, the comparison is established in a physically consistent manner through unit conversion and nondimensional mapping (e.g. using Ja, Eo and related groups), while acknowledging that certain differences remain, such as the reduced density ratio in simulations and the experimental.

To this end, I developed a controllable single-bubble boiling facility based on patterned ITO glass heaters, combined with synchronized high-speed imaging and quantitative data acquisition. A dedicated image-processing pipeline (Section 4.6) then extracts bubble dynamics (e.g. base position, size, and departure timing) from shadowgraphy frames. Wall superheat is obtained via an indirect reconstruction based on electrical heat flux and $Nu{\cdot}Ja$ scaling (Section 4.5), after demonstrating that direct resistance thermometry of the ITO layer lacks the required 1–3 K sensitivity at millisecond time scales. This facility allows the assessment of bubble dynamics under well-defined boundary conditions, offers a valuable benchmark for evaluating the predictive capability of the numerical model.

4.1 Objective and Innovation

A single-bubble experiment provides an unobstructed view of the entire bubble life cycle—from nucleation to growth and eventual detachment—while avoiding the masking effects of neighboring bubbles. However, conventional pool-boiling studies rarely achieve this isolation: even when a "single" nucleation site is selected, additional bubbles often appear nearby and interfere with the dynamics (see Fig. 4.1). Such interference makes it difficult to extract quantitative parameters (e.g., departure diameter, frequency, and contact line behavior) with sufficient accuracy for model validation.

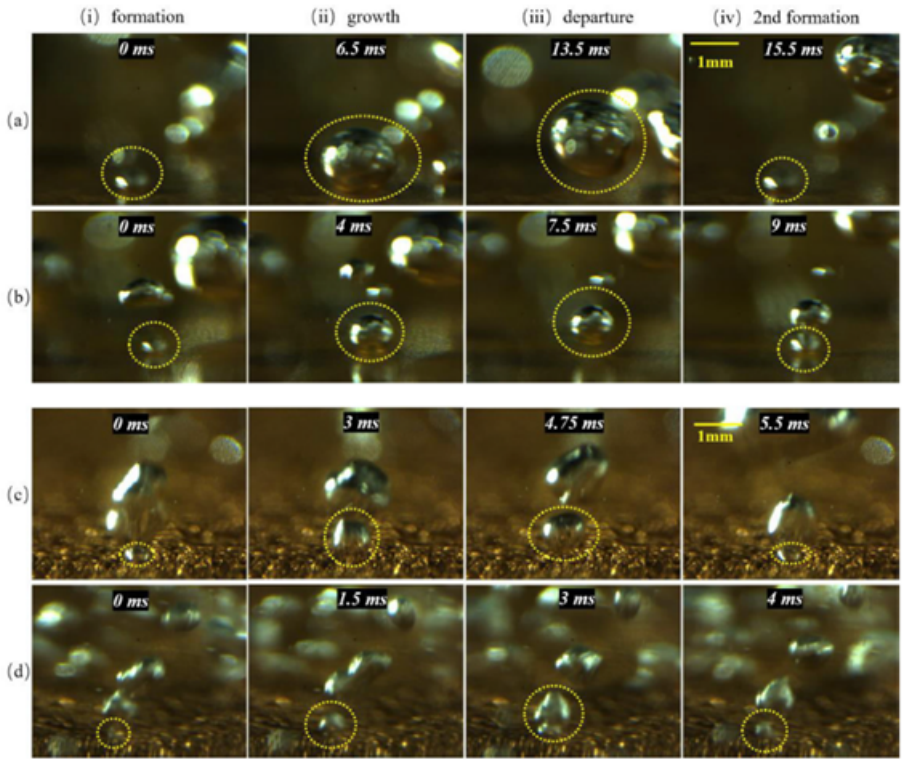

FIG. 4.1: Typical "single-bubble" experiments reported in the literature are influenced by multiple interfering bubbles, making quantitative interpretation difficult. [3]

To overcome this limitation, I designed a repeatable single-bubble facility using transparent indium–tin-oxide (ITO) glass heaters. The ITO coating ensures uniform Joule heating, while its optical transparency allows synchronous high-speed visualization. By laser-etching localized conductive regions, I was able to confine nucleation to a single site, thereby guaranteeing isolated bubble dynamics over

a wide Jakob-number range and for various surface wettabilities. This configuration provides three key advantages: Isolated nucleation control: Localized heating ensures one active nucleation site without interference from neighboring bubbles. Configurational flexibility: Replaceable ITO coupons allow systematic variation of cavity geometry and wettability. High-fidelity validation: The simultaneous measurement of wall temperature, heat flux, and bubble dynamics directly supports comparison with the LBM simulations and the $d_w(Ja, \theta)$ model developed in Chapter 6.

The resulting platform therefore serves as both an innovation in boiling experimentation and a benchmark dataset for validating mesoscopic numerical models.

4.2 Experimental Apparatus Design

Bubble nucleation is highly sensitive to surface roughness, cavity size, and heater geometry. To minimize unwanted nucleation and ensure a single active site, I adopted smooth glass substrates coated with ITO film. The effective bubble departure diameters in water (typically 1–3 mm [119]) guided the design of 20 mm × 20 mm ITO coupons, which provide sufficient clearance for bubble growth and optical access.

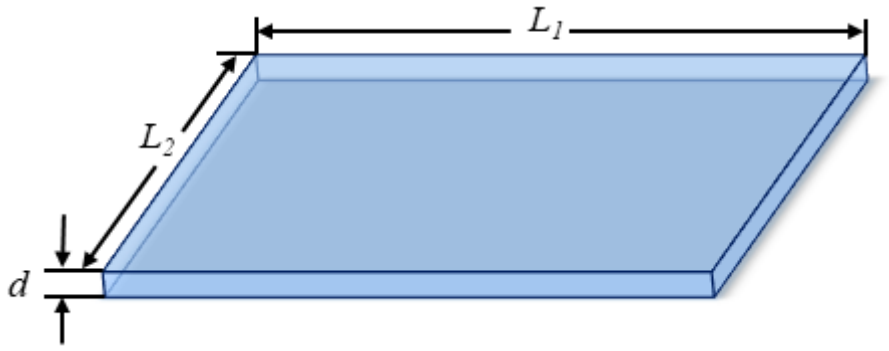

FIG. 4.2: Schematic Diagram of ITO Conductive Glass

ITO glass combines optical transparency with ohmic heating. Its sheet resistance R_s—the resistance measured across any square element—is given by: [120]

$$R_s = \frac{\rho L}{S} = \frac{\rho L_1}{d L_2}$$

where ρ is the resistivity of the coating material and d its thickness (See Fig. 4.2). Selecting a commercial sheet resistance of 10–15 Ω ensures uniform Joule heating without excessive current.

The core of the test section is shown schematically in Fig. 4.3 All functional components are integrated into a threaded peek plug for rapid assembly and replacement.

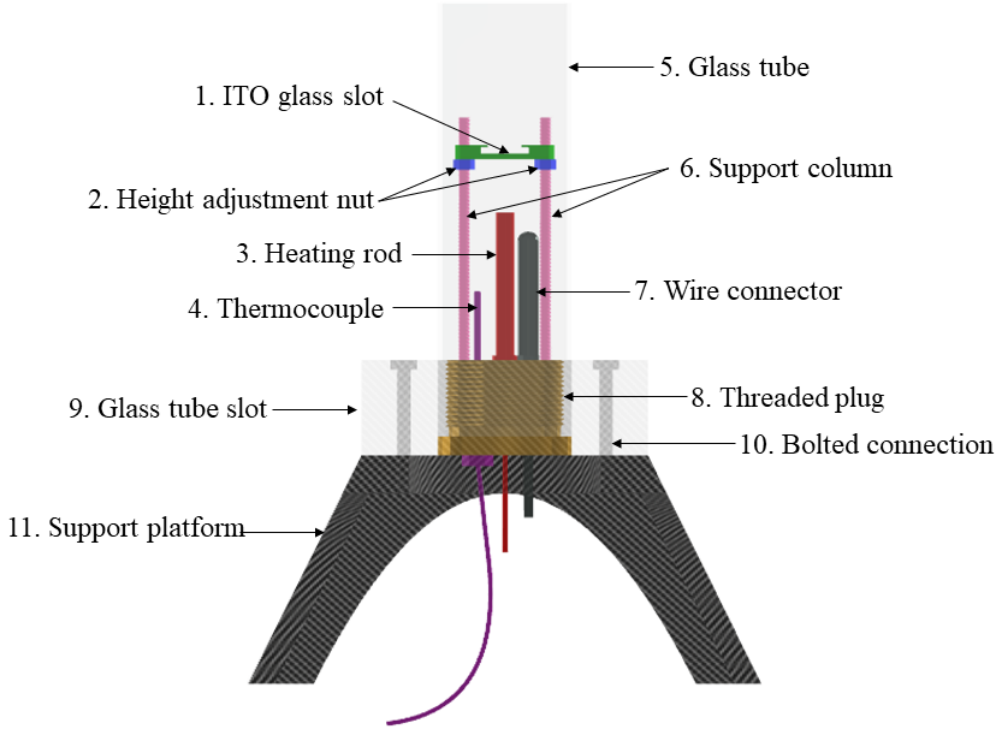

Fig. 4.3: Exploded view of the single-bubble generator. Numbers correspond to part list in 4.1.

In addition to the aforementioned bubble generation apparatus, the complete experimental testing system also includes a DC power supply, a multifunctional electrical measurement instrument, a high-speed camera, a light source, and a data monitoring and acquisition system.

Power supply: A Hameg HMP4040 (0–30 V, 300 W, ±0.01 %) [121] drives the cartridge heater; an independent Keithley 2460 [122] sourcemeter biases the ITO film.
Visualisation: A Photron high-speed camera [123] records up to 15 000 fps at 4k resolution, illuminated by a 150 W Phlox LMX LED back-light.
Data acquisition: All voltages, currents and PT100 readings are synchronised through a National Instruments DAQ and logged in LabVIEW [124] for real-time

control and post-processing (See Fig. 4.4). Overall accuracy is within ±0.01 % for electrical signals and ±0.2 K for temperature.

TABLE 4.1: Component list of the bubble-generator module

No.	Component	Function / Specification
1	ITO glass slot	20 × 20 × 1.5 mm recess; positions heater coupon
2	Height-adjustment nut	Fine vertical alignment of ITO surface (M4, stainless steel)
3	Cartridge heater	24 V, 100 W; primary heat input
4	PT100 sensor	−200 °C to 600 °C; wall-temperature feedback
5	Quartz glass tube	56 mm OD, 52 mm ID; optical enclosure
6	Support columns	M4 stainless rods; carry slot and sensor wiring
7	MIL-spec connector	Ø8 mm; water-tight electrical feed-through
8	Threaded brass plug	Ø50 mm; integrates heater, sensors, wiring
9	Tube seat	56 × 56 × 3.5 mm groove; seals quartz tube
10	Bolted joint	Provides mechanical preload
11	3-D printed base	Rigid support; quick interchangeability

The complete testing system is illustrated in Fig. 4.4.

Overall, the experimental device we designed using the above scheme has the following advantages:

Single-site control: Laser-etched micro-cavity on ITO guarantees one active nucleation site, eliminating multi-bubble interference.

In-situ optical access: transparent heater and quartz enclosure provide unobstructed high-speed imaging of the microlayer and contact line.

Modularity: threaded plug and replaceable ITO coupons allow rapid variation of cavity geometry, surface wettability and heater power.

Cost-effective: all components are homemade or 3-D printed, keeping fabrication costs low.

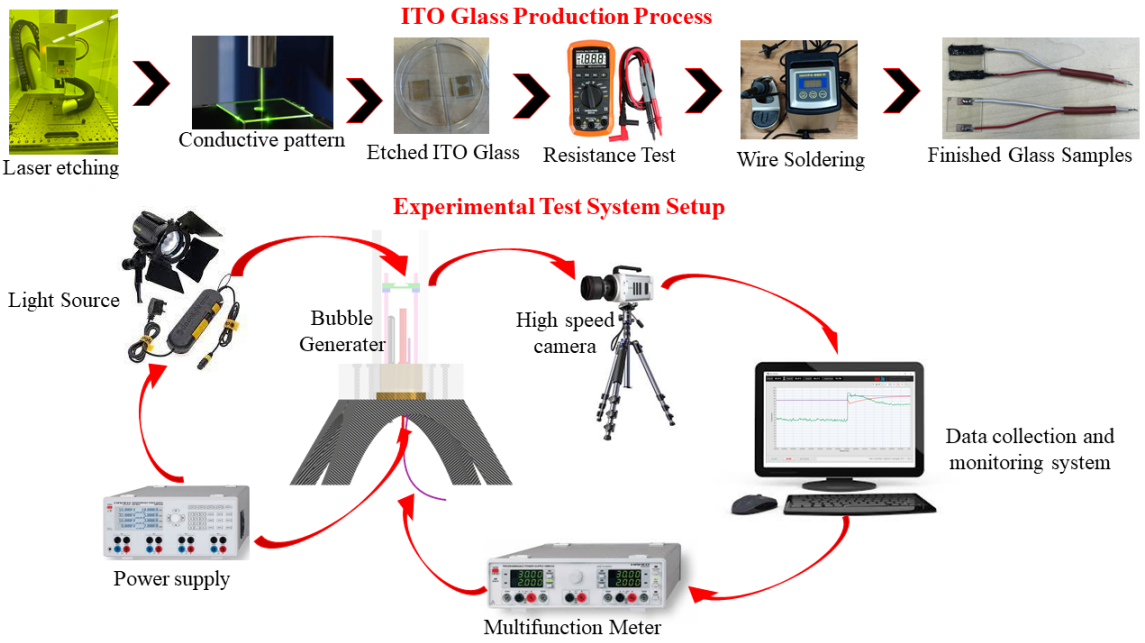

FIG. 4.4: Integrated test system: power supplies, multifunction meter, high-speed imaging and LabVIEW control.

4.3 Key Technical Challenges and Solutions

A critical design challenge in using ITO glass as a microheater lies in forming stable and reliable electrical connections to its smooth, non-porous surface. Since the glass substrate is submerged in water under boiling conditions, the connection must also withstand prolonged thermal cycling and moisture exposure.

To address this, I systematically evaluated three candidate methods—conductive adhesive tape, metal clips, and silver-paste sintering—and benchmarked their performance both in air and under boiling conditions (See Fig. 4.5).

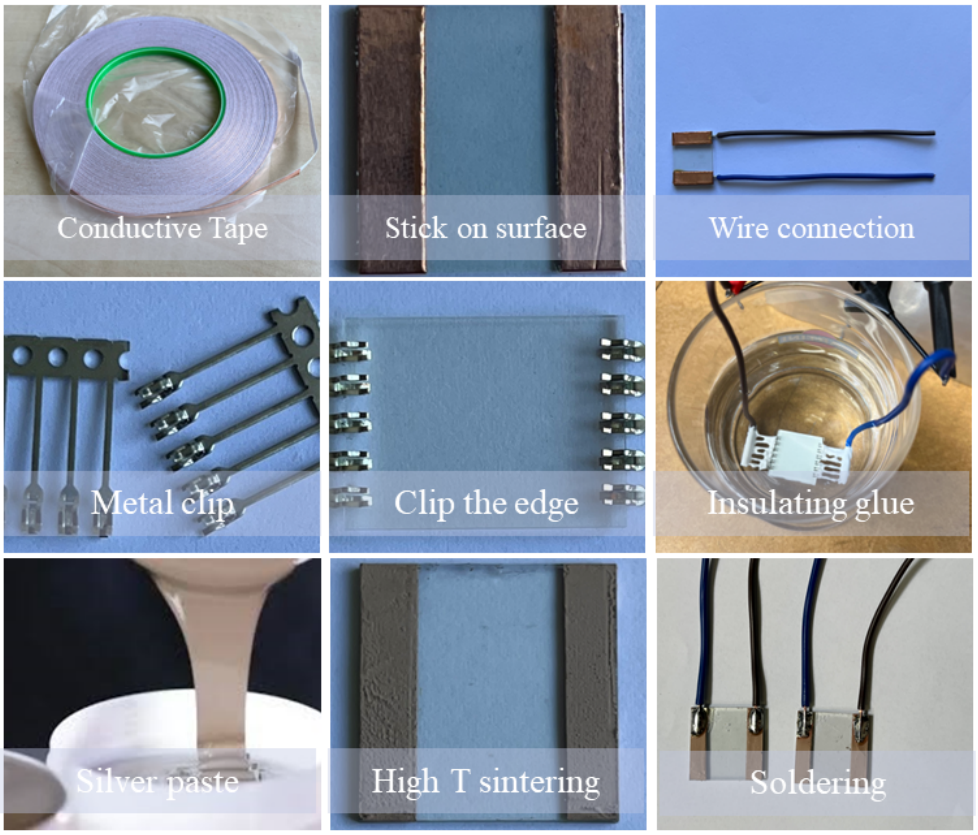

FIG. 4.5: Three methods for wire–ITO connection: (top) adhesive tape, (middle) metal clip, (bottom) silver paste with sintering.

Each configuration was tested on a 20 mm × 20 mm ITO coupon with $R_{\square} = 14\,\Omega$ at voltages up to 20 V and currents of 0.1–0.5 A. Table 4.2 summarises the static resistance and power output.

TABLE 4.2: Electrical performance of different connection methods.

Method	Resistance Range (Ω)	Power Range (W)	Stability in Water
Conductive tape	14.38–14.44	0.14–3.61	Delaminated at 0.3 A
Metal clips	14.25–14.26	0.14–3.56	Corrosion and electrolysis
Silver paste	14.26–14.27	0.14–3.57	Stable >24 h immersion

The conductive tape lost adhesion during boiling, likely due to moisture ingress and thermal degradation of the glue. Metal clips, though initially stable, suffered from corrosion and bubble formation at the contact site due to electrochemical reactions (See Fig. 4.6).

FIG. 4.6: Wire connection power test results

Only the sintered silver-paste connection provided long-term mechanical and electrical stability. Silver paste was printed through a mesh stencil, cured at 160°C for 30 minutes in a muffle furnace, then soldered with copper leads. Fig.4.7 shows the fabricated ITO glass heaters after electrical wiring, where copper pads were soldered to the etched regions to ensure stable current supply during the experiments.

FIG. 4.7: Final ITO sample prepared via silver-paste sintering and soldering.

In addition to electrical connection, precise control of the nucleation site is another central challenge. To localize Joule heating, I introduced three etched geometries with conductive widths of 1, 2, and 3 mm. As shown in Fig. 4.8(a), the schematic

illustrates the concept of restricting current flow through a narrow region, which increases local resistance and heat generation. Fig. 4.8(b) shows the corresponding laser-etched glass samples. Empirical trials revealed that the 1 mm design was most effective, as it concentrated sufficient heat to reliably trigger nucleation at a single spot while suppressing secondary activation nearby.

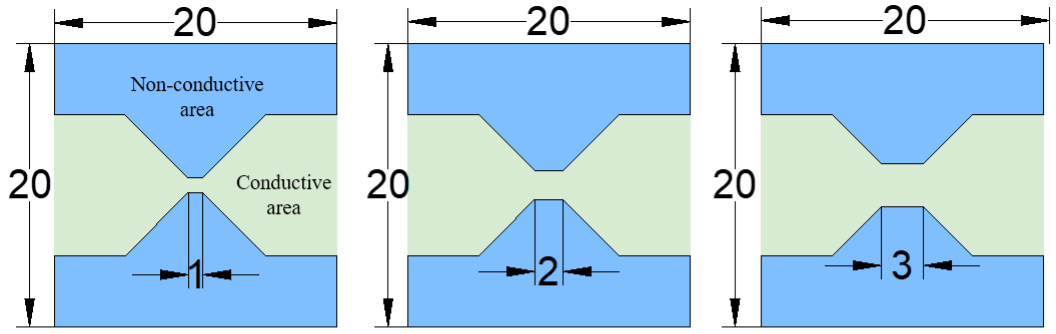

(a): Schematic design of laser-etched ITO glass with variable heating widths (1–3 mm).

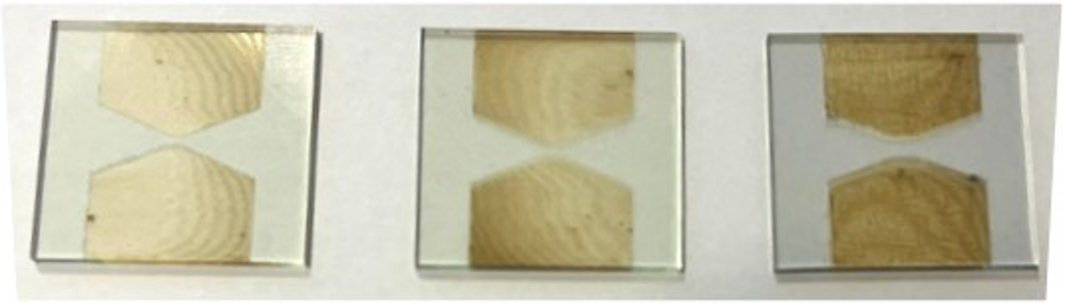

(b): Fabricated ITO glass samples corresponding to the schematic designs.

FIG. 4.8: Design and fabrication of laser-etched ITO glass heaters with localized heating widths (1–3 mm)

Together, these two solutions—sintered silver connection and micro-patterned heaters—form the basis of a robust and repeatable single-bubble generation system.

4.4 General measurement-uncertainty assessment

Accurate quantification of measurement uncertainty is essential for any boiling experiment because derived parameters—wall superheat, local heat flux, Jakob number, bubble departure diameter—enter directly into model validation. Following the ISO "Guide to the Expression of Uncertainty in Measurement" (GUM)[125],

we consider both *type-A* (statistical) and *type-B* (systematic) contributions for each sensor, then combine them by root-sum-square.

For a generic variable x recorded N times,

$$\sigma_x = \sqrt{\frac{\sum_{i=1}^{N}(x_i - \underline{x})^2}{N-1}}, \quad u_x = \sqrt{\sigma_x^2 + b_x^2}, \tag{4.1}$$

where σ_x is the sample standard deviation (*type-A*) and b_x the tolerance or calibration bias specified by the manufacturer (*type-B*).

Surface and fluid temperatures are measured by a PT100 Class A platinum resistance thermometer (± 0.10 K at 0–100 °C). Applying (4.1) with $x \equiv T$ gives:

$u_T = \sqrt{\sigma_T^2 + 0.10^2}$ K.

A four-probe setup[126] (Agilent 34420 A, 6½-digit) yields: $b_R = 0.1\ \Omega$. The combined standard uncertainty is:

$u_R = \sqrt{\sigma_R^2 + 0.1^2}\ \Omega$.

DC power is supplied by a Keysight E36313A (0.01 V / 0.01 A accuracy). Hence $b_U = 0.01$ V, $b_I = 0.01$ A; total uncertainties u_U, u_I follow from (4.1).

The spatial resolution of the high-speed camera (Phantom VEO 710L, 1024 × 768 px, 3.0 μm px^{-1}) yields $b_L = 0.02$ mm. Random scatter σ_L is obtained from at least 30 frames per bubble.

TABLE 4.3: Standard uncertainties of primary measurements ($k = 1$). Values in brackets are typical numbers obtained in this work

Quantity	Symbol	Bias b_x	Std. dev. σ_x	Combined u_x
Temperature	T	0.10 K	(0.03–0.05) K	0.11 K
Resistance (ITO)	R	0.10 Ω	0.04 Ω	0.11 Ω
Voltage	U	0.001 V	0.0006 V	0.0012 V
Current	I	0.001 A	0.0005 A	0.0011 A
Bubble linear dimension	L	0.02 mm	0.010 mm	0.022 mm

Heat flux on the ITO surface is evaluated by $q'' = UI/A$, and wall superheat by $\Delta T = T_w - T_{sat}$. Standard uncertainty propagation[127] gives:

$$u_{q''} = \sqrt{\left(\frac{\partial q''}{\partial U} u_U\right)^2 + \left(\frac{\partial q''}{\partial I} u_I\right)^2},$$
$$u_{Ja} = \sqrt{\left(u_T/(h_{fg}/c_p)\right)^2 + \left(u_{q''} \cdots\right)^2}, \tag{4.2}$$

where the second term in (eq. 4.2) may be omitted if Ja is defined only by ΔT. The budgets in Table 4.3 translate to relative expanded uncertainties ($k = 2$) of:

$$U_{q''} \approx 3.2\%, \quad U_{Ja} \approx 3.5\%, \quad U_{D^*} \approx 2.8\%.$$

These values are lower than the $\pm 5\%$ tolerance generally accepted for pool-boiling benchmarks [128], demonstrating that the present facility provides a reliable basis for validating numerical simulations. The remaining discrepancies can thus be attributed primarily to modeling assumptions rather than measurement errors.

4.5 Surface temperature measurement and calibration approach

Accurate determination of the wall superheat, $\Delta T = T_w - T_{\text{sat}}$, is essential since the Jakob number, $Ja = c_p \Delta T / h_{fg}$, is the primary non-dimensional parameter governing the thermal driving in the present study. Conventional techniques such as infra-red thermography or micro-thermocouples cannot deliver the required $\mathcal{O}(1-3)\,\text{K}$ resolution at millisecond time scales. Therefore, an alternative strategy was explored: first examining the feasibility of using the ITO heating layer itself as an in-situ resistance thermometer, followed by the adoption of an indirect reconstruction method.

4.5.1 Electrical stability of the ITO coating

The first prerequisite for resistance-based thermometry is the electrical stability of the ITO film under repeated Joule heating. Fig. 4.9 shows the measured resistance of an ITO-coated glass sample under three steady current loads (0.11,

0.12, and 0.13 A). A four-probe configuration was employed to eliminate lead and contact resistance effects. The mean sheet resistance remained close to 82 Ω with fluctuations below ±0.1 Ω and a standard deviation of about 0.11 Ω. These results confirm that the ITO layer is electrically stable and does not suffer from degradation such as micro-cracking during operation, ensuring its reliability as a heater element.

However, the very small temperature coefficient of resistance (α) implies that the resistance change associated with wall superheats of only a few kelvins is well below the detection limit of the measurement system.

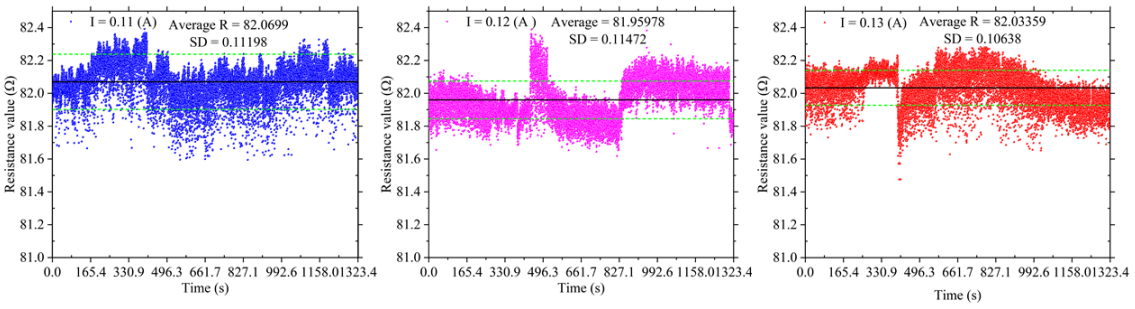

FIG. 4.9: Variation of ITO Resistance Over Time Under Different Currents

4.5.2 Silicone-oil bath calibration

To directly assess the resistance–temperature sensitivity of ITO, a dedicated calibration set-up was constructed, as illustrated in Fig. 4.10. The ITO glass coupon (connection scheme shown in Fig. 4.11) was suspended in a well-stirred silicone oil bath whose temperature was precisely controlled by a thermostat from 20 to 120°C with a stability of ±0.05 K. At each set-point, the oil temperature and the corresponding ITO voltage–current response were recorded to obtain the resistance:

$$R(T) = \frac{U}{I}.$$

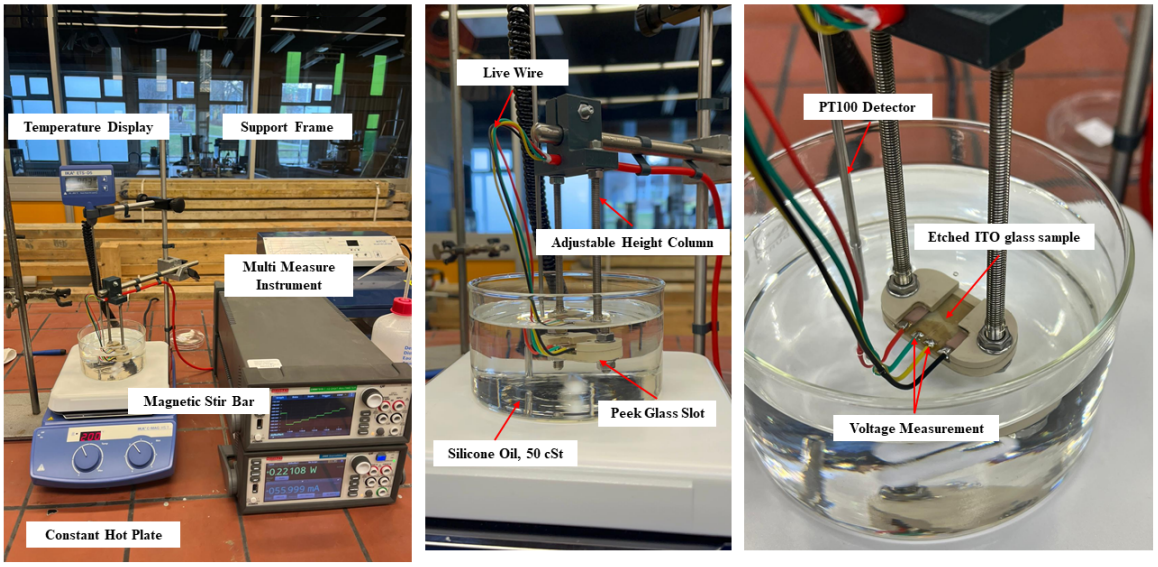

FIG. 4.10: Calibration assembly for determining the resistance–temperature relation of ITO samples using a silicone-oil bath with controlled temperature.

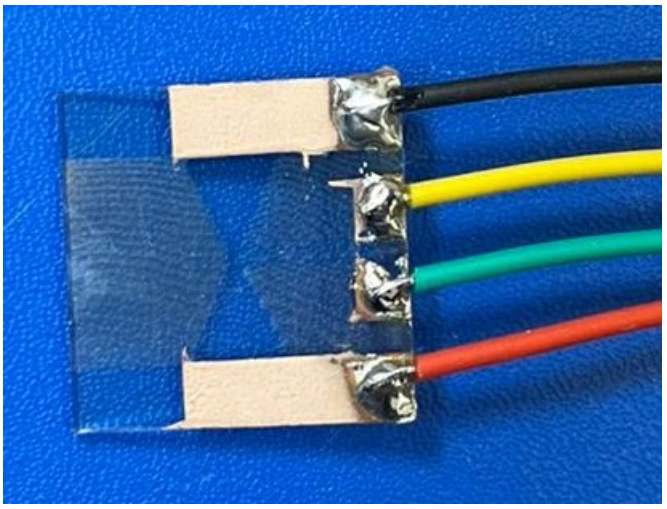

FIG. 4.11: Four-probe wiring of the ITO calibration sample. Green/yellow wires measure the voltage across the nucleation region, while red/black wires serve as current supply leads.

Linear regression of the measured $R(T)$ relation yielded an average temperature coefficient:

$$\alpha = \frac{1}{R_0}\frac{\mathrm{d}R}{\mathrm{d}T} \approx 5.7 \times 10^{-5}\,\mathrm{K}^{-1},$$

which is nearly two orders of magnitude smaller than that of typical metallic thin films ($\alpha \sim 10^{-3}\,\mathrm{K}^{-1}$). Given the digital multimeter resolution of $0.01\,\Omega$, the

minimum resolvable temperature rise was estimated as

$$\delta T = \frac{\delta R}{R_0 \alpha} \approx 18 \text{ K},$$

which is far larger than the $1-3\,\mathrm{K}$ wall superheats relevant for nucleation. Thus, while the calibration confirmed the excellent stability of the ITO coating, it also demonstrated that direct resistance thermometry is infeasible for the present application.

4.5.3 Indirect reconstruction via $Nu \cdot Ja$ scaling

Because the direct resistance approach cannot provide the required sensitivity, the wall superheat is instead reconstructed indirectly from the electrical heat flux. The key observation is that the product of the Jakob and Nusselt numbers can be expressed in terms of directly measurable quantities:

$$Ja = \frac{c_p \, \Delta T}{h_{fg}}, \qquad q'' = h \, \Delta T, \qquad Nu = \frac{h \, L}{\lambda}. \tag{4.3}$$

Eliminating ΔT and h yields:

$$Ja \, Nu = \frac{c_p \, q'' \, L}{\lambda \, h_{fg}}, \tag{4.4}$$

where the local heat flux $q'' = UI/A$ is obtained electrically, while the characteristic bubble length L is extracted from high-speed imaging. This formulation contains only directly measurable quantities and water properties, enabling the reconstruction of Ja once the correlation $Nu = f(Ja)$ is established. Based on this indirect approach, the bubble dynamics under controlled thermal driving are analyzed in the subsequent sections.

4.6 Image processing and bubble recognition

In addition to recording bubble dynamics using high-speed imaging, a dedicated image-processing pipeline was employed to quantitatively analyze bubble nucleation, growth, and detachment on high-temperature heating surfaces. The method

was specifically designed and custom-developed for this project to transform raw shadowgraphy sequences into segmented and labeled bubble maps, enabling the extraction of key geometric and dynamic parameters. The framework comprises six principal modules: image preprocessing, background subtraction, bubble region identification, void fraction estimation, feature extraction, and graphical visualization. The entire algorithm is implemented in C and executed in a Linux environment using the X11 graphical library [129]. The development of the code was not part of the candidate's work. It was made available in a functioning state. For completeness of the documentation and a full understanding of the obtained results, a sysatematic description of each processing step is provided below.

4.6.1 Image Preprocessing and Background Modeling

The raw dataset consists of grayscale images with a resolution of 191×119 pixels and 8-bit intensity values (0–255). To account for stationary background structures, a pixel-wise background model is constructed by analyzing the intensity histogram at each pixel location across the entire sequence [130]. The most frequently occurring intensity is assigned as the reference background value $U_{\max}(x, y)$:

$$U_{\max}(x, y) = \arg\max_i \Big(\#\,\text{of frames where } U_t(x, y) = i \Big).$$

This approach is robust against temporary darkening effects caused by bubble shadows and provides a stable representation of the static environment.

4.6.2 Background Subtraction and Contrast Enhancement

To highlight bubble regions, which appear as local shadows, each frame is processed by grayscale inversion followed by background subtraction [131]:

$$C_t(x, y) = \max\big(0,\, U_{\max}(x, y) - U_t(x, y)\big). \tag{4.5}$$

The resulting contrast field $C_t(x, y)$ accentuates bubble contours as bright spots. A column-wise maximum contrast $C_{\max}(y) = \max_{x,t} C_t(x, y)$ is then used to define adaptive thresholds [132]. Two thresholds are employed: a starting threshold $c_{\text{tr}} =$

$\frac{1}{4}C_{\max}$ for initiating bubble detection, and a continuation threshold $c_{\text{tr0}} = \frac{1}{6}C_{\max}$ for region growth.

4.6.3 Bubble Region Detection via Recursive Flood Fill

Bubble boundaries are detected using a recursive flood-fill algorithm [133]. A pixel is considered a seed if it is unassigned and satisfies $C_t(x, y) > C_{\max}(y)/\texttt{ctr}$ (empirical factor, e.g. 2). From each seed, adjacent pixels are recursively included if they exceed the continuation threshold $C_t(x, y) > C_{\max}(y)/\texttt{ctr0}$ (e.g. 4). Each connected region is labeled with a unique bubble identifier b_i.

4.6.4 Internal Bright Spot Correction

Due to illumination artifacts, bubble shadows occasionally contain bright interiors. These spurious regions are detected by re-applying the flood-fill procedure to unassigned pixels. If an interior region is in contact with exactly one bubble, it is reassigned to that bubble; otherwise, it is excluded from void fraction analysis. This step prevents over-segmentation and preserves the topological integrity of each bubble.

4.6.5 Void Fraction Estimation

The brightness distribution within each bubble is interpreted as an approximate measure of local void fraction. For bubble i, the normalized field is computed as:

$$\varepsilon(x, y) = \frac{C_t(x, y)}{C_{\max,i}}, \quad \text{for } b(x, y) = i, \tag{4.6}$$

where $C_{\max,i}$ denotes the maximum brightness within bubble i. This normalization enables a qualitative mapping between optical shadow intensity and vapor content.

4.6.6 Feature Extraction

For each identified bubble i, various geometric and dynamic properties are extracted:

Center of mass:

$$x_i = \frac{\sum_{(x,y)\in i} x \cdot \varepsilon(x,y)}{\sum_{(x,y)\in i} \varepsilon(x,y)}, \quad y_i = \frac{\sum_{(x,y)\in i} y \cdot \varepsilon(x,y)}{\sum_{(x,y)\in i} \varepsilon(x,y)}.$$

Projected area:

$$A_i = \sum_{(x,y)\in i} \varepsilon(x,y).$$

Volume estimate (axisymmetric assumption):

$$V_i = \sum_{y} \frac{\pi}{4} d_{x,i}^2(y),$$

where $d_{x,i}(y)$ is the bubble width at height y.

Maximum dimensions:

$$d_{x,\max,i} = \max_{y} \sum_{x} \varepsilon(x,y), \quad d_{y,\max,i} = \max_{x} \sum_{y} \varepsilon(x,y).$$

Bubble base (root) position:

The lowest vertical location of the bubble, $y_{0,i}$, is determined by interpolating the void fraction profile where $\varepsilon = 0.5$. This baseline (See Fig. 4.12) provides a reference for identifying bubble departure events.

Moment of inertia:

$$M_i = \sum_{(x,y)\in i} \varepsilon(x,y) \left[(x - x_i)^2 + (y - y_i)^2\right].$$

Appearance time:

The first frame in which each bubble ID is detected.

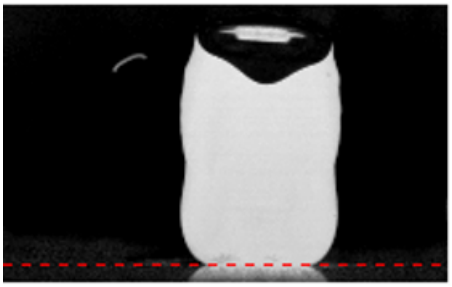

FIG. 4.12: Definition of the bubble base position. The red dashed line denotes the lowest vertical coordinate ($y_{0,i}$) of the bubble, determined by interpolating void fraction contours at $\varepsilon = 0.5$. This baseline is later used to identify the instant of bubble detachment.

4.6.7 Visualization and Output

The final stage produces color-coded images in which each bubble is assigned a distinct random color and its brightness corresponds to the local void fraction (See Fig. 4.13) . Bubble IDs are overlaid for visual tracking. At the same time, quantitative features are exported to structured `.txt` files, and processed sequences can be converted into video format using `ffmpeg` for visualization.

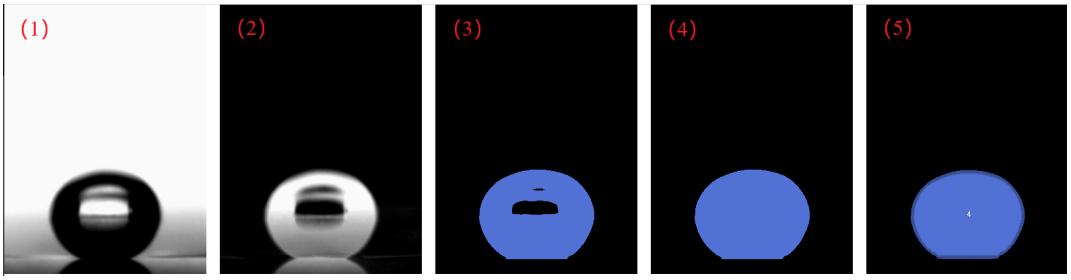

FIG. 4.13: Step-by-step illustration of the bubble recognition process. From left to right: (1) raw grayscale image; (2) background-removed and contrast-enhanced image; (3) initial flood-fill segmentation; (4) corrected bubble region after bright spot filling; (5) final visualization with bubble ID overlay and void fraction encoding.

This image-processing pipeline enables automated extraction of dynamic bubble properties from high-speed shadowgraphy data. By integrating background modeling, recursive segmentation, and void fraction normalization, the method provides a robust basis for analyzing bubble nucleation, growth, and detachment in boiling systems.

4.7 Overall uncertainty and influential parameters

While the single-bubble facility and the image-processing pipeline provide a controlled and repeatable basis for validation, several experimental uncertainties must be acknowledged and the most influential parameters highlighted.

Measurement and reconstruction.

(1) The wall superheat is reconstructed indirectly from electrical heat flux via the $Nu \cdot Ja$ scaling; its accuracy depends on (i) voltage/current calibration, (ii) ITO

active area A, and (iii) property inputs (λ, c_p, h_{fg}). These propagate to $u_{q''}$ and u_{Ja} (Sec. 4.5), yielding typical expanded uncertainties below 5% for q'' and Ja.

(2) Direct ITO resistance thermometry was shown to be insensitive at the required 1–3 K level; thus any residual bias primarily stems from the Nu–Ja correlation and from length-scale extraction in imaging.

(3) Bubble dimensions and departure timing are derived from high-speed images; finite pixel size and thresholding cause a $2\text{–}3 \times 10^{-2}$ mm length bias and a temporal uncertainty of one frame interval, respectively. Apparent contact-angle extraction is affected by illumination and contouring, with a typical $\pm 3°$–$5°$ margin.

Boundary conditions and apparatus.

(1) The ITO heater provides nearly uniform Joule heating, but local nonuniformity may arise near etched constrictions and silver-paste pads; this mainly affects microlayer dynamics and early growth.

(2) The present experiments were conducted under an open pool configuration, where the liquid surface is exposed to the ambient atmosphere. Consequently, the system pressure is not strictly fixed at the standard value of 101.325 kPa but varies slightly with the laboratory air pressure and the liquid column height. As a result, the effective saturation temperature of water may differ slightly from the nominal 100 °C and fluctuate with atmospheric conditions. In addition, the presence of non-condensable gases and trace impurities can alter the local vapor pressure near the interface, thereby affecting the onset of nucleation and bubble growth rate. Overall, such environmental and boundary effects represent an inherent source of experimental uncertainty, though their influence is minimized through real-time monitoring of ambient conditions and appropriate corrections during data processing.

Surface state and repeatability.

(1) Surface roughness and wettability can drift after repeated cycles (fouling, microcracks in coating), shifting the activation threshold of secondary sites.

(2) Environmental perturbations (weak vibrations, background convection) influence contact-line wandering; repeat runs and statistical aggregation mitigate these effects.

Key experimental control parameters.

(1) **Thermal driving**—wall superheat (or Ja) via electrical power—dominates nucleation onset, growth rate, and departure frequency.

(2) **Wettability**—set by ITO surface treatment/overlayers—modulates base adhesion and $d_w(Ja, \theta)$ trends used for model confrontation.

(3) **Heater pattern geometry**—etched width and active area—localizes nucleation; narrower tracks enhance isolation but increase local nonuniformity.

(4) **Optical sampling**—frame rate, exposure, and magnification—controls temporal and spatial resolution of the extracted metrics.

4.8 Summary of this chapter

This chapter introduced a controllable single-bubble boiling facility tailored for quantitative comparison with the LBM framework. Micro-patterned ITO heaters were employed to enforce isolated nucleation, while optical transparency enabled synchronous high-speed imaging and electrical measurements. After confirming the electrical stability of the ITO coating, a silicone-oil calibration demonstrated that direct resistance thermometry lacks the sensitivity required for millisecond-scale, 1–3 K wall superheats; consequently, wall temperature was reconstructed indirectly from q'' and an $Nu \cdot Ja$ scaling. The overall experimental uncertainty and key control parameters have been analyzed in Section 4.7, which complements the quantitative measurement assessment presented earlier and establishes the reliability boundaries for comparison with the numerical results. A dedicated image-processing pipeline then delivered automated extraction of bubble features—including a robust definition of the bubble base $y_{0,i}$ for departure detection—yielding time-resolved, repeatable metrics.

If we combined Chapter. 2.5, although the experiments and simulations are not strictly one-to-one due to scale and density-ratio differences, the use of unit conversion and nondimensional groups ensures a physically consistent basis for comparison. The resulting data set and analysis provide a reliable experimental benchmark against which the LBM predictions can be validated. The next chapter uses these measurements to confront numerical results—focusing on departure diameter/frequency and their Ja–wettability dependence.

Chapter 5

Experimental validation of Single Bubble Dynamics

This chapter presents a systematic experimental investigation of single-bubble boiling dynamics and pool boiling behavior, supported by high-speed visualization, quantitative image processing, and direct comparison with numerical simulations. The primary aim is to obtain measurable parameters that characterize bubble nucleation, growth, departure, and collapse behavior, thereby establishing an experimental benchmark for validating the predictive capability of the numerical model. It should also be emphasized that the experiments are necessarily performed under slightly subcooled conditions, since in an open pool boiling setup at atmospheric pressure it is practically impossible to maintain the bulk liquid exactly at the saturation temperature. Heat losses to the environment, natural convection, and the thermal inertia of the liquid reservoir typically keep the liquid temperature a few degrees below saturation.

In contrast, the saturated condition in the simulations eliminates this offset and therefore represents an idealized limit in which nucleation occurs once the wall temperature exceeds the saturation threshold. While this prevents a strict one-to-one comparison of absolute values, the qualitative trends in bubble dynamics (nucleation sequence, growth, departure frequency, and wettability dependence) remain directly comparable. Hence, the experiments provide realistic validation benchmarks, whereas the simulations offer controlled insight into the sensitivity of boiling behavior to boundary conditions and surface properties.

The chapter is organized as follows. Section 5.1 provides high-speed visualization results of a single bubble's complete life cycle, offering qualitative insights into nucleation, growth, detachment, and condensation. Section 5.2 examines pool boiling regimes, distinguishing between nucleate boiling and the onset of transition boiling. Section 5.3 introduces the image-processing pipeline developed for bubble contour recognition and dynamic feature extraction. Section 5.4 presents quantitative measurements of bubble geometry and kinematics, including projection area, equivalent diameters, ovality, and trajectories. Finally, Section 5.5 compares experimental measurements with lattice Boltzmann simulations, focusing on dimensionless departure diameters, detachment frequencies, and their dependence on superheating and wettability.

5.1 Single Bubble Experimental Results

The complete evolution of a single bubble—including nucleation, growth, departure, and collapse—was captured using a high-speed camera at 3000 fps with a 300 μs exposure time. The experiment was conducted at an initial liquid temperature of 90°C, with bubble nucleation observed at 89.3°C. The applied current on the ITO substrate was 0.11 A, corresponding to a heating power of 0.882 W.

5.1.1 Nucleation Stage

Fig. 5.1 shows the initial nucleation process in six frames. Initially (Frames 278, 279), the liquid–solid interface remains undisturbed, indicating that no phase change has occurred. In Frame 3, a small hemispherical vapor nucleus abruptly forms at the heated center of the ITO surface, implying localized superheating and near-instantaneous nucleation. As the sequence progresses (Frames 280–283), the bubble rapidly expands. It grows symmetrically upward, while maintaining attachment at the base. The appearance of internal brightness results from multiple light reflections at the gas–liquid interface, confirming the formation of a well-defined vapor cavity. The bubble shape evolves from hemispherical to more ellipsoidal as it grows, accompanied by vapor accumulation inside the cavity. During this expansion, the curvature of the interface decreases, which slightly reduces the internal Laplace pressure while the vapor volume continues to increase.

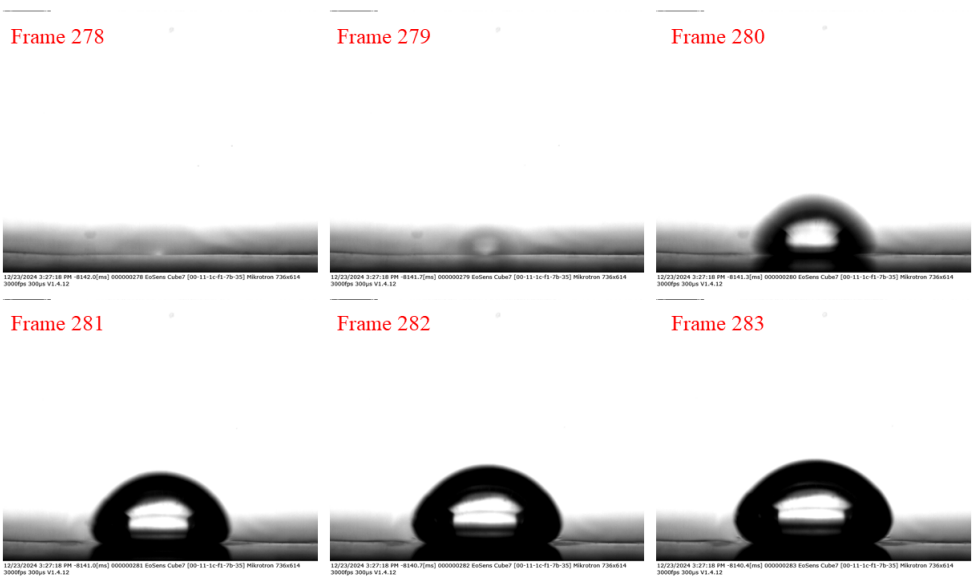

FIG. 5.1: Bubble nucleation captured over six consecutive frames.

5.1.2 Growth Stage

The subsequent growth process is presented in Fig. 5.2. In the early frames (286, 2287), the bubble continues expanding in a nearly spherical form. Its base remains well anchored to the heated substrate, indicating strong adhesion and dominance of surface tension forces. The bright cavity persists, showing that the internal vapor remains stable.

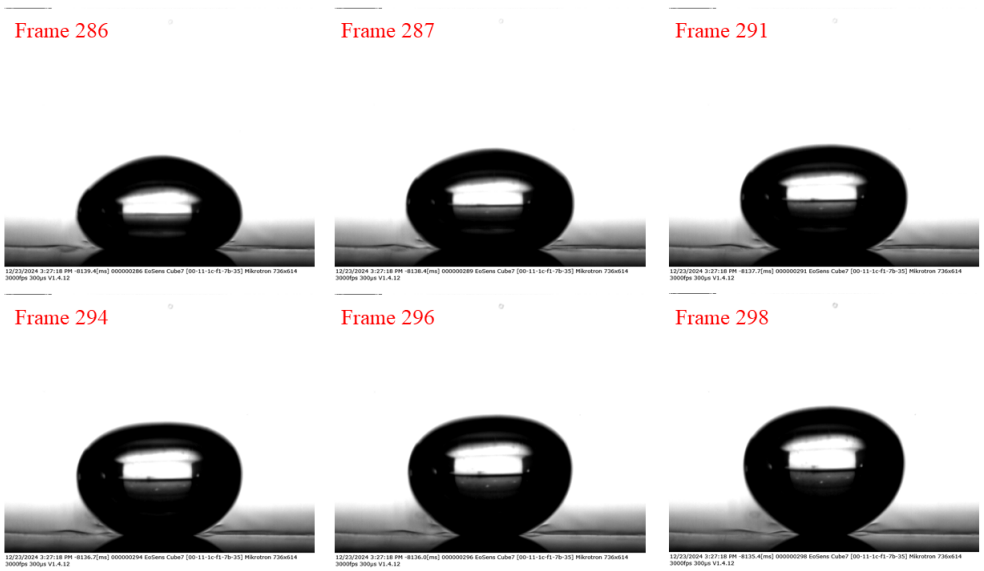

FIG. 5.2: Bubble growth sequence highlighting symmetry and pressure build-up.

From Frames 291 to 298, the bubble undergoes accelerated vertical elongation. The top becomes more pointed, while the sidewalls expand laterally. The shape deviation from a perfect sphere suggests increasing buoyancy influence. Despite continued growth, the interface remains smooth and symmetric, indicating minimal perturbation from the surrounding fluid at this stage. The strong internal brightness reflects sustained evaporation and high vapor content.

5.1.3 Departure Stage

Fig. 5.3 illustrates the bubble detachment process. In Frames 300, 301, the bubble reaches its maximum vertical size. The neck connecting the bubble to the surface starts to constrict, indicating the onset of detachment. Surface tension and buoyancy forces are now in direct competition.

In Frames 303 and 304, the lower interface narrows further, while the bubble starts lifting off. The internal reflections persist, confirming that the cavity remains pressurized. Frames 305-307 show full detachment from the surface. The bubble adopts a more rounded, free-rising form. Its upward motion is now primarily governed by buoyancy and the inertial response of the surrounding liquid.

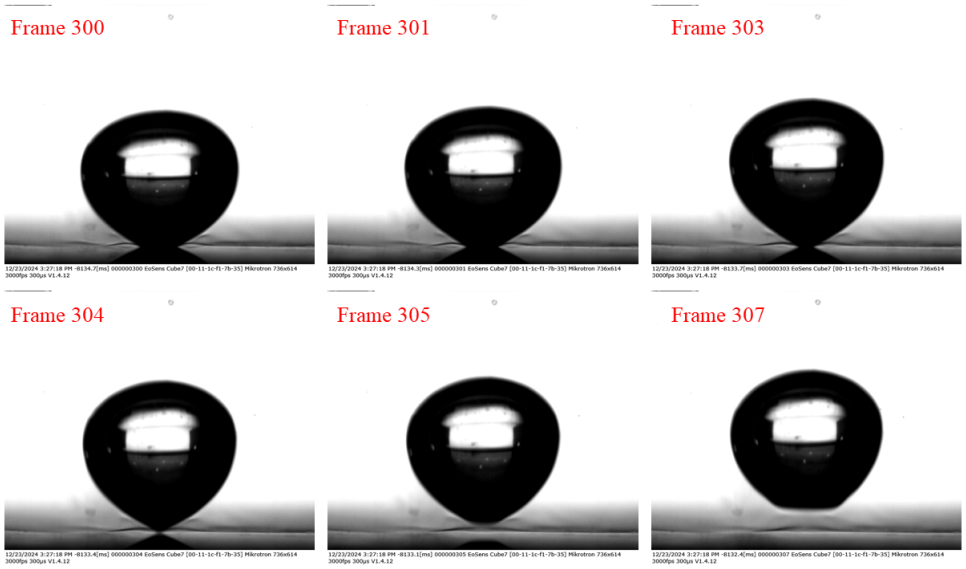

FIG. 5.3: Bubble departure process showing gradual necking and lift-off.

5.1.4 Collapse Stage

After detachment, the bubble ascends into the bulk liquid, as shown in Fig. 5.4. In Frames 313–316, the bubble maintains a smooth hemispherical profile, and internal reflections are still visible. However, minor deformations begin to appear, especially in the upper portion.

In Frames 323–327, the bubble undergoes significant shape distortion. The upper interface collapses inward, possibly due to pressure gradients or local shear in the surrounding fluid. By Frames 335–340, the bubble has broken symmetry and begins to disintegrate. The disappearance of the internal bright region suggests the vapor has condensed or dispersed, and the bubble's structural integrity is lost, marking the end of its lifecycle.

It is important to note that this experiment was conducted in a subcooled liquid environment, with the bulk liquid temperature maintained at approximately 90°C, below the saturation point. Consequently, once the bubble detaches and leaves the heated surface, it can no longer receive sufficient heat to sustain its vapor phase. As the bubble ascends, it encounters cooler liquid and rapidly loses heat, leading to its condensation and collapse. This behavior is characteristic of vapor bubbles in subcooled boiling conditions.

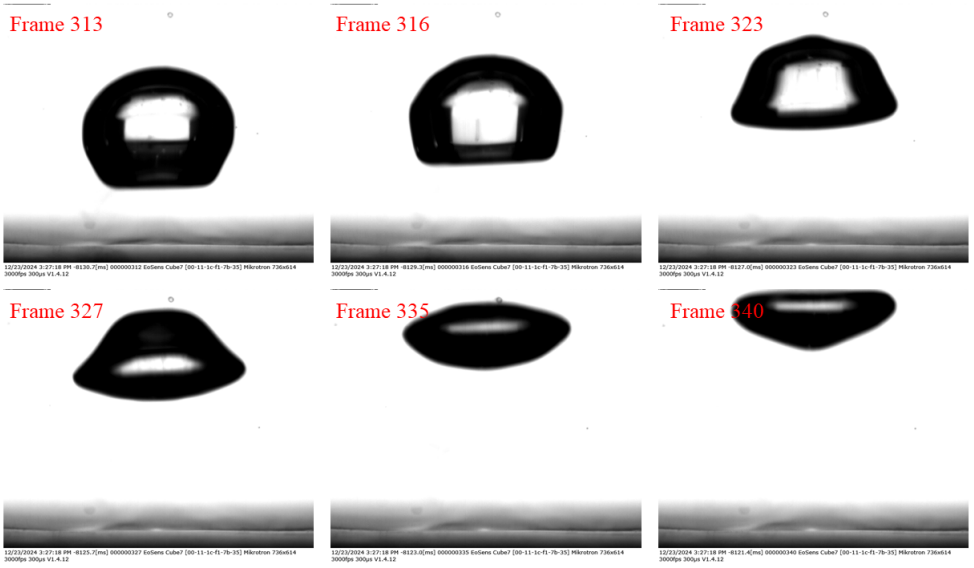

FIG. 5.4: Bubble collapse and deformation during ascent.

The experimental visualization clearly captures the dynamic phases of bubble evolution: rapid nucleation, symmetric growth, delayed detachment, and eventual

collapse. Although the simulations presented in Chapter 3.1 were performed under saturated boiling conditions, the temporal sequence of bubble evolution observed in the experiments shows strong qualitative agreement with the numerical results.

In both cases, the bubble undergoes a four-stage cycle: (i) sudden nucleation triggered by localized superheating, (ii) symmetric growth anchored at the heated surface, (iii) necking and detachment driven by the interplay of surface tension and buoyancy, and (iv) post-departure shrinkage and disappearance. This correspondence confirms that the implemented numerical model successfully captures the essential interfacial dynamics of single-bubble boiling.

It should be noted, however, that the subsequent collapse of the detached bubble observed in the experiments is specific to the subcooled boiling regime: once the vapor cavity detaches, it cannot be sustained in the cooler bulk liquid and rapidly condenses. In contrast, under the saturated conditions adopted in the present simulations, the detached bubble would remain stable and continue to rise rather than disappearing. This difference highlights that the small degree of subcooling in the experiments does not significantly affect the nucleation, growth, and detachment sequence, but mainly influences the post-detachment behavior through condensation in the liquid bulk. Nevertheless, the strong consistency in the nucleation–growth–detachment stages between experiments and simulations provides a solid basis for validating the predictive capability of the model.

5.2 Pool Boiling Experimental Results

To complement the numerical simulations presented in the previous chapters, a series of pool boiling experiments were conducted in order to provide direct physical evidence of bubble dynamics and to verify whether the observed regimes follow the classical boiling curve. These experiments serve two main purposes: (*i*) to qualitatively validate the nucleation, growth, and detachment phenomena predicted in the numerical models, and (*ii*) to establish a comparative basis with the theoretical framework of pool boiling. Due to equipment limitations and the potential risk of damaging the ITO heating substrates, the film boiling regime beyond the Leidenfrost point was not investigated. Nevertheless, the captured nucleate and transition boiling stages already cover the essential part of the boiling curve and allow meaningful comparisons with simulation and theory.

In particular, the single-bubble experiments were directly used to validate the LBM simulations by comparing the nucleation, growth, and detachment sequence, thereby confirming that the numerical model can reproduce the essential interfacial dynamics observed in reality. At the same time, the experimental facility is capable of capturing the entire boiling curve, including regime transitions, which provides the opportunity for future extensions of the validation framework. In the present thesis, however, the comparison is deliberately restricted to single-bubble dynamics, in order to establish a clear one-to-one correspondence with the numerical results and to avoid the additional uncertainties associated with multi-bubble interactions and macroscopic boiling heat transfer.

The experiments were carried out on ITO conductive glass substrates without localized laser etching, such that the entire surface served as a uniform heating element. High-speed visualization enabled frame-by-frame analysis of bubble dynamics under different heating conditions. The working fluid was initially maintained at 97 °C, slightly below saturation, ensuring that the onset of nucleate boiling could be observed with controlled superheating.

5.2.1 Nucleate Boiling Regime

Fig. 5.5 shows a sequence of high-speed images captured during pool boiling at a heating power of 1.837 W and an applied current of 0.15 mA. In this regime, vapor bubbles form intermittently and predictably at distinct nucleation sites on the heated ITO surface. Due to the large size of the heating area relative to the bubble footprint, multiple bubbles emerge independently without mutual interference. The images depict a stable cycle of bubble nucleation, growth, and detachment, consistent with classical descriptions of nucleate boiling.

The formed bubbles rise vertically through the liquid column, maintaining hemispherical or slightly elongated shapes, with minimal interaction among them. This behavior reflects efficient heat transfer dominated by discrete bubble events and strong liquid–wall thermal coupling. Although dynamic surface temperature measurements are not yet available, the regularity and isolation of the bubbles suggest that the system remains well within the nucleate boiling regime.

These observations provide direct experimental confirmation of the isolated bubble cycle predicted in Ref.[134] thereby validating the assumptions of the numerical model under moderate superheat conditions.

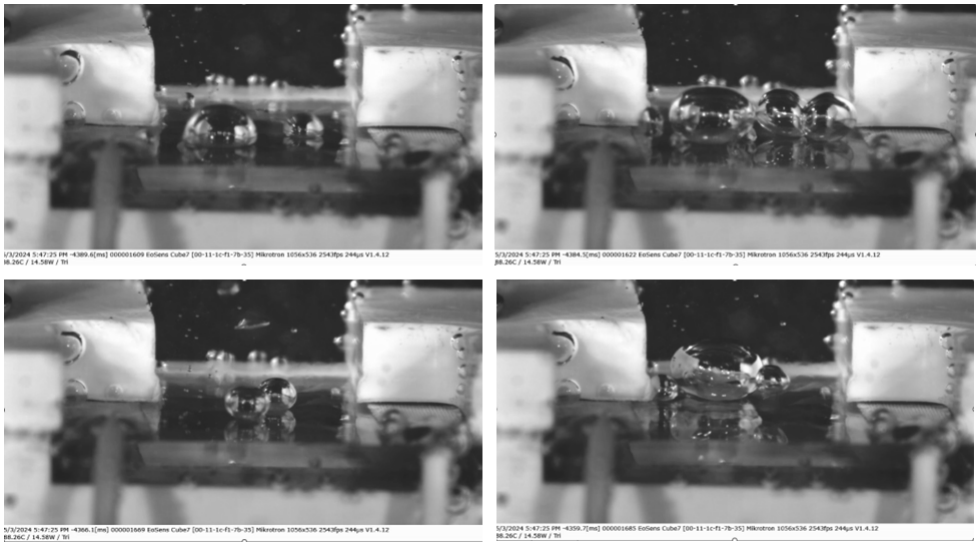

FIG. 5.5: Nucleate boiling regime: independent bubble nucleation and detachment. Heating power: 1.837 W; $I = 0.15$ mA.

5.2.2 Transition Boiling Regime

As the power input is increased to 3.582 W with a corresponding current of 0.19 mA, the system transitions into a more unstable regime, as illustrated in Fig. 5.6. Although the bulk liquid remains at 97 °C, the heated surface experiences a significantly higher local temperature, likely exceeding the critical threshold for nucleate boiling.

This regime is characterized by intensified bubble activity and strong liquid agitation near the surface. In contrast to the isolated behavior observed previously, vapor bubbles now appear in clusters, frequently merging to form large vapor structures. The surface becomes increasingly populated by coalescing bubbles, some of which no longer complete a full detachment cycle.

The recorded frames capture the onset of vapor film patches—regions where large bubbles coalesce and begin to spread horizontally across the surface. This marks the beginning of transition boiling, a metastable regime between nucleate and film boiling. In this state, the local vapor layer is not yet continuous but exhibits

fluctuating behavior due to the competition between bubble-induced evaporation and surface rewetting.

These observations serve as an essential experimental reference for the onset of heat transfer deterioration, complementing the numerical predictions of interfacial instability and vapor accumulation at higher superheat.

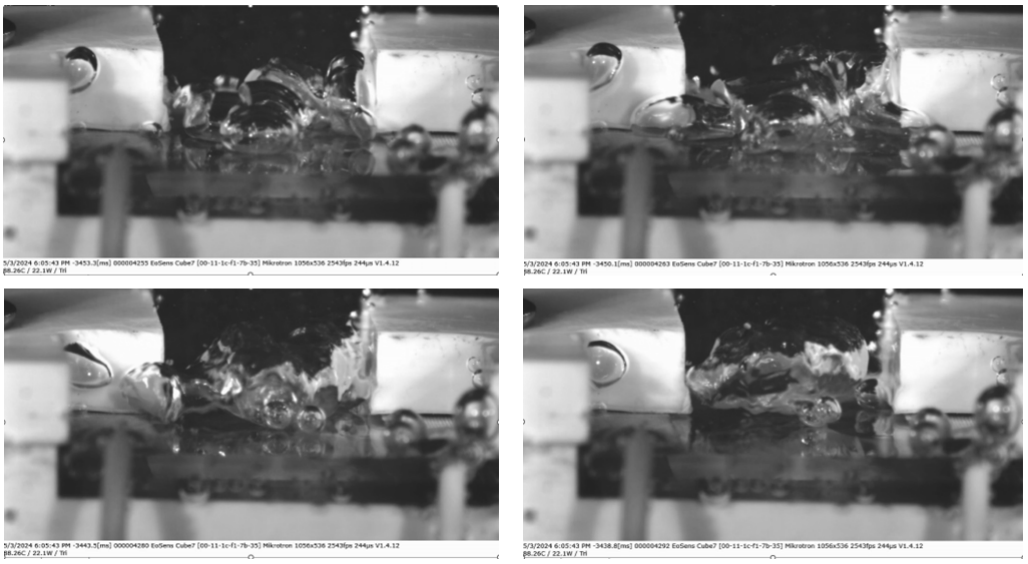

FIG. 5.6: Transition boiling regime: intensified bubble interaction and vapor accumulation. Heating power: 3.582 W; $I = 0.19$ mA.

The comparative analysis of nucleate and transition boiling regimes highlights the critical role of surface temperature and heat flux in governing interfacial phenomena. While nucleate boiling ensures efficient heat transfer via isolated bubble cycles, the transition regime reflects increasing thermal resistance and vapor entrapment. The experimental results are consistent with the classical boiling curve (See section 1.2.2) and provide valuable benchmarks for validating the numerical simulations presented in this thesis. Future work will incorporate calibrated surface thermometry and quantitative heat flux measurements to complement the qualitative visual data shown here.

5.3 Image Recognition Results

Fig. 5.7 provides a comprehensive comparison between the raw experimental images (left of each pair) captured via high-speed photography and the processed

results generated by the proposed image recognition algorithm (right of each pair). This comparison serves as a direct validation of the algorithm's ability to accurately extract bubble features from experimental data. Four representative dynamic conditions are shown, allowing for a thorough evaluation of the algorithm's accuracy, adaptability, and robustness.

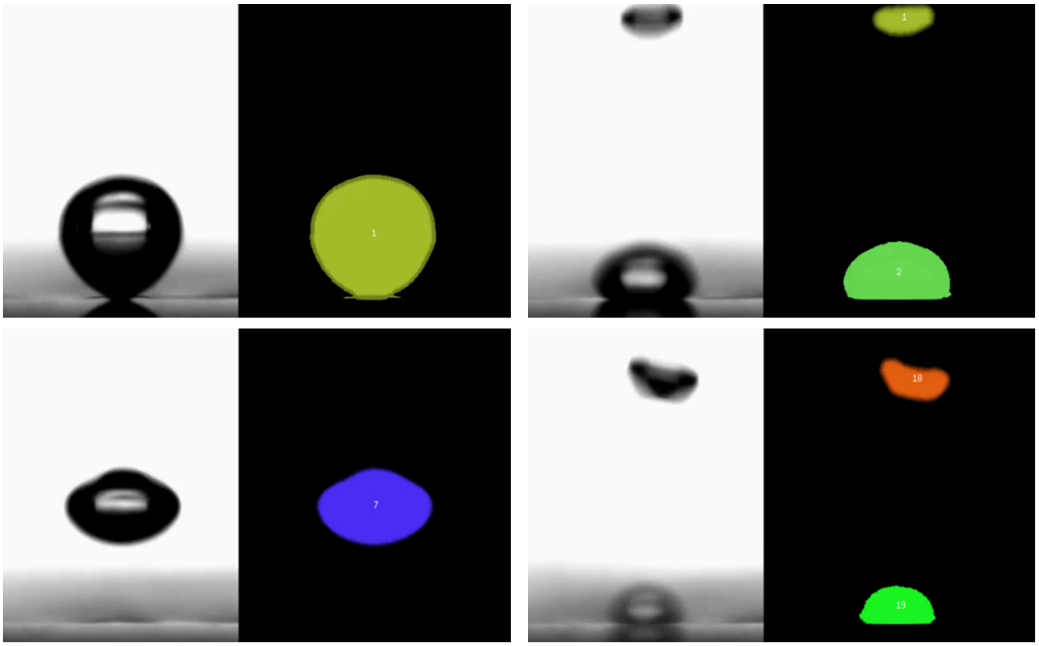

FIG. 5.7: Comparison between experimental visualization (left) and recognition results (right). Each pair illustrates the performance of the bubble recognition algorithm under different dynamic conditions.

In the top-left pair, a single vapor bubble is observed growing on the heated surface, exhibiting a smooth and nearly spherical shape. The corresponding segmented result confirms that the algorithm successfully isolates the bubble with high contour fidelity, assigning it a unique identifier (bubble 1) and preserving its morphology. This demonstrates the capability of the recognition routine to detect and label individual bubbles during the early nucleation and growth stages.

In the top-right pair, the configuration is more complex: one bubble remains attached to the surface while another has already detached and is rising into the subcooled liquid. Although the raw grayscale image may give the impression of an additional faint structure, the segmentation correctly identifies two physically distinct bubbles and labels them as bubble 1 and bubble 2. This confirms that the method can reliably resolve multiple, spatially separated structures within the

same frame, a necessary feature for capturing the complete dynamics of bubble generation, growth, and detachment.

In the bottom-left pair, a transitional moment is shown where the bubble is about to detach. Despite the asymmetric deformation and non-uniform brightness, the algorithm preserves the boundary integrity and labels the structure as bubble 7, confirming that recognition remains effective even under non-ideal imaging conditions.

Finally, in the bottom-right pair, the scene becomes more complex: the upper bubble exhibits significant distortion and elongation during its upward motion, while a new nucleation cycle begins on the heated surface. The recognition algorithm captures this complexity by correctly assigning distinct labels (bubbles 18 and 19) and maintaining a clear separation between them. This robustness in handling overlapping shadows, variable brightness, and rapidly evolving contours demonstrates the versatility of the approach.

Taken together, these comparisons confirm the high consistency between experimental observations and algorithm outputs. The recognition algorithm not only accurately identifies bubble contours, but also remains reliable across different bubble sizes, positions, and shapes. This provides a solid foundation for extracting time-resolved quantitative features of bubble dynamics, which will be further elaborated in the next subsection.

5.4 Obtainable bubble dynamic parameters

By applying an image recognition algorithm to high-speed photographic sequences, a series of key bubble dynamic parameters can be accurately extracted. These parameters provide valuable insights into the evolution of individual bubbles throughout the full cycle of nucleation, growth, and departure. The following analysis categorizes these parameters according to their temporal evolution and physical significance.

5.4.1 Evolution of Bubble Projection Area Over Time

Fig. 5.8 reports the time evolution of the bubble projection area for three initial liquid temperatures (90, 93, and 95 ℃), corresponding to different subcoolings. All curves exhibit the characteristic growth–decay pattern associated with a single-bubble cycle. The peak of each curve marks the instant of detachment, from which the size and time at departure are obtained:

$$
\begin{aligned}
T_{\text{init}} = 90\,^{\circ}\text{C}: &\quad t_d \approx 0.00133 \text{ s},\ A_d \approx 4.91 \text{ mm}^2,\\
T_{\text{init}} = 93\,^{\circ}\text{C}: &\quad t_d \approx 0.00167 \text{ s},\ A_d \approx 5.40 \text{ mm}^2,\\
T_{\text{init}} = 95\,^{\circ}\text{C}: &\quad t_d \approx 0.00200 \text{ s},\ A_d \approx 5.86 \text{ mm}^2.
\end{aligned}
$$

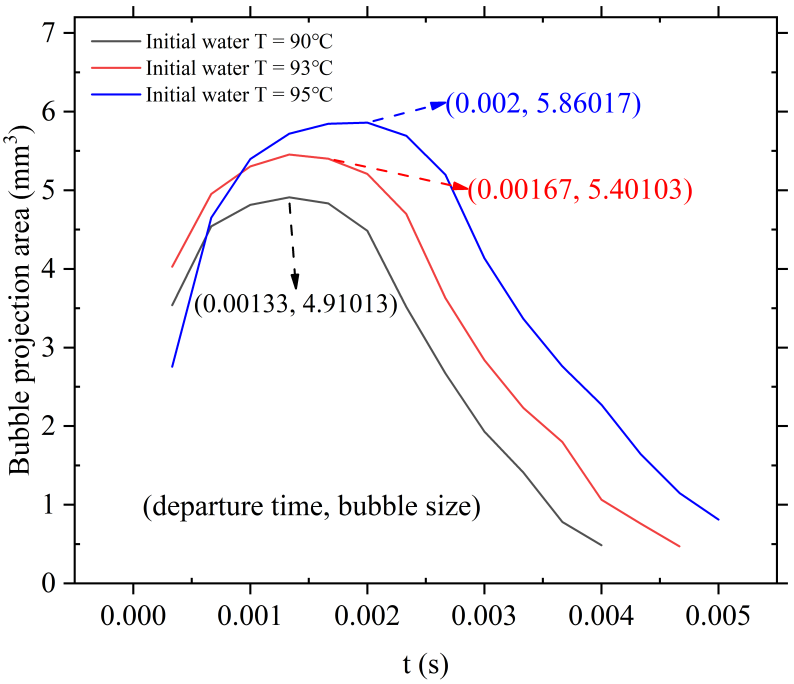

FIG. 5.8: Time evolution of bubble projection area at different initial liquid temperatures (90°C, 93°C, and 95°C). The markers indicate the departure time t_d and the corresponding area A_d for each case. Higher temperatures result in larger maximum areas due to reduced subcooling.

Both t_d and A_d increase monotonically with T_{init}, i.e. with decreasing subcooling. Relative to 90 ℃, the detachment time increases by about +25.6% (93 ℃) and +50.4% (95 ℃), while the corresponding departure area increases by about +10.0% and +19.4%, respectively. This trend is consistent with the physical picture that weaker subcooling reduces condensation losses prior to departure, allowing the bubble to grow larger and persist longer before necking and lift-off [135, 136]. This

extracted departure metrics (t_d, A_d) provide quantitative benchmarks for subsequent comparison.

5.4.2 Variation of Maximum Horizontal and Vertical Diameters

Fig. 5.9 presents the temporal evolution of the maximum horizontal diameter (D_x) and vertical diameter (D_y) of a bubble during a complete departure cycle. In the early nucleation stage, the bubble exhibits a flattened shape with $D_x > D_y$. As the bubble grows and buoyancy increases, the vertical dimension expands rapidly, eventually causing D_y to surpass D_x. This reflects the elongation of the bubble during the rising and detachment process.

A separate examination of the horizontal diameter (D_x) reveals a clear growth pattern: an initial rapid expansion followed by a gradual decrease. This trend corresponds to the different stages of the bubble lifecycle — rapid expansion immediately after nucleation, quasi-isothermal growth, detachment from the surface, and subsequent condensation leading to collapse. The dominant physical mechanisms shift from heat conduction and phase change during early growth, to thermal equilibrium and dissipation during the post-detachment phase under subcooled liquid conditions. These observations provide further insight into the evolution of bubble morphology and dynamic surface tension characteristics throughout the boiling cycle.

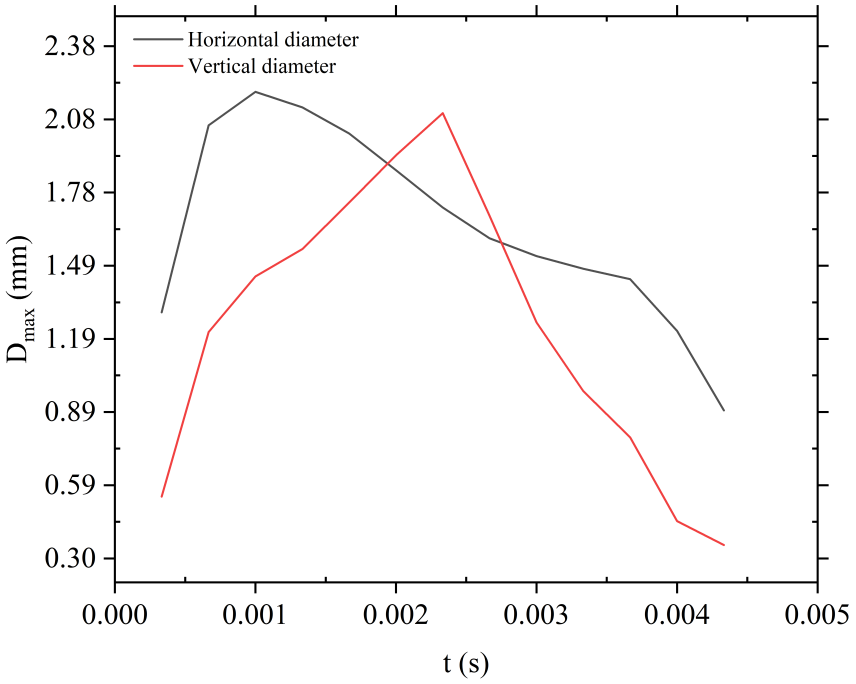

FIG. 5.9: Time evolution of the maximum horizontal and vertical bubble diameters during a single growth-departure cycle. The bubble shape transitions from oblate to elongated as vertical stretching dominates near departure.

5.4.3 Evolution of Bubble Ovality

Fig. 5.10 illustrates the temporal variation of bubble ovality, defined as the ratio of the horizontal to vertical diameters (D_x/D_y), under different initial liquid temperatures. The experimental results show that at lower initial temperatures (e.g., 90°C), the bubble exhibits a higher ovality, indicating a more flattened shape. In contrast, as the liquid temperature approaches saturation (e.g., 95°C), the bubble tends to become more spherical, resulting in a lower ovality value.

This trend highlights the influence of subcooling on bubble deformation behavior. Under high subcooling conditions (i.e., lower liquid temperatures), limited local heat transfer restricts vertical bubble growth while promoting horizontal expansion, leading to more oblate bubble shapes. As the degree of subcooling decreases, the thermal environment becomes more favorable for isotropic growth, thereby reducing bubble asymmetry.

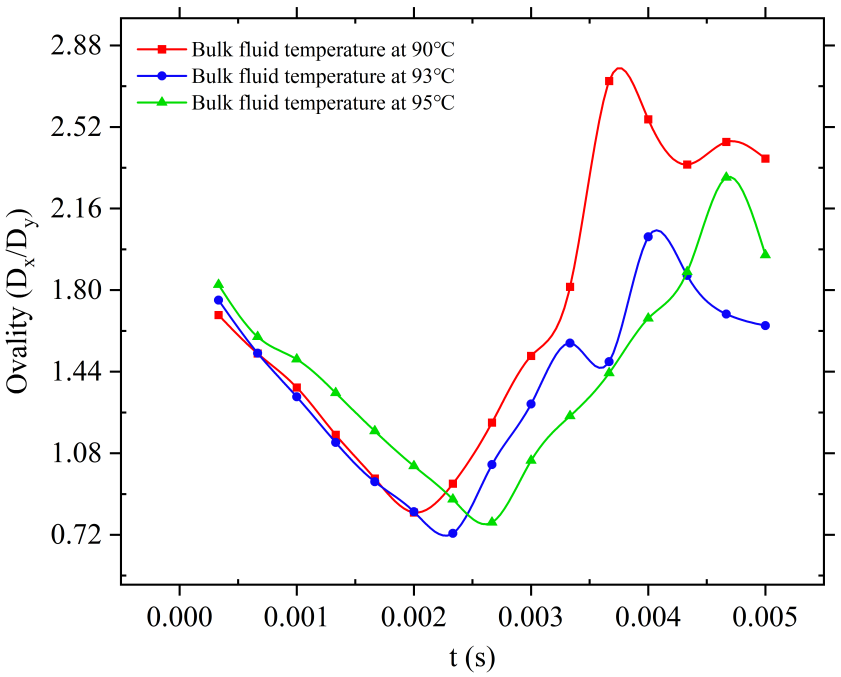

FIG. 5.10: Bubble ovality (D_x/D_y) under different initial liquid temperatures.

5.4.4 Evolution of the lowest bubble point

Fig. 5.11 shows the temporal evolution of the lowest bubble point, i.e., the minimum vertical position of the vapor–liquid interface ($z_{\min}$), for different initial liquid temperatures. This parameter is particularly useful for identifying the moment of bubble detachment from the heated surface. As illustrated in the figure, the sudden upward jump in $z_{\min}$ corresponds to the instant of bubble departure, when the bubble loses its contact with the heater due to the combined effects of buoyancy and surface tension imbalance.

It is observed that with increasing subcooling (lower initial liquid temperature), the bubble departs earlier, and the upward displacement of the lowest bubble point becomes smaller. This indicates that bubbles in more subcooled liquids detach at a smaller size and with a reduced departure height. Such behavior can be attributed to enhanced condensation and stronger liquid shear in highly subcooled environments, which promote detachment before significant bubble growth occurs. Therefore, the evolution of the lowest bubble point provides a clear indication of the bubble departure dynamics under different thermal conditions.

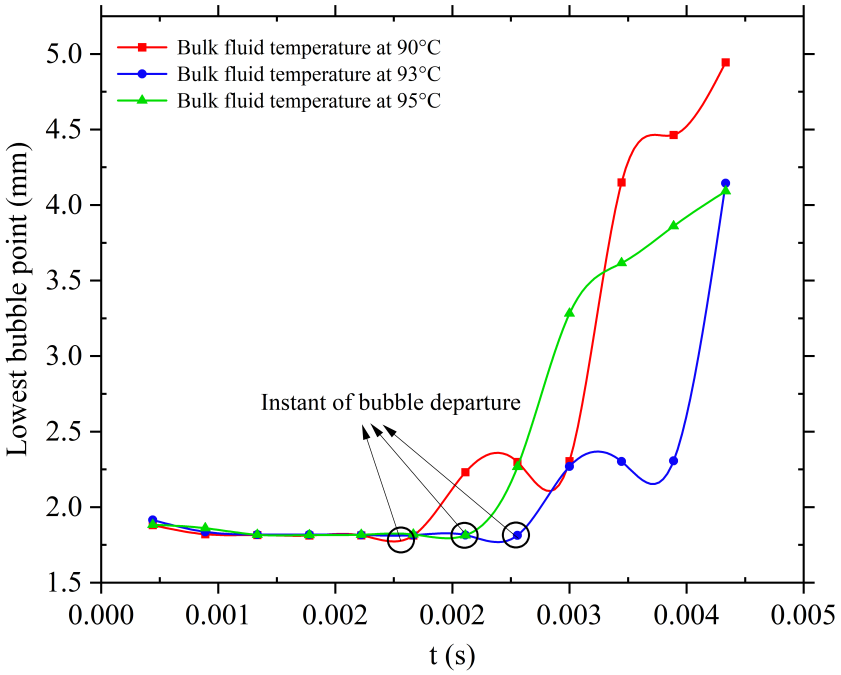

FIG. 5.11: Temporal evolution of the lowest bubble point at different initial liquid temperatures, highlighting the instant of bubble departure.

5.4.5 Evolution of the Bubble Center Position

Fig. 5.12 illustrates the temporal evolution of the bubble center position at an initial liquid temperature of 90°C. The plotted trajectory shows the bubble motion in the x–z plane, where the z-axis denotes the vertical direction opposing gravity and the x-axis represents the horizontal displacement. It can be observed that the bubble ascends predominantly along the z-axis with only minor lateral excursions in the x-direction, indicating that the surrounding liquid environment remained relatively quiescent during the experiment without significant transverse disturbances.

As the bubble detaches from the heated surface and subsequently condenses, slight lateral oscillations emerge in its trajectory. This phenomenon can be attributed to local flow disturbances induced by the collapse of preceding bubbles, which in turn perturb the rising motion of subsequent bubbles. Such trajectory tracking provides valuable insights into convective interactions and the role of the surrounding flow field in governing bubble dynamics during the departure and condensation phases.

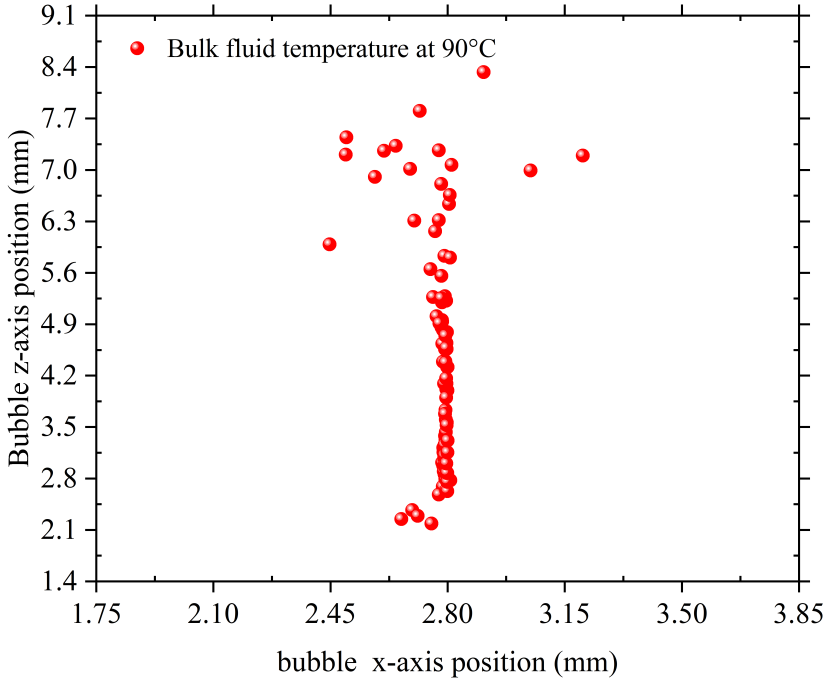

FIG. 5.12: Bubble trajectory at an initial water temperature of 90°C (x–z projection).

The above analyses demonstrate that the implemented image recognition algorithm not only captures the geometric contour of the bubble with high precision, but also enables detailed quantification of its dynamic characteristics across different thermal conditions. These measurable parameters—such as projection area, maximum diameters, shape ratio, nucleation point, and center trajectory—reveal the nuanced effects of subcooling on bubble behavior and provide a robust experimental foundation for subsequent theoretical modeling and numerical validation.

5.5 Experimental comparative analysis of numerical results

To strengthen the connection between the experimental measurements and the numerical simulations presented in the previous chapters, this section establishes a comparative framework. The primary aim is to validate the predictive capability of the LBM model against experimental evidence and classical theoretical correlations. By doing so, I intend to show that the model captures the essential physical mechanisms governing bubble nucleation, growth, and detachment, which

in turn demonstrates its reliability for investigating boiling phenomena in more complex configurations. Moreover, this comparative analysis also provides a basis for assessing state-of-the-art boiling models and closure laws typically used in CFD simulations. Hence, the results presented here should not be viewed solely as a direct comparison, but rather as a validation step that consolidates the role of the LBM framework within the broader landscape of boiling heat transfer modeling.

5.5.1 Relationship between departure diameter and frequency

This subsequent subsections detail specific relationships of interest, beginning with the departure diameter–frequency correlation. To investigate the relationship between bubble departure frequency f and departure diameter D, I conducted a comparative analysis using experimental measurements, LBM simulations, and theoretical correlations. Our objective is to assess the consistency of observed trends with well-established scaling laws.

A classical force-balance model for bubble departure diameter was proposed by Zeng et al. [137], which laid the foundation for subsequent scaling formulations. Building on this framework, Zhang et al. [138] developed a unified scaling model that consolidates diverse experimental datasets and theoretical correlations into a single curve. Their analysis identified two limiting mechanisms governing bubble detachment: the rewetting-dominated regime and the thermal diffusion-dominated regime. These yield the following characteristic scaling laws:

$$f \propto C_1 g^{1/2} D^{-1/2} \quad \text{(rewetting dominated)} \tag{5.1}$$

$$f \propto C_2 D^{-2} \quad \text{(thermal diffusion dominated)} \tag{5.2}$$

where C_1 and C_2 are constants determined by the thermal properties of the wall and the working fluid. To unify data across different conditions, Zhang et al. introduced reduced forms of frequency and diameter, expressed as:

$$f^* = f \left(\frac{\sigma}{g\,\Delta\rho\,D^3} \right)^{1/2}, \qquad D^* = D \left(\frac{g\,\Delta\rho}{\sigma} \right)^{1/2}, \tag{5.3}$$

where σ is the surface tension, g the gravitational acceleration, and $\Delta\rho = \rho_l - \rho_v$ the density difference between liquid and vapor. This normalization collapses frequency–diameter data from various fluids and operating conditions onto a single curve bounded by the two theoretical limits, as shown in Fig. 5.13.

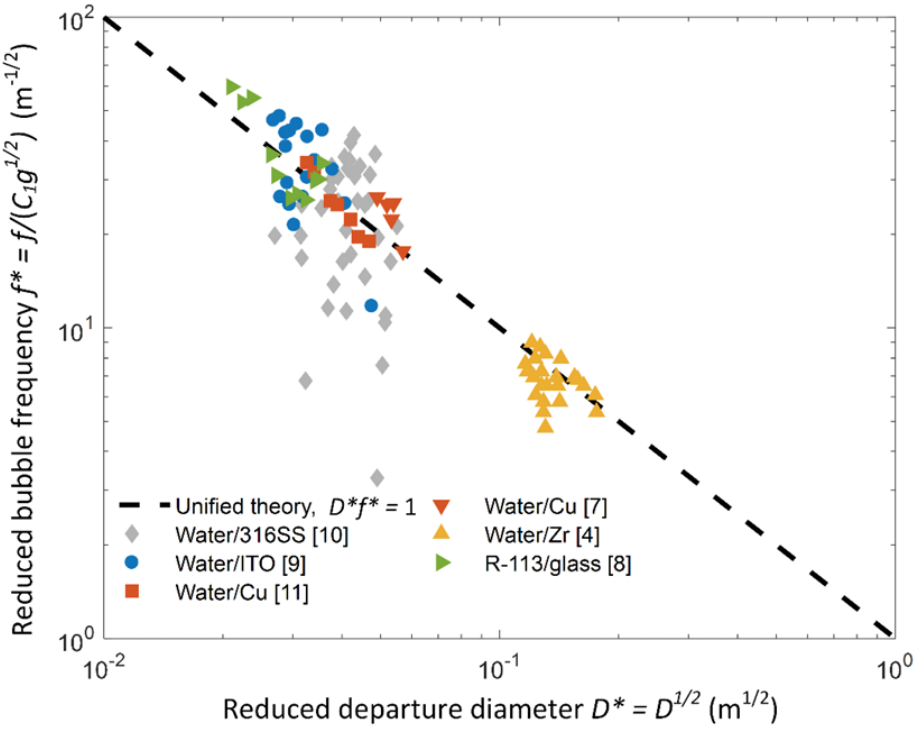

FIG. 5.13: Unified scaling proposed by Zhang et al. [4], showing experimental datasets collapsed into a universal trend in dimensionless coordinates.

To ensure consistency between experimental and numerical datasets, the Eötvös number $Eo = \Delta\rho g D^2/\sigma$ was kept identical in both cases, thereby guaranteeing comparable buoyancy-to-surface-tension ratios governing bubble detachment.

In our experiments, we measured the bubble departure diameter and frequency under varying heating conditions. As illustrated in Fig. 5.14, a power-law fit to the experimental data yields the following:

$$f = 0.112 \cdot D^{-1.11} \tag{5.4}$$

This exponent lies between the two limiting values of –0.5 and –2.0, supporting the physical validity of our measurements and indicating a mixed control mechanism involving both wall rewetting and thermal recovery.

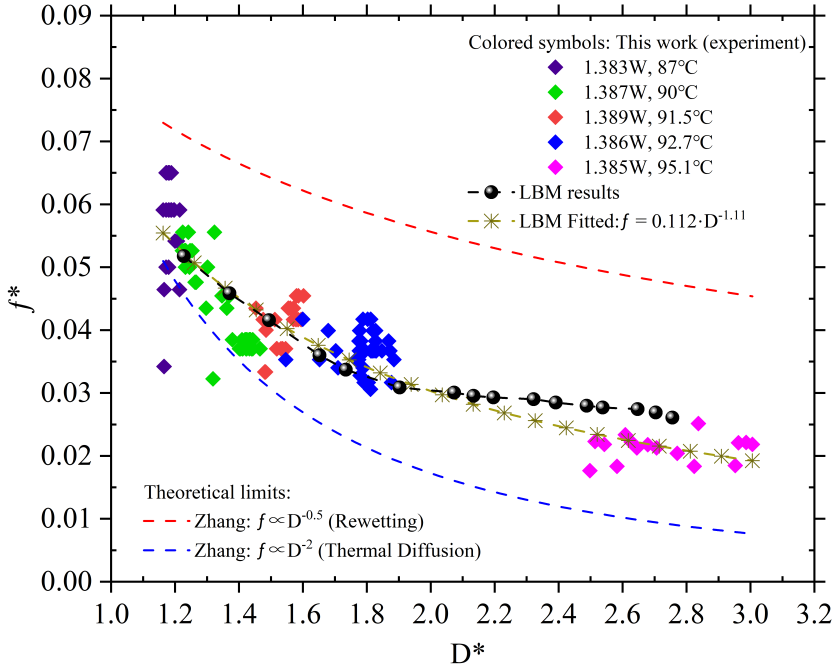

FIG. 5.14: Experimental and LBM results of bubble departure frequency f versus departure diameter D. The fitted power law $f = 0.112D^{-1.11}$ lies between the two theoretical bounds.

In order to establish the credibility of the present LBM approach, its predictions were systematically compared with several classical empirical correlations, namely those of Jakob [139], Zuber [140], Cole [141], and Mikic & Rohsenow [142], which represent the foundational models for characterizing bubble departure frequency and diameter in nucleate boiling. Fig. 5.15 shows that the dimensionless frequency f^* decreases monotonically with increasing reduced diameter D^*, in agreement with both theoretical expectations and experimental observations. While some deviations in magnitude are observed, especially at small scales, the overall trends confirm the inverse correlation between detachment frequency and bubble size.

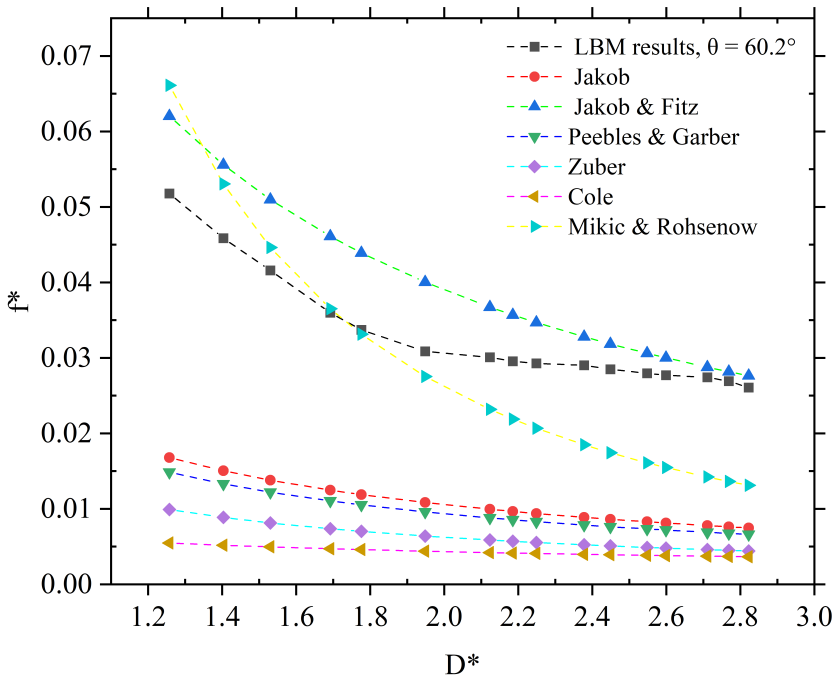

FIG. 5.15: Comparison of dimensionless bubble frequency f^* versus diameter D^* between LBM results and classical theoretical models.

In conclusion, our results, both experimental and numerical, are consistent with the unified model of Zhang et al. and reinforce the hypothesis that bubble departure frequency is primarily governed by the interplay between rewetting dynamics and thermal diffusion at the heated surface.

5.5.2 Comparison of Dimensionless Departure Diameter D^* Based on Ja · Nu

To directly compare our numerical and experimental results on bubble departure diameter, we introduce a dimensionless variable constructed from the product of the Jacob number (Ja) and the Nusselt number (Nu), denoted as Ja · Nu. This approach was motivated by a practical limitation in the experiment: the exact surface temperature of the ITO heating layer could not be reliably measured. As a result, conventional computation of Ja based on wall superheat was not feasible.

To circumvent this, we reformulated the Jacob number using the relation:

$$\mathrm{Ja} \cdot \mathrm{Nu} = \frac{c_p \cdot q'' \cdot L}{\lambda \cdot h_{LV}} \tag{5.5}$$

where q'' is the heat flux, λ is thermal conductivity, and h_{LV} is the latent heat of vaporization. This formulation provides a consistent thermal driving force for both the LBM simulations and the experiments.

Moreover, due to the significant discrepancy in the liquid-vapor density ratio between experiments and LBM (approximately 2044 vs. 17.1), direct comparison in dimensional space would be physically inconsistent. To address this, dimensionless scaling was applied, including normalization of the departure diameter as D^* and matching of Eötvös numbers ($Eo_{\text{exp}} \approx Eo_{\text{LBM}}$) and thermal driving forces ($Ja_{\text{exp}} \approx Ja_{\text{LBM}}$).

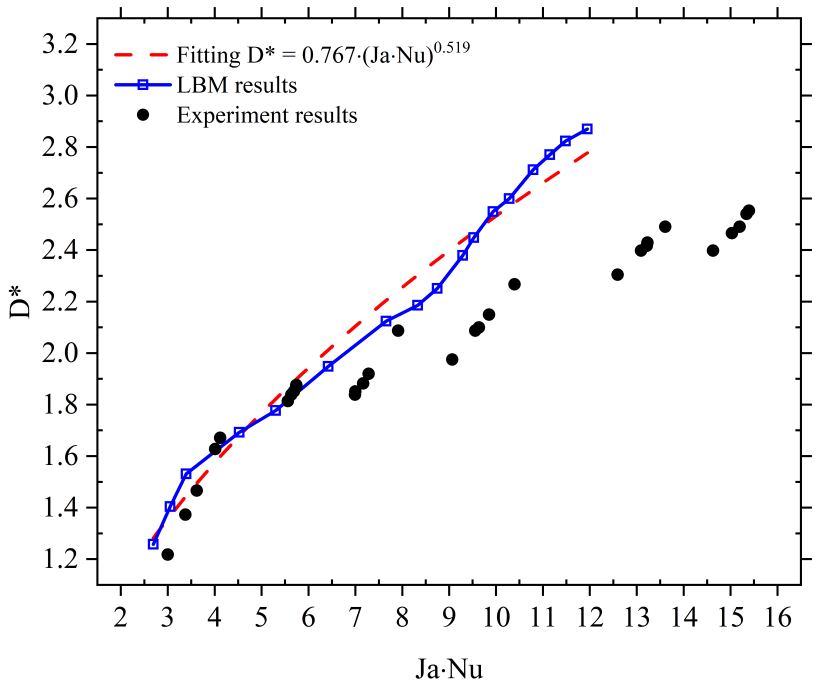

FIG. 5.16: Comparison of dimensionless departure diameter D^* as a function of $\text{Ja} \cdot \text{Nu}$ between LBM results and experiments.

As shown in Fig. 5.16, the comparison reveals strong agreement between the experimental and LBM results. Both datasets follow a consistent increasing trend of departure diameter with increasing $\text{Ja} \cdot \text{Nu}$, reflecting enhanced thermal forcing. The fitted power-law curve,

$$D^* = 0.767 \cdot (\text{Ja} \cdot \text{Nu})^{0.519} \tag{5.6}$$

shows excellent alignment with the numerical and experimental data, confirming the robustness of the dimensionless formulation and validating the physical similarity between the two approaches.

It is worth noting that certain discrepancies emerge between the numerical and experimental results at higher values of $\mathrm{Ja} \cdot \mathrm{Nu}$. Several factors may contribute to these deviations. First, the pseudopotential LBM employed in this study is limited by the relatively low liquid-to-vapor density ratio ($\rho_l/\rho_v \approx 17.1$) compared to the experimental value (~ 2000), which can lead to an underestimation of inertia-driven bubble departure at elevated heat fluxes. In addition, the diffuse interface treatment in the model tends to smooth the vapor liquid boundary, thereby reducing sharp interfacial dynamics observed in experiments.

It is also important to note that experimental subcooling conditions may further contribute to the discrepancies at larger bubble diameters. In a subcooled liquid environment, the enhanced condensation at the bubble–liquid interface reduces vapor retention and promotes earlier collapse or shrinkage after detachment. This effect can suppress the maximum departure diameter observed in experiments compared to the saturated boiling simulations, where no additional condensation sink is present. Hence, both numerical limitations and experimental subcooling jointly explain the deviations at elevated thermal loads.

Second, experimental uncertainties must be considered, particularly the fact that the true wall temperature of the ITO heating surface cannot be measured directly. While the use of the $\mathrm{Ja} \cdot \mathrm{Nu}$ criterion provides a consistent basis for comparison, errors may be amplified at higher heat flux conditions. Furthermore, in experiments, bubble–bubble interactions and localized heating inhomogeneities may accelerate the onset of detachment, whereas the simulation is restricted to an idealized single-bubble configuration.

Finally, it is possible that the system approaches the transition to film boiling at high $\mathrm{Ja} \cdot \mathrm{Nu}$, a regime that lies beyond the current modeling framework. From my point of view, these above considerations explain the increasing divergence between experimental observations and numerical predictions in the high thermal load regime.

5.5.3 Comparison of departure frequency f^* Based on $\mathrm{Ja} \cdot \mathrm{Nu}$

In addition to departure diameter, the departure frequency of bubbles is a critical parameter for evaluating phase-change dynamics under varying thermal conditions

and surface properties. Due to the same challenge in measuring the exact heating surface temperature in experiments, we adopt a consistent dimensionless formulation using the product $\mathrm{Ja} \cdot \mathrm{Nu}$ as the scaling group. This allows direct comparison between simulation and experimental results, even under differing density ratios and thermal properties.

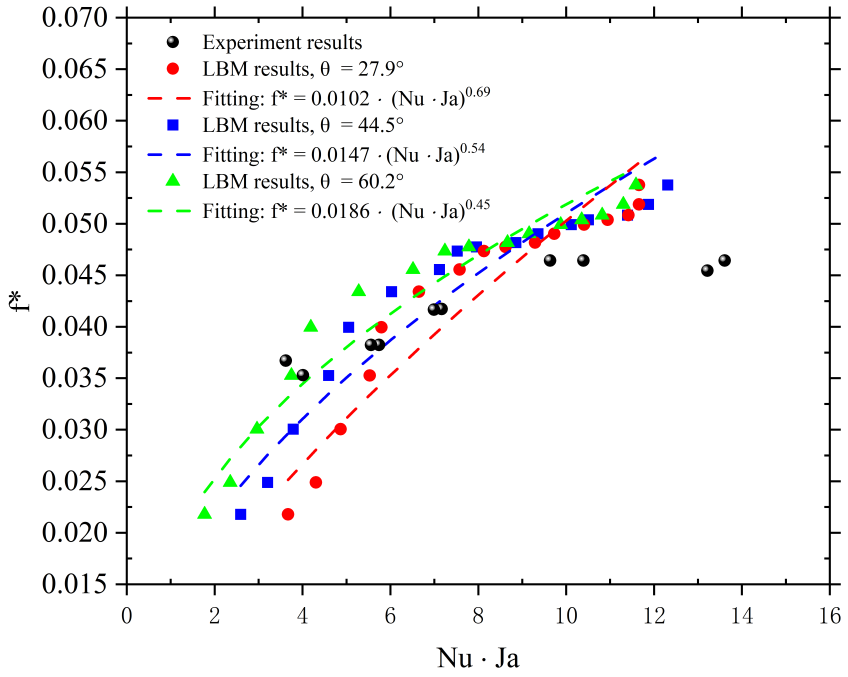

FIG. 5.17: Comparison of dimensionless bubble departure frequency f^* as a function of $\mathrm{Ja} \cdot \mathrm{Nu}$ across different contact angles in LBM simulations and experiments.

Fig. 5.17 shows the relationship between the dimensionless departure frequency f^* and $\mathrm{Ja} \cdot \mathrm{Nu}$ across various contact angles. LBM simulations with three distinct wettability conditions (contact angles of 27.9°, 44.5°, and 60.2°) are compared against experimental data. All datasets exhibit a monotonic increase in f^* with increasing $\mathrm{Ja} \cdot \mathrm{Nu}$, which reflects stronger thermal driving leading to more frequent bubble departure events.

Power-law fits of the form:

$$f^* = a \cdot (\mathrm{Ja} \cdot \mathrm{Nu})^b \tag{5.7}$$

were applied to each wettability case. The fitted exponents range from 0.45 to 0.69, capturing the variation in surface wettability and its influence on bubble

dynamics. The LBM results demonstrate consistent agreement with the experimental trendlines, validating the model's ability to predict departure frequency under combined thermal and interfacial conditions.

To ensure physical comparability, the LBM simulations were configured to match key thermophysical parameters such as the Eötvös number, Jacob number, and surface tension ratio, as listed in Table 5.1. Despite inherent limitations in replicating the exact density ratio of the experimental system, this matching strategy ensures that the dominant driving forces are appropriately scaled.

TABLE 5.1: Thermophysical properties used in experiments and LBM simulations for dimensional consistency.

Quantity	Experiment	LBM
Temperature T	366.15 K (93°C)	0.86 T_c
Pressure P	0.078568 MPa	0.0894
Liquid density ρ_l	963.26 kg/m^3	6.489
Vapor density ρ_v	0.47111 kg/m^3	0.3796
Density ratio ρ_l/ρ_v	2044	17.1
Latent heat h_{LV}	2274.73 kJ/kg	0.5472
Specific heat c_p	4.2082 kJ/kg·K	6
Surface tension σ	0.06025 N/m	0.4579

These results confirm that the LBM framework can reliably capture the frequency behavior of bubble detachment across a range of thermal loads and wettability conditions.

5.6 Summary of this chapter

This chapter presented a comprehensive investigation of single-bubble dynamics under controlled thermal conditions by combining high-speed experimental imaging with lattice Boltzmann simulations. A dedicated image recognition algorithm was developed to extract quantitative bubble features such as projection area, maximum diameter, shape ratio, nucleation site, and centroid trajectory, thereby enabling detailed characterization of bubble growth, detachment, and condensation.

A key distinction lies in the thermal boundary conditions: the experiments were conducted under subcooled boiling due to the open configuration of the setup, whereas the simulations assumed saturated boiling states using the pseudo-potential LBM framework. To reconcile these differences, the $\mathrm{Ja} \cdot \mathrm{Nu}$ similarity criterion was introduced as a bridging parameter, ensuring that both approaches can be compared within a consistent physical framework. This treatment highlights the complementary roles of experiments (capturing realistic thermal effects such as subcooling) and simulations (isolating fundamental dynamics under idealized conditions).

The comparative results demonstrate that subcooling in experiments leads to reduced bubble size, higher departure frequency, and rapid post-detachment condensation, while the LBM simulations under saturation reproduce the essential nucleation–growth–detachment sequence with good agreement in scaling trends. Despite quantitative deviations at higher thermal loads—primarily due to density ratio limitations and diffuse interface effects in the model—the consistency in overall dynamics validates the predictive capability of the implemented LBM framework.

Taken together, these findings confirm that the LBM model faithfully captures the key physical mechanisms of boiling at the mesoscale and can therefore be extended to investigate more complex configurations beyond the single-bubble case. Moreover, the validated framework provides a valuable basis for assessing and refining closure laws commonly employed in state-of-the-art CFD boiling models, thereby bridging mesoscopic simulation insights with macroscopic predictive tools. This connection will be further elaborated in the subsequent chapters.

Chapter 6

Comparison: LBM Results with state of the art models

In this chapter, I provide a systematic comparison between the LBM simulation results and state-of-the-art correlations as well as the force-balance model. It should be emphasized at the outset that all comparisons are carried out in a dimensionless framework, ensuring that the observed discrepancies directly reflect the underlying bubble dynamics rather than artifacts of unit selection.

The structure of this chapter is as follows. Section 6.1 extracts and analyzes key dynamic parameters, including the initial bubble diameter, departure diameter, and departure frequency. In Section 6.2, the dimensionless departure diameter D^* and departure frequency f^* are compared against multiple correlations to evaluate their applicability under varying Jakob numbers (Ja) and wettability conditions. Sections 6.3 – 6.5 then focus on a diagnostic assessment of the force-balance model, revealing the systematic underestimation of unsteady drag (F_{du}) due to the assumption of a fixed contact diameter (d_w), and introducing a $Ja-dependent$ dynamic contact diameter model. Finally, Section 6.6 investigates the influence of contact angle on bubble departure and proposes a nonlinear correlation that accounts for the combined effects of both Ja and θ.

6.1 Key Bubble Dynamic Parameters

In boiling heat transfer, the bubble diameter d^* (initial D^*_{int} and departure D^*) and departure frequency (f^*) are recognized as the key descriptors of bubble dynamics, as they directly govern the associated heat transfer performance. These quantities also constitute the fundamental parameters in numerical simulations, experiments, and theoretical modeling—for instance, in CFD models, their simultaneous consideration is essential for achieving closure.

This subsection presents a preliminary LBM-based analysis of the dependence of these parameters on the Ja, providing the groundwork for the subsequent discussion on theoretical correlations and force-balance models. In addition, for clarity and subsequent comparisons, the Ja range is divided into three regimes:

Low-Ja regime ($Ja < 0.2$)
Moderate-Ja regime ($0.2 < Ja < 0.38$)
High-Ja regime ($Ja > 0.38$)

6.1.1 Initial bubble diameter

The initial bubble diameter, D_{init}, refers to the observable size of a vapor bubble at the moment it nucleates on the heated surface. Unlike the departure diameter, which is determined by the balance of forces at the point of detachment, D_{init} is more sensitive to local thermophysical properties and nucleation conditions, such as superheat level, wettability, and heat conduction near the wall.

Fig. 6.1 shows the variation of the dimensionless initial diameter D^*_{init} with Ja as obtained from LBM simulations. At lower $Ja < 0.25$, D^*_{init} remains nearly constant, suggesting that the thermal driving force is insufficient to significantly influence the initial bubble growth. Beyond this threshold, a rapid nonlinear increase is observed, this trend suggests that higher superheat levels strongly enhance the vaporization process and the associated bubble expansion during the initial growth stage. This transition reflects the shift from thermally constrained to thermally activated bubble formation regimes.

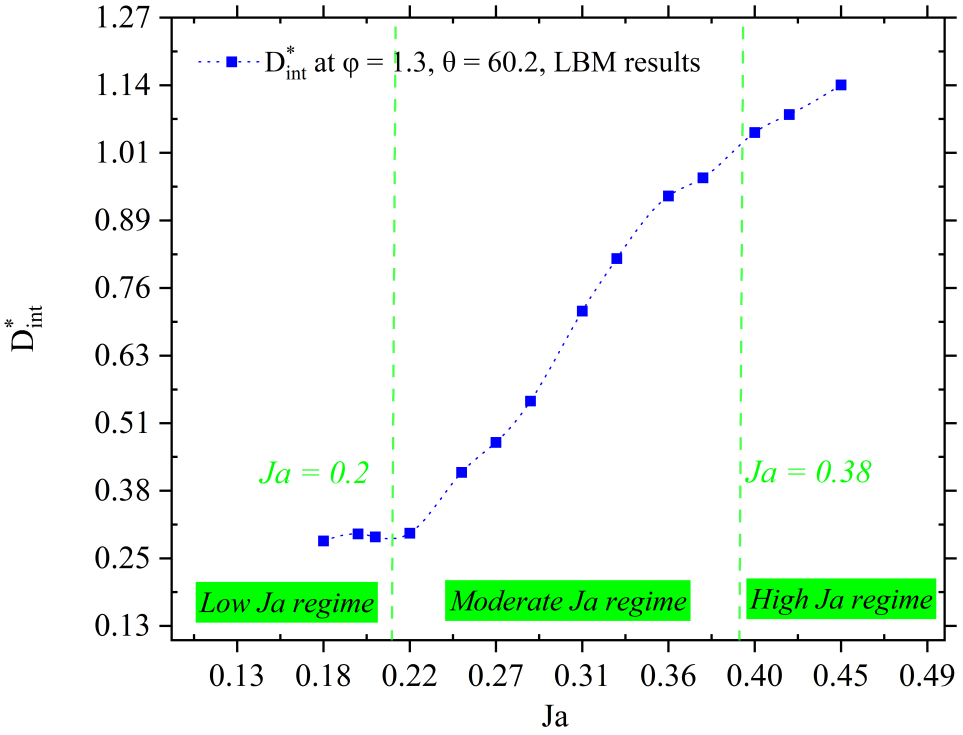

FIG. 6.1: Apperent Initial bubble diameter under different Ja

6.1.2 Bubble departure diameter

The bubble departure diameter, D^*, defines the equivalent size of a vapor bubble at detachment [143] and is widely used to characterize local boiling intensity.

Fig. 6.2 illustrates the dependence of the bubble departure diameter D^* on the Ja under different contact angle conditions ($\varphi = 1.3, \varphi = 1.5, \varphi = 1.7$) obtained form the LBM calculations. Overall, D^* increases monotonically with increasing Ja, highlighting the dominant role of thermal driving forces in bubble detachment. This trend was validated by the experiments shown in Chapter 5.

Specifically: At low-Ja regime: D^* increases rapidly with Ja, and the influence of wettability (contact angle θ) is pronounced, indicating that surface conditions strongly govern bubble dynamics in this regime.

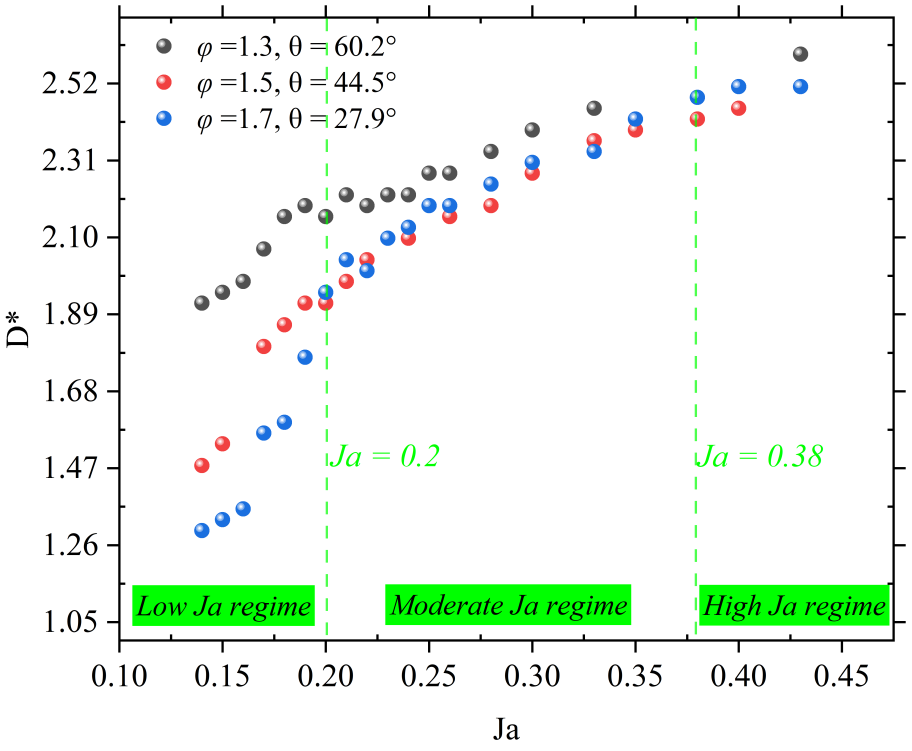

FIG. 6.2: Variation of dimensionless bubble detachment diameter with Ja

At Moderate-Ja regime: The growth rate of D^* slows down, while the impact of wettability diminishes and thermal effects become increasingly dominant.
At High-Ja regime: D^* approaches a saturation trend, with results under different contact angles converging, suggesting that superheat (Ja) becomes the primary factor controlling bubble departure diameter.

These observations reveal the coupled dependence of bubble departure diameter on both superheat and wettability, and provide the physical basis for the systematic comparison with theoretical models in the following sections.

6.1.3 Bubble departure frequency

The bubble departure frequency (f) characterizes how often phase-change events occur at the heated wall and plays a crucial role in determining boiling efficiency. A higher frequency implies more frequent vapor removal and liquid replenishment, thereby enhancing heat transfer. Fig. 6.8 presents the variation of the dimensionless departure frequency, defined as $f^* = f/f_c$, with respect to the Ja, where the

characteristic frequency is given by $f_c = \sqrt{g/\ell_c}$ obtained from the LBM calculations.

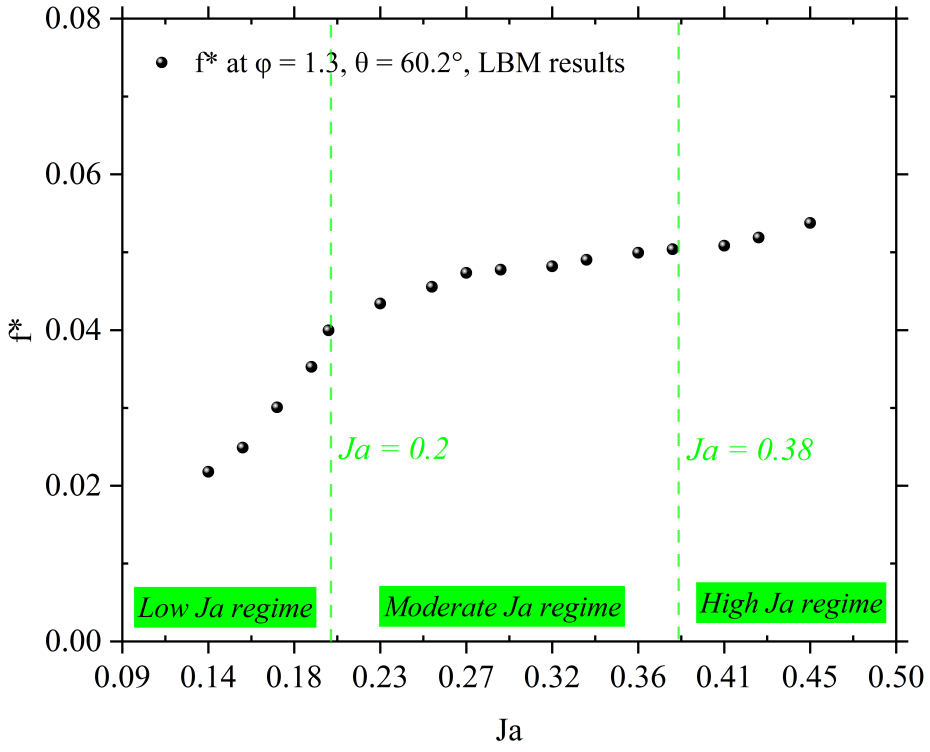

FIG. 6.3: Variation of the departure frequency with Ja

The LBM results exhibit a smooth and monotonic increase in f^* with increasing Ja, indicating that higher superheat leads to more frequent bubble departure. This behavior is consistent with enhanced vapor generation and reduced nucleation delay time under stronger thermal driving forces. In the low-Ja regime ($Ja < 0.2$): the departure frequency increases sharply, reflecting the strong sensitivity of nucleation and detachment to thermal activation and is validated by the experiemental data shown in Chapter5.

In the moderate-Ja regime ($0.2 < Ja < 0.38$): the numerical results indicate that the growth of f^* slows down. My conjecture is that, in this regime, the bubble dynamics are not solely governed by thermal driving forces but are also significantly influenced by inertia. This inertial contribution may even be amplified, leading to a form of dynamic balance between thermal and inertial effects—a hypothesis that will be further examined in the subsequent force-balance analysis.

In the high-Ja regime ($Ja > 0.38$), the LBM results suggest a weakly increasing trend of the dimensionless departure frequency f^*. This observation should, however, be interpreted with caution. While the numerical model indicates continued sensitivity of bubble dynamics to superheating, it does not capture practical boiling limits such as the critical heat flux (CHF), wall dryout, or material damage. In reality, further superheating beyond this point would likely induce a transition to film boiling or even destruction of the heating surface, conditions under which the concept of bubble departure frequency is no longer meaningful. Therefore, the simulated increase at high Ja primarily reflects the internal consistency of the LBM framework, rather than an experimentally accessible regime.

These results demonstrate that the departure frequency is primarily governed by the superheat level. The monotonic trend captured by LBM emphasizes its capability to resolve the coupling of thermal and inertial effects across different boiling regimes.

6.2 Comparison with Classical Correlations

Departure Diameter (D^*) Comparison

A wide range of correlations exist [113, 144] for predicting bubble departure diameter (Fritz, Cole, RPI, Gorenflo, etc.). For this study, we select representative static and dynamic models to benchmark against our LBM results.

For clarity, we here distinguish between static and dynamic models. Static (quasi-static) models assume a force balance at the instant of bubble departure, typically between buoyancy and surface tension, without explicitly accounting for bubble growth dynamics or transient heat transfer. In contrast, dynamic models incorporate the time-dependent evolution of the bubble, considering either inertial effects during bubble growth and detachment or thermal diffusion as the controlling mechanism. In addition, purely empirical correlations derived from regression of experimental data are listed separately as a fourth category. Table 6.3 summarizes representative models under these categories.

Table 6.2 summarizes the principal correlations for bubble departure diameter. Since many of these correlations were originally derived from experimental data,

Table 6.1: Comparison of Bubble Departure Diameter Models by Mechanism

Mechanism Type	**Representative Models**	**Main Characteristics**	**Applicability & Limitations**
Static	Fritz, Cole & Rohsenow, RPI	Balance between buoyancy and surface tension;	Suitable for low Ja; ignores inertia and heat transfer effects
Inertia-dominated	Cole Dynamic, Ruckenstein	Considers growth acceleration and detachment inertia;	Better at medium/high Ja; sensitive to initial/boundary conditions
Thermal-diffusion controlled	Van Stralen, Zwick, Golorin	Bubble growth driven by heat conduction and Ja; includes thermal diffusivity α	Valid for high Ja with strong thermal gradients; less accurate under turbulence
Empirical/fitting-based	Kim, Gorenflo, Kocamustafaogullari	Regression from large data sets; includes Ja, density ratio, σ, etc.	Accurate within fitting range; weak physical interpretability, limited generality

their applicability is inherently limited by the ranges and conditions of the underlying experiments. Consequently, while they provide valuable guidance, their assumptions and validation ranges must be carefully considered when applied to broader or different boiling regimes.

TABLE 6.2: Summary of bubble departure diameter correlations

Model	**Type**	**Considered Parameters**	**Experimental Basis**
Fritz (1935)	Static	σ, g, $(\rho_l - \rho_v)$, θ	Yes; water/mixtures; saturation boiling
Kocamustafaogullari & Ishii (1983)	Static	σ, g, $(\rho_l - \rho_v)$	Yes; pool boiling; saturation
Gorenflo et al. (1986)	Dynamic	σ, Ja, μ	Yes; water/mixtures
Ruckenstein (1961)	Dynamic	thermal diffusion, Ja	No; theoretical model
Van Stralen & Zijl (1978)	Dynamic	Pr, α	Yes but water only; pool boiling
Cole & Rohsenow (1969)	Dynamic	inertia, ΔT_w	Yes; pool boiling
Golorin (1978)	Dynamic	thermal–inertial mix	Yes; empirical fitting
Kim et al. (2006)	Dynamic	Ja–coupled inertia/thermal	Yes but water only; empirical model
RPI closure (1976)	Semi-theoretical	Ja, σ, g	No; widely used in CFD tools

Note: Green = experimentally supported; Red = limited or fluid-specific validation

According to the correlations proposed by various models, the departure diameter can generally be expressed in the following form (See ref. [145]):

$$D_{\mathrm{d}} = A \cdot Ja^{B} \cdot \left(\frac{\sigma}{\rho_l - \rho_v} \right)^{C} \tag{6.1}$$

where A, B, and C are constants whose values may vary depending on the specific focus of the study.

TABLE 6.3: Bubble Departure Diameter Models under Different Mechanisms

Model	**Formula**	**Key Parameters**	**Remarks**
Lee et al.	$D_d = \left(50\sqrt{27\,Ja\,\alpha\sqrt{\frac{\rho_l}{\sigma}}}\right)^2$	$Ja, \alpha, \rho_l, \sigma$	Empirical, based on Ja
RPI Model	$D_w = 2\left[\frac{3}{4}\cdot\frac{\sigma}{g(\rho_l-\rho_v)}\cdot(2R_c)\right]^{1/3}$	$\sigma, g, \rho_l, \rho_v$	
	$R_c = \frac{2\sigma T_{sat}}{\rho_v h_{lv}\Delta T_w}$	$T_{sat}, h_{lv}, \Delta T_w$	Based on R_c and ΔT
Fritz Model	$D_d = C\cdot\sqrt{\frac{2\sigma}{g(\rho_l-\rho_v)}}$	$\sigma, g, \rho_l, \rho_v$	Classic quasi-static
Cole	$D_d = C\cdot\ Ja\cdot\sqrt{\frac{2\sigma}{g(\rho_l-\rho_v)}}$	$Ja, \sigma, g, \rho_l, \rho_v$	Adds Ja to Fritz model
Van Stralen & Zijl	$D_d = 2.63\left(\frac{Ja^2\alpha_l^2}{g}\right)^{1/3}\left[1+\left(\frac{2\pi}{3Ja}\right)^{0.5}\right]^{1/4}$	Ja, α_l, g	Based on pulsation theory
Gorenflo	$D_d = c\left(\frac{Ja^4\alpha_l^4}{g}\right)^{1/3}\left[1+\left(\frac{2\pi}{3Ja}\right)^{1/2}\right]^{4/3}$	Ja, α_l, g	Extension of Van Stralen
Ruckenstein	$D_d = \left[\frac{3\pi\rho_l^2\alpha_l^{0.5}(\rho_l-\rho_v)^{0.5}}{\sigma^{3/2}}\right]^{1/2}\cdot Ja^{4/3}\cdot\left[\frac{2\sigma}{g(\rho_l-\rho_v)}\right]^{1/2}$	$Ja, \alpha_l, \sigma, g, \rho_l, \rho_v$	Diffusion considered
Cole & Rohsenow	$D_d = C\cdot Ja^{5/4}\cdot\left[\frac{2\sigma g_c}{g(\rho_l-\rho_v)}\right]^{1/2}$	$Ja, \sigma, \rho_l, \rho_v$	Modified Ja
Golorin	$D_d = \frac{0.0099\sigma}{g(\rho_l-\rho_v)} + \left(\frac{15.6\rho_l}{g(\rho_l-\rho_v)}\right)^{1/3}\cdot(0.6\alpha Ja)$	$\sigma, g, \rho_l, \rho_v, \alpha, Ja$	Surface tension and thermal growth
Kim	$D_d = 0.1649\left(\frac{\sigma}{g(\rho_l-\rho_v)}\right)^{1/2} Ja^{0.7}$	$\sigma, g, \rho_l,\ \rho_v, Ja$	Nonlinear Ja
Kacamasta..i	$D_d = 2.64\times10^{-5}\left(\frac{\sigma}{g(\rho_l-\rho_v)}\right)^{1/2}\left(\frac{\rho_l-\rho_v}{\rho_l}\right)^{0.9}$	$\sigma, g,\ \rho_l, \rho_v$	Density-ratio-based

Fig. 6.4 presents the predictions of different correlations over a range of Jakob numbers, along with the LBM simulation results. To distinguish between model types, color coding is used: red symbols indicate static models, green symbols denote dynamic models, and black symbols represent the RPI closure model. Open symbols correspond to correlations without experimental validation, while solid symbols are derived from experimental datasets. The blue stars represent the LBM numerical results at a contact angle of $\theta = 60.2°$. It is worth noting that among the considered models, the RPI correlation has been singled out (indicated by black symbols in Fig. 6.4) because of its particular importance. Unlike the purely static or dynamic models, the RPI model is one of the most widely adopted closure laws for wall boiling in CFD simulations. Although a more detailed discussion of the RPI model will be provided later, it is highlighted here to emphasize its relevance and to facilitate comparison with both the LBM and experimental results.

It is evident that the LBM-predicted dimensionless departure diameter D^* exhibits a clear increasing trend with Ja, consistent with the overall behavior of most dynamic models, and validated experimentally in this work. However, a comparison with static models (e.g., Fritz [146]) reveals significant deviations.

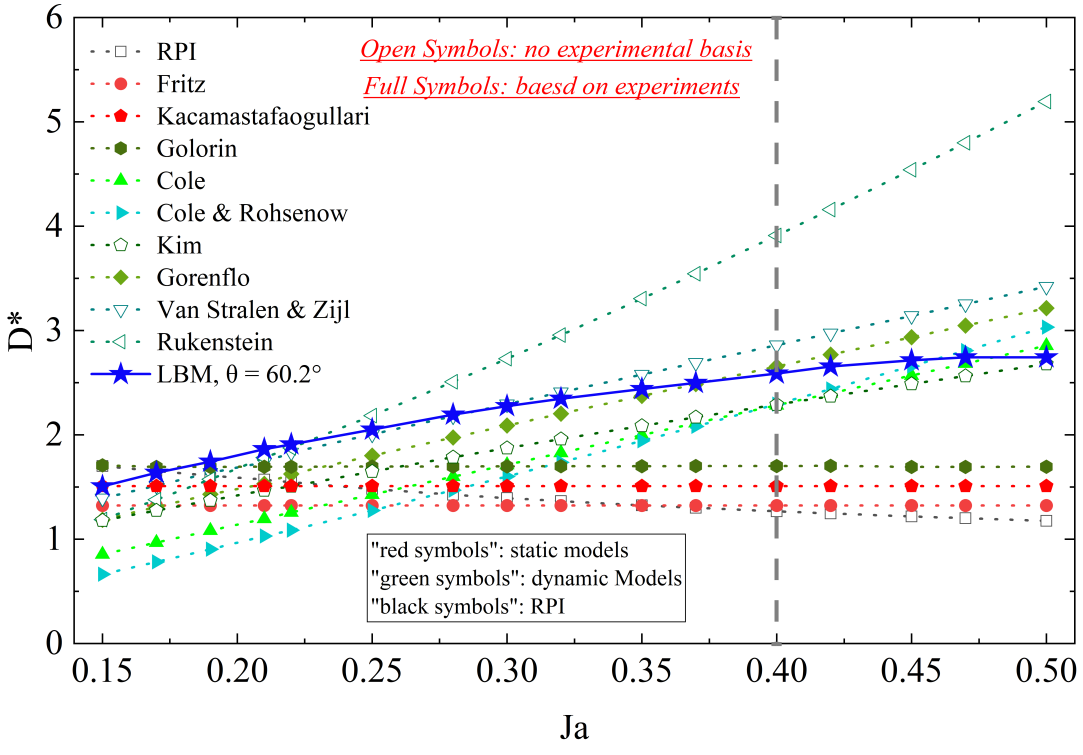

FIG. 6.4: Variation of dimensionless bubble detachment diameter with Ja
Comparison of different theoretical models

Fig. 6.5 further isolates the comparison between LBM results and static models, as well as the RPI model commonly used in conventional CFD. The results indicate that static models predict nearly constant departure diameters, showing insensitivity to thermal driving forces, i.e., independent of the Jakob number. In the low Jakob number regime ($Ja < 0.2$), the static models remain relatively close to the LBM predictions, suggesting that under weak thermal driving the quasi-static force balance is still the dominant mechanism. However, as the Jakob number increases ($Ja > 0.2$), the discrepancy between LBM and static models widens, clearly highlighting their limitations in capturing thermal effects. Therefore, static correlations can be regarded as acceptable for low-superheating conditions but should not be applied when significant thermal driving is present, where dynamic effects become dominant.

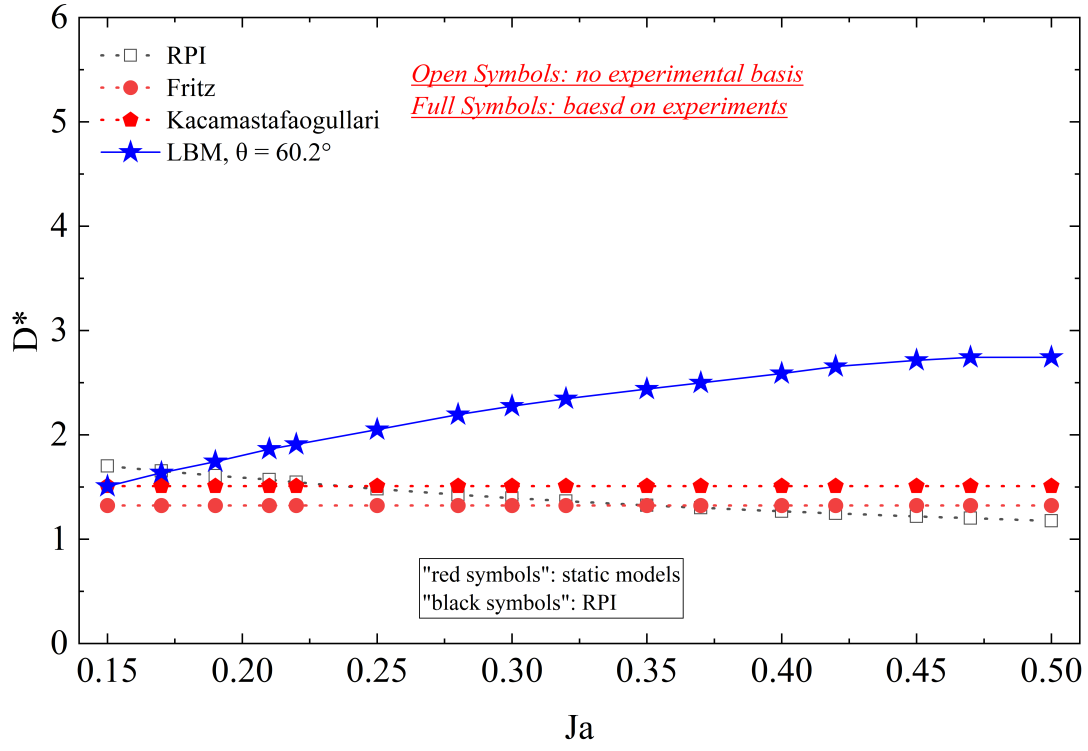

Fig. 6.5: Variation of dimensionless bubble detachment diameter with Ja
Comparison of different theoretical models

It is worth noting that among the theoretical correlations, the RPI closure model is widely implemented in commercial boiling solvers due to its empirical robustness and computational convenience. However, its prediction shows a counterintuitive trend: the dimensionless bubble departure diameter D^* decreases with increasing Jakob number. This contradicts the general understanding that stronger thermal

driving forces (higher Ja) should lead to larger departing bubbles, thereby revealing the limitation of the RPI model in capturing thermal-driven bubble departure dynamics.

To further clarify this behavior, the RPI formulation can be revisited:

$$D_w = 2\left[\frac{3}{4}\cdot\frac{\sigma}{g(\rho_l-\rho_v)}\cdot(2R_c)\right]^{1/3}, \quad R_c = \frac{2\sigma T_{sat}}{\rho_v h_{lv}\Delta T_w}$$

Here, D_w is interpreted as the bubble diameter, while R_c denotes the characteristic radius. In the RPI model, R_c corresponds to the cavity radius at the wall, rather than the equivalent radius of the entire bubble, as illustrated in Fig. 3.2. From the expression, it is clear that R_c is inversely proportional to the wall superheat ΔT_w, while the Jakob number is proportional to ΔT_w:

$$Ja = \frac{c_{p,l}\Delta T_w}{h_{lv}} \quad \Rightarrow \quad \Delta T_w \propto Ja \quad \Rightarrow \quad R_c \propto \frac{1}{Ja}$$

Thus, as the Jakob number increases, R_c decreases, leading to a smaller predicted D_w. Mathematically, this explains the decreasing trend of the RPI model with Ja.

From a physical standpoint, however, the RPI model does not directly predict the volumetric departure diameter of the bubble. Instead, it evaluates the "critical cavity size" required for bubble detachment under given thermal conditions. Therefore, the decreasing D_w reflects the fact that the minimum nucleation site size required for detachment becomes smaller at higher superheats, which is physically reasonable. Nevertheless, when directly interpreted as the departure diameter, the RPI model appears to contradict physical intuition.

Consequently, while the RPI model remains valuable for wall heat transfer closure and nucleation site activation modeling, it is less suitable for directly estimating the actual bubble departure diameter under varying thermal conditions. In contrast, the LBM approach inherently captures interfacial dynamics and thermal driving effects, providing physically consistent predictions where D^* increases with Ja and eventually saturates at high superheat levels.

We next compare the LBM results with dynamic models in Fig. 6.6. In the low Ja range (below 0.2), the LBM prediction exhibits a strong positive correlation with Ja, consistent with most dynamic models such as those of Cole, Gorenflo, and Kim. Among them, Van Stralen's model provides the best agreement across the full

range. This can be attributed to its incorporation of both thermal diffusivity and inertial effects—key factors in dynamic bubble growth—which are also naturally resolved in the LBM framework.

It is worth noting that models like Ruckenstein predict an overly aggressive increase in D^*, while Golorin's results lie significantly below others. These differences primarily stem from their empirical treatment of the Ja-dependence. Notably, our LBM results show a saturation plateau beyond $Ja = 0.4$, capturing a physical phenomenon often observed in boiling curves: the transition toward film boiling where vapor accumulation impedes further growth. Such nonlinearity is difficult to model analytically but emerges naturally in LBM, showcasing its advantage in simulating nonlinear phase-change behavior.

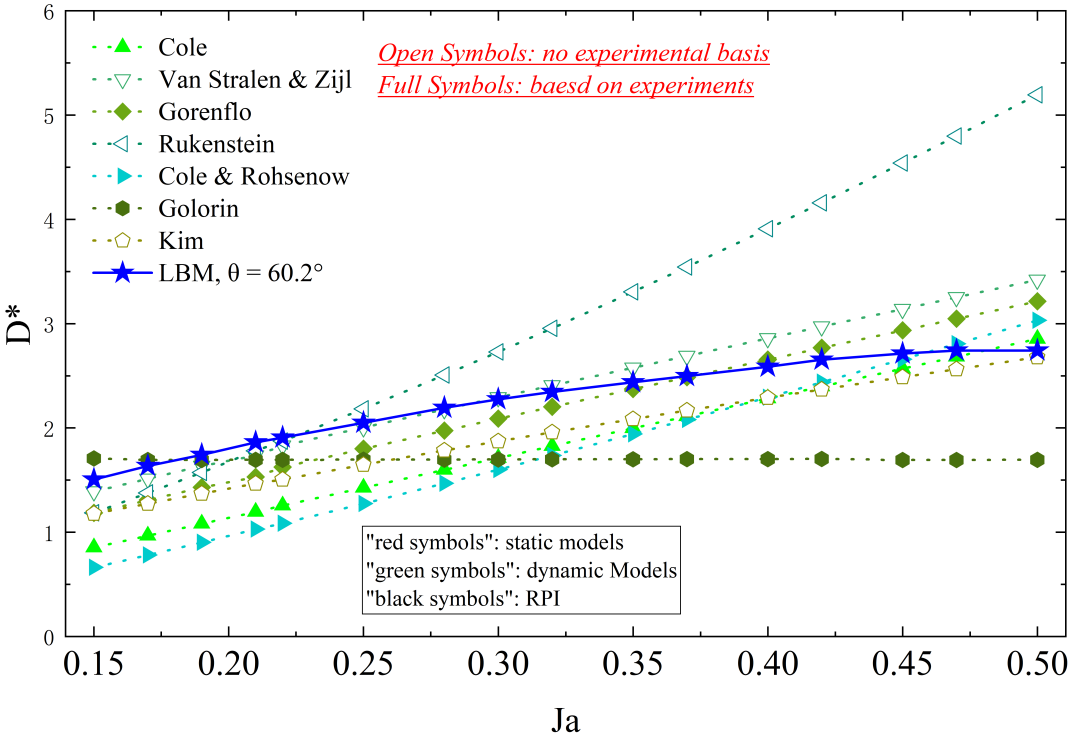

FIG. 6.6: Variation of dimensionless bubble detachment diameter with Ja
Comparison of different theoretical models

A wide range of theoretical correlations has been proposed to predict bubble departure diameter, each providing useful insights but often constrained by specific assumptions or limited experimental ranges. In contrast, the LBM model offers a more versatile and physically consistent framework that simultaneously incorporates thermal, hydrodynamic, and interfacial dynamics. This enables the prediction of bubble departure across a broad spectrum of thermal conditions and,

importantly, captures nonlinear transitions that lie beyond the reach of conventional models.

Fig. 6.7 presents the variation of the dimensionless bubble departure diameter D^* with the Jakob number Ja, obtained from LBM simulations under three different contact angles ($\theta = 27.9°, 44.5°, 60.2°$). These results are systematically compared with representative theoretical models, including Fritz, Cole, Ruckenstein, Gorenflo, and others.

Several key observations can be drawn from this comparison:
Low Jakob number regime ($Ja < 0.20$): The LBM results for all contact angles converge and align well with quasi-static models such as Fritz and Cole & Rohsenow. At low thermal driving forces, the bubble departure is dominated by a static force balance between buoyancy and surface tension, while thermal and inertial effects remain negligible.
Moderate regime ($0.20 < Ja < 0.38$): The departure diameter D^* shows a clear upward trend, and the influence of surface wettability becomes more pronounced. This transition highlights the increasing role of dynamic mechanisms such as bubble growth acceleration and thermal diffusion, indicating that inertia and heat transfer significantly affect detachment.
High Jakob number regime ($Ja > 0.38$): Quasi-static models such as Fritz and RPI predict nearly constant D^*, failing to capture the increasing trend observed in simulations. In contrast, dynamic and thermally-driven models (e.g., Ruckenstein, Kim, Golorin) provide better agreement, especially for $\theta = 60.2°$, where the LBM results closely match the predictions of Golorin's model.
Distinct discrepancies among models: Some models, such as Ruckenstein, significantly overpredict the departure diameter due to overestimated thermal effects, while others like Kocamustafaogullari or RPI show minimal sensitivity to Ja, underestimating the thermally activated growth and departure behaviors.
Unified trend captured by LBM: The two vertical dashed lines at $Ja = 0.2$ and $Ja = 0.38$ may be interpreted as transition boundaries between different dominant mechanisms. LBM simulations exhibit a smooth and continuous evolution of D^* across the entire range, capturing the transition from quasi-static to inertia- and diffusion-dominated regimes. This highlights the robustness of LBM in resolving multi-mechanism coupling in boiling dynamics.

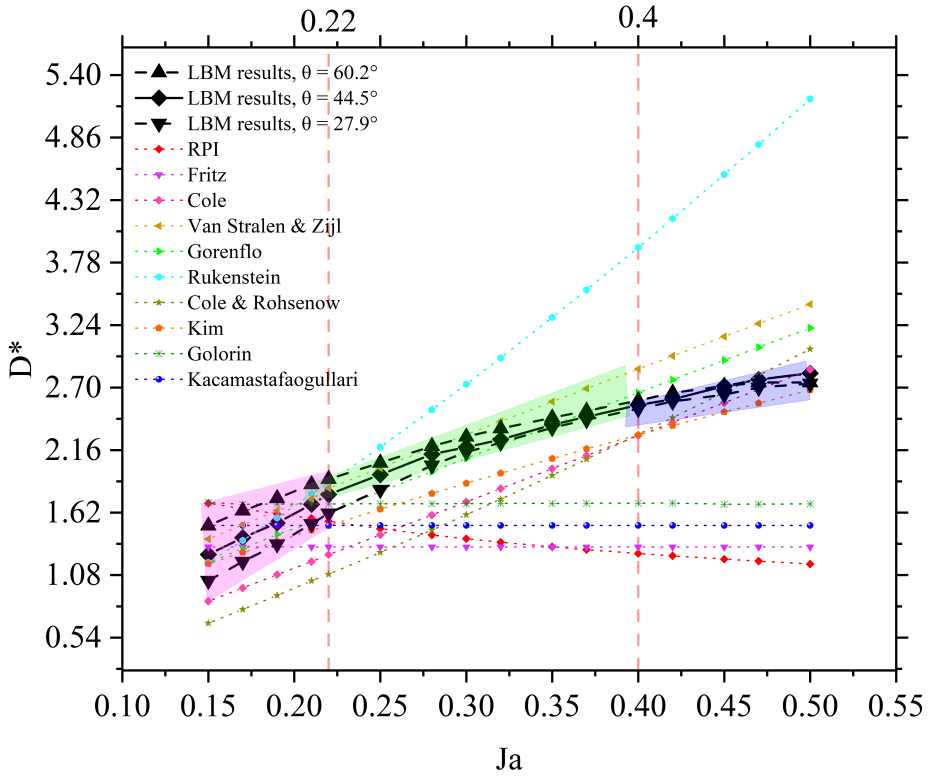

FIG. 6.7: Variation of dimensionless bubble detachment diameter with Ja Comparison of different theoretical models

It is also important to highlight that most of the classical correlations do not explicitly account for the influence of surface wettability, i.e., the contact angle θ, on bubble departure diameter. This omission limits their predictive capability for surfaces with different wetting characteristics. In contrast, the LBM framework inherently incorporates the wettability effect through the implemented solid–fluid interaction model, enabling a direct assessment of how θ alters the detachment process. As shown in Fig. 6.7, the LBM results systematically capture the θ-dependence across all Ja regimes, thereby providing an additional advantage over traditional empirical or semi-theoretical models.

In conclusion, Fig. 6.7 demonstrates the strong dependence of bubble departure diameter on both Ja and surface wettability, while simultaneously illustrating the predictive limitations of classical correlations in different regimes. Static correlations can only be applied to low Ja, whereas dynamic models capture the Ja-dependency only when their parameters are properly chosen. The agreement between LBM results and selected theoretical models within their valid ranges provides further validation of the LBM framework for capturing complex interfacial phenomena in boiling systems.

Departure frequency (f^*) Comparison

For the bubble departure frequency f^*, the LBM simulations are able to directly provide its variation with the Jakob number Ja. In this subsection, the numerical results are systematically compared with several classical theoretical correlations, including those proposed by Jakob, Fritz, Peebles, Zuber, Cole, Mikic & Rohsenow, and Hamzekhani. As shown in Fig. 6.8, the simulation results exhibit a monotonically increasing trend with Ja, indicating that under stronger superheating, bubble nucleation accelerates, the growth cycle shortens, and bubbles depart more frequently. Importantly, this monotonic behavior is consistent with the unified theoretical framework proposed by Zhang et al. [138] and has also been confirmed by the experimental data presented in Chapter 5, thereby providing cross-validation between theory, experiment, and simulation.

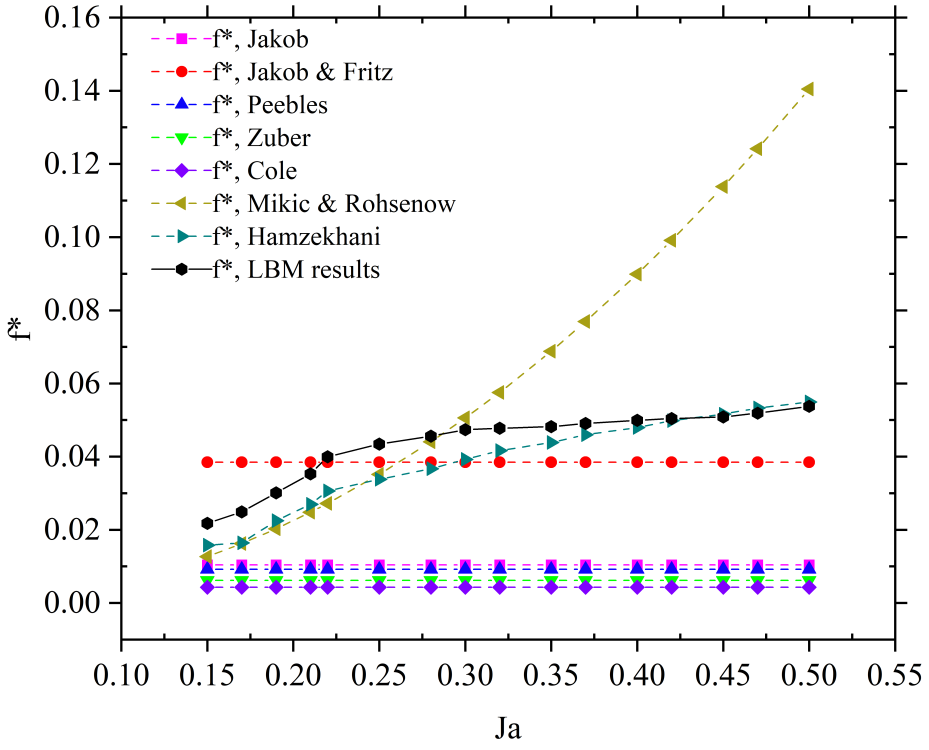

FIG. 6.8: Variation of the departure frequency with Ja

In contrast, the predictions of different theoretical correlations show significant discrepancies. The models of Jakob, Peebles, Cole, and Zuber predict nearly constant f^*, exhibiting very low sensitivity to Ja. These correlations are usually based on quasi-static or weak thermal driving assumptions and therefore fail to capture the marked increase of frequency at moderate and high superheating. The Jakob & Fritz model shows some agreement with LBM results at intermediate Ja

(around $Ja = 0.25{-}0.3$), but still underestimates the overall frequency. The Mikic & Rohsenow model, which incorporates transient heat transfer and thermal boundary layer effects, performs reasonably well at low Ja, but significantly overestimates frequency at higher Ja. This may result from its aggressive scaling between superheat and heat transfer rate, and the simplified assumption of heat flux partitioning. The Hamzekhani model, as a semi-empirical formulation, accounts for more complex boiling dynamics and shows a better agreement with LBM results within $Ja \in [0.2, 0.5]$, suggesting that its empirical correction effectively reflects unsteady mechanisms.

A closer comparison indicates that around $Ja \approx 0.25$, the LBM results start to deviate from static models and exhibit an increasing frequency trend. This demonstrates that inertial and thermal diffusion effects gradually become important in this range. For $Ja > 0.38$, only dynamic or semi-empirical models are able to reasonably capture the frequency rise. In contrast to most theoretical models that rely on specific assumptions (e.g., steady-state conditions or neglecting thermal delays), the LBM simulations naturally incorporate interfacial dynamics, thermal diffusion, and inertial effects. As a result, the predicted frequency evolves smoothly and continuously across the entire range of superheating, bridging different dominant mechanisms.

It should be noted that in the experimental studies (see Chapter 5), it is difficult to directly obtain Ja because this requires precise measurement of local superheat and thermophysical properties. Therefore, the experiments employed the combined parameter $Nu \cdot Ja$ as a descriptor of thermal response. Within this framework (see Fig. 5.17), when the LBM results are converted into the $Nu \cdot Ja$ representation, they exhibit consistent scaling with the experimental data. This not only validates that the increasing trend of f^* with Ja predicted by LBM is also observed in experiments, but also reveals the systematic influence of wettability: smaller contact angles lead to higher bubble departure frequencies.

In summary, two key points are highlighted in this subsection: (i) the LBM simulations are capable of directly capturing the intrinsic relationship between bubble departure frequency and Ja, which is ignored by most classical models; and (ii) when transformed into the $Nu \cdot Ja$ framework commonly used in experiments, the LBM results remain in good agreement with experimental observations, thereby building an effective bridge between numerical predictions and experimental measurements.

6.3 Force-Balance Analysis of Bubble Departure Diameter

In the previous subsection 6.2, a comparative analysis was conducted based on empirical correlations, numerical simulations, and experimental observations, focusing on key parameters such as bubble departure diameter and frequency, which serve as macroscopic indicators of boiling dynamics. Building on this, the present subsection further incorporates the force-balance (FB) framework to elucidate the underlying mechanisms governing bubble detachment. By quantitatively characterizing the competition among buoyancy, surface tension, inertia, and hydrodynamic drag, the FB analysis enables a more fundamental interpretation of departure phenomena. Furthermore, the dependence of the bubble departure diameter on the Jakob number (Ja) is examined within this framework, thereby allowing a direct comparison across theoretical models, LBM simulations, and experimental data. This integrative approach provides a more comprehensive understanding of bubble departure under varying thermal and wettability conditions.

Force-balance model and the simplification used in this work

Since the seminal studies by Klausner *et al.* [147](1993), Zeng *et al.* [148], and Situ *et al.* [149], many force-balance (FB) models have been proposed for predicting the bubble departure diameter. Among them, the framework of Sugrue *et al.* [5] is one of the most comprehensive. As sketched in Fig. 6.9, it considers all major forces acting on a bubble growing on an *inclined* heated plate under flow: buoyancy (F_b), quasi-steady drag (F_{qs}), unsteady drag (F_{du}), shear lift (F_{SL}), hydrodynamic/pressure term (F_h), contact pressure (F_{cp}), and surface tension (F_s). The condition of bubble departure is determined by the balance of the vertical and horizontal components of these forces, i.e.

$$\sum_i F_{i,y} \geq 0.$$

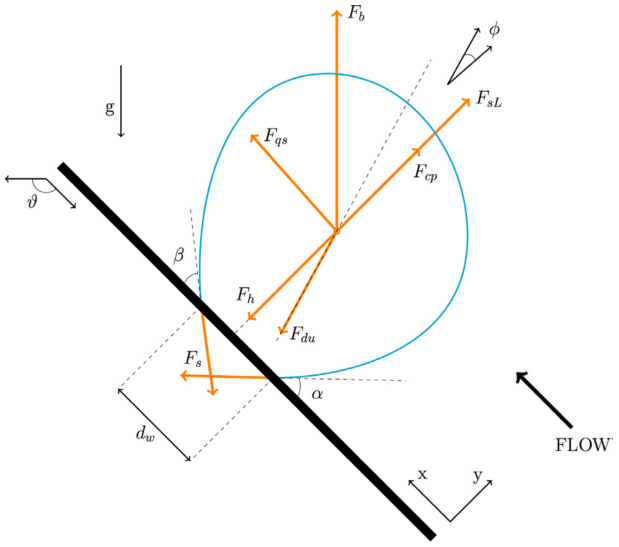

FIG. 6.9: Comprehensive force-balance model by Sugrue *et al.* [5] for an inclined heated plate.

In the original Sugrue formulation, the vertical component of surface tension is written as:

$$F_{sy}^{\text{Sugrue}} = -\,d_w\,\sigma\,\frac{\pi}{\alpha-\beta}\,\big(\cos\beta-\cos\alpha\big), \tag{6.2}$$

where α and β are geometric angles that describe the bubble–wall configuration and the projection of gravity relative to the inclined surface. These angles are crucial for decomposing capillarity on arbitrarily inclined plates.

To enable a direct comparison with our LBM simulations, we simplify the framework to a horizontal heated plate in a stagnant liquid (Fig. 6.10). In this limit, the flow-related forces F_{qs}, F_{SL}, F_h, and the horizontal capillary component F_{sx} are negligible. The vertical force balance then reduces to:

$$A(D^*, d_w) \;=\; F_{sy} \;+\; F_{du} \;+\; F_b \;+\; F_{cp}, \qquad \text{detachment if } A(D^*, d_w) \geq 0, \tag{6.3}$$

with $D^* = D_b/\ell_c$ the dimensionless departure diameter and d_w the wall contact diameter. In the horizontal case we replace the angle pair (α, β) by the static contact angle θ, and use the following alternative expression for the vertical capillary force:

$$F_{sy}^{\text{alt}} \;=\; -\,\pi\,d_w\,\sigma\,\sin\theta, \tag{6.4}$$

which will be referred to as "altern. F_{sy}" in the comparisons that follow.

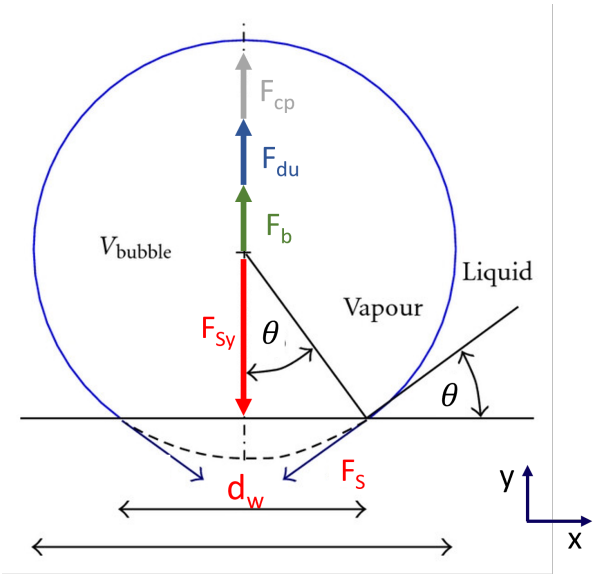

FIG. 6.10: Schematic of the horizontal-plate model simplification adopted in this study

Table 6.4 summarizes the vertical force components used in our analysis and highlights the difference between the original and alternative forms of F_{sy}.

TABLE 6.4: Vertical force components: Sugrue (inclined plate) vs. this work (horizontal plate).

Force	Sugrue (inclined plate)	This work (horizontal plate)
Surface tension, F_{sy}	$-\,d_w\sigma\dfrac{\pi}{\alpha-\beta}\big(\cos\beta-\cos\alpha\big)$ (Eq. 6.2)	$-\,\pi d_w\sigma\sin\theta$ (Eq. 6.4)
Unsteady drag, F_{du}	$\rho_l\pi R^2\Big(\dfrac{2}{\sqrt{\pi}}\sqrt{\nu t}\,\dot{R}\Big)$	Same expression; t, R, $\dot{R}$ taken from LBM growth history
Buoyancy, F_b	$\dfrac{4}{3}\pi R^3(\rho_l-\rho_v)g$	Same expression
Contact pressure, F_{cp}	$\dfrac{\pi d_w^2\sigma}{4R}$	Same expression

In order to establish a consistent comparison between the departure diameters predicted by LBM and those estimated by the force–balance (FB) model, it is essential to prescribe two key input parameters: the bubble growth time t and the contact diameter d_w.

Bubble growth time (t): In this study, t is defined as the bubble lifetime from nucleation to departure. Unlike classical FB models where t is often assumed or indirectly inferred, here it can be directly extracted from the LBM simulations as a function of the Jakob number Ja. Figure 6.11 illustrates that t decreases sharply for $Ja \lesssim 0.30$ and gradually approaches a plateau at higher superheats. These LBM-derived values of $t(Ja)$ are inserted into the evaluation of the unsteady drag force F_{du} in Eq. (6.3).

Contact diameter (d_w): The contact diameter is a crucial geometric parameter that strongly affects the vertical force balance. In the FB formulation, it directly enters both:

$$F_{sy} = -\, d_w \pi \sigma \sin\theta, \tag{6.5}$$

$$F_{cp} = +\, \frac{\pi d_w^2 \sigma}{4R}. \tag{6.6}$$

Therefore, d_w simultaneously controls the adhesive resistance at the triple line *and* the microlayer pressure recovery. Despite this dual role, d_w is often oversimplified in the literature. Following Sugrue *et al.* [5], a widely used prescription is

$$d_w = 0.025\, D^*,$$

where D^* is the departure diameter. This constant ratio was originally calibrated for inclined-wall configurations. As will be shown later, applying it directly to horizontal-wall boiling leads to systematic discrepancies, particularly at low-to-moderate Ja, where d_w should in fact evolve dynamically with bubble growth.

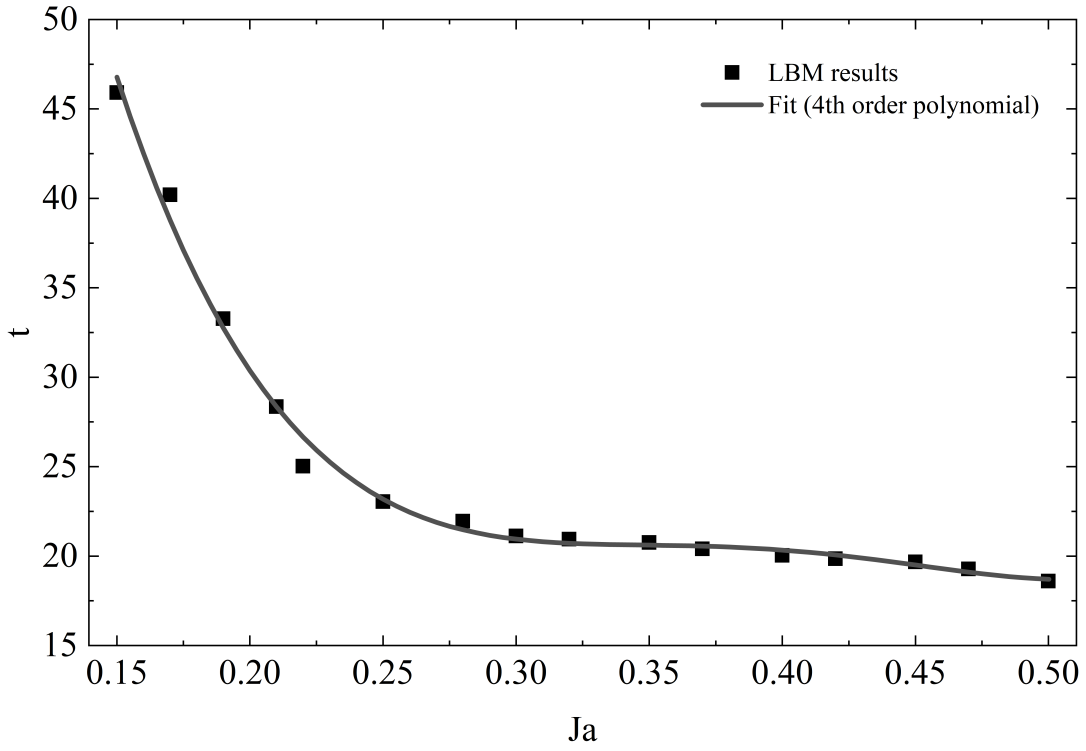

FIG. 6.11: Bubble growth time t (nucleation-to-departure lifetime) as a function of Ja, used as input to the force-balance (FB) evaluation.

Together, these two parameters close the FB model and allow the calculation of F_{sy}, F_{du}, F_b, and F_{cp} for direct comparison with LBM predictions. A key outcome of this study is that the assumed linear dependence between d_w and D^* (Eq. 6.3) is not valid across the entire Ja range, and this oversimplification is a primary source of the mismatch between FB analysis and numerical simulations.

Baseline force–balance analysis with linear scaling of d_w

Fig. 6.12 presents the variation of the bubble departure diameter with the Jakob number (Ja) at a fixed contact angle of $\theta = 60.2°$. The left ordinate corresponds to the dimensionless departure diameter D^* obtained from LBM simulations, while the right ordinate shows the individual vertical force components and their algebraic sum F_{sum} evaluated from the Sugrue force–balance (FB) model.

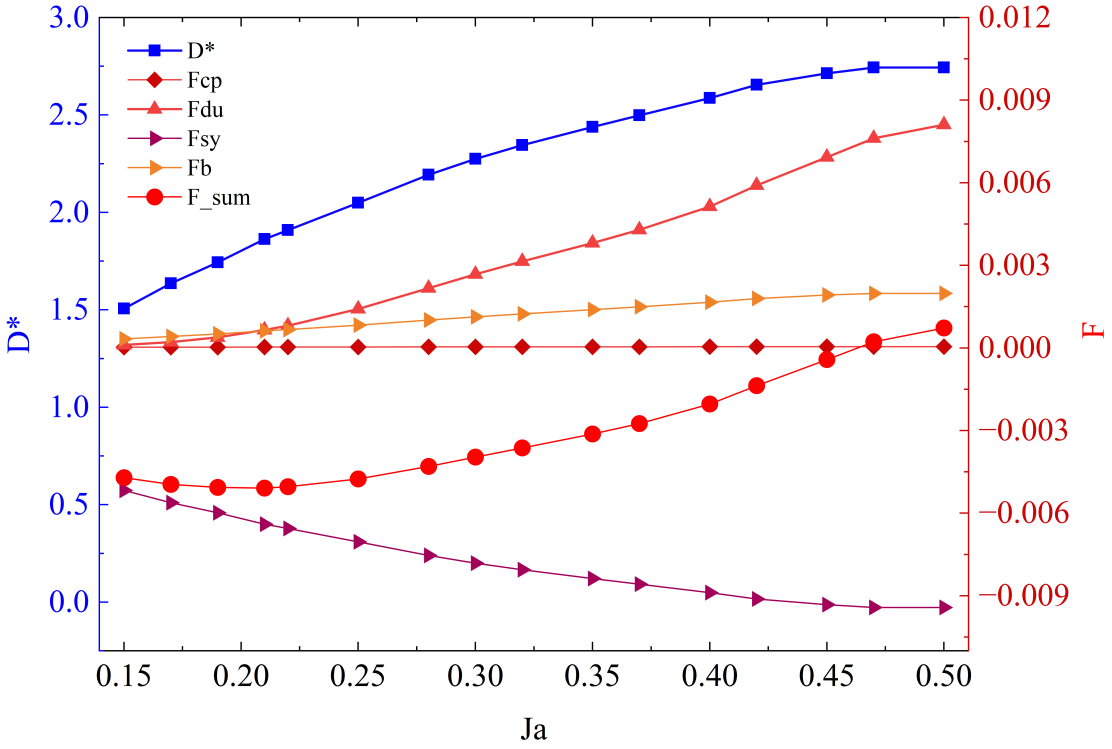

FIG. 6.12: Baseline force–balance (FB) evaluation at a fixed contact angle $\theta = 60.2°$ using the constant contact diameter $d_w = 0.025D_b$. Left ordinate (blue): LBM departure diameter D^*. Right ordinate (red): individual vertical forces and their algebraic sum $F_{\text{sum}} = \sum_i F_{i,y}$.

It can be observed that the buoyancy force (F_b) and the unsteady drag force (F_{du}) both increase steadily with Ja, reflecting stronger thermal driving at higher superheats. The contact pressure (F_{cp}) remains nearly constant across the considered range. The vertical component of surface tension (F_{sy}) is negative, acting as a stabilizing force, and its magnitude decreases with increasing Ja, consistent with the flattening of the bubble neck during rapid growth. The total vertical force F_{sum} approaches zero only at sufficiently high Jakob numbers, $Ja \gtrsim 0.45$, thereby fulfilling the detachment criterion ($F_{\text{sum}} \geqslant 0$). This indicates that, under weak thermal driving, the force–balance model predicts that bubbles should remain attached to the surface.

In contrast, the LBM simulations show that regular bubble departure already occurs once $Ja \approx 0.15$, with the departure diameter D^* increasing monotonically with Ja. This clear discrepancy highlights that in the low-to-moderate Ja regime, the FB model significantly underestimates bubble detachment relative to the numerical results.

The origin of this mismatch cannot be attributed to a single factor. A plausible hypothesis is that certain parameterizations within the FB framework—most notably the empirical treatment of the contact diameter d_w—may be overly simplified. This simplification could suppress the model's ability to capture inertial and thermal effects at low Ja. To test this hypothesis, the following subsection will examine in more detail the role of d_w and its possible dynamic dependence on Ja.

Comparison between force–balance model and LBM simulations

To further assess the predictive capability of the force–balance (FB) model, Figure 6.13 compares the departure diameter D^* obtained from LBM simulations with that determined by fulfilling the FB criterion (i.e., the algebraic sum of the vertical forces equals zero) in the Sugrue model at a fixed contact angle of $\theta = 60.2°$. The red solid line corresponds to the original Sugrue formulation, the pink dashed line represents the modified model using the alternative surface tension expression (altern. F_{sy}), and the blue solid line denotes the LBM results.

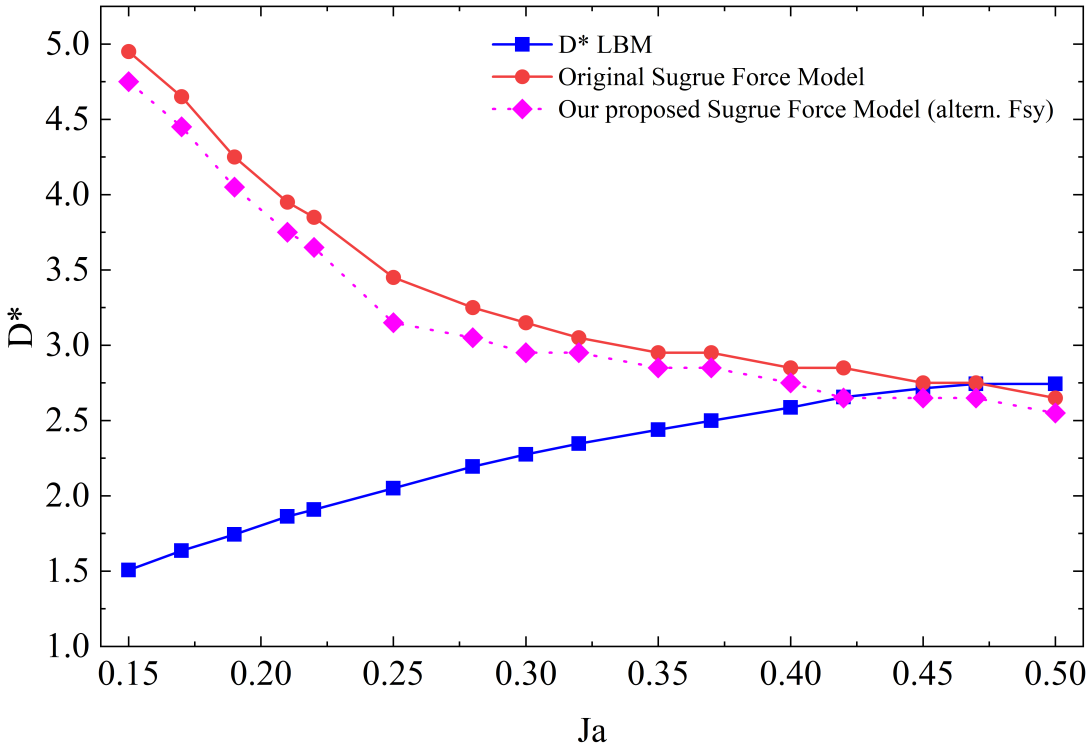

FIG. 6.13: Departure diameter D^* versus Ja at $\theta = 60.2°$: LBM simulation results (blue solid line) compared with force–balance (FB) predictions determined from the criterion $\sum F = 0$, including the original Sugrue model (red solid line) and the modified formulation with alternate F_{sy} (pink dashed line).

It is evident that in the high-Jakob-number regime ($Ja \gtrsim 0.43$), all three predictions converge, indicating that under strong thermal driving the FB model can reasonably capture the departure diameter trend. However, in the low-to moderate Ja range ($Ja \lesssim 0.40$), a pronounced discrepancy emerges: while the LBM simulations predict a monotonically increasing D^* with Ja, the Sugrue model yields a decreasing trend, leading to a reversed physical behavior. The alternative surface tension term,

$$F_{sy} = -\, d_w\, \pi\sigma \sin\theta,$$

improves the agreement to some extent by reducing the deviation in the low-Ja regime, yet it still fails to fully reproduce the monotonically increasing trend observed in the LBM simulations. This indicates that, even with a refined treatment of F_{sy}, the FB framework exhibits systematic deficiencies under weak superheating.

Such discrepancies suggest that the source of error is not solely attributed to the form of the surface tension contribution. Instead, it is likely also linked to the treatment of the contact diameter d_w. In the existing formulation, d_w is simplified as a proportionality, $d_w = 0.025 D_b$, which may underestimate the dynamic role of d_w during bubble growth and detachment. Based on this hypothesis, the following subsection will investigate the relationship between d_w and the Jakob number, and propose an improved representation that better reflects both the numerical results and the underlying physical mechanism.

The preceding discussion was restricted to a fixed contact angle $\theta = 60.2°$ in order to isolate the effect of the Jakob number on bubble departure. However, in practical boiling processes, the contact angle, as an indicator of surface wettability, also plays a significant role in bubble attachment and detachment. It is therefore instructive to extend the comparison to multiple contact angles, in order to assess how wettability influences the discrepancies between LBM simulations and force-balance predictions.

To this point, our discussion has mainly focused on the fixed contact angle $\theta = 60.2°$, in order to isolate the effect of the Jakob number on bubble departure. However, in practical boiling processes, the contact angle itself is also a key factor, since it reflects the influence of surface wettability on bubble attachment and detachment.

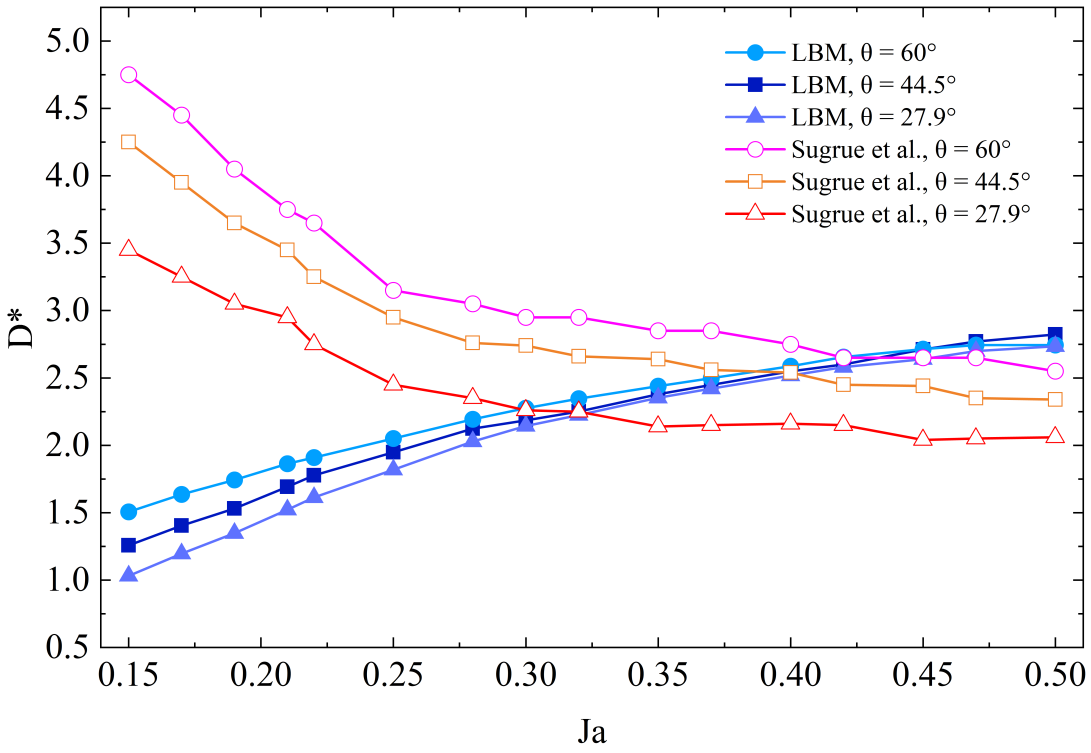

FIG. 6.14: Departure diameter D^* versus Ja for three contact angles: LBM results (solid blue shades) versus original Sugrue predictions (hollow warm shades).

Fig. 6.14 presents a comparison between LBM simulations and the Sugrue force-balance model at three typical contact angles ($\theta = 60.0°$, $44.5°$, and $27.9°$). The following observations can be made:

1. LBM results (solid blue lines) consistently show a monotonic increase of D^* with Ja across all contact angles; 2. The original Sugrue model (hollow warm symbols) still predicts a decreasing trend at low Ja, in contrast to the monotonic increase from LBM; 3. The absolute magnitude of the departure diameter decreases with decreasing θ, which is consistent with the classical prediction based on surface tension that increased wettability leads to smaller bubble departure diameters [150, 151].

These results highlight that, although discrepancies between the force-balance framework and LBM remain in the low-to-moderate superheat regime, the role of contact angle cannot be ignored. This suggests that a more refined force-balance formulation may need to incorporate the influence of contact angle in a systematic manner, particularly when extending the model beyond the high-Ja regime.

6.4 Force Distribution Diagnosis and Error Identification

I analyze the variation of individual force components with respect to the non-dimensional bubble diameter d^* under two representative superheat conditions: $Ja = 0.17$ and $Ja = 0.47$. Consistent with the model description in the previous subsection, these force evaluations are carried out for a horizontal heated plate without external flow.

As shown in Fig. 6.15, under the low superheat condition of $Ja = 0.17$, the total vertical force F_{sum} remains negative throughout the entire bubble growth range, indicating that the force balance model predicts no bubble departure. Specifically, the contact pressure F_{cp} is negligible, while the buoyancy force F_b and the vertical component of surface tension F_{sy} exhibit little variation with bubble diameter, showing weak size dependence. Although the unsteady drag force F_{du} increases with the non-dimensional bubble diameter d^*, its magnitude remains insufficient to overcome the opposing capillary force. As a result, F_{sum} stays negative, revealing a significant underestimation of the inertial contribution by the model.

It is worth noting that at $Ja = 0.17$, the LBM simulations predict a departure diameter of approximately $D^* \approx 1.6$. In stark contrast, the baseline FB model requires a much larger bubble diameter value of $d^* \approx 4.5$ to satisfy the detachment criterion. Moreover, if the LBM-obtained diameter is directly inserted into the FB formulation, the resulting total vertical force remains negative, thereby erroneously suggesting "no departure." This discrepancy clearly demonstrates that the FB model significantly underestimates the inertial contribution at low superheats, which shifts the predicted onset of detachment to unrealistically large bubble sizes.

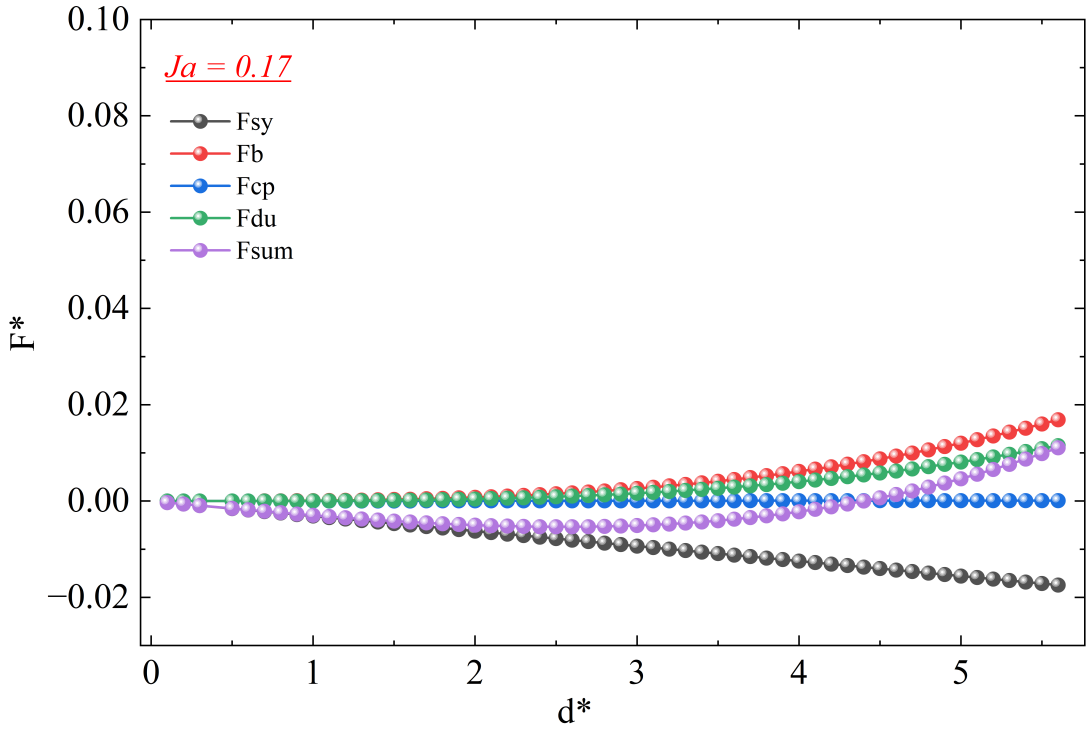

FIG. 6.15: Bubble diameter d^* versus Forces F* for $\theta = 60.2°$, $Ja = 0.17$.

In contrast, in Fig. 6.16, at a higher superheat level of $Ja = 0.47$, the unsteady drag force F_{du} rises sharply and becomes the dominant upward force. This increase is sufficient to shift F_{sum} from negative to positive, thereby satisfying the detachment criterion. While F_b and F_{sy} remain nearly constant and F_{cp} is still negligible, the rapid escalation of F_{du} plays a critical role in enabling bubble departure.

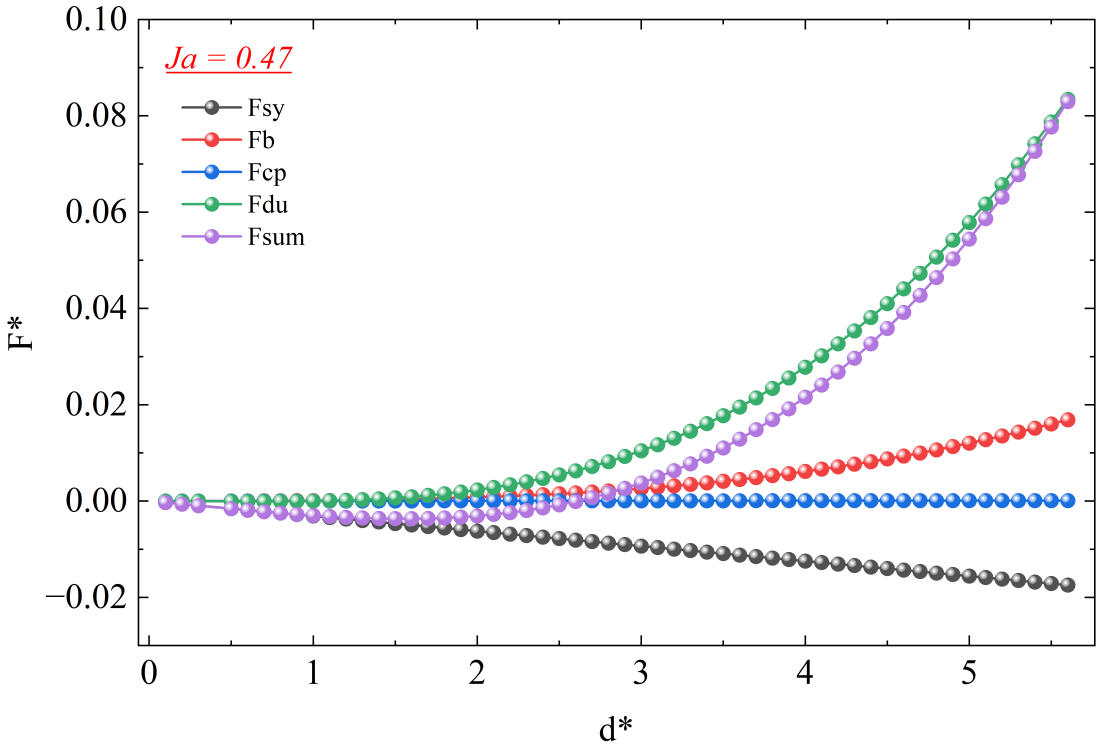

FIG. 6.16: Departure diameter d^* versus Forces for $\theta = 60.2°$, $Ja = 0.47$.

A comparison of the two cases reveals that the model's ability to predict departure strongly depends on the responsiveness of F_{du} to variations in Ja. However, adopting a fixed ratio between d_w and D^* leads to systematic underestimation of F_{du} at low Ja, which limits the accuracy of the predictions, especially in the inertia-dominated regime.

To systematically summarize the model deviations under different superheat conditions, Table 6.5 outlines the dominant upward force, the associated error mechanism, and the resulting behavior of the predicted departure diameter across different Ja intervals. Specifically, in the low Ja regime (≤ 0.25), the underestimated F_{du} causes an unphysical decrease in the predicted departure diameter with increasing Ja. In the transitional range (0.25–0.40), F_{du} rises sharply, and the total force approaches the detachment threshold. At high Ja values (≥ 0.40), F_{du} dominates the upward balance, and the FB model predictions begin to converge with the LBM results.

TABLE 6.5: Dominant upward force and error source across different Ja ranges

Ja Range	Dominant Upward Force	Constant d_w Error Mechanism	Resulting Behavior
≤ 0.25	$F_b \approx F_{sy}$	F_{du} severely underestimated	d^* decreases with Ja
0.25–0.40	F_{du} rapidly increases	Transitional regime	F_{sum} approaches zero
≥ 0.40	F_{du} dominates	Force balance satisfied	FB aligns with LBM

These observations reinforce that the constant d_w assumption fails in low superheat conditions and motivate the introduction of a Ja-dependent contact diameter model in the next section. Therefore, future improvements to the model should incorporate a Ja-dependent formulation of d_w, allowing for a more accurate representation of F_{du} and improved predictive capability across a wider range of operating conditions.

6.5 Dynamic (Ja-dependent) Contact Diameter Model

The diagnostic analysis in the previous section highlighted that the key source of discrepancy between the force–balance (FB) model and LBM results lies in the treatment of the contact diameter d_w. In the original formulation by Sugrue *et al.*, d_w was prescribed as a fixed ratio of the bubble departure diameter, $d_w = 0.025\, D^*$. As demonstrated, this simplification systematically underestimates the inertial contribution (F_{du}) at low Ja, leading to the reversed trend in predicted departure diameters.

To address this limitation, we adopt an inverse strategy: the LBM-predicted departure diameter D^* is inserted into the FB balance:

$$A(D^*, d_w) = \sum_i F_{i,y} = 0,$$

and the corresponding d_w is solved for, thereby obtaining a dynamically varying contact diameter as a function of Ja. The resulting d_w values increase markedly with Ja, ranging from near-zero at $Ja \approx 0.15$ to approximately 0.08–0.09 at

$Ja \approx 0.50$, consistent with the physical picture of a widening neck during bubble growth under stronger thermal driving (See red dots in Fig.6.17).

Guided by this analysis, we propose a new empirical model to describe the dependence of the normalized contact diameter on Ja:

$$\frac{d_w}{D^*} = a_0 + a_1 \cdot Ja^m, \qquad (a_0, a_1, m) = (0.015,\ 0.14,\ 2.00).$$

The coefficients were obtained by nonlinear least-squares fitting to the LBM data at a fixed contact angle of $\theta = 60.2°$.

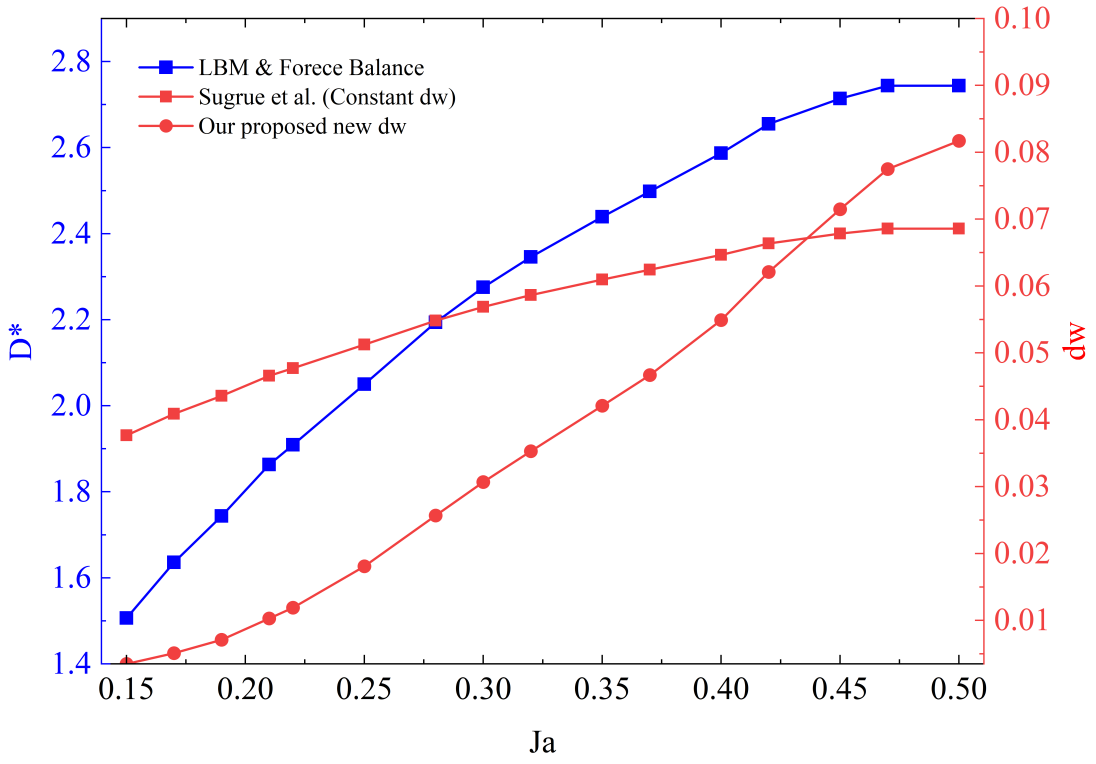

FIG. 6.17: Validation of the proposed Ja-dependent contact diameter model against LBM predictions.

As shown in Fig. 6.17, this modified formulation provides a consistent description across the entire Ja range: the FB predictions using the dynamic $d_w(Ja)$ align closely with the LBM departure diameters, thereby overcoming the deficiencies of the constant d_w assumption and extending the predictive capability of the force–balance model.

To further validate the applicability of the proposed dynamic contact diameter model, the inverse analysis was extended to different wettability conditions, namely

$\theta = 60.2°$, 44.5°, and 27.9°. The corresponding variation of the departure diameter D^* and the contact diameter d_w with Jakob number Ja is shown in Fig. 6.18.

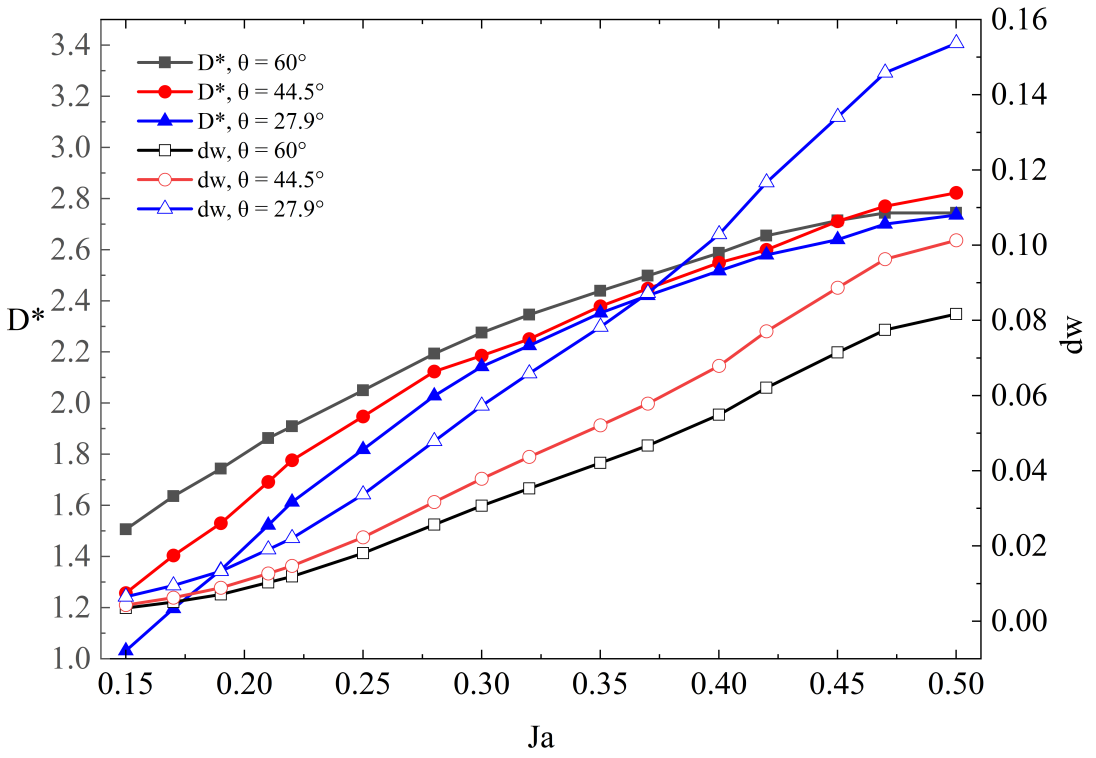

FIG. 6.18: Comparison of D^* and d_w versus Jakob number under varying contact angles

Several important observations can be drawn. First, under all contact angle conditions, both D^* and d_w increase monotonically with Ja, which confirms the general validity of the dynamic contact diameter concept. Second, the magnitude of d_w is strongly dependent on wettability: smaller contact angles (hydrophilic surfaces) correspond to larger d_w, while larger contact angles (hydrophobic surfaces) lead to smaller d_w. This trend is consistent with classical capillarity theory, in which stronger wettability promotes the expansion of the three-phase contact line and thus enlarges the effective contact area.

More importantly, the relative difference between $D^*(Ja)$ and $d_w(Ja)$ also exhibits a clear dependence on contact angle. Under strongly wetting conditions ($\theta \approx 27.9°$), the reconstructed d_w increases most rapidly with Ja, reaching values above 0.12 at $Ja = 0.50$. In contrast, for moderately hydrophobic conditions ($\theta \approx 60.2°$), d_w grows more gradually and tends to saturate around 0.08–0.09. These results indicate that, beyond thermal driving (represented by Ja), interfacial wettability

also plays a key role in determining the dynamic evolution of the effective contact diameter.

In summary, this extended analysis suggests that the proposed empirical $d_w(Ja)$ model should be further generalized to explicitly include contact-angle effects. A more general form may be expressed as:

$$\frac{d_w}{D^*} = a_0(\theta) + a_1(\theta) \cdot Ja^{m(\theta)},$$

which provides a unified framework to capture both thermal driving and wettability influences on bubble departure.

6.6 Effect of Contact Angle (θ) on Departure Diameter (D^*)

To quantify the role of surface wettability, I examine how the contact angle θ affects the dimensionless bubble departure diameter D^*. Fig. 6.19 contrasts LBM predictions with a classical static correlation (Fritz [146]) for three representative contact angles, $\theta = 27.9°$, $44.5°$ and $60.2°$. And two observations stand out: Static correlations show weak θ-sensitivity. Within the tested range, the Fritz model varies little with θ, which is consistent with its quasi-static balance between buoyancy and surface tension and the absence of explicit inertial/thermal coupling. LBM reveals a clear θ-dependence, most pronounced at lower Ja. For fixed Ja, D^* increases with θ in the LBM data, indicating that surfaces with poorer wettability (larger θ) promote larger departure sizes. The trend weakens as Ja increases, when thermal/inertial effects dominate the detachment process.

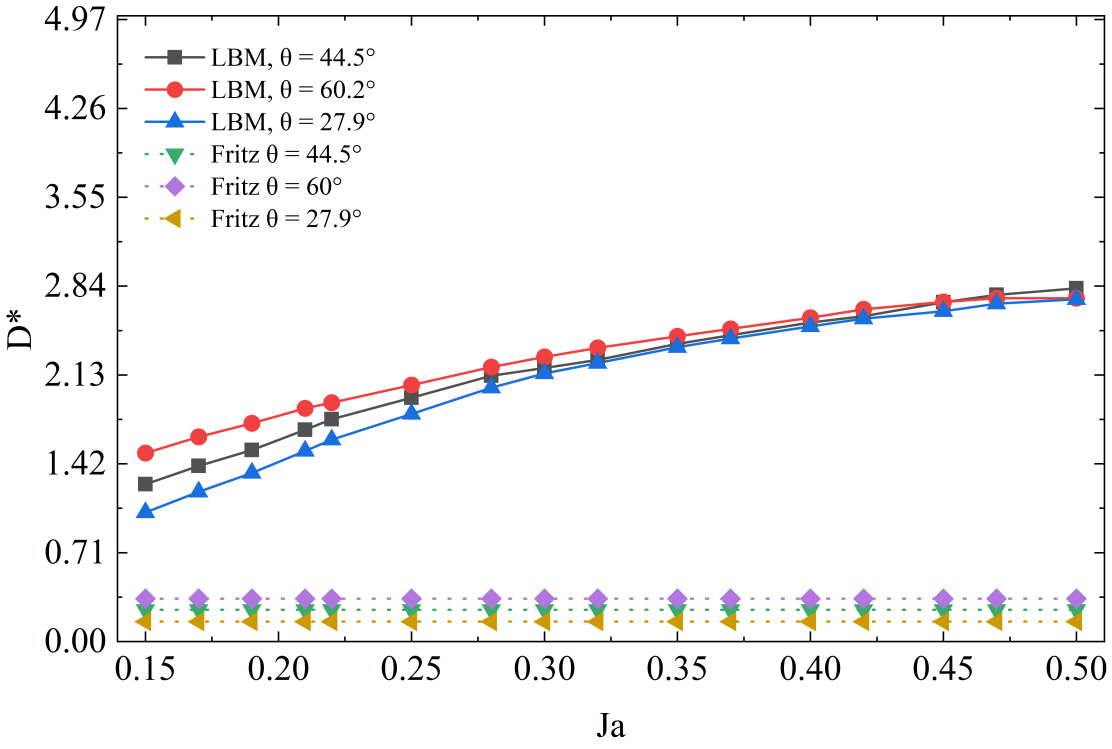

FIG. 6.19: Comparison of LBM Predictions and Fritz Model for D^* under Varying Contact Angles

These findings suggest that wettability and thermal driving act jointly on departure: θ modulates the capillary constraint near the contact line, while Ja controls the available thermal energy and the associated inertial growth. To capture this combined influence in a compact form, we propose the following two-variable correlation for D^*:

$$D^*(Ja, \theta) \;=\; A\,\theta^{\,c}\,Ja^{\,d} + B, \tag{6.7}$$

where (A, c, d, B) are obtained by nonlinear least-squares fitting to the LBM dataset spanning the three contact angles:

$$A = 12.82, \qquad c = 0.02, \qquad d = 0.108, \qquad B = -10.$$

As shown in Fig. 6.20, Eq. (6.7) reproduces the monotonic increase of D^* with both Ja and θ, with a maximum absolute deviation within $\sim 2.5\%$ across the explored range. We stress that this correlation is intended as a concise descriptor over the present parameter window; its coefficients are empirical and may require recalibration if the operating range (fluids, θ, Ja) is extended.

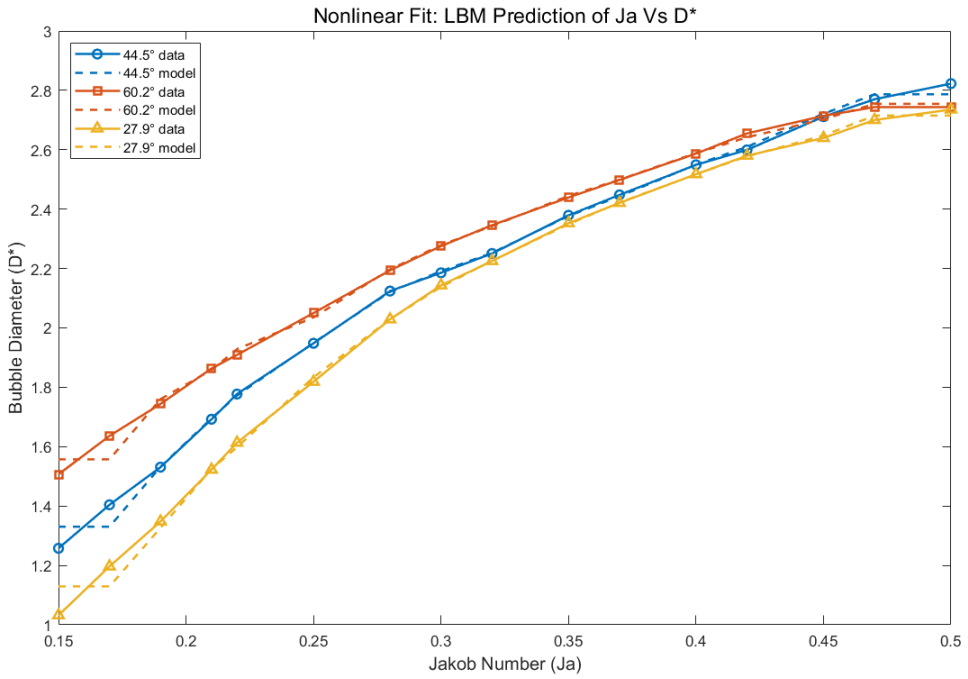

FIG. 6.20: Nonlinear Correlation of D^* versus Ja under Various Contact Angles: LBM Data and Fitted Model

6.7 Summary of This Chapter

This chapter systematically compared the LBM simulation results with existing empirical correlations and force–balance (FB) models, both of which are commonly adopted closures in traditional CFD frameworks. All comparisons were carried out in a non-dimensional framework to ensure that the differences among models directly reflect the intrinsic bubble dynamics, independent of the choice of physical units. The work in this chapter progresses from parameter extraction, to empirical validation, and finally to mechanical diagnosis and model refinement.

First (Section 6.1), key bubble dynamic parameters such as the initial diameter, departure diameter, and departure frequency were extracted from LBM simulations. These parameters were shown to capture distinct phases of the boiling process and demonstrated clear dependence on the Jakob number Ja. Among them, the departure diameter D^* and departure frequency f^* were identified as the core indicators linking bubble dynamics with boiling heat transfer intensity.

Second (Section 6.2), the LBM results were compared with a wide range of classical empirical correlations. The analysis revealed that static correlations (e.g., Fritz) are only valid at low superheat conditions, while dynamic or semi-empirical models (e.g., Ruckenstein, Hamzekhani) provide partial improvements but lack universality. This systematic comparison highlighted the limitations of conventional models and simultaneously confirmed the predictive advantages of LBM in resolving multi-mechanism coupling.

Building on this (Sections 6.3–6.5), a diagnostic evaluation of the Sugrue FB model was performed. By decomposing buoyancy, contact pressure, surface tension, and unsteady drag contributions, it was found that the common assumption of a fixed contact diameter $d_w = 0.025D^*$ leads to a significant underestimation of inertial effects in the low-to-moderate Ja regime. As a result, the FB model incorrectly predicts opposite trends to those observed in simulations. To address this limitation, this chapter introduced an innovative Ja-dependent dynamic contact diameter model. By back-calculating from LBM results, an empirical correlation for d_w/D^* as a function of Ja was developed, which substantially improved prediction accuracy in the low-to-moderate Ja regime. This represents a novel extension to the traditional force–balance framework.

Finally (Section 6.6), the influence of surface wettability was investigated. LBM simulations demonstrated a strong dependence of D^* on contact angle θ, especially at low Ja, whereas classical static models failed to capture this trend. Based on numerical data, a new two-variable nonlinear correlation $D^*(Ja, \theta)$ was proposed, which accurately reproduces the monotonic dependence on both Ja and θ with high fidelity. This formulation effectively bridges the gap between numerical simulations and theoretical predictions, providing a more comprehensive description of bubble departure.

In summary, the key contributions of this chapter are as follows:
Establishment of a unified comparison framework between LBM, empirical correlations, and FB models under a non-dimensional formulation;
Identification of the limitations of the fixed contact diameter assumption, which systematically underestimates inertial effects at low-to-moderate Ja;
Proposal of a novel Ja-dependent dynamic contact diameter model, calibrated by LBM data;
Extension of the departure diameter analysis to include surface wettability, leading to a new two-variable correlation that incorporates both Ja and θ.

Overall, this chapter not only deepens the understanding of the physical mechanisms governing bubble dynamics but also provides improved predictive frameworks that extend beyond traditional models. These findings form a solid foundation for the development of more universal closures in multiphase boiling simulations.

In addition, it is worth noting that although a three-dimensional (3D) version of the numerical framework has also been implemented, the simulations presented in this chapter were mainly conducted in a two-dimensional (2D) domain. This simplification is widely adopted in lattice Boltzmann studies of boiling and bubble dynamics [152–154], as it allows the dominant interfacial physics—such as bubble nucleation, growth, departure, and wettability effects—to be captured with much lower computational cost and higher spatial resolution. The 2D pseudopotential LBM has been shown to reproduce the essential mechanisms of bubble evolution, including surface deformation, capillary effects, and liquid–vapor interactions [155, 156].

Nevertheless, quantitative deviations are expected when comparing the 2D simulations with 3D experimental results, since a 2D bubble represents a cylindrical structure with unit depth, whereas real bubbles are approximately spherical in three dimensions. This geometric difference modifies the surface-to-volume ratio and consequently alters the Laplace pressure, buoyancy–viscous balance, and heat transfer pathways [157, 158]. As a result, discrepancies in the absolute values of bubble departure diameter, growth rate, and local heat flux are unavoidable. Previous studies have also demonstrated that 2D and 3D simulations yield consistent trends in nucleate and film boiling regimes, while stronger geometric sensitivity appears in the transition regime [157, 159].

In the present work, quantitative comparisons between 2D simulations and 3D experimental observations were conducted to assess the predictive capability of the model. The simulated bubble departure diameter, growth rate, and heat flux exhibit consistent trends and comparable magnitudes to experimental measurements, with deviations remaining within a reasonable range. These discrepancies originate from multiple sources rather than from dimensional simplification alone. In particular, the limited density ratio achievable in the pseudopotential LBM differs from that of the real liquid–vapor system, which affects the balance between buoyancy, surface tension, and inertia. In addition, the experimentally measured

contact angle and surface characteristics are influenced by material heterogeneity, oxidation, and roughness, whereas the wettability in simulations is prescribed through an idealized interfacial parameter. These differences inevitably contribute to the overall quantitative deviation. If we consider it purely from the perspective of two-dimensional geometric configuration, the 2D configuration still plays an important role: its cylindrical bubble representation alters the interface curvature and heat transfer pathways compared with the spherical geometry in 3D, which represents a physical manifestation of dimensional effects rather than a numerical artifact. Overall, the observed discrepancies result from the combined influence of geometric, thermophysical, and surface-wettability factors. Future work will extend the current framework to fully three-dimensional simulations [160], which will allow for more realistic density ratios, complex surface conditions, and a systematic quantification of dimensional effects for closer agreement with experimental observations.

Chapter 7

Numerical Extension Implementations

The previous chapters established and validated a robust numerical framework for simulating single bubble boiling behavior under various thermal and wettability conditions, confirming the model's accuracy in capturing bubble dynamics in two-dimensional domains. Building on this foundation, this chapter extends the numerical investigation to more complex and application-oriented scenarios.

First, pool boiling simulations are conducted over surfaces with varying structured surface, and mixed-wettability surfaces are introduced to propose a potential way in enhancing boiling performance. Then, preliminary three-dimensional simulations of single bubble nucleation are presented, aiming to explore the model's scalability and applicability to more realistic configurations.

These extended implementations not only demonstrate the versatility of the proposed model but also provide valuable insights for future design and optimization of boiling surfaces in thermal management applications. Unless otherwise stated, time is reported in dimensionless form $t^* = t/t_0$ throughout this chapter, where $t_0 = l_0/u_0$ is the gravity–capillary time built from the capillary length l_0 and velocity u_0 introduced in Chapter 2.

7.1 Single Bubble Nucleation on Structured surface

Microscale features of the heated surface modify the local interfacial curvature and wettability, lowering the nucleation energy barrier. The numerical simulation in this subsection provide a framework for subsequent investigations into how structured surfaces, compared with a flat heater under identical superheat, influence nucleation behavior. For example, they enable comparative analyses of the onset of nucleate boiling (ONB) and of differences in the nucleation–departure cycle across various surface architectures.

7.1.1 Rectangular microheater surface

Fig. 7.1 presents the simulated evolution of a single bubble on a rectangular microheater surface. The results show that the initial nucleation sites emerge at the concave corners of the structured surface rather than at the central bottom of the groove ($t^* = 17.1$). This preferential corner nucleation is followed by the growth of two distinct vapor embryos, which expand in volume and subsequently merge into a larger vapor structure at $t^* = 18.7$. As the merged bubble continues to grow ($t^* = 22.5$), it spans across the groove opening and exhibits a dynamic expansion pattern similar to that on a planar surface. In the later stage ($t^* = 28.5$), necking occurs near the bubble base, eventually leading to detachment at $t^* = 31.2$.

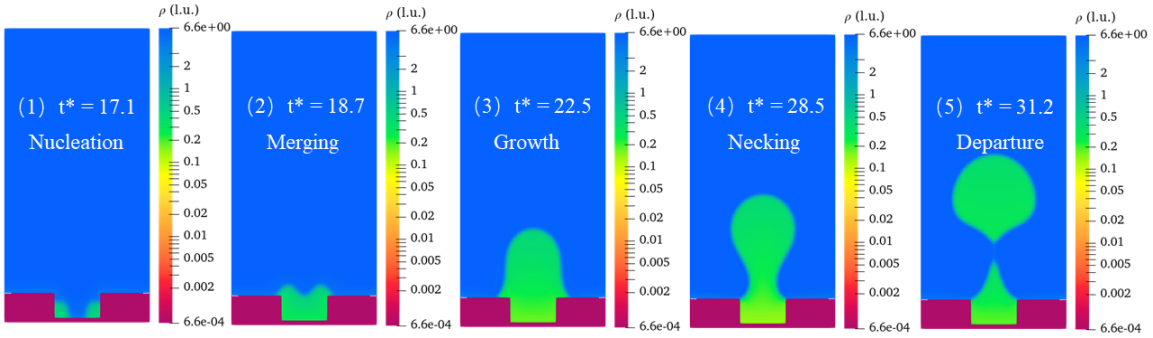

FIG. 7.1: Time evolution of bubble nucleation and departure on a rectangular microheater surface ($T_s = 0.9T_c$, $\Delta T = 0.01T_c$, $\theta \approx 63.2°$).

This corner-dominated nucleation behavior is consistent with the observations reported by Li *et al.* [6], who attributed the phenomenon to the combined effects of

local hydrodynamics, density gradients, and surface thermodynamics in concave geometries. Firstly, the confined geometry at the corner alters the local density distribution, enhancing the density gradient and amplifying the resultant fluid–fluid interaction forces in the vapor-preferred direction.

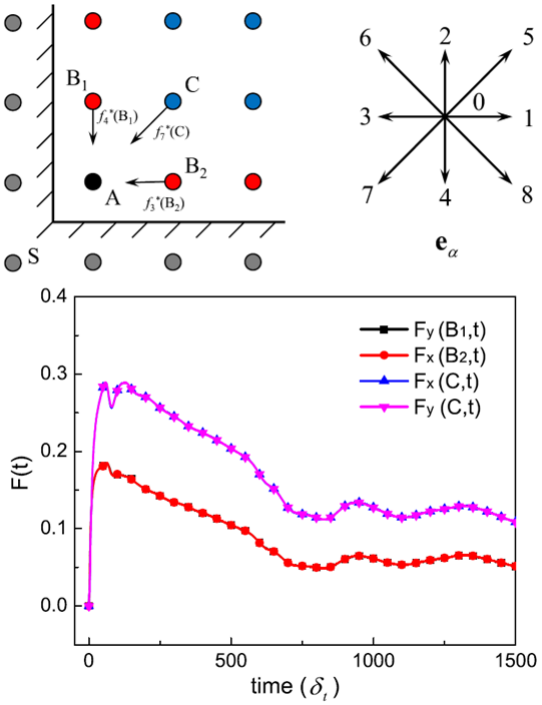

FIG. 7.2: Temporal evolution of pseudopotential interaction forces at selected points in the corner region [6].

Secondly, as illustrated in Fig. 7.2, the pseudopotential interaction force analysis at representative lattice points near the corner reveals that the vertical force component (F_y) remains positive throughout the nucleation stage, which favors upward vapor expansion and accelerates density depletion in the corner region. In addition, from a thermodynamic perspective, concave regions possess a lower surface energy compared to planar sites, thereby reducing the energy barrier for phase change initiation.

7.1.2 V-shaped microheater surface

Fig. 7.3 illustrates the nucleation and evolution of a single bubble on a V-shaped microheater surface. At the early stage ($t^* = 10.2$), nucleation occurs precisely at the bottom tip of the V-groove, indicating that the concave apex serves as a

preferred nucleation site. The bubble then grows rapidly along the vertical axis toward the groove opening ($t^* = 12.3$), driven by the strong temperature gradient near the apex.

At $t^* = 14.3$, the growth rate decreases markedly, entering a quasi-stationary phase where the bubble–liquid interface remains in contact with both inclined walls of the V-groove. This growth arrest is followed by a necking process near the groove outlet ($t^* = 16.9$), and eventually, the bubble detaches from the heated surface at $t^* = 21.7$.

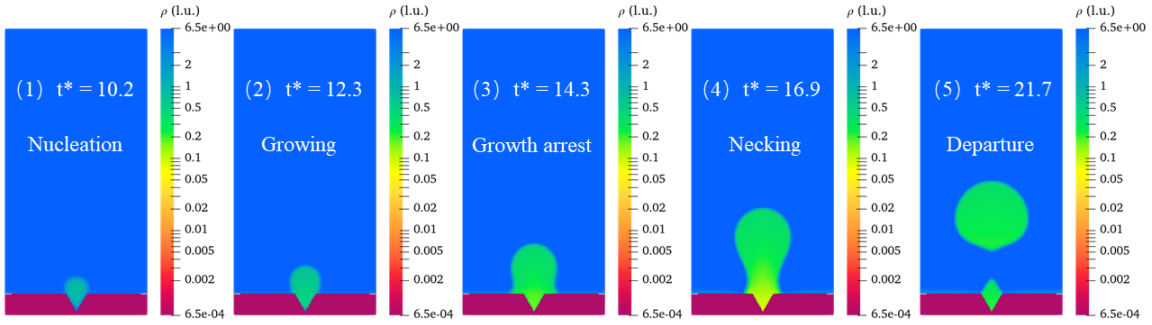

FIG. 7.3: Time evolution of bubble nucleation and departure on a V-shaped microheater surface ($T_s = 0.90T_c$, $\Delta T = 0.01T_c$, $\theta \approx 63.2°$).

Compared with the rectangular-groove and planar surfaces, the V-groove geometry introduces distinct bubble dynamics. Firstly, the inclined walls promote lateral expansion of the bubble, increasing its footprint area on the heated surface and delaying the onset of buoyancy-dominated rise. Secondly, the confinement effect within the V-shaped cavity enhances liquid–vapor contact, resulting in a more stable triple-phase line and suppressing premature detachment. This is consistent with the observation that the bubble in the V-groove maintains a larger volume before departure. Lastly, the altered wetting configuration due to the groove geometry may lead to asymmetric interface curvature, influencing both the local capillary pressure and the force balance governing departure.

Overall, the microscale features of structured surfaces modify local interfacial properties and thereby influence the nucleation energy barrier. Experimental studies have also demonstrated that such engineered surfaces can significantly enhance boiling heat transfer by increasing nucleation site density and stabilizing liquid supply [161–164]. The present simulations qualitatively reproduce these trends by

showing delayed detachment and larger bubble volumes on V-shaped grooves. Nevertheless, a direct quantitative comparison with experimental heat transfer data is not yet available, and further investigations combining detailed force decomposition and wettability analyses are required to fully elucidate the mechanisms and to assess the degree of heat transfer enhancement.

7.2 Pool Boiling Numerical Simulations

This chapter presents a numerical investigation of pool boiling, with particular attention to how boundary and surface conditions shape the observed regimes and heat-transfer response. Because physical pool-boiling experiments vent vapor to the surroundings while lattice Boltzmann simulations often impose a no-slip top wall that can artificially trap vapor, we first benchmark two common top-boundary treatments—no-slip velocity versus constant-pressure—to identify which more faithfully represents open-system boiling and to clarify their implications for heat transfer. Building on this, we employ a grooved structured surface to examine how varying degrees of superheat modulate boiling dynamics, successfully reproducing the three canonical regimes: nucleate boiling, transition boiling, and film boiling. Finally, we extend the analysis to hydrophilic–hydrophobic mixed surfaces.

7.2.1 Pool Boiling: Boundary condition effects

Velocity outlet boundary condition

Firstly, for the velocity boundary condition, as shown in Fig. 7.4, the computational domain is set to 300 lu × 150 lu. The system is initialized with a flat gas-liquid interface, with the liquid occupying the lower region and the gas distributed above. After initializing the density field, a temperature of T_b is applied to the bottom wall, where $T_b = T_s + 0.12T_s$, to simulate the superheated condition of the wall commonly observed in practical boiling scenarios. The Zou-He [165] velocity boundary conditions are applied to both the top and bottom walls, where a no-slip condition [166] ($u_x = u_y = 0$) is enforced. Periodic boundary conditions are imposed on the left and right boundaries to form a closed system. The saturation temperature is set to $T_s = 0.86T_c$, consistent with previous chapters. The

degree of superheat is $0.12T_c$, and the contact angle corresponds to a hydrophilic condition $\varphi = 1.2$.

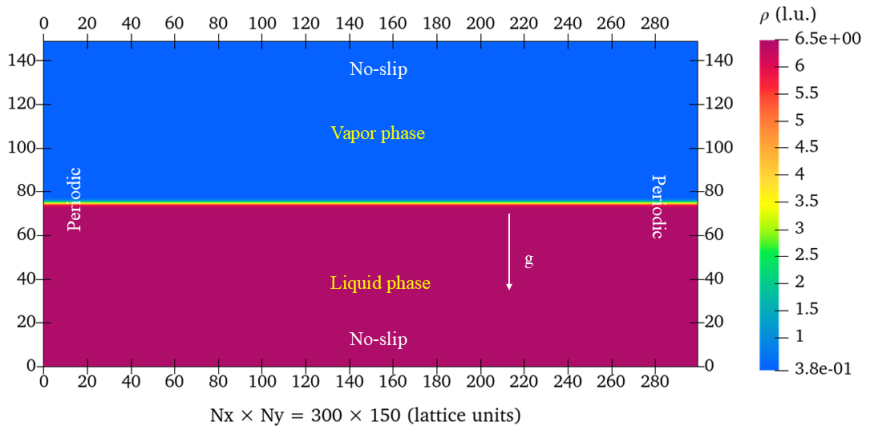

FIG. 7.4: Boundary and initial configuration for pool boiling under Zou-He velocity boundary conditions .

Fig. 7.5 presents the simulation results based on the numerical model described in Chapter 2, illustrating the density field evolution of a two-dimensional pool-boiling phase change process at various dimensionless times t^* (time normalized by t_0; see Chapter 2). During the initial stage ($t^* = 8.15$), temperature perturbations at the bottom surface trigger the formation of small vapor nuclei uniformly distributed along the heating area. In the subsequent period from $t^* = 23.09$ to $t^* = 130.41$, local vapor bubbles grow rapidly and rise upward, followed by bubble coalescence and breakup driven by buoyancy forces [167].

During the stage of $t^* = 258.10$ to $t^* = 365.42$, a region of high density gradually develops near the upper boundary. Although it may visually appear as a vapor cap, the color scale indicates that this region actually corresponds to condensed liquid rather than vapor. The top wall in this simulation is implemented as a no-slip velocity boundary using the Zou–He scheme and maintained at a constant temperature ($T_{\text{up}} = T_s$), effectively acting as a heat sink. This condition establishes a negative temperature gradient pointing toward the wall, which promotes condensation of the rising vapor. As a result, a thin liquid layer forms and accumulates near the upper boundary. This condensed layer suppresses the upward motion of newly generated bubbles, leading to periodic drainage of liquid plumes along the vertical direction. Consequently, the system gradually transitions from

a vigorous nucleate boiling regime into a metastable state that resembles the onset of transition boiling, consistent with the qualitative description reported in Ref. [117].

When $t^* > 380$, localized overheating occurs beneath the condensed liquid layer because the heat flux from the bottom cannot be efficiently transferred through the dense liquid region. This leads to the intermittent formation of column-shaped vapor channels that penetrate upward through the liquid layer. The appearance of these vapor paths indicates that the system is approaching a quasi-steady boiling regime, in which the interplay between condensation at the top and vapor generation at the bottom reaches a dynamic equilibrium.

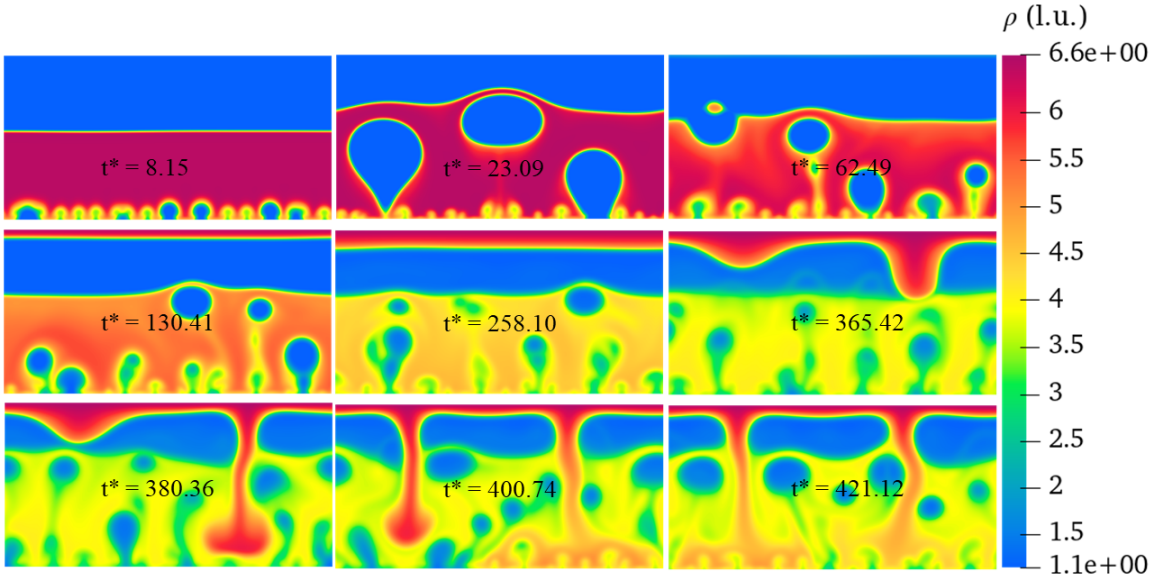

FIG. 7.5: Evolution of the density field during pool boiling with Zou–He velocity boundary conditions. $(\rho, l.u.)$

Fig. 7.6 presents the evolution of the temperature field at various dimensionless times t^*. In the initial stage ($t^* = 8.15$), a distinct thermal gradient forms as the bottom wall is superheated while the upper region remains near the saturation temperature. Localized temperature increases are observed around the nucleated vapor bubbles, indicating the onset of a phase change driven by the input of wall heat. By $t^* = 23.09$, thermal plumes develop prominently around the expanding vapor bubbles, reflecting the strong coupling between latent heat absorption and localized evaporation. As the system evolves through $t^* = 62.49$ to $t^* = 130.41$,

rising vapor bubbles efficiently transport heat upward, leading to a vertically stratified temperature field. The regions surrounding the vapor-liquid interfaces exhibit temperature dips, which are consistent with heat consumption during continuous vapor generation.

During the intermediate stage ($t^* = 258.10$–365.42), vapor accumulates near the top boundary, forming a stable vapor cap. This acts as a thermal insulator, suppressing upward heat transport and resulting in elevated temperatures in the lower liquid region. Consequently, a more uniform temperature field appears in the upper domain, while the bottom region sustains active boiling because of persistent superheat. In the later phase ($t^* > 380$), localized superheated zones emerge beneath the vapor cap, where thermal energy accumulates due to limited heat dissipation. These regions eventually give rise to vapor jets that penetrate the upper interface. The resulting high-temperature cores indicate a strong thermal–hydrodynamic coupling and highlight the insulating effect of the vapor layer [168]. Overall, the observed temperature evolution aligns well with thermodynamic expectations, showcasing wall-induced superheating, latent heat-driven cooling, and the development of vapor-induced thermal resistance.

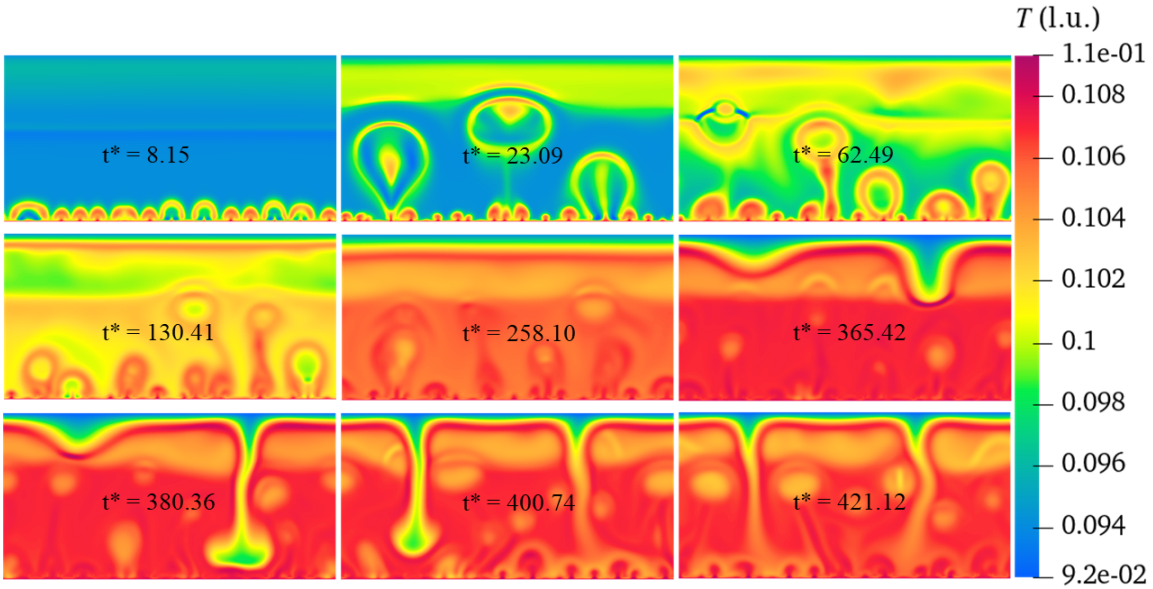

FIG. 7.6: Evolution of the temperature field under the velocity boundary condition $(T, l.u.)$.

Fig. 7.7 illustrates the evolution of the pressure field at various times t^*, corresponding to the same stages as the density and temperature distributions. In

the early stage ($t^* = 8.15$), the pressure field exhibits a sharp horizontal gradient through the liquid-vapor interface, with the liquid region maintaining a higher pressure due to its higher density and temperature near the heated bottom wall.

As the vapor bubbles nucleate and grow ($t^* = 23.09$–62.49), distinct low-pressure regions form within the vapor cores, surrounded by a higher-pressure liquid. This pressure difference drives the bubble expansion and vertical rise, in accordance with the Young–Laplace [75] relation and the buoyancy effect. Between $t^* = 130.41$ and 365.42, the coalescence of vapor bubbles and the formation of a vapor cap lead to a more stratified pressure distribution. The upper vapor layer shows a relatively uniform lower pressure, while the superheated liquid beneath retains a higher pressure, sustaining continuous bubble generation. The flattening of the pressure gradient near the top further confirms the insulating effect of the vapor cap, limiting pressure-driven upward flow. In the later stages ($t^* > 380$), as vapor jets begin to penetrate the upper interface, localized high-pressure zones appear beneath the cap due to accumulated thermal energy and constrained expansion. These regions correspond to the observed superheated liquid cores and are responsible for driving vigorous vapor eruptions. Overall, the pressure field evolution is thermodynamically consistent with the dynamic interplay of phase change, buoyancy, and capillarity, providing further insight into the mechanisms underlying boiling heat transfer [169].

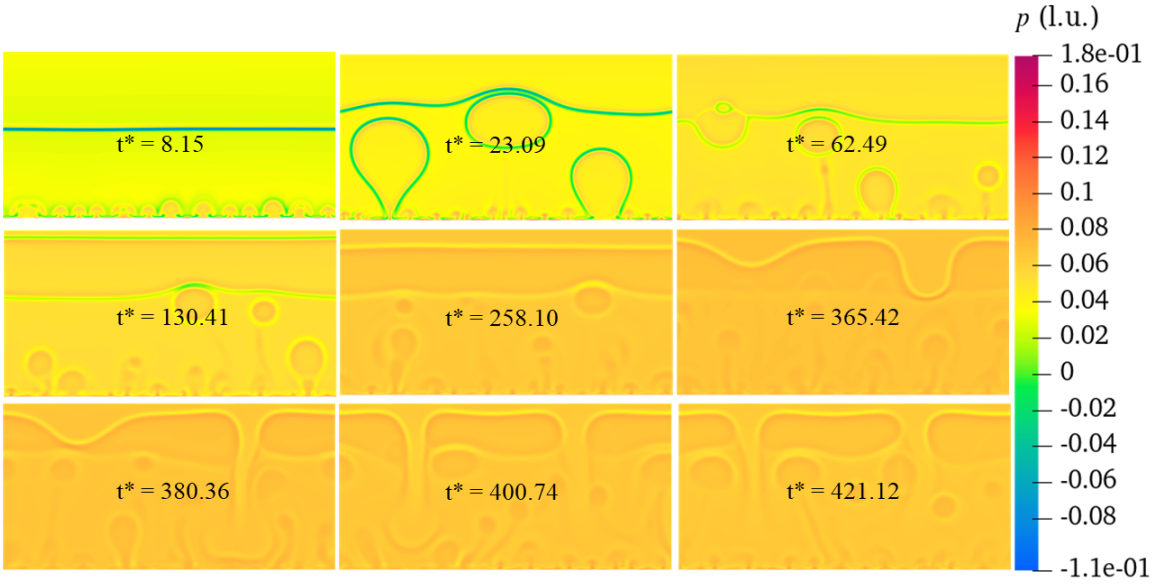

FIG. 7.7: Evolution of the pressure field under the velocity boundary condition ($p, l.u.$).

Constant pressure outlet boundary condition

Fig. 7.8 illustrates the geometric boundary condition under constant pressure. The computational domain is maintained at 300 lu × 150 lu. A constant pressure boundary is applied at the top wall; in practical implementation, since pressure is recovered through the equation of state, it is sufficient to impose a fixed density. Here, the pressure is determined using the Peng–Robinson (PR) EOS [117]. Compared to the velocity boundary setup, the initial liquid height is adjusted. The physical fact that a pressure boundary allows continuous vapor outflow during the boiling process, which may lead to instability in the overall system pressure [170]. Thus, a reduced liquid level is initialized. Specifically, the liquid–vapor interface is set at one-third of the domain height (NY/3), with the upper two-thirds occupied by vapor to mitigate large pressure gradients. All other parameters remain consistent with the velocity boundary case. The corresponding simulation results and detailed analysis are presented in the following description.

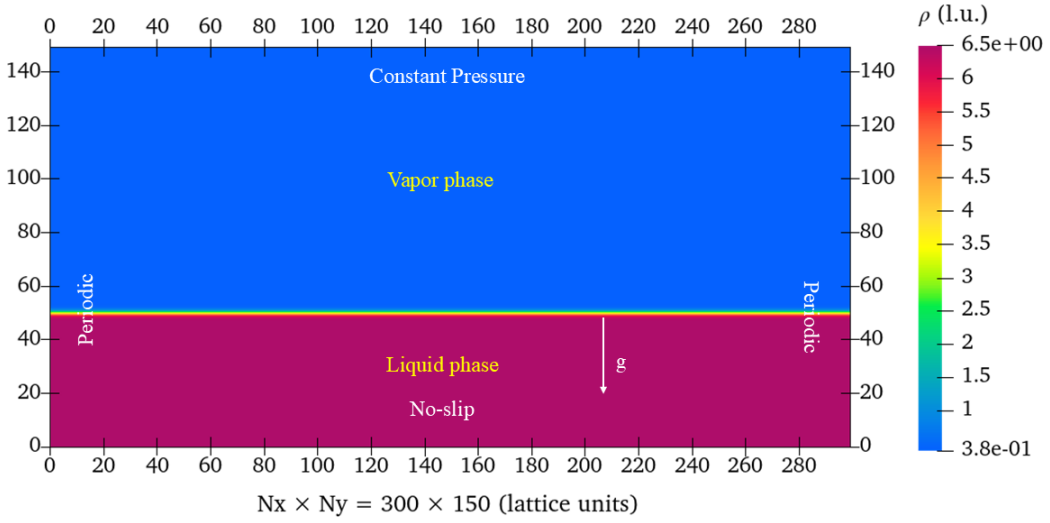

FIG. 7.8: Boundary and initial configuration for pool boiling under constant-pressure conditions

Fig. 7.9 presents the temporal evolution of the density field during the pool boiling process with the top boundary set as a constant pressure condition. Compared to the velocity boundary case, the constant pressure condition allows vapor bubbles to escape freely, making the system more representative of an open configuration. From the figure, it can be observed that during the initial stage ($t^* = 4.06$–9.51), the heat input from the bottom wall gradually triggers the nucleation of uniformly distributed microbubbles, with a relatively stable liquid–vapor interface. As time

progresses ($t^* = 38.04$–89.06), vapor bubbles grow rapidly and rise, which can be clearly observed along the time axis. Multiple bubbles are continuously released from the heated bottom wall, leading to pronounced fluctuations at the interface. However, unlike the velocity boundary case, there is no clear formation of a 'vapor cap', indicating that the pressure limit suppresses vapor accumulation and effectively mitigates vapor build-up near the top of the domain.

In the later stage ($t^* > 153.50$), the thickness of the liquid layer gradually decreases, and the number of vapor bubbles decreases as the boiling process weakens. By $t^* = 262.18$, only a few isolated vapor nuclei remain, and the liquid has almost completely evaporated. This suggests a faster release of thermal energy and more efficient vapor removal under the constant pressure boundary condition [171]. Compared to the vapor retention caused by the "vapor cap" under the velocity boundary, the constant pressure boundary facilitates the formation of vapor escape pathways. This difference manifests in the boiling behavior: the velocity boundary quickly drives the system into a quasi-steady boiling state, whereas the constant pressure boundary results in no evident metastable phase. Moreover, the enhanced heat dissipation in the constant pressure case shortens the overall boiling cycle, which is consistent with thermodynamic principles, that in an open system, the enhanced vapor removal suppresses the increase in internal pressure and significantly influences bubble dynamics and heat transfer behavior [171].

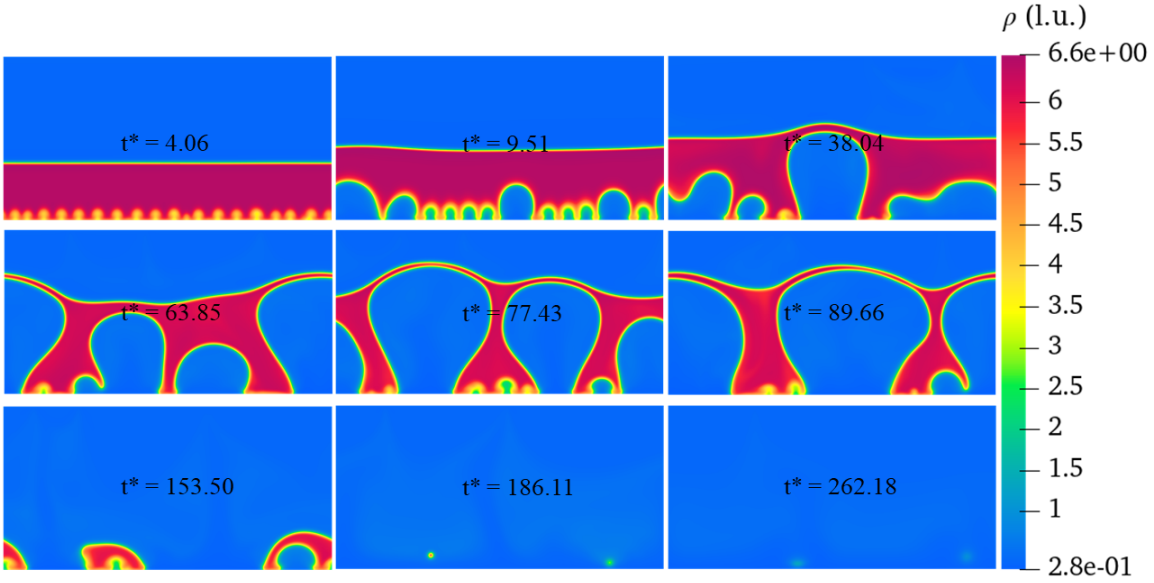

FIG. 7.9: Evolution of the density field under the constant-pressure boundary $(\rho, l.u.)$.

Fig. 7.10 illustrates the temporal evolution of the temperature field under the constant pressure boundary condition applied to the top wall. During the initial stage ($t^* = 4.06$–9.51), the liquid near the bottom is rapidly heated, forming a pronounced temperature gradient, while the upper region remains close to the saturation temperature. As a result, the system exhibits a thermally stratified structure.

In the intermediate stage ($t^* = 38.04$–89.66), with the nucleation and departure of vapor bubbles, multiple convective thermal plumes develop within the liquid. Heat is transported upward through bubble-induced disturbances, leading to large-scale fluctuations in the temperature field. During this process, the temperature distribution becomes highly non-uniform, reflecting a strong coupling between thermal and flow fields. In the later stage ($t^* > 153.50$), the liquid gradually evaporates. Although the bottom region remains at a high temperature, the upper domain exhibits a relatively stable thermal profile because of the smooth removal of vapor bubbles. By $t^* = 262.18$, the temperature in most regions drops significantly, indicating that a substantial amount of thermal energy has been dissipated.

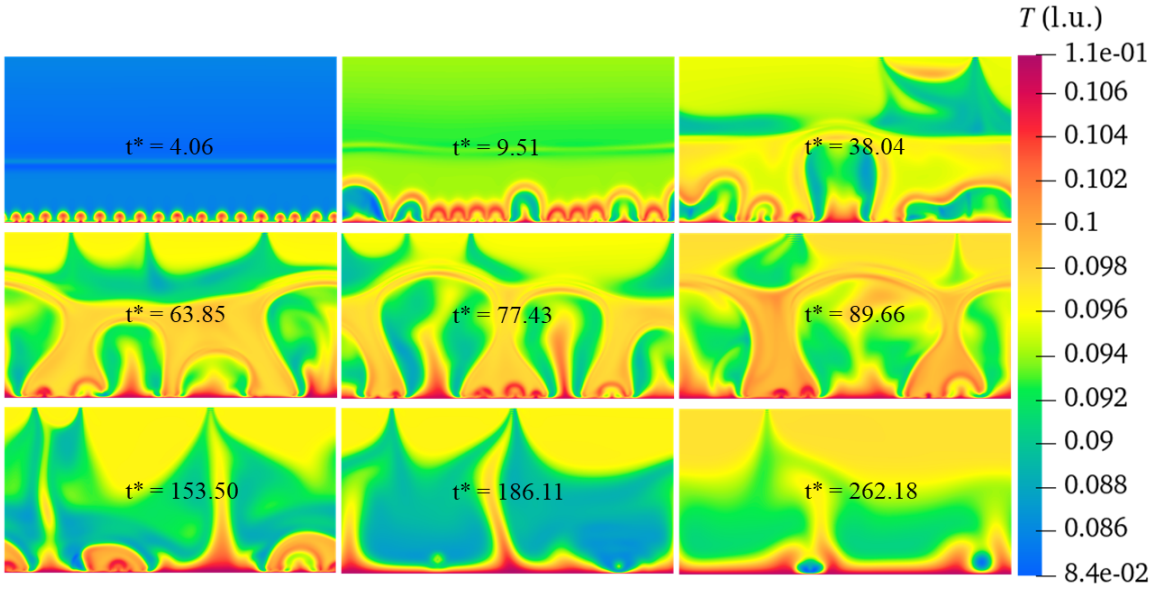

Fig. 7.10: Evolution of the temperature field under the constant-pressure boundary $(T, l.u.)$.

Compared to the velocity limit case, the current condition allows vapor to escape freely, thus preventing the formation of a 'vapor cap' near the top boundary. As a result, the upper region does not develop a strong thermal resistance layer and

heat is transferred more efficiently. The temperature evolution is more uniform over time and the system does not maintain a prolonged metastable boiling state as seen in the velocity boundary scenario. Instead, it undergoes a more rapid thermal decay, which aligns with the expected behavior of an open system.

Fig. 7.11 presents the temporal evolution of the pressure field under the constant pressure boundary condition. During the initial stage ($t^* = 4.06$–9.51), the heating of the liquid at the bottom causes a gradual increase in local pressure, while the top boundary maintains a lower pressure due to the prescribed constant density. As a result, a stable vertical pressure gradient is established throughout the system. In the intermediate stage ($t^* = 38.04$–89.66), with rapid growth and coalescence of the vapor bubbles, low-pressure regions develop inside the bubbles, which are surrounded by a high-pressure liquid. The overall shape of the pressure field closely follows the gas–liquid interface, indicating a well-defined capillary pressure distribution.

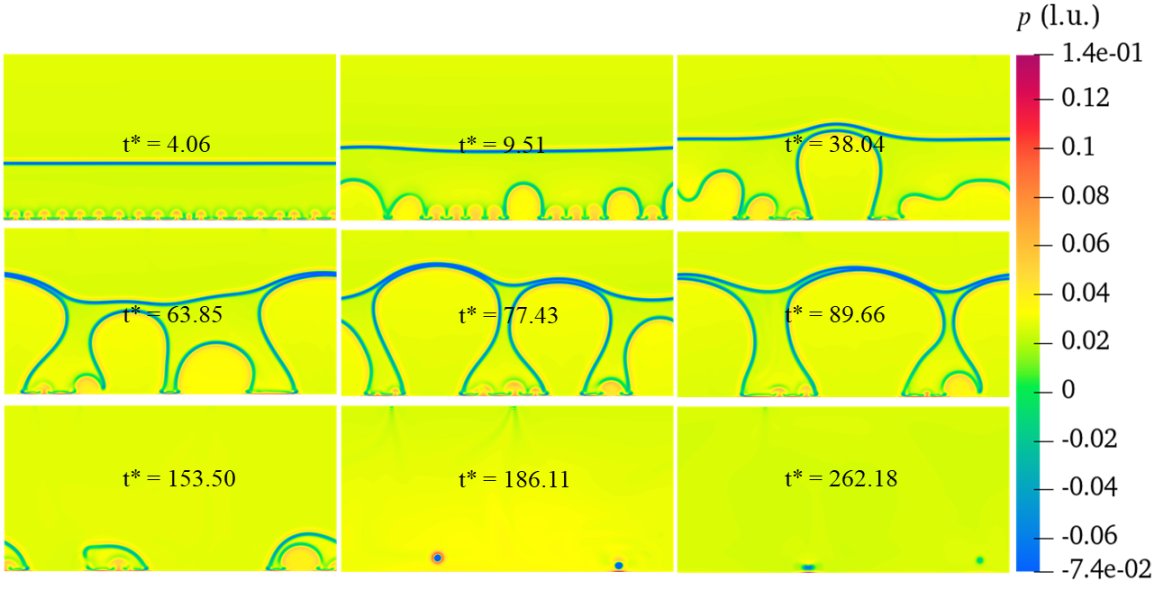

FIG. 7.11: Evolution of the pressure field under the constant-pressure boundary $(p, l.u.)$.

In the later stage ($t^* > 153.50$), as the liquid content decreases, the pressure field gradually stabilizes. By $t^* = 262.18$, the system returns to a predominantly low-pressure state, suggesting completion of the boiling process and attainment of a relatively stable thermodynamic equilibrium.

Observed outcome

Based on the analysis of two-dimensional pool boiling phenomena under both boundary conditions, it can be concluded that for pool boiling that exchanges with an ambient reservoir (no external cross-flow), the constant-pressure boundary reproduces the essential physics more closely, including continuous vapor removal, no artificial vapor retention, and a higher effective heat-release rate. In contrast, the constant-velocity boundary is useful for studying confined or closed systems and for probing cap formation and critical behavior, but it may overpredict thermal resistance and induce localized overpressure near the top wall. These findings are consistent with previous numerical studies, which likewise reported that constant-pressure boundaries are more suitable for simulating open boiling systems with continuous vapor release, whereas constant-velocity boundaries are typically applied in confined domains where pressure buildup and recirculation are of interest [172–174].

7.2.2 Pool Boiling on structured surface

Real heaters are often patterned to trigger nucleation, sustain rewetting, and vent vapor. After the flat–wall baseline, we test a rectangular–grooved surface to see how geometry shifts the boiling regime and heat transfer, using the more physical constant–pressure top boundary.

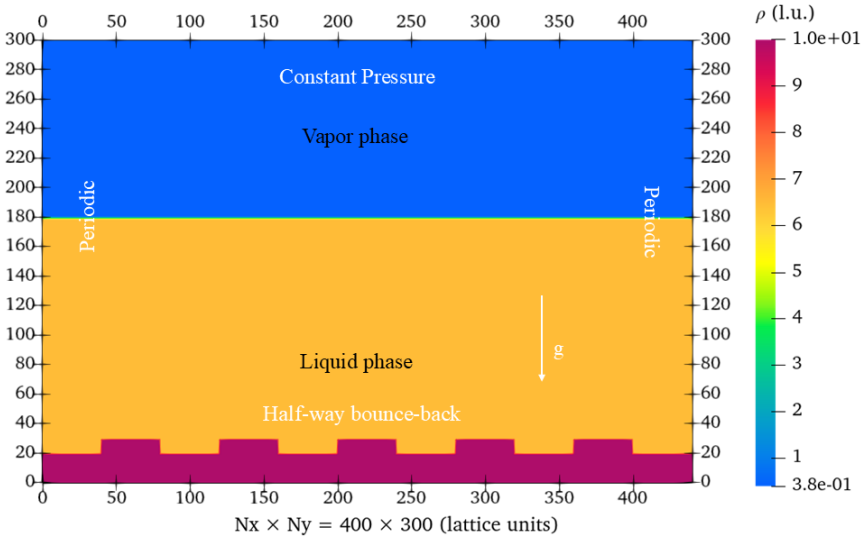

FIG. 7.12: Schematic of the rectangular structured surface configuration with a constant-pressure outlet and periodic lateral boundaries.

The bottom wall is a periodic rectangular groove array (Fig. 7.12); the top is constant pressure to allow vapor escape. The wall is held at $T_s = 0.90T_c$ with three superheats $\Delta T = \{0.12, 0.23, 0.29\}T_c$. The surface is hydrophilic ($\varphi = 1.2$); all other parameters follow the flat-interface case.

As shown in Fig. 7.13, the initial stage ($t^* < 61.2$) is characterized by gradual liquid heating without visible bubble formation. Bubbles nucleate preferentially at the groove corners due to localized density gradients and surface energy minima. In the subsequent growth and departure stage ($81.5 < t^* < 93.7$), bubbles follow the single-bubble dynamics observed in earlier sections, exhibiting regular growth, occasional sliding along the wall, and periodic detachment. Fluid disturbance is minimal, and the interface remains stable—typical of the nucleate boiling regime.

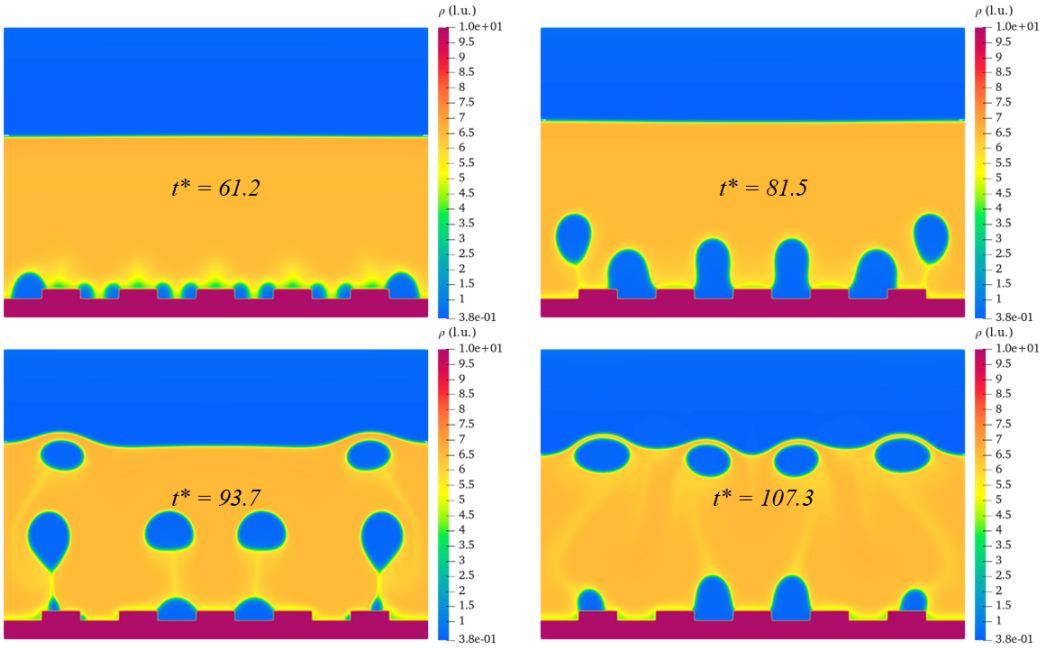

FIG. 7.13: Structured surface pool boiling under $\Delta T = 0.12T_c$ (nucleate boiling).

With higher wall superheat (Fig. 7.14), bubble nucleation occurs earlier than at lower superheat $\Delta T = 0.12T_c$ ($t^* \approx 5.6$), and multiple small bubbles rapidly coalesce to form larger vapor structures covering the grooves. Frequent detachment events ($43.5 < t^* < 73.4$) significantly disturb the interface, while shear effects between liquid and vapor promote irregular nucleation patterns. By $t^* \approx 115.5$, a thickened vapor layer develops near the wall, indicating the onset of transition boiling with unstable interface oscillations but without a fully continuous vapor film.

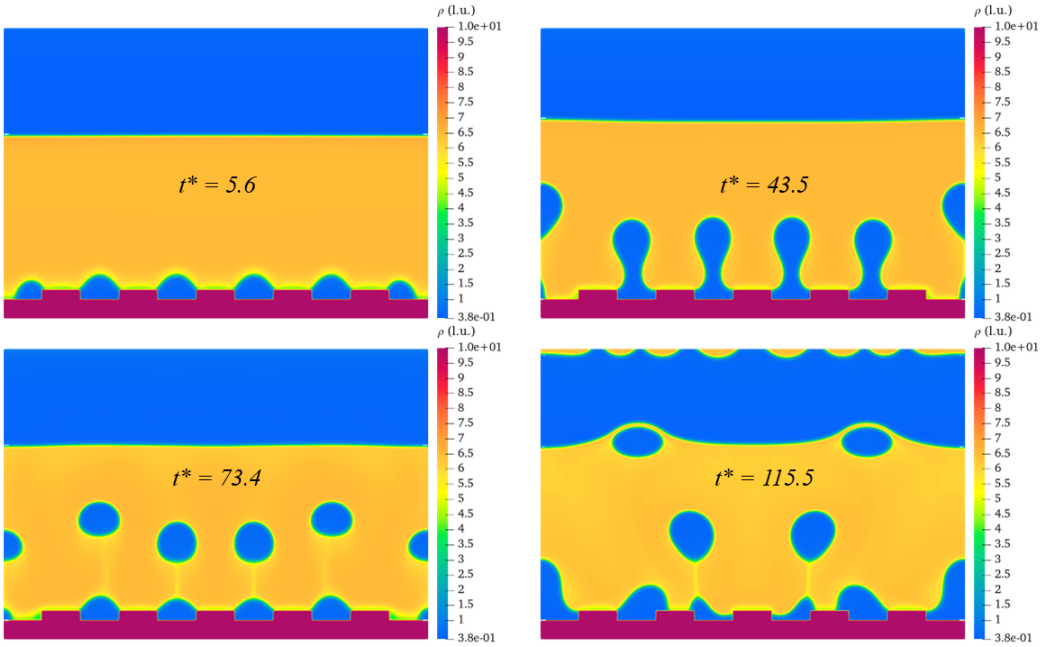

FIG. 7.14: Structured surface pool boiling under $\Delta T = 0.23T_c$ (transition boiling).

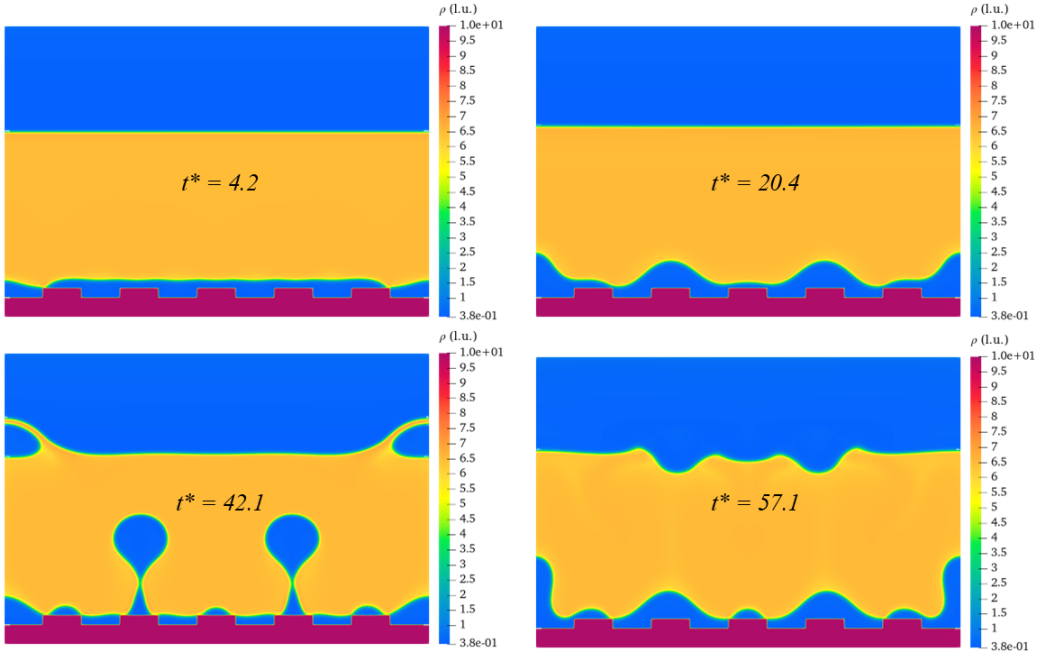

FIG. 7.15: Structured surface pool boiling under $\Delta T = 0.29T_c$ (film boiling).

Under intense heating (Fig. 7.15), bubbles nucleate almost immediately ($t^* \approx 4.2$) and expand rapidly, merging into a continuous vapor layer that blankets the heated surface. This marks the film boiling regime, where the vapor layer acts as a thermal insulator, reducing wall heat transfer efficiency. The persistent vapor coverage

leads to a notable decline in effective heat flux despite the high wall superheat, consistent with the classical boiling curve trend.

Findings on the grooved heater

$\Delta T = 0.12T_c$ (nucleate): groove corner sites seed stable nuclei and the cavities act as liquid reservoirs, leading to earlier ONB and periodic bubble departure with effective rewetting.
$\Delta T = 0.23T_c$ (transition): intermittent vapor patches span adjacent ribs and heat–flux oscillations strengthen, indicating enhanced interface instability.
$\Delta T = 0.29T_c$ (film): a persistent vapor blanket forms across the crests; heat transfer degrades.
Together, the three cases show a clear superheat-driven progression from nucleate → transition → film boiling on the structured surface. Grooves consistently promote nucleation, but their net effect depends on regime: they enhance departure and rewetting at low ΔT, amplify instabilities at intermediate ΔT, and trap vapor at high ΔT. Thus, texturing shifts regime boundaries and modifies the boiling curve relative to a flat heater, guiding designs that boost heat transfer while delaying film boiling.

7.2.3 Mixed wettability surface

Furthermore, this study proposes an implementation scheme for mixed wettability conditions. Taking a computational domain of 200lu × 400lu as an example, the heating section length is set to 80lu, with hydrophilic intervals of 10lu, where the contact angle of the hydrophilic regions is 15 ° and that of the hydrophobic regions is 140 °. The contact angle for the nonheating section is set to 90 °. Fig. 7.16 illustrates the contact angle distribution in this configuration. The bottom boundary is divided into regions of distinct wettability, with blue indicating the hydrophilic section and green the hydrophobic section. This configuration is used to investigate the influence of spatially varying surface wettability on bubble dynamics and local heat flux.

As the implementation of mixed wettability boundary conditions has only recently been completed, a comprehensive set of simulation cases has not yet been performed. Here, I primarily illustrate the numerical setup of the mixed hydrophilic–hydrophobic surface and use the local heat flux distribution as a representative

output to highlight the influence of surface wettability contrast. More systematic investigations under varied operating conditions will be pursued in future work.

FIG. 7.16: Numerical setup of a mixed hydrophilic–hydrophobic surface. ($\Delta T = 0.15T_c$, $\Delta\rho = 0.2$, and $\varphi = 1.2$).

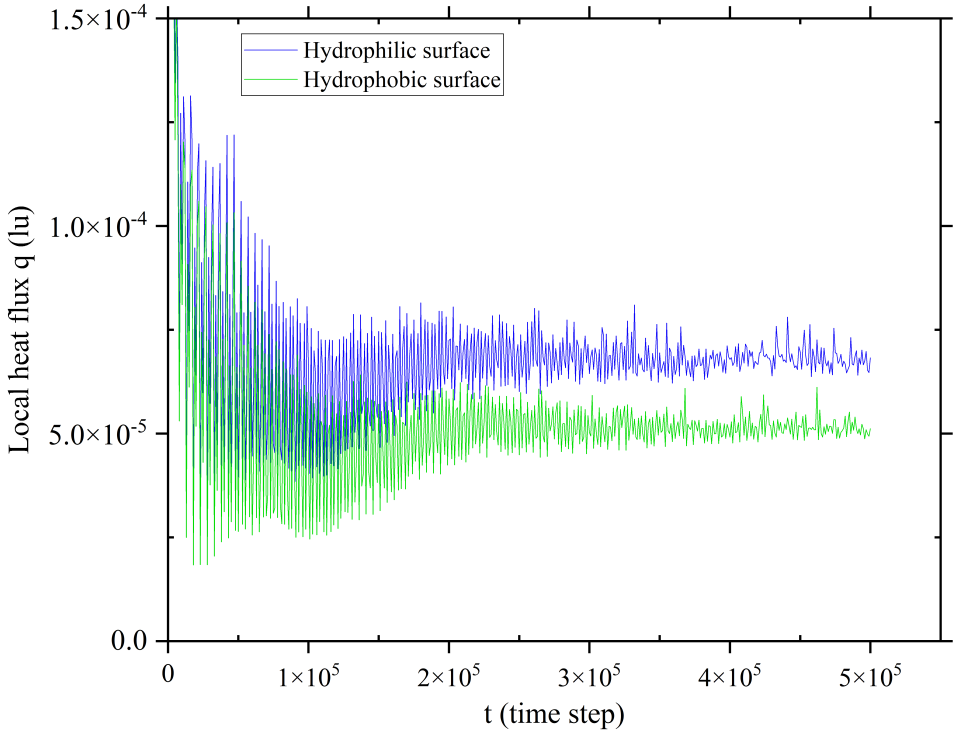

FIG. 7.17: Local heat flux on Mixed Surface
$\Delta T = 0.15T_c$, $\Delta\rho = 0.2$ and $\varphi = 1.2$

As shown in Fig. 7.17, the pronounced early–time oscillations in the wall heat flux $q(t)$ stem from: (i) start-up transients; (ii) the intrinsic burstiness of bubble cycles (rapid contact-line motion and capillary waves); and (iii) discrete-lattice sampling of wall gradients, which makes the finite-difference estimate of q sensitive to small interface shifts. For quantitative reporting, we therefore use a cycle-averaged (running-mean) heat flux over windows of 5×10^3–10^4 time steps to reveal the trend while retaining physically meaningful cycle-to-cycle variability.

Under identical heating, the local heat-flux histories also depend on wettability: hydrophilic surfaces yield slightly higher cycle-averaged q than hydrophobic ones. This is consistent with faster liquid replenishment and more effective rewetting

on hydrophilic walls, which shortens dry-patch residence time and enhances heat transfer.

7.3 Boiling Curve in Pool Boiling

Effect of Heating Mode: Fixed Temperature vs. Constant Heat Flux

This section consolidates the boiling curves obtained under different heating modes (fixed wall temperature vs. constant heat flux) and wettability conditions (controlled by φ). Unless otherwise stated, the saturation temperature is $T_s = 0.86T_c$, the latent heat is $h_{fg} = 0.5702$ following Ref. [99].

Fig. 7.18 compares the boiling curves under identical wettability ($\varphi = 1.2$, $\theta \approx 63.2°$).

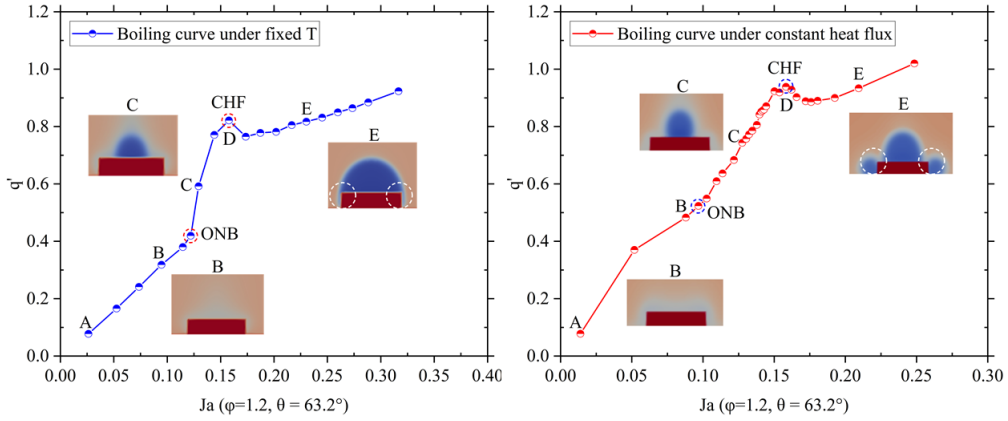

FIG. 7.18: Boiling curves under fixed wall temperature (left) and constant heat flux (right) at $\varphi = 1.2$ ($\theta \approx 63.2°$). ONB and CHF are highlighted; insets show representative interface morphologies at points B–E.

In both cases, the curve evolves through the canonical regimes of natural convection, nucleate boiling, and transition boiling, with the critical heat flux (CHF) identified at the peak q'.

The A–B segment shows a near-linear increase of q' with Ja, with no visible nucleation (inset B). The onset of nucleate boiling (ONB) occurs at

$$\text{Dirichlet: } Ja_{\text{ONB}} \approx 0.12, \qquad \text{Neumann: } Ja_{\text{ONB}} \approx 0.103.$$

The earlier ONB under constant heat flux is attributed to more uniform energy supply and the avoidance of localized wall overheating. After ONB (B–C–D), vigorous bubble formation and departure cause a rapid rise in q'. Both modes reach CHF at $Ja_{\mathrm{CHF}} \approx 0.158$, while the peak heat flux differs:

$$q'_{\mathrm{CHF}} \approx 0.821 \text{ (fixed } T\text{)}, \qquad q'_{\mathrm{CHF}} \approx 0.938 \text{ (constant } q\text{)}.$$

The higher q'_{CHF} under Neumann heating stems from a stable nucleation zone and frequent surface refreshment that reduce vapor-induced thermal resistance.

Beyond CHF (D–E), a temporary drop in q' is observed due to the development of a vapor layer on the wall (inset E), followed by partial recovery as the film becomes unstable. Under fixed-T heating, the top-domain vapor retention is stronger, whereas constant-q heating facilitates vapor removal and sustains a higher overall heat-transfer level.

It should be emphasized that the present boiling curves obtained from the LBM simulations cannot be quantitatively compared with literature data, either numerical or experimental. Direct comparison would require full consistency of model formulation and parameters, including the choice of the equation of state, collision operator, forcing scheme, boundary conditions, and the unit conversion strategy. Since these aspects vary substantially across different implementations, quantitative agreement cannot be expected.

Nevertheless, the qualitative trends observed in this study align well with previous findings. In particular, both experimental [175, 176] and numerical [164, 177] investigations reported that increasing surface wettability or applying hybrid wettability patterns lowers the incipient wall superheat and enhances heat transfer performance, which is consistent with the present LBM results.

Accordingly, the present analysis focuses on systematic comparisons across different operating conditions within the same modeling framework, which provides a controlled basis for assessing the role of surface wettability.

Effect of Wettability: $\varphi = 1.5$ vs. $\varphi = 1.7$

Fig. 7.19 reports the variation of the average local heat flux q with Ja for two hydrophilic surfaces.

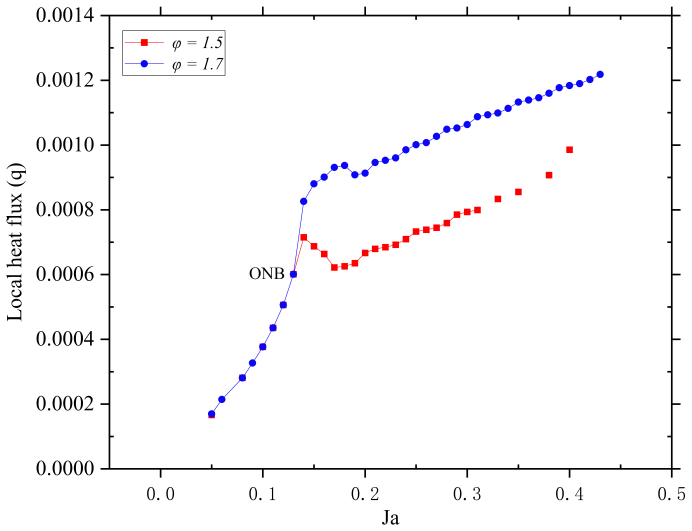

FIG. 7.19: Effect of wettability on local heat flux: comparison of $\varphi = 1.5$ and $\varphi = 1.7$. ONB occurs at $Ja \approx 0.12$ for both cases; post-ONB the more hydrophilic surface ($\varphi = 1.7$) sustains higher q and a smoother increase with Ja.

This wettability dependence has also been reported in previous LBM-based investigations. For instance, Gong and Cheng [172, 178] demonstrated that enhanced hydrophilicity promotes liquid replenishment and stabilizes bubble departure, while Zhang et al. [179, 180] systematically quantified the effect of contact angle on bubble dynamics and boiling heat transfer, which is consistent with the present findings.

Both curves exhibit a linear natural-convection branch up to $Ja \approx 0.12$, where ONB occurs almost simultaneously, indicating that in the present parameter window ONB is primarily governed by wall superheat rather than the modest wettability change. After ONB, the more hydrophilic surface ($\varphi = 1.7$) reaches a higher q immediately and, after a shallow notch around $Ja \approx 0.18$–0.20, keeps increasing monotonically with Ja.

This trend reflects rapid bubble departure, a stable three-phase contact line, and efficient rewetting that suppress persistent vapor coverage. For $\varphi = 1.5$, q shows a pronounced dip right after ONB (local minimum at $Ja \approx 0.15$–0.20) and then recovers gradually. The temporary deterioration is attributed to longer bubble residence and coalescence-induced vapor patches (pseudo dry-out) that reduce the effective heat-transfer area and add thermal resistance.

Within the explored range, heating mode primarily shifts ONB and the achievable CHF heat flux, while wettability governs the post-ONB performance via bubble departure dynamics and surface rewetting. Pursuing a more hydrophilic state (here, $\varphi = 1.7$) enhances nucleate-boiling heat transfer and mitigates transient dry-out, and a constant heat-flux supply further elevates the attainable heat flux at CHF.

7.4 Summary of this Chapter

This chapter extended the validated MRT–pseudopotential LBM to pool–boiling scenarios that are closer to practical use and distilled modeling choices that materially affect predictions. We first contrasted two common top–boundary treatments on a flat pool: a no–slip (velocity) outlet versus a constant–pressure outlet. We then examined a rectangular–grooved heater under increasing superheat and, where relevant, contrasted wettability settings to expose their impact on local and global heat transfer. (All 3D implementation and checks are moved to Appendix C to keep the focus here on 2D pool boiling). The main conclusions are as follows:

Effect of the top boundary condition: A no–slip (velocity) top traps vapor and forms a persistent *vapor cap*, raising thermal resistance and producing a metastable transition–boiling regime with large heat–flux oscillations. A constant–pressure top vents vapor continuously, yields smoother field evolution and higher effective heat release, and better represents an open pool. We therefore adopt the constant–pressure outlet for subsequent pool–boiling studies.

Effect of surface geometry: On a grooved heater, superheat drives a clear progression nucleate $\rightarrow$ transition $\rightarrow$ film boiling. Grooves seed nucleation at corners and act as liquid reservoirs: they enhance departure and rewetting at low ΔT, amplify interface instabilities at intermediate ΔT, and can trap vapor at high ΔT. Thus, texturing shifts regime boundaries and modifies the boiling curve relative to a flat heater.

Effect of wettability: Under identical heating, hydrophilic settings (smaller apparent θ via the virtual–density scheme) show slightly higher cycle–averaged wall heat flux due to faster liquid replenishment and shorter dry–patch residence; hydrophobic settings show the opposite trend.

On heat–flux oscillations: Early–time peaks reflect start–up transients, the

burstiness of bubble cycles (contact–line/capillary dynamics), and discrete sampling of wall gradients. We report running–average heat fluxes (window 5×10^3–10^4 time steps) to reveal trends while retaining physically meaningful cycle–to–cycle variability.

The present configurations are designed to emulate open pool boiling conditions without imposed cross–flow, using a single–component liquid–vapor system. Within this framework, several numerical aspects have a direct impact on the boiling response. For instance, the thermophysical properties are governed by the chosen equation of state, here the Peng–Robinson EOS, which reproduces coexistence reasonably but tends to be less accurate on the dilute–vapor branch and near the critical point [164, 179]. Similarly, the diffuse–interface representation inherent in the pseudopotential model requires sufficient grid resolution near solid boundaries to minimize spurious currents [172]. As a result, the boiling curves reported in this chapter are not intended as absolute CHF benchmarks; instead, they should be interpreted as sensitivity analyses that reveal how boundary conditions, geometry, and surface wettability steer the simulated boiling regimes.

Overall, these calculations clarify which modeling choices are most appropriate for capturing the physics of open pool boiling. In particular, they demonstrate that (i) constant–pressure outlets more faithfully reproduce vapor release into an open reservoir, (ii) structured surfaces modify local interfacial dynamics and promote nucleation, and (iii) increased wettability systematically enhances heat transfer. This provides not only guidance for subsequent application–oriented simulations, but also physical insight into the mechanisms controlling bubble dynamics and heat–transfer performance.

Chapter 8

Conclusion and Outlook

This dissertation has focused on the study of single-bubble boiling using the lattice Boltzmann method (LBM), in close connection with experimental validation and theoretical model comparisons. A comprehensive numerical framework was developed, systematically evaluated, and extended to address fundamental questions of bubble dynamics and boiling heat transfer.

8.1 Conclusions

The numerical framework implemented in this work integrates several submodels that together constitute a state-of-the-art multiphase LBM method. At its core lies the Huang-MRT pseudopotential model, which, based on a third-order Chapman–Enskog expansion, significantly improves numerical stability while enabling controllable adjustment of surface tension and the liquid–vapor density ratio. On top of this, a virtual-density wetting scheme was introduced to achieve stable and accurate control of the contact angle, while the Peng–Robinson equation of state was employed to ensure thermodynamic consistency and to extend the attainable density ratio. Combined with an improved collision operator, these submodels form a complete and advanced LBM framework. It is worth emphasizing that such a combination is not available in existing open-source codes such as OpenLB, and was therefore specifically developed in this work to advance the capabilities of multiphase LBM simulations.

The simulations carried out with this framework successfully reproduced the entire single-bubble life cycle, including nucleation, growth, departure, and collapse. Importantly, the LBM approach intrinsically accounts for all relevant physical mechanisms during the boiling process, which constitutes a clear advantage compared with traditional CFD methods that typically rely on empirical closure assumptions. The analysis demonstrated that both surface wettability and wall superheat, represented by the Jakob number, play a decisive role in determining the bubble departure diameter and frequency. Furthermore, systematic comparison of fixed-temperature and constant-flux boundary conditions revealed distinct differences in bubble cycle evolution and in the distribution of local heat flux.

To strengthen confidence in the predictive capability of the developed framework, a dedicated single-bubble boiling facility was designed and employed to generate reference data under controlled conditions. An image-processing algorithm was implemented to automatically extract bubble geometry and quantitative features from high-speed recordings. The comparison showed that the LBM model can quantitatively predict bubble departure diameter and frequency in good agreement with experiments. This constitutes, to the best of our knowledge, the first experimental validation of the present code and the integrated set of models. Despite certain limitations of the experimental setup, this validation represents a clear step forward compared with many existing LBM studies, which often lack direct experimental confirmation.

The developed tool was further used to systematically compare LBM predictions with classical empirical correlations and theoretical models for bubble departure diameter, including those of Fritz, Cole, and Ruckenstein. The results showed that while static correlations provide valid predictions only at low Jakob numbers, they fail to capture dynamic effects at higher superheats. Beyond this, the framework was demonstrated to be suitable for assessing closure models such as the force-balance approach. This capability allowed the strengths and weaknesses of such models to be identified, and enabled the proposal of an improved departure-diameter correlation that incorporates both contact angle and Jakob number, thereby providing new physical insights.

Finally, the validated LBM framework was applied to structured heating surfaces and more complex boundary conditions. The results revealed the influence of surface wettability and geometry on bubble nucleation and departure behavior. Preliminary boiling curves were obtained, suggesting that the model can be used as a

quantitative tool for investigating heat-transfer enhancement mechanisms. Overall, this dissertation establishes a comprehensive framework that not only advances the numerical modeling of single-bubble boiling, but also provides theoretical and experimental cross-validation, setting a solid basis for future developments.

8.2 Outlook

Although significant progress has been made in this work, several directions remain open for further exploration. One important task is to further increase the physical fidelity of simulations. Current density ratios are still lower than those of real water–steam systems, and future efforts should focus on improving the attainable density ratio, incorporating realistic thermophysical properties, and considering temperature-dependent transport coefficients. Including additional physical effects such as Marangoni stresses will further enhance realism.

Another critical step is the extension to three-dimensional simulations, which are necessary to capture bubble morphology, coalescence, and vapor chimney dynamics more faithfully. Alongside, the framework should be extended from single-bubble cases to subcooled boiling and flow boiling conditions, which are of direct relevance for engineering applications. Being validated already for single-bubble boiling, the present code has the potential to be applied to complex boiling scenarios, and consequently to support the optimization of heat-transfer surfaces and systems in advanced thermal management technologies.

Further development is also expected in the field of closure modeling and multiscale coupling. The correlations proposed in this dissertation, such as the departure diameter expressed as a function of contact angle and Jakob number, can serve as closure laws for engineering-scale CFD models. At the same time, the insights gained from LBM simulations can be used to address limitations of existing force-balance models, particularly regarding the accurate representation of the bubble contact area. Such improvements will strengthen the link between mesoscopic simulations and macroscopic boiling models.

Finally, the experimental platform should be further upgraded to enable broader validation of the numerical framework. This includes advanced diagnostics such as temperature sensor arrays, improved heater designs, and extended measurements

with different fluids and surface materials. Such data would provide a more comprehensive benchmark for testing and extending the predictive capability of the LBM approach.

8.3 Closing Remarks

In conclusion, this dissertation has demonstrated that the Huang-MRT pseudopotential LBM approach, complemented with virtual-density wetting control, a thermodynamically consistent equation of state, and validation against experiments, represents a powerful and versatile framework for studying single-bubble boiling. The framework intrinsically incorporates the key physical mechanisms of boiling, distinguishes itself from traditional CFD methods, and provides a solid foundation for bridging microscopic insights and engineering-scale modeling.

Looking ahead, with continuous improvements in numerical fidelity and experimental validation, the LBM-based approach developed here is expected to contribute significantly to the understanding, prediction, and optimization of boiling heat transfer in advanced applications.

Appendix A: LBM Models and Forcing Schemes

.1 LBM Phase Separation Models

The most widely used are the color-gradient model; free-energy model; phase-field model; and pseudopotential (Shan–Chen) model. Each model has distinct theoretical foundations, numerical features, and application domains.

Color Gradient model

The color gradient model achieves phase separation by assigning different color indices to immiscible fluid components and introducing an interfacial force based on the local color gradient [181]:

$$\mathbf{F}_{\text{interface}} = -\kappa \nabla \phi$$

where ϕ is a color function and κ controls the surface tension. This model is effective in simulating immiscible two-phase flows such as oil–water or benzene–water systems. Recent developments have extended its capability to moderately high Reynolds numbers and density ratios [182–184]. However, due to its lack of thermodynamic consistency and inability to couple temperature or latent heat effects, it is not suitable for phase-change phenomena such as boiling.

Free-Energy Model

The free-energy model is built on a thermodynamically consistent formulation [185], using a free-energy functional to describe interfacial physics:

$$\mathcal{F} = \int \left(\psi(\phi) + \frac{\kappa}{2} |\nabla \phi|^2 \right) d\mathbf{x}$$

with the interfacial force derived as:

$$\mathbf{F}_{\text{interface}} = -\phi \nabla \mu, \quad \mu = \psi'(\phi) - \kappa \nabla^2 \phi.$$

While the free-energy model offers thermodynamic consistency and supports phase equilibrium and latent heat modeling, it suffers from numerical instability near

sharp interfaces and lacks Galilean invariance [63]. Although improved formulations—such as stress tensor corrections [186] and entropy-based schemes [187]—have enhanced its accuracy, they come at the cost of significantly increased computational effort. Given these limitations, especially in dynamic boiling simulations requiring both robustness and efficiency, the free-energy model is not adopted in this study.

Phase-Field Model

The phase-field model describes interfacial dynamics using the Cahn–Hilliard equation [188] coupled with the Navier–Stokes equations:

$$\frac{\partial \phi}{\partial t} + \nabla \cdot (\phi \mathbf{u}) = \nabla \cdot (M \nabla \mu)$$

where ϕ is the order parameter, M is mobility, and μ is the chemical potential derived from a free-energy functional [189].

The phase-field model provides accurate control over interface thickness and surface tension, making it well suited for high density ratio flows and interfacial phenomena such as droplet coalescence and breakup [**?**]. It is often applied to multiphase problems involving large Reynolds and Weber numbers and has demonstrated strong accuracy in capturing complex interface dynamics [2, 185, 190]. However, the need to solve the Cahn–Hilliard equation introduces significant computational cost and memory overhead. For relatively simple cases such as single bubble rising or boiling, this model is less favored because of its reduced efficiency. Therefore, it is not adopted in this study.

Pseudo-potential Model

The pseudopotential model, introduced by Shan and Chen [2], induces phase separation through an interparticle force derived from a density-dependent pseudopotential function:

$$\mathbf{F}(\mathbf{x}) = -G\psi(\mathbf{x}) \sum_i w_i \psi(\mathbf{x} + \mathbf{e}_i)\mathbf{e}_i.$$

The SC model is conceptually simple and efficient, requiring only local interactions. Recent advances in force schemes, EOS design, and MRT collision [191, 192] have enabled it to simulate flows with density ratios up to 1000, Re $>$ 6000, and We $>$ 400, reaching experimentally relevant regimes. Moreover, it has been successfully extended to model phase-change heat transfer such as boiling and condensation, with natural support for liquid-vapor co-existence and surface tension.

Considering the objectives of this study, namely, simulation of single bubble nucleation and departure during pool boiling, the pseudopotential model offers the best trade-off between physical fidelity and numerical efficiency. Capture key phase-change features, allow for interface evolution without explicit tracking, and can be coupled with temperature fields via appropriate force and energy source terms. Therefore, the pseudopotential model is adopted as the foundational framework in this work.

A comparative overview of the four LBM models is summarized in Table A.1.

TABLE A.1: Comparison of LBM models.

Model	**Advantages**	**Limitations**	**Typical Applications**
Color-gradient [35]	Sharp interface, immiscible flows	Lacks thermodynamic consistency; not for phase change	Oil–water flow, interface breakup
Free-energy [36]	EOS-compatible with thermodynamic consistency	High cost; interface-near stability issues	Multiphase equilibrium; interfacial physics
Phase-field [37]	Precise interface control; topology changes	Cahn–Hilliard adds significant cost	Droplet dynamics, coalescence, emulsification
Pseudopotential (SC) [2]	Phase-change capable; simple	Weak σ control; moderate EOS accuracy	Boiling, condensation, bubble dynamics

.2 Forcing Schemes in Pseudopotential LBM

As mentioned in the previous section, forcing schemes play a critical role in multiphase LBM simulations. In the pseudopotential LBM, phase separation is driven

by an interparticle interaction force, which is introduced into the evolution equation as a source term. More broadly, various forces, such as gravity, surface tension, or fluid-structure interactions, can be incorporated through similar formulations. However, the form and implementation of force terms directly affect the stability, isotropy, and accuracy of the model. This section focuses on several commonly used force schemes in pseudopotential LBM, including the Shan–Chen [2], Gong [38], and Guo [39] formulations, and compares their characteristics and suitability for multiphase flow simulations.

Shan-Chen Interaction Force

The original force formulation proposed by Shan and Chen [2] is given by:

$$\mathbf{F}_{\mathrm{SC}}(\mathbf{x}) = -Gc_s^2\psi(\mathbf{x})\nabla\psi(\mathbf{x}),$$

where G is the interaction strength and $\psi(\rho)$ is the pseudopotential function that models the effective attraction between particles. The corresponding non-ideal equation of state (EOS) takes the form:

$$p = \rho c_s^2 + \frac{Gc_s^2}{2}\psi^2,$$

which can be inverted to yield:

$$\psi(\rho) = \sqrt{\frac{2(p-\rho c_s^2)}{Gc_s^2}}.$$

This flexibility allows custom EOS formulations $p(\rho, T)$ to be embedded using appropriate choices of $\psi(\rho)$. The commonly used pseudopotential forms are summarized in Table A.2, each offering different advantages depending on the target EOS and the desired simulation accuracy.

The discrete implementation of Eq. (.2) is typically written as:

$$\mathbf{F}_{\mathrm{SC}}(\mathbf{x}) = -\psi(\mathbf{x})\sum_i Gw_i\psi(\mathbf{x}+\mathbf{e}_i)\mathbf{e}_i,$$

which is straightforward and efficient, but can suffer from anisotropy and spurious currents near interfaces, especially at large density ratios.

TABLE A.2: Commonly used functions in pseudopotential LBM

Formulation	Expression	Remarks
Shan–Chen (SC)	$\psi(\rho) = 1 - e^{-\rho}$	Simple form; suitable for low density ratios [2].
Polynomial form	$\psi(\rho) = \rho_0 \left(1 - e^{-\rho/\rho_0}\right)$	Tunable ρ_0; high density ratio capable [191].
EOS-based form	$\psi(\rho) = \sqrt{\frac{2(p-\rho c_s^2)}{G c_s^2}}$	EOS-based (PR, vdW); enhances thermodynamic consistency [193].

Gong's Forcing Scheme

To improve isotropy and interface consistency, Gong et al. [194]introduced a modified form based on the potential gradient :

$$\mathbf{F}_{\text{Gong}} = -\beta c_s^2 \psi(\mathbf{x}) \nabla \psi(\mathbf{x}) - (1-\beta) c_s^2 \nabla \left(\frac{\psi^2(\mathbf{x})}{2} \right),$$

where $\beta \in [0, 1]$ is a weighting coefficient that depends on the choice of EOS. The discrete implementation is as follows:

$$\mathbf{F}_{\text{Gong}}(\mathbf{x}) = -\beta \psi(\mathbf{x}) \sum_i G w_i \psi(\mathbf{x} + \mathbf{e}_i) \mathbf{e}_i - \frac{1-\beta}{2} \sum_i G w_i \psi^2(\mathbf{x} + \mathbf{e}_i) \mathbf{e}_i.$$

The recommended values of β for typical EOS are given in Table A.3.

TABLE A.3: Weighting factor β for different EOS in Gong force

EOS	S-C	van der Waals	Peng–Robinson
β	0.886	0.55	1.16

Guo's Forcing Scheme

Guo et al. [39] developed an improved force incorporation method that directly modifies the evolution equations:

$$f_i(\mathbf{x} + \mathbf{e}_i \Delta t, t + \Delta t) = f_i(\mathbf{x}, t) - \frac{1}{\tau} \left[f_i - f_i^{\text{eq}} \right] + \Delta t \, F_i,$$

where the forcing term F_i is given by:

$$F_i = \omega_i \left[\frac{\mathbf{e}_i - \mathbf{u}}{c_s^2} + \frac{(\mathbf{e}_i \cdot \mathbf{u})\mathbf{e}_i}{c_s^4} \right] \cdot \mathbf{F}.$$

This method improves Galilean invariance [51], reduces spurious velocities [195], and maintains second-order accuracy in time, making it a widely adopted method in modern pseudopotential models.

Table A.4 summarizes the characteristics of the three force schemes.

TABLE A.4: Comparison of SC, Gong, and Guo forces in LBM

Force Scheme	**Advantages**	**Disadvantages**	**Typical Application**
Shan–Chen (SC)	Simple implementation	Poor isotropy, spurious currents at high density ratios	Early models
Gong	Improved isotropy, EOS-adaptable	More complex implementation	Law density ratio simulations
Guo	Galilean invariant, second-order accuracy	Requires reformulation of evolution equation	Dynamic flows with strong phase change

In addition to the above, the G values in different force schemes can affect key properties such as density ratio, droplet size, surface tension, and phase separation rate. The relevant principles and analysis can be found in the references [196][197][198].

Appendix B: Figures for Wettability Calibration

This appendix gathers the multi–panel snapshots and extended calibration plots referenced in Sec. 2.9. They illustrate the monotonic control of the apparent contact angle θ using the virtual density parameters φ (hydrophilic side) and $\Delta\rho$ (hydrophobic side) on flat and curved walls, in 2D and 3D.

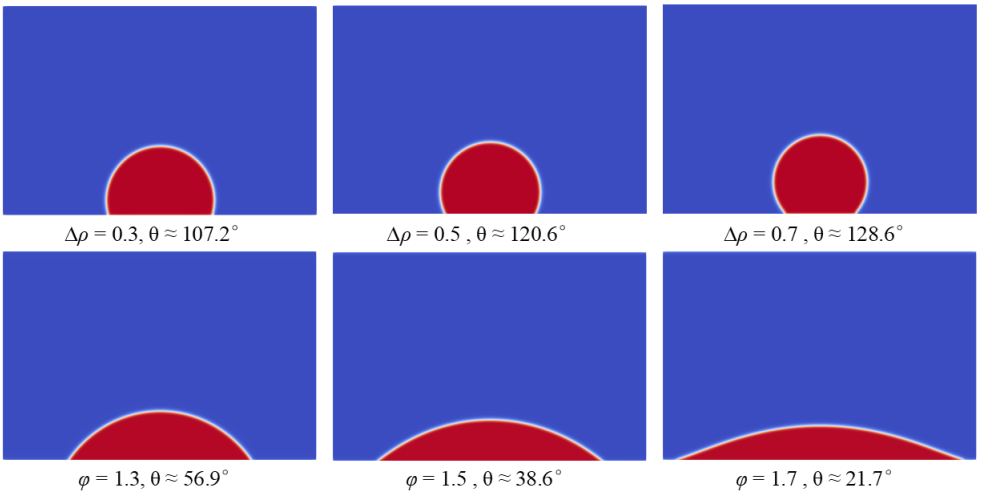

FIG. B.1: 2D flat wall: final contact angles for several φ and $\Delta\rho$ settings.

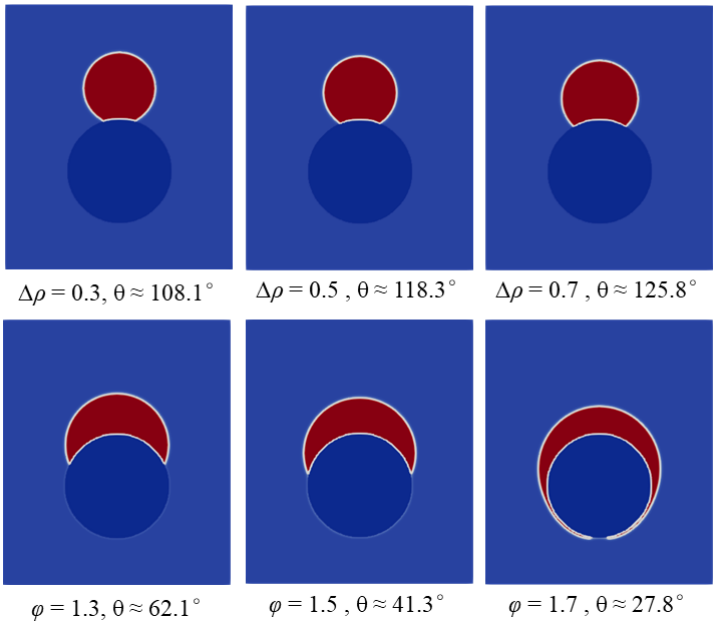

FIG. B.2: 2D curved wall: contact–angle control via the virtual–density scheme.

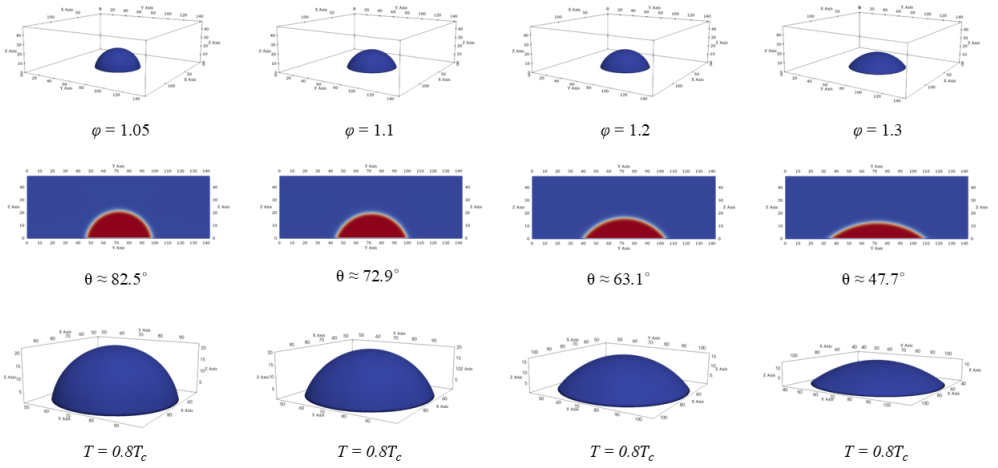

FIG. B.3: 3D flat wall (hydrophilic): contact angles tuned by φ.

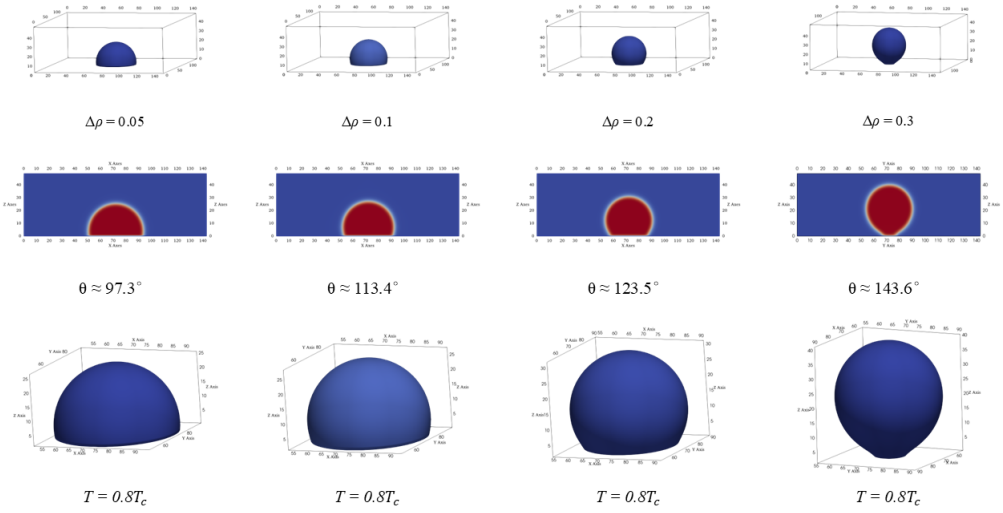

FIG. B.4: 3D flat wall (hydrophobic): contact angles tuned by $\Delta\rho$.

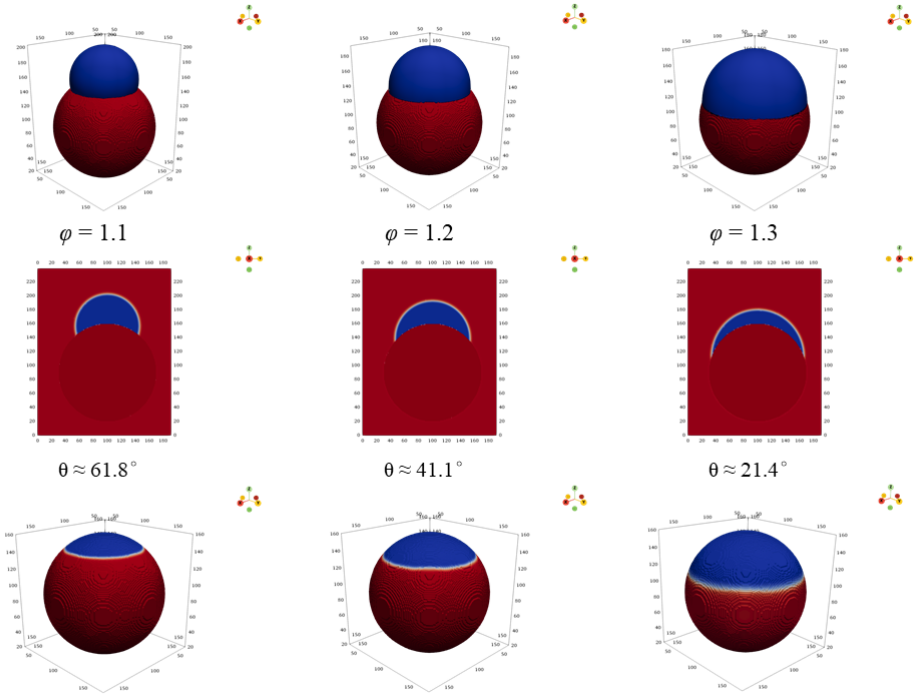

FIG. B.5: 3D curved wall (hydrophilic): contact angles tuned by φ.

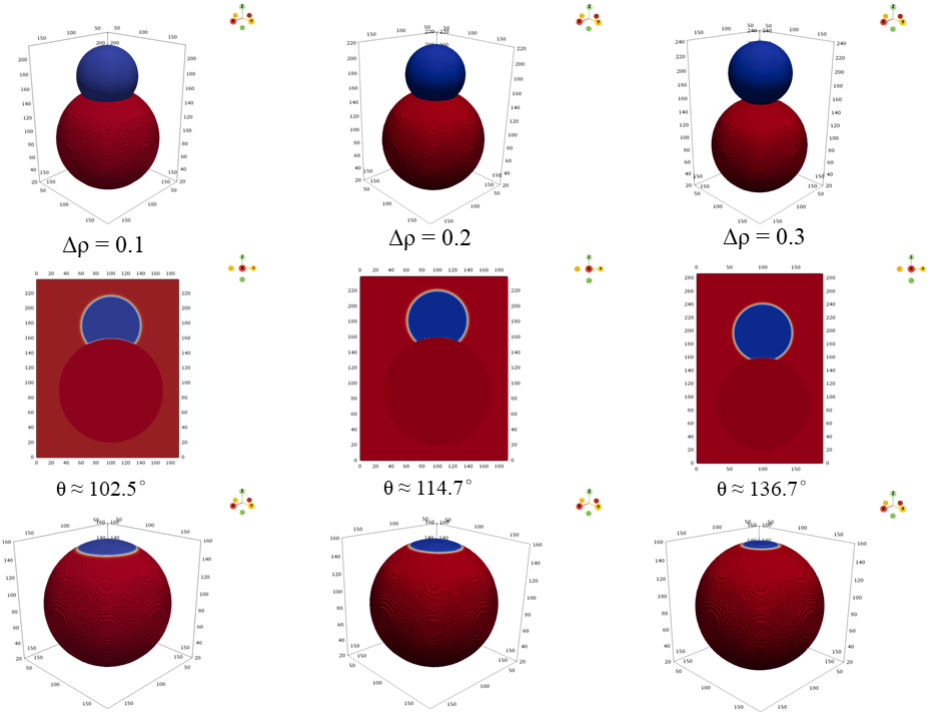

FIG. B.6: 3D curved wall (hydrophobic): contact angles tuned by $\Delta\rho$.

Appendix C: 3D numerical implementation

This appendix documents minimal 3D scalability checks of the framework. The goal is not to produce a full 3D boiling study, but to verify that the 2D methodology generalizes to 3D with stable interfaces and controllable wetting. We use a D3Q19 lattice with Huang–MRT collision, Guo forcing, the Peng–Robinson EOS, and the virtual–density wetting scheme extended to 3D. OpenMP parallelization is employed for modest domains.

.1 Model benchmark test

Fig.1 illustrates the implementation of a steady-state droplet in 3D. To ensure computational efficiency, OpenMP-based parallelization is employed. Consequently, the simulation domain is set to $96lu96lu96lu$, and the initial diameter of the drop is specified as $d = 20lu$. The simulation results demonstrate a well-formed droplet.

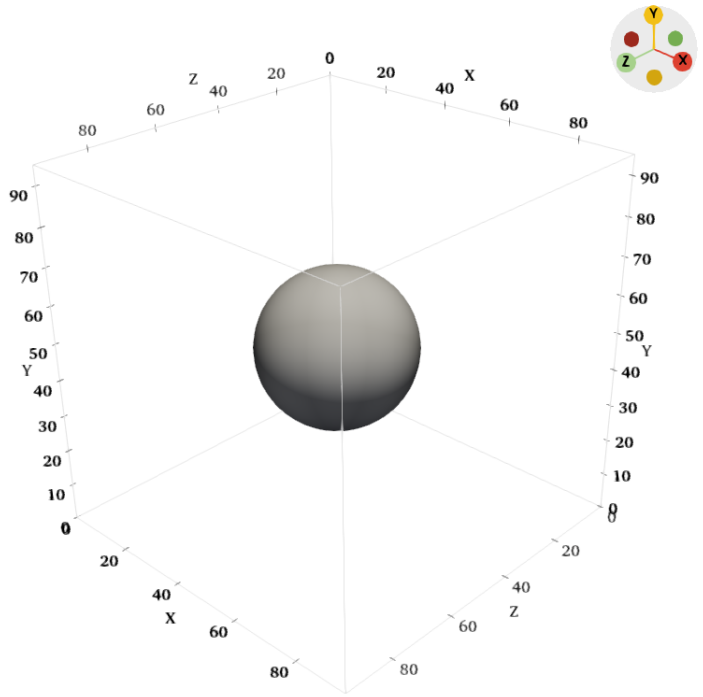

FIG. .1: 3D Steady Droplet

Fig.2 illustrates the steady-state distribution of the density field for a three-dimensional droplet. As shown, the droplet exhibits a typical "cap-like" structure, attached to

the solid surface, with a high-density region corresponding to the liquid phase and a surrounding low-density region representing the gas phase. A distinct yet non-sharp transition zone exists between the two phases, which appears as a diffuse interfacial band. This is a characteristic feature of the pseudopotential model[199].

In fact, in the pseudopotential framework, the liquid-gas interface is modeled as a diffuse interface with finite thickness, rather than a sharp, discontinuous boundary [200]. This means that the density across the interface changes smoothly, rather than abruptly. The underlying mechanism lies in the nonlocal interaction force, derived from the density gradient and the pseudopotential function, which inherently produces a gradual transition between phases.

Moreover, the thickness of this diffuse interface is controllable [201]. It is influenced by factors such as the initial width of the interface, the form of the pseudopotential function (e.g., in the Shan–Chen model), and the strength of the interaction (G). Therefore, the presence of a diffuse interfacial band in the simulation results not only aligns well with the physical theory of the pseudopotential model, but also serves as an indirect validation of the model's ability to capture interfacial dynamics realistically.

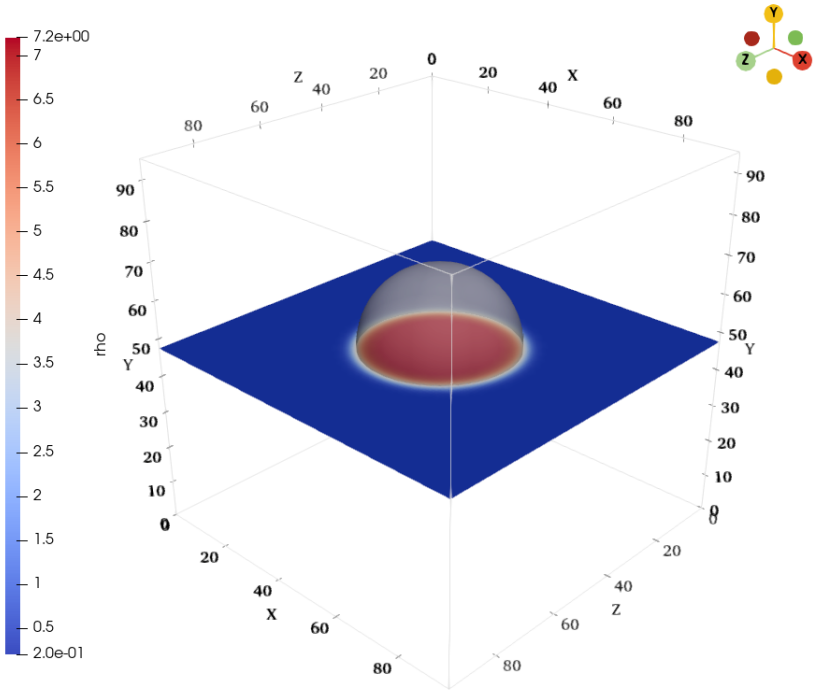

FIG. .2: Density distribution of a 3D steady droplet

Fig.3 illustrates the pressure distribution of a steady-state droplet in a three-dimensional domain. In this figure, the central transparent hemispherical shape represents the droplet itself, visualized through an isosurface of density corresponding to the liquid phase. The horizontal red slice displays the pressure field in the XY plane. A prominent feature in the pressure distribution is the appearance of a negative pressure ring near the base of the droplet, indicated by a gradual color transition from red to blue.

Upon closer inspection, this negative pressure is not a manifestation of a physical vacuum, but rather an outcome of the effective pressure field [202] calculated within the pseudopotential model. In such models, the pressure is derived from an equation of state (EOS), and in regions of sharp density gradients, namely, the liquid-gas interface, the nonlinear terms in the equation of state give rise to steep pressure variations. This leads to a local pressure collapse near the interface.

Physically, this negative pressure reflects the effect of surface tension. According to capillary theory [203], surface tension induces a pressure difference across the interface, which drives the droplet into a spherical shape to minimize free energy. In pseudopotential LBM, surface tension is not applied explicitly; instead, it emerges from the interplay between the nonlinear equation of state and the pseudopotential function. Therefore, the negative pressure region seen here is a numerical manifestation of the capillary pressure difference.

Moreover, this pressure distribution highlights the diffuse interface characteristic of the pseudopotential model. Unlike sharp interface methods, the liquid and gas phases in this model are connected through a finite-thickness transition zone, within which variables such as density and pressure vary smoothly. This results in the pressure transition band observed in the figure.

In summary, the negative pressure region around the droplet in Fig.3 is consistent with theoretical expectations of the multiphase pseudopotential LBM.

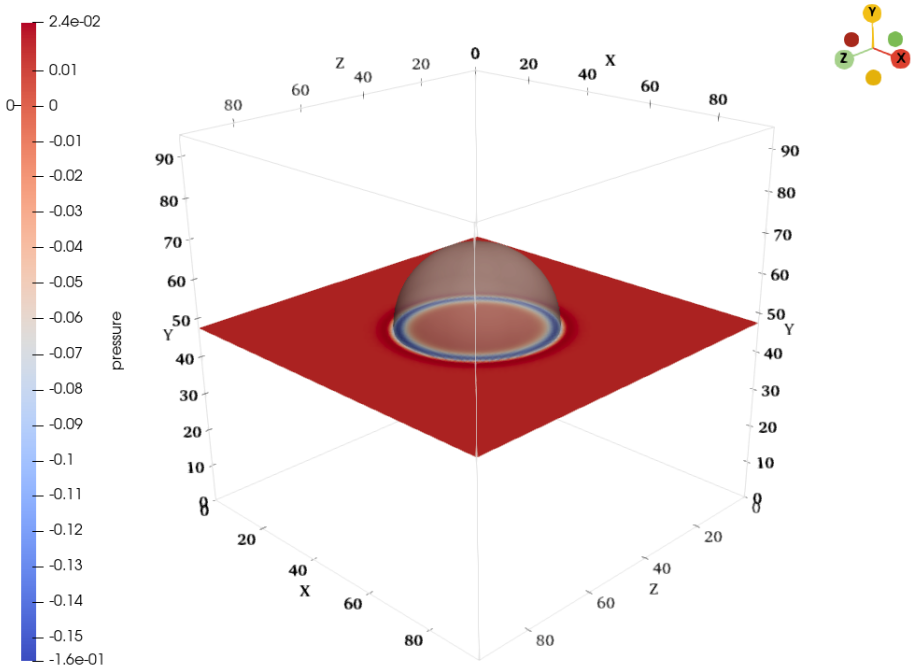

FIG. .3: Pressure distribution of a 3D steady droplet

Fig.4 presents the multiphysical field distribution of a three-dimensional steady-state droplet, including a combined visualization of the density, pressure, and velocity fields. In this figure, the semitransparent spherical isosurface represents the droplet itself, corresponding to the high-density liquid-phase region. Two mutually orthogonal cutting planes illustrate the pressure and density distributions, distinguished by a red-to-blue color map. In addition, the blue streamlines depict the velocity field, clearly revealing the circulation structures surrounding the droplet. The density field cutting plane indicates that the gas-liquid interface is not a sharp discontinuity but rather exhibits a finite-thickness diffuse interface, which is a characteristic feature of the pseudopotential model. In the pressure field, negative pressure regions are observed near the interface. The formation of such regions originates from the uneven distribution of the pseudopotential force in areas of steep density gradients.

The velocity field, as shown by the streamlines, displays multiple symmetrically distributed recirculation zones near the droplet interface. These local vortices are mainly concentrated around the contact region between the droplet and the surrounding gas, suggesting that interfacial tension gradients induce typical capillary-driven circulations, akin to the Marangoni effect [204]. Moreover, the overall magnitude of the velocity is relatively low, indicating that the droplet is in a

quasi-static equilibrium state with a stable interface and no intense convective motion.

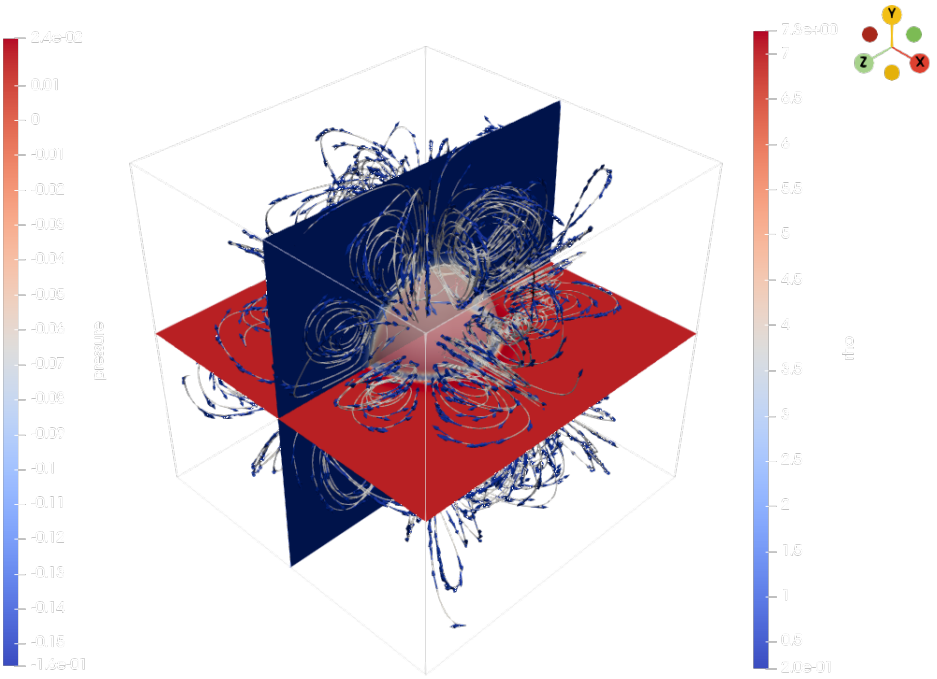

FIG. .4: Multiphysical field distribution of a 3D Steady Droplet

In summary, the combined multiphysics visualization validates the stability and effectiveness of the pseudopotential multiple-relaxation-time lattice Boltzmann model (MRT-LBM) for three-dimensional multiphase simulations. The present model successfully reproduces a stably attached droplet and accurately captures key phenomena including interfacial tension effects, interface-driven flows, and interphase property transitions. The results demonstrate that the model we implemented has strong potential to simulate droplet dynamics, boiling, and complex heat transfer problems in multiphase systems.

.2 3D single bubble nucleation

These results confirm that the improved virtual density method exhibits excellent scalability and numerical stability when extended from two-dimensional (2D) to three-dimensional (3D) simulations. It enables accurate and flexible control of static contact angles on both flat and curved surfaces by tuning the virtual density parameter φ. Throughout the simulations, the liquid–gas interface remains physically consistent and free from nonphysical oscillations, while droplet

shapes maintain smoothness and symmetry under various geometric conditions. This demonstrates that the method offers a robust and versatile framework for simulating wetting behavior on complex surfaces, including applications involving porous media, patterned substrates, and curvature-dependent wettability. Fig.5 illustrates the 3D single-bubble phase transition process. In this numerical simulation, the computational domain is defined as $80lu \times 80lu \times 160lu$. This case employs the improved virtual density formulation introduced in Chapter 2 to achieve the implementation of 3D contact angle. The results effectively validate the applicability and scalability of the improved virtual density formulation in 3D numerical simulations.

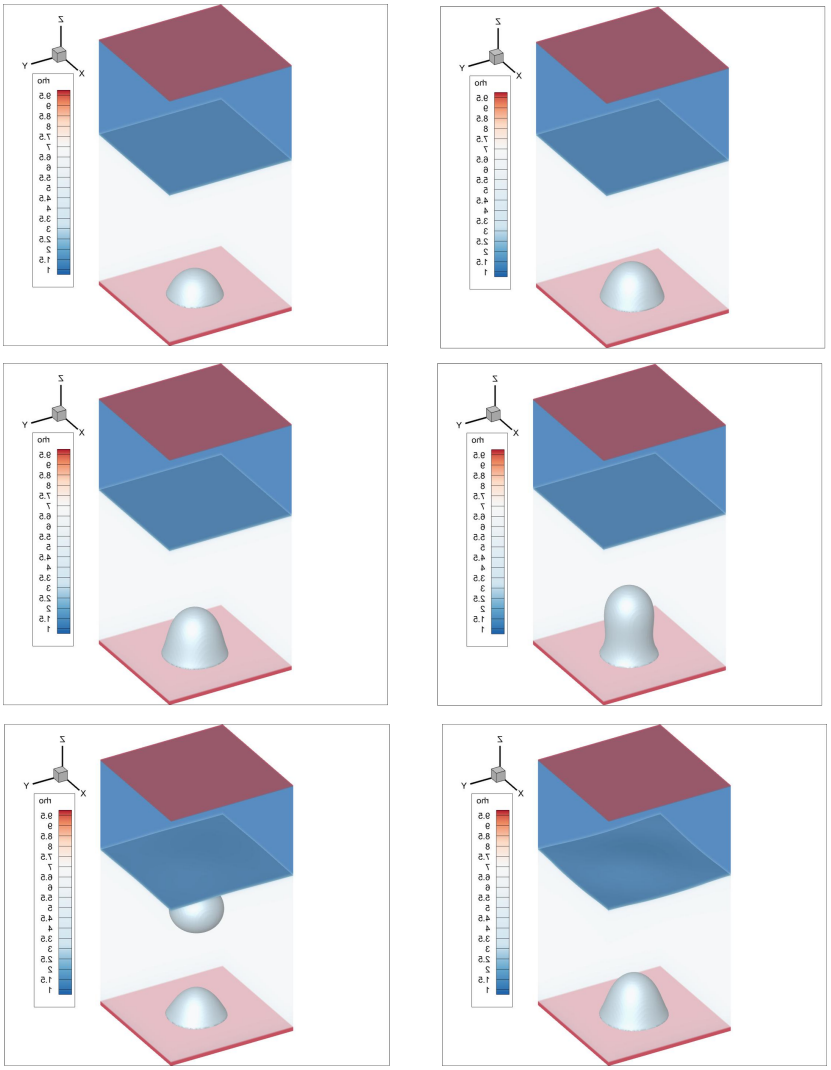

FIG. .5: 3D bubble nucleation implementation
$\Delta T = 0.08T_c, \theta \approx 90°$

Appendix D: Derivation of the Latent Heat of Vaporization for a General EOS

The latent heat of vaporization represents the energy required to transform a unit mass of liquid into vapor at constant temperature and pressure. For any thermodynamic model in which the pressure p is expressed as a function of temperature T and density ρ, i.e. $p = p(\rho, T)$, it is possible to derive the corresponding latent heat directly from the equation of state (EOS) without relying on tabulated data.

The starting point is the differential form of the internal energy:

$$\mathrm{d}u = T\,\mathrm{d}s - p\,\mathrm{d}v, \tag{1}$$

where $v = 1/\rho$ is the specific volume and s the specific entropy. Combining this with the thermodynamic identity for entropy,

$$\left(\frac{\partial s}{\partial T}\right)_v = \frac{c_v}{T}, \quad \left(\frac{\partial s}{\partial v}\right)_T = \left(\frac{\partial p}{\partial T}\right)_v, \tag{2}$$

gives the temperature derivative of internal energy at constant T:

$$\mathrm{d}u = \left[T\left(\frac{\partial p}{\partial T}\right)_v - p\right]\mathrm{d}v. \tag{3}$$

For an isothermal process ($\mathrm{d}T = 0$), substituting $v = 1/\rho$ and integrating Eq. (3) yields

$$u(\rho, T) = u_0(T) - \int_{\rho_0}^{\rho}\left[\frac{T}{\rho^2}\left(\frac{\partial p}{\partial T}\right)_\rho - \frac{p}{\rho^2}\right]\mathrm{d}\rho, \tag{4}$$

where $u_0(T)$ is a reference energy dependent on temperature.

The specific enthalpy is defined as $h = u + p/\rho$. Substituting Eq. (4) gives

$$h(\rho, T) = u_0(T) + \frac{p}{\rho} - \int_{\rho_0}^{\rho}\left[\frac{T}{\rho^2}\left(\frac{\partial p}{\partial T}\right)_\rho - \frac{p}{\rho^2}\right]\mathrm{d}\rho. \tag{5}$$

Equation (5) provides the general expression for the specific enthalpy corresponding to any EOS of the form $p = p(\rho, T)$. Once the functional form of p is known, the enthalpy can be obtained by numerical or analytical integration. The latent heat of vaporization at a given temperature is then evaluated as the enthalpy difference between saturated vapor and liquid:

$$h_{fg}(T) = h_v(T, \rho_v) - h_l(T, \rho_l), \tag{6}$$

where ρ_v and ρ_l are the corresponding coexistence densities at saturation.

For illustration, consider the Peng–Robinson (PR) equation of state,

$$p = \frac{RT\rho}{1 - b\rho} - \frac{a(T)\rho^2}{1 + 2b\rho - b^2\rho^2}, \tag{7}$$

where $a(T)$ accounts for temperature dependence through

$$a(T) = a_c\,\alpha(T), \qquad \alpha(T) = \left[1 + m\left(1 - \sqrt{T/T_c}\right)\right]^2, \tag{8}$$

and $m = 0.37464 + 1.54226\,\omega - 0.26992\,\omega^2$ depends on the acentric factor ω.

Substituting Eq. (7) into Eq. (5), the integrand can be explicitly evaluated to yield the temperature-dependent enthalpy $h(\rho, T)$ for the PR-EOS. Then, by inserting the saturated liquid and vapor densities (ρ_l, ρ_v), one obtains the latent heat via Eq. (6). This approach provides a thermodynamically consistent way to evaluate h_{fg} for any fluid described by an analytical EOS, and has been shown to agree well with tabulated vapor–liquid data when appropriate EOS parameters are used.

Bibliography

[1] S. Nukiyama, "The maximum and minimum values of the heat q transmitted from metal to boiling water under atmospheric pressure," *International Journal of Heat and Mass Transfer*, vol. 9, no. 12, pp. 1419–1433, 1966.

[2] X. Shan and H. Chen, "Lattice boltzmann model for simulating flows with multiple phases and components," *Physical review E*, vol. 47, no. 3, p. 1815, 1993.

[3] M. Yang, Z. Zhao, Y. Zhang, X. Pu, and X. Liu, "Visualization experiment on the evolution of vapor bubbles in pool boiling heat transfer enhancement of the smooth and porous surfaces using ultrasonic waves," *International Journal of Heat and Mass Transfer*, vol. 203, p. 123807, 2023.

[4] L. Zhang, S. Gong, Z. Lu *et al.*, "A unified relationship between bubble departure frequency and diameter during saturated nucleate pool boiling," *International Journal of Heat and Mass Transfer*, vol. 165, p. 120640, 2021.

[5] R. Sugrue and J. Buongiorno, "A modified force-balance model for prediction of bubble departure diameter in subcooled flow boiling," *Nuclear Engineering and Design*, vol. 305, pp. 717–722, 2016.

[6] Q. Li, Y. Yu, and Z. Wen, "How does boiling occur in lattice boltzmann simulations?" *Physics of Fluids*, vol. 32, no. 9, 2020.

[7] V. P. Carey, *Liquid-vapor phase-change phenomena: an introduction to the thermophysics of vaporization and condensation processes in heat transfer equipment*. CRC Press, 2020.

[8] M. Cooper and A. Lloyd, "The microlayer in nucleate pool boiling," *International Journal of Heat and Mass Transfer*, vol. 12, no. 8, pp. 895–913, 1969.

[9] G. Wang and P. Cheng, "An experimental study of flow boiling instability in a single microchannel," *International communications in heat and mass transfer*, vol. 35, no. 10, pp. 1229–1234, 2008.

[10] B. Mikic and W. Rohsenow, "A new correlation of pool-boiling data including the effect of heating surface characteristics," 1969.

[11] N. Khan, D. Pinjala, and K. Toh, "Pool boiling heat transfer enhancement by surface modification/micro-structures for electronics cooling: a review," in *Proceedings of 6th Electronics Packaging Technology Conference (EPTC 2004)(IEEE Cat. No. 04EX971)*. IEEE, 2004, pp. 273–280.

[12] J. P. Holman, "Heat transfer to freon 12 near the critical state in a thermal syphon type apparatus," 1958.

[13] M. Jakob and W. Linke, "Boiling heat transfer," *Phys. Z*, vol. 636, pp. 267–273, 1935.

[14] P. Cheng, X. Quan, S. Gong, L. Dong, and F. Hong, "Recent studies on surface roughness and wettability effects in pool boiling," in *International Heat Transfer Conference Digital Library*. Begel House Inc., 2014.

[15] S. Ostrach, "Natural convection in enclosures," 1988.

[16] P. Griffith and J. D. Wallis, "The role of surface conditions in nucleate boiling," Cambridge, Mass.: Massachusetts Institute of Technology, Division of …, Tech. Rep., 1958.

[17] J. M. Ramilison and J. Lienhard, "Transition boiling heat transfer and the film transition regime," 1987.

[18] P. J. Berenson, "Film-boiling heat transfer from a horizontal surface," 1961.

[19] K. Baumeister and F. Simon, "Leidenfrost temperature—its correlation for liquid metals, cryogens, hydrocarbons, and water," 1973.

[20] W. M. Rohsenow and J. A. Clark, "Heat transfer and pressure drop data for high heat flux densities to water at high subcritical pressures," Cambridge, Mass.: MIT Division of Industrial Cooperation, 1951, Tech. Rep., 1951.

[21] K. Engelberg-Forster and R. Greif, "Heat transfer to a boiling liquid—mechanism and correlations," *Journal of Heat Transfer*, vol. 81, no. 1, pp. 43–52, 1959.

[22] N. Zuber, "Nucleate boiling. the region of isolated bubbles and the similarity with natural convection," *International Journal of Heat and Mass Transfer*, vol. 6, no. 1, pp. 53–78, 1963.

[23] C.-Y. Han, "The mechanism of heat transfer in nucleate pool boiling," Ph.D. dissertation, Massachusetts Institute of Technology, 1962.

[24] J. T. Cieśliński *et al.*, "A study on flow field measurement around growing and rising vapour bubbles by use of piv technique," *Experimental Thermal and Fluid Science*, vol. 29, no. 7, pp. 843–850, 2005.

[25] V. Voulgaropoulos *et al.*, "Flow behavior around single nucleate boiling bubble quantitatively grasped by particle tracking visualization," *International Journal of Heat and Mass Transfer*, vol. 188, p. 122602, 2022.

[26] A. Jain, J. Kim *et al.*, "Experimental investigation of bubble nucleation, growth and departure using synchronized ir thermometry, two-colour lif and piv," *Experimental Thermal and Fluid Science*, vol. 109, p. 109847, 2019.

[27] M. Mondal *et al.*, "Independent microscale sensing of phase interface and time- and space-resolved wall temperature and heat flux measurements during nucleate boiling with constant heat flux boundary conditions," *International Journal of Heat and Mass Transfer*, 2024, advanced MEMS-based measurement.

[28] M. Schepperle *et al.*, "Noninvasive platinum thin-film microheater/temperature sensor array for boiling heat flux measurement," *Experimental Thermal and Fluid Science*, 2022, high-resolution heater–sensor arrays.

[29] A. Aliseda and T. J. Heindel, "X-ray flow visualization in multiphase flows: progress, challenges, and opportunities," *Annual Review of Fluid Mechanics*, vol. 53, pp. 543–567, 2021.

[30] R. Zboray *et al.*, "High-frame-rate fast-neutron imaging of air–water two-phase flow in a thin rectangular channel," *[arXiv or Journal]*, 2015, fast neutron radiography for two-phase flow visualization.

[31] J. P. McHale, J. Buongiorno, L.-W. Hu, and T. McKrell, "Analysis of surface roughness effects on nucleate boiling," *International Journal of Multiphase Flow*, vol. 57, pp. 282–292, 2013.

[32] D. Attinger, C. Frankiewicz, A. R. Betz, T. M. Schutzius, R. Ganguly, A. Das, C.-J. Kim, and C. M. Megaridis, "Surface engineering for phase change heat transfer: A review," *arXiv preprint arXiv:1409.5363*, 2014.

[33] J. Buongiorno, D. G. Cahill, C. H. Hidrovo, S. Moghaddam, A. J. Schmidt, and L. Shi, "Micro- and nano-scale measurement methods for phase change heat transfer on planar and structured surfaces," *arXiv preprint arXiv:1408.0277*, 2014.

[34] —, "Roles of boiling surface characterized by micro-structures," in *Proceedings of NURETH-16*, 2015.

[35] A. K. Gunstensen, D. H. Rothman, S. Zaleski, and G. Zanetti, "Lattice boltzmann model of immiscible fluids," *Physical review A*, vol. 43, no. 8, p. 4320, 1991.

[36] M. C. Sukop and D. Or, "Lattice boltzmann method for modeling liquid-vapor interface configurations in porous media," *Water Resources Research*, vol. 40, no. 1, 2004. [Online]. Available: https://agupubs.onlinelibrary.wiley.com/doi/abs/10.1029/2003WR002333

[37] G. Caginalp and P. Fife, "Phase-field methods for interfacial boundaries," *Physical Review B*, vol. 33, no. 11, p. 7792, 1986.

[38] S. Gong and P. Cheng, "Numerical investigation of droplet motion and coalescence by an improved lattice boltzmann model for phase transitions and multiphase flows," *Computers & Fluids*, vol. 53, pp. 93–104, 2012.

[39] Z. Guo, C. Zheng, and B. Shi, "Discrete lattice effects on the forcing term in the lattice boltzmann method," *Phys. Rev. E*, vol. 65, p. 046308, Apr 2002. [Online]. Available: https://link.aps.org/doi/10.1103/PhysRevE.65.046308

[40] S. Nekoeian, A. S. Goharrizi, M. Jamialahmadi, S. Jafari, and F. Sotoudeh, "A novel shan and chen type lattice boltzmann two phase method to study the capillary pressure curves of an oil water pair in a porous media," *Petroleum*, vol. 4, no. 3, pp. 347–357, 2018. [Online]. Available: https://www.sciencedirect.com/science/article/pii/S2405656117301761

[41] P. L. Bhatnagar, E. P. Gross, and M. Krook, "A model for collision processes in gases. i. small amplitude processes in charged and neutral

one-component systems," *Phys. Rev.*, vol. 94, pp. 511–525, May 1954. [Online]. Available: https://link.aps.org/doi/10.1103/PhysRev.94.511

[42] A. Zhang, D. Su, C. Li, Y. Gao, Z. Dong, S. Bai, B. Jiang, and F. Pan, "Three-dimensional phase-field lattice-boltzmann simulations of a rising bubble interacting with obstacles: Shape quantification and parameter dependence," *Physics of Fluids*, vol. 34, no. 10, 2022.

[43] H. Grad, "Principles of the kinetic theory of gases," in *Thermodynamik der Gase/Thermodynamics of Gases*. Springer, 1958, pp. 205–294.

[44] G. Puppo, "Kinetic models of bgk type and their numerical integration," *arXiv preprint arXiv:1902.08311*, 2019.

[45] Q. Liu, Y.-L. He, D. Li, and Q. Li, "Non-orthogonal multiple-relaxation-time lattice boltzmann method for incompressible thermal flows," *International Journal of Heat and Mass Transfer*, vol. 102, pp. 1334–1344, 2016.

[46] L. Xuhui, S. Xiaowen, and D. Wenyang, "Theoretical progress on regularized lattice boltzmann collision models," *ACTA AERODYNAMICA SINICA*, vol. 40, no. 3, pp. 46–64, 2022. [Online]. Available: http://kqdlxxb.xml-journal.net/en/article/doi/10.7638/kqdlxxb-2020.0426

[47] C. Shu, N. Liu, and Y. Chew, "A novel immersed boundary velocity correction–lattice boltzmann method and its application to simulate flow past a circular cylinder," *Journal of Computational Physics*, vol. 226, no. 2, pp. 1607–1622, 2007. [Online]. Available: https://www.sciencedirect.com/science/article/pii/S0021999107002513

[48] F. Lado, "Perturbation correction to the radial distribution function," *Phys. Rev.*, vol. 135, pp. A1013–A1017, Aug 1964. [Online]. Available: https://link.aps.org/doi/10.1103/PhysRev.135.A1013

[49] S. Kutluay, A. Bahadir, and A. Özdeş, "Numerical solution of one-dimensional burgers equation: explicit and exact-explicit finite difference methods," *Journal of Computational and Applied Mathematics*, vol. 103, no. 2, pp. 251–261, 1999. [Online]. Available: https://www.sciencedirect.com/science/article/pii/S0377042798002611

[50] P. Yuan and L. Schaefer, "Equations of state in a lattice boltzmann model," *Physics of Fluids*, vol. 18, no. 4, p. 042101, 04 2006. [Online]. Available: https://doi.org/10.1063/1.2187070

[51] Z. Guo, C. Zheng, and B. Shi, "Discrete lattice effects on the forcing term in the lattice boltzmann method," *Physical Review E*, vol. 65, no. 4, p. 046308, 2002.

[52] A. Kupershtokh, D. Medvedev, and D. Karpov, "On equations of state in a lattice boltzmann method," *Computers & Mathematics with Applications*, vol. 58, no. 5, pp. 965–974, 2009, mesoscopic Methods in Engineering and Science. [Online]. Available: https://www.sciencedirect.com/science/article/pii/S0898122109001011

[53] R. Huang, L. Lan, and Q. Li, "Lattice boltzmann simulations of thermal flows beyond the boussinesq and ideal-gas approximations," *Phys. Rev. E*, vol. 102, p. 043304, Oct 2020. [Online]. Available: https://link.aps.org/doi/10.1103/PhysRevE.102.043304

[54] P. Lallemand and L.-S. Luo, "Theory of the lattice boltzmann method: Acoustic and thermal properties in two and three dimensions," *Phys. Rev. E*, vol. 68, p. 036706, Sep 2003. [Online]. Available: https://link.aps.org/doi/10.1103/PhysRevE.68.036706

[55] R. Huang and H. Wu, "Third-order analysis of pseudopotential lattice boltzmann model for multiphase flow," *Journal of Computational Physics*, vol. 327, pp. 121–139, 2016.

[56] X. He and L.-S. Luo, "A theory of the lattice boltzmann method: From the boltzmann equation to the navier–stokes equation," *Physical Review E*, vol. 56, no. 6, pp. 6811–6817, 1997.

[57] J. F. Lutsko, "Chapman-enskog expansion about nonequilibrium states with application to the sheared granular fluid," *Physical Review E*, vol. 73, no. 2, Feb. 2006. [Online]. Available: http://dx.doi.org/10.1103/PhysRevE.73.021302

[58] F. Dubois, B. M. Boghosian, and P. Lallemand, "General fourth order chapman-enskog expansion of lattice boltzmann schemes," 2025. [Online]. Available: https://arxiv.org/abs/2302.07535

[59] M. Gao, P. Cheng, and X. Quan, "An experimental investigation on effects of an electric field on bubble growth on a small heater in pool boiling," *International Journal of Heat and Mass Transfer*, vol. 67, pp. 984–991, 2013. [Online]. Available: https://www.sciencedirect.com/science/article/pii/S0017931013007680

[60] N. Zuber, "Nucleate boiling. the region of isolated bubbles and the similarity with natural convection," *International Journal of Heat and Mass Transfer*, vol. 6, no. 1, pp. 53–78, 1963. [Online]. Available: https://www.sciencedirect.com/science/article/pii/0017931063900292

[61] D. d'Humières, "Generalized lattice boltzmann equations," in *Rarefied Gas Dynamics: Theory and Simulations*, ser. Progress in Astronautics and Aeronautics, B. D. Shizgal and D. P. Weaver, Eds. Washington, DC: AIAA, 1992, vol. 159, pp. 450–458.

[62] D. d'Humières, I. Ginzburg, M. Krafczyk, P. Lallemand, and L.-S. Luo, "Multiple-relaxation-time lattice boltzmann models in three dimensions," *Philosophical Transactions of the Royal Society A*, vol. 360, no. 1792, pp. 437–451, 2002.

[63] P. Lallemand and L.-S. Luo, "Theory of the lattice boltzmann method: Dispersion, dissipation, isotropy, galilean invariance, and stability," *Physical review E*, vol. 61, no. 6, p. 6546, 2000.

[64] F. Gong, P. Cheng, Y. He, and Z. Wang, "Improved wetting boundary condition for pseudopotential lattice boltzmann modeling of multiphase flows," *Physical Review E*, vol. 81, no. 6, p. 066704, 2010.

[65] Q. Li, Y. Yu, and K. H. Luo, "Implementation of contact angles in pseudopotential lattice boltzmann simulations with curved boundaries," *Physical review E*, vol. 100, no. 5, p. 053313, 2019.

[66] Q. Li, K. H. Luo, and X. J. Li, "Lattice boltzmann modeling of multiphase flows at large density ratio with an improved pseudopotential model," *Phys. Rev. E*, vol. 87, p. 053301, May 2013. [Online]. Available: https://link.aps.org/doi/10.1103/PhysRevE.87.053301

[67] J. Z. Simon, "Higher-derivative lagrangians, nonlocality, problems, and solutions," *Phys. Rev. D*, vol. 41, pp. 3720–3733, Jun 1990. [Online]. Available: https://link.aps.org/doi/10.1103/PhysRevD.41.3720

[68] M. H. Carpenter, C. A. Kennedy, H. Bijl, S. A. Viken, and V. N. Vatsa, "Fourth," p. 157.

[69] S. Osher and J. A. Sethian, "Fronts propagating with curvature-dependent speed: Algorithms based on hamilton-jacobi formulations," *Journal of Computational Physics*, vol. 79, no. 1, pp. 12–49, 1988. [Online]. Available: https://www.sciencedirect.com/science/article/pii/0021999188900022

[70] Q. Li, Q. Kang, M. Francois, Y. He, and K. Luo, "Lattice boltzmann modeling of boiling heat transfer: The boiling curve and the effects of wettability," *International Journal of Heat and Mass Transfer*, vol. 85, pp. 787–796, 2015. [Online]. Available: https://www.sciencedirect.com/science/article/pii/S0017931015001544

[71] P. Yuan and L. Schaefer, "Equations of state in a lattice boltzmann model," *Physics of fluids*, vol. 18, no. 4, 2006.

[72] Q. Li, K.-H. Luo, and Q. Kang, "A coupled lattice boltzmann model for thermal flows with phase change," *International Journal of Heat and Mass Transfer*, vol. 55, no. 23-24, pp. 8100–8108, 2012.

[73] L. Fei and K. H. Luo, "Consistent forcing scheme in the cascaded lattice boltzmann method," *Physical Review E*, vol. 96, no. 5, p. 053307, 2017.

[74] Z. Guo, C. Zheng, and B. Shi, "Thermal lattice boltzmann equation for low mach number flows: Decoupling model," *Physical Review E*, vol. 75, no. 3, p. 036704, 2007.

[75] T. Young, "Iii. an essay on the cohesion of fluids," *Philosophical transactions of the royal society of London*, no. 95, pp. 65–87, 1805.

[76] S. Gong, Z. Hu, and P. Cheng, "A mesoscopic approach for nanoscale evaporation heat transfer characteristics," *International Journal of Heat and Mass Transfer*, vol. 231, p. 125856, 2024.

[77] G. Son, V. K. Dhir, and N. Ramanujapu, "A lattice boltzmann study on nucleate boiling heat transfer," *Numerical Heat Transfer, Part B: Fundamentals*, vol. 66, no. 1, pp. 35–58, 2014.

[78] S.-C. Wang, Z.-X. Tong, Y.-L. He, and X. Liu, "Unit conversion in pseudopotential lattice boltzmann method for liquid–vapor phase change simulations," *Physics of Fluids*, vol. 34, no. 10, 2022.

[79] E. W. Lemmon, M. L. Huber, and M. O. McLinden, "NIST Standard Reference Database 23: Reference Fluid Thermodynamic and Transport Properties (REFPROP)," https://www.nist.gov/srd/refprop, 2022, version 10.0, National Institute of Standards and Technology.

[80] J. R. MACDONALD, "Review of some experimental and analytical equations of state," *Rev. Mod. Phys.*, vol. 41, pp. 316–349, Apr 1969. [Online]. Available: https://link.aps.org/doi/10.1103/RevModPhys.41.316

[81] G. M. Kontogeorgis and I. G. Economou, "Equations of state: From the ideas of van der waals to association theories," *The Journal of Supercritical Fluids*, vol. 55, no. 2, pp. 421–437, 2010, 100th year Anniversary of van der Waals' Nobel Lecture. [Online]. Available: https://www.sciencedirect.com/science/article/pii/S0896844610003864

[82] O. Redlich and J. N. Kwong, "On the thermodynamics of solutions. v. an equation of state. fugacities of gaseous solutions." *Chemical reviews*, vol. 44, no. 1, pp. 233–244, 1949.

[83] G. Soave, "Equilibrium constants from a modified redlich-kwong equation of state," *Chemical engineering science*, vol. 27, no. 6, pp. 1197–1203, 1972.

[84] S. Ramdharee, E. Muzenda, and M. Belaid, "A review of the equations of state and their applicability in phase equilibrium modeling," 2013.

[85] D.-Y. Peng and D. B. Robinson, "A new two-constant equation of state," *Industrial & Engineering Chemistry Fundamentals*, vol. 15, no. 1, pp. 59–64, 1976.

[86] G. M. Kontogeorgis and I. G. Economou, "Equations of state: From the ideas of van der waals to association theories," *The Journal of Supercritical Fluids*, vol. 55, no. 2, pp. 421–437, 2010.

[87] W. Wagner and H.-J. Kretzschmar, "Iapws industrial formulation 1997 for the thermodynamic properties of water and steam," *International steam tables: properties of water and steam based on the industrial formulation IAPWS-IF97*, pp. 7–150, 2008.

[88] E. Díaz-Herrera, J. A. Moreno-Razo, and G. Ramírez-Santiago, "Wetting phenomenon in the liquid-vapor phase coexistence of a partially miscible

lennard-jones binary mixture," *Physical Review E—Statistical, Nonlinear, and Soft Matter Physics*, vol. 70, no. 5, p. 051601, 2004.

[89] H. B. Callen, *Thermodynamics and an Introduction to Thermostatistics*, 2nd ed. John Wiley & Sons, 1985.

[90] H. Liu, "The maxwell crossover and the van der waals equation of state," *arXiv preprint arXiv:2010.14739*, 2020.

[91] K. Pedersen, P. Thomassen, and A. Fredenslund, "Srk-eos calculation for crude oils," *Fluid Phase Equilibria*, vol. 14, pp. 209–218, 1983.

[92] L. S. Pan, J. Lou, H. Y. Li, and C. W. Kang, "A diffuse interface model for two-phase flows with phase transition," *Physics of Fluids*, vol. 31, no. 9, 2019.

[93] Q. Li and K. Luo, "Achieving tunable surface tension in the pseudopotential lattice boltzmann modeling of multiphase flows," *Physical Review E—Statistical, Nonlinear, and Soft Matter Physics*, vol. 88, no. 5, p. 053307, 2013.

[94] H. Huang, M. Sukop, and X. Lu, "Multiphase lattice boltzmann methods: Theory and application," 2015.

[95] R. Finn, "Capillary surface interfaces," *Notices of the AMS*, vol. 46, no. 7, pp. 770–781, 1999.

[96] J. Yang and E. S. Boek, "A comparison study of multi-component lattice boltzmann models for flow in porous media applications," *Computers & Mathematics with Applications*, vol. 65, no. 6, pp. 882–890, 2013.

[97] S. A. Nabavizadeh, M. Eshraghi, and S. D. Felicelli, "A comparative study of multiphase lattice boltzmann methods for bubble-dendrite interaction during solidification of alloys," *Applied Sciences*, vol. 9, no. 1, p. 57, 2018.

[98] Q. Li, K. H. Luo, Q. Kang, Y. He, Q. Chen, and Q. Liu, "Lattice boltzmann methods for multiphase flow and phase-change heat transfer," *Progress in Energy and Combustion Science*, vol. 52, pp. 62–105, 2016.

[99] S. Gong and P. Cheng, "Lattice boltzmann simulations for surface wettability effects in saturated pool boiling heat transfer," *International Journal of Heat and Mass Transfer*, vol. 85, pp. 635–646, 2015.

[100] S. Gong, F. Hong, Q. Guo, L. Zhang, and P. Cheng, "Mesoscopic approach for nanoscale liquid-vapor interfacial statics and dynamics," *International Journal of Heat and Mass Transfer*, vol. 194, p. 123104, 2022.

[101] D. Viswanath and N. Kuloor, "Latent heat of vaporization, surface tension, and temperature." *Journal of Chemical and Engineering Data*, vol. 11, no. 1, pp. 69–72, 1966.

[102] X. Sun, Y. Fang, W. Zhao, and S. Xiang, "New alpha functions for the peng–robinson cubic equation of state," *ACS omega*, vol. 7, no. 6, pp. 5332–5339, 2022.

[103] C. Chauveau, M. Birouk, and I. Gökalp, "An analysis of the d2-law departure during droplet evaporation in microgravity," *International journal of multiphase flow*, vol. 37, no. 3, pp. 252–259, 2011.

[104] T. J. Collins, "Imagej for microscopy," *Biotechniques*, vol. 43, no. sup1, pp. S25–S30, 2007.

[105] R. Chen, M.-C. Lu, V. Srinivasan, Z. Wang, and S. K. Cho, "Nanostructured surfaces for enhanced boiling heat transfer," *Nano Letters*, vol. 9, no. 2, pp. 548–553, 2009.

[106] S. G. Kandlikar, "Fundamental issues related to flow boiling in minichannels and microchannels," *Experimental Thermal and Fluid Science*, vol. 26, no. 2-4, pp. 389–407, 2002.

[107] S. Gong and P. Cheng, "A lattice boltzmann method for simulation of liquid–vapor phase-change heat transfer," *International Journal of Heat and Mass Transfer*, vol. 55, no. 17-18, pp. 4923–4927, 2012.

[108] Q. Li, Q. Kang, M. M. Francois, A. J. Hu, and X. Y. Lu, "Lattice boltzmann modeling of boiling heat transfer: The boiling curve and the effects of wettability," *International Journal of Heat and Mass Transfer*, vol. 85, pp. 787–796, 2015.

[109] S. Shin, M. Shirota, and A. L. Yarin, "Hydrodynamics of bubble growth during nucleate boiling under a thin liquid layer," *International Journal of Heat and Mass Transfer*, vol. 79, pp. 260–272, 2014.

[110] H. Jo, H. S. Ahn, S. H. Kang, and M. H. Kim, "A study of nucleate boiling heat transfer on hydrophilic, hydrophobic and heterogeneous wetting surfaces," *International Journal of Heat and Mass Transfer*, vol. 54, pp. 5643–5652, 2011. [Online]. Available: https://api.semanticscholar.org/CorpusID:122258801

[111] S. Gong and P. Cheng, "Lattice boltzmann simulation of periodic bubble nucleation, growth and departure from a heated surface in pool boiling," *International Journal of Heat and Mass Transfer*, vol. 64, pp. 122–132, 2013. [Online]. Available: https://www.sciencedirect.com/science/article/pii/S0017931013002652

[112] T. Sun, W. Li, and S. Yang, "Numerical simulation of bubble growth and departure during flow boiling period by lattice boltzmann method," *International Journal of Heat and Fluid Flow*, vol. 44, pp. 120–129, 2013. [Online]. Available: https://www.sciencedirect.com/science/article/pii/S0142727X13000908

[113] R. L. Mohanty and M. K. Das, "A critical review on bubble dynamics parameters influencing boiling heat transfer," *Renewable and Sustainable Energy Reviews*, vol. 78, pp. 466–494, 2017.

[114] S. Gong and P. Cheng, "Lattice boltzmann simulations for surface wettability effects in saturated pool boiling heat transfer," *International Journal of Heat and Mass Transfer*, vol. 85, pp. 635–646, 2015. [Online]. Available: https://www.sciencedirect.com/science/article/pii/S0017931015001714

[115] C. Zhang, P. Cheng, and F. Hong, "Mesoscale simulation of heater size and subcooling effects on pool boiling under controlled wall heat flux conditions," *International Journal of Heat and Mass Transfer*, vol. 101, pp. 1331–1342, 2016. [Online]. Available: https://www.sciencedirect.com/science/article/pii/S0017931016302927

[116] Q. Li, K.-H. Luo, Y. Gao, and Y.-L. He, "Coupling improved pseudopotential model with a thermal lattice boltzmann model for simulating liquid–vapor phase change," *International Journal of Heat and Mass Transfer*, vol. 92, pp. 1041–1058, 2016.

[117] Q. Li, Q. Kang, M. M. Francois, Y. He, and K. Luo, "Lattice boltzmann modeling of boiling heat transfer: The boiling curve and the effects of wettability," *International Journal of Heat and Mass Transfer*, vol. 85, pp. 787–796, 2015.

[118] S. Wu, H. Dai, H. Wang, C. Shen, and X. Liu, "Role of condensation on boiling heat transfer in a confined chamber," *Applied Thermal Engineering*, vol. 185, p. 116309, 2021. [Online]. Available: https://www.sciencedirect.com/science/article/pii/S1359431120337881

[119] S. A. A. Fazel, "Prediction of bubble departing diameter in pool boiling of mixtures by ann using modified relu," *Heliyon*, vol. 10, no. 11, 2024.

[120] R. M. Mutiso, M. C. Sherrott, A. R. Rathmell, B. J. Wiley, and K. I. Winey, "Integrating simulations and experiments to predict sheet resistance and optical transmittance in nanowire films for transparent conductors," *ACS nano*, vol. 7, no. 9, pp. 7654–7663, 2013.

[121] N. G. Kottke, M. Vaupel, M. Tajmar, W. Konrad, N. Saks, and F. G. Hey, "Comparison of the thermionic emission properties of lab6 and c12a7," in *Proceedings of the 36th International Electric Propulsion Conference, Vienna, Austria*, 2019, pp. 15–20.

[122] A. Battai, "Steuerung eines keithley 2400 sourcemeters über eine rs-232 schnittstelle mit hilfe von scpi befehlen," Ph.D. dissertation, Fachhochschule Dortmund, 2022.

[123] H.-H. Kim, J.-H. Kim, and A. Ogata, "Time-resolved high-speed camera observation of electrospray," *Journal of Aerosol Science*, vol. 42, no. 4, pp. 249–263, 2011.

[124] J. Jerome, *Virtual instrumentation using LabVIEW*. PHI Learning Pvt. Ltd., 2010.

[125] R. J. Moffat, "Describing the uncertainties in experimental results," *Experimental thermal and fluid science*, vol. 1, no. 1, pp. 3–17, 1988.

[126] M. Yamashita, T. Nishii, and H. Mizutani, "Resistivity measurement by dual-configuration four-probe method," *Japanese journal of applied physics*, vol. 42, no. 2R, p. 695, 2003.

[127] R. H. Dieck, *Measurement uncertainty: methods and applications*. ISA, 2007.

[128] J. J. Kennedy, "A review of uncertainty in in situ measurements and data sets of sea surface temperature," *Reviews of Geophysics*, vol. 52, no. 1, pp. 1–32, 2014.

[129] W. Gropp, E. Karrels, and E. Lusk, "Mpe graphics-scalable x11 graphics in mpi," in *Proceedings Scalable Parallel Libraries Conference*. IEEE, 1994, pp. 49–54.

[130] O. Barnich and M. Van Droogenbroeck, "Vibe: A universal background subtraction algorithm for video sequences," *IEEE Transactions on Image processing*, vol. 20, no. 6, pp. 1709–1724, 2010.

[131] W. Xia, Y. Zhang, Y. Yang, J.-H. Xue, B. Zhou, and M.-H. Yang, "Gan inversion: A survey," *IEEE transactions on pattern analysis and machine intelligence*, vol. 45, no. 3, pp. 3121–3138, 2022.

[132] L. Neumann and J. Matas, "Real-time scene text localization and recognition," in *2012 IEEE conference on computer vision and pattern recognition*. IEEE, 2012, pp. 3538–3545.

[133] B. Kumar, U. K. Tiwari, S. Kumar, V. Tomer, and J. Kalra, "Comparison and performance evaluation of boundary fill and flood fill algorithm," *Int. J. Innov. Technol. Explor. Eng*, vol. 8, no. 12, pp. 9–13, 2020.

[134] Q. Li, K. Luo, and X. Li, "Lattice boltzmann modeling of multiphase flows at large density ratio with an improved pseudopotential model," *Physical Review E—Statistical, Nonlinear, and Soft Matter Physics*, vol. 87, no. 5, p. 053301, 2013.

[135] H. K. Forster and N. Zuber, "Growth of a vapor bubble in a superheated liquid," *Journal of Applied Physics*, vol. 25, no. 4, pp. 474–478, 1954.

[136] B. Mikic, W. Rohsenow, and P. Griffith, "On bubble growth rates," *International Journal of Heat and Mass Transfer*, vol. 12, no. 5, pp. 649–651, 1969.

[137] L. Z. Zeng, J. Klausner, and R. Mei, "A unified model for the prediction of vapor bubble departure diameters in boiling systems—i. pool boiling,"

International Journal of Heat and Mass Transfer, vol. 36, no. 9, pp. 2261–2270, 1993.

[138] L. Zhang, S. Gong, Z. Lu, P. Cheng, and E. N. Wang, "A unified relationship between bubble departure frequency and diameter during saturated nucleate pool boiling," *International Journal of Heat and Mass Transfer*, vol. 165, p. 120640, 2021.

[139] M. Jakob, *Heat Transfer*. New York: John Wiley & Sons, 1949.

[140] N. Zuber, "Nucleate boiling. the region of isolated bubbles and the similarity with natural convection," *International Journal of Heat and Mass Transfer*, vol. 6, no. 1, pp. 53–78, 1963.

[141] R. Cole, "A photographic study of pool boiling in the region of the critical heat flux," *AIChE Journal*, vol. 6, no. 4, pp. 533–538, 1960.

[142] B. B. Mikic and W. M. Rohsenow, "A new correlation of pool-boiling data including the effect of heating surface characteristics," *Journal of Heat Transfer*, vol. 91, no. 2, pp. 245–250, 1969.

[143] R. L. Mohanty and M. K. Das, "A critical review on bubble dynamics parameters influencing boiling heat transfer," *Renewable and Sustainable Energy Reviews*, vol. 78, pp. 466–494, 2017. [Online]. Available: https://www.sciencedirect.com/science/article/pii/S136403211730607X

[144] V. Guichet, S. Almahmoud, and H. Jouhara, "Nucleate pool boiling heat transfer in wickless heat pipes (two-phase closed thermosyphons): A critical review of correlations," *Thermal Science and Engineering Progress*, vol. 13, p. 100384, 2019.

[145] M. Ghazivini, M. Hafez, A. Ratanpara, and M. Kim, "A review on correlations of bubble growth mechanisms and bubble dynamics parameters in nucleate boiling," *Journal of Thermal Analysis and Calorimetry*, vol. 147, no. 11, pp. 6035–6071, 2022.

[146] W. Friz, "Maximum volume of vapor bubbles," *Physic. Zeitschz.*, vol. 36, pp. 379–354, 1935.

[147] J. F. Klausner, R. Mei, D. Bernhard, and L. Zeng, "Vapor bubble departure in forced convection boiling," *International journal of heat and mass transfer*, vol. 36, no. 3, pp. 651–662, 1993.

[148] L. Zeng, J. Klausner, D. Bernhard, and R. Mei, "A unified model for the prediction of bubble detachment diameters in boiling systems—ii. flow boiling," *International journal of heat and mass transfer*, vol. 36, no. 9, pp. 2271–2279, 1993.

[149] R. Situ, T. Hibiki, M. Ishii, and M. Mori, "Bubble lift-off size in forced convective subcooled boiling flow," *International Journal of Heat and Mass Transfer*, vol. 48, no. 25-26, pp. 5536–5548, 2005.

[150] W. Fritz, "Berechnung des maximalvolumens von dampfblasen," *Physikalische Zeitschrift*, vol. 36, pp. 379–388, 1935.

[151] H. C. Unal, "Maximum bubble diameter, maximum bubble-growth time and bubble-growth rate during the subcooled nucleate flow boiling of water up to 17.7 mn/m^2," *International Journal of Heat and Mass Transfer*, vol. 19, no. 6, pp. 643–649, 1976.

[152] Q. Li, K. H. Luo, Q. J. Kang, and Y. L. He, "Lattice boltzmann modeling of boiling heat transfer: The boiling curve and the effects of wettability," *International Journal of Heat and Mass Transfer*, vol. 85, pp. 262–272, 2015.

[153] Q. Li, K. H. Luo, and Q. J. Kang, "Lattice boltzmann methods for multiphase flow and phase-change heat transfer," *Progress in Energy and Combustion Science*, vol. 52, pp. 62–105, 2016.

[154] A. Jaramillo, V. P. Mapelli, and L. Cabezas-Gómez, "Pseudopotential lattice boltzmann method for boiling heat transfer: A mesh refinement procedure," *Applied Thermal Engineering*, vol. 213, p. 118705, 2022.

[155] M. dos Santos Guzella and L. Cabezas-Gómez, "Pseudopotential lattice boltzmann method simulation of boiling heat transfer at different reduced temperatures," *Fluids*, vol. 10, no. 4, p. 90, 2025.

[156] W. Zhao, J. Liang, M. Sun, X. Cai, and P. Li, "Hybrid phase-change lattice boltzmann simulation of the bubble nucleation and different boiling regimes of conjugate boiling heat transfer," *arXiv preprint*, vol. arXiv:1911.10747, 2019.

[157] X. Ma and P. Cheng, "3d simulations of pool boiling above smooth horizontal heated surfaces by a phase-change lattice boltzmann method," *International Journal of Heat and Mass Transfer*, vol. 131, pp. 1095–1108, 2019.

[158] A. Mukherjee, D. N. Basu, and P. K. Mondal, "Algorithmic augmentation in the pseudopotential-based lattice boltzmann method for simulating the pool boiling phenomenon with high-density ratio," *Physical Review E*, vol. 103, no. 5, p. 053302, 2021.

[159] L. Fei, J. Chen, Y. Wang, and Q. Kang, "Mesoscopic simulation of 3d pool boiling using the cascaded lattice boltzmann method," *Physics of Fluids*, vol. 32, no. 10, p. 103312, 2020.

[160] J. Wang, H. Liu, Y. Li, and P. Cheng, "3d pseudopotential lattice boltzmann simulation of pool boiling on structured surfaces," *Chemical Engineering Science*, vol. 280, p. 118907, 2023.

[161] R. Chen, M. C. Lu, V. Srinivasan, Z. Wang, H. H. Cho, and A. Majumdar, "Nanowires for enhanced boiling heat transfer," *Nature Nanotechnology*, vol. 4, pp. 377–383, 2009.

[162] A. K. Das, G. P. Narayan, and S. V. Garimella, "Pool boiling on microstructured surfaces," *Journal of Heat Transfer*, vol. 132, no. 6, p. 061502, 2010.

[163] M. C. Lu and S. G. Kandlikar, "Nanoscale surface modification techniques for pool boiling enhancement – a critical review and future directions," *International Journal of Heat and Mass Transfer*, vol. 54, no. 19–20, pp. 4419–4431, 2011.

[164] C. Li and Z. Wang, "Boiling heat transfer on structured surfaces: A review," *International Journal of Heat and Mass Transfer*, vol. 81, pp. 75–104, 2015.

[165] Q. Zou and X. He, "On pressure and velocity boundary conditions for the lattice boltzmann bgk model," *Physics of Fluids*, vol. 9, no. 6, pp. 1591–1598, 06 1997. [Online]. Available: https://doi.org/10.1063/1.869307

[166] Q. Lin, S. Wang, Z. Ma, J. Wang, and T. Zhang, "Lattice boltzmann simulation of flow and heat transfer evolution inside encapsulated phase change materials due to natural convection melting," *Chemical Engineering Science*, vol. 189, pp. 154–164, 2018.

[167] S. Michaie, R. Rullière, and J. Bonjour, "Experimental study of bubble dynamics of isolated bubbles in water pool boiling at subatmospheric pressures," *Experimental Thermal and Fluid Science*, vol. 87, pp. 117–128, 2017.

[168] Y. Feng, H. Li, K. Guo, X. Lei, and J. Zhao, "Numerical study on saturated pool boiling heat transfer in presence of a uniform electric field using lattice boltzmann method," *International Journal of Heat and Mass Transfer*, vol. 135, pp. 885–896, 2019.

[169] A. Mukherjee and S. G. Kandlikar, "Numerical study of single bubbles with dynamic contact angle during nucleate pool boiling," *International Journal of Heat and Mass Transfer*, vol. 50, no. 1-2, pp. 127–138, 2007.

[170] L. Yang, A. Guo, and W. Zhang, "Computational fluid dynamics simulation of subcooled flow boiling in vertical rectangular 2-mm narrow channel," *Advances in Mechanical Engineering*, vol. 7, no. 7, p. 1687814015594349, 2015.

[171] A. Stojanović, V. Stevanović, M. M. Petrović, and D. Živković, "Numerical investigation of nucleate pool boiling heat transfer," *Thermal science*, vol. 20, pp. S1301–S1312, 2016.

[172] S. Gong and P. Cheng, "Numerical simulation of nucleate boiling near a vertical wall by lattice boltzmann method," *International Journal of Heat and Mass Transfer*, vol. 55, no. 9–10, pp. 2509–2523, 2012.

[173] G. Hazi and A. Markus, "On the choice of boundary conditions in lattice boltzmann simulations of phase separation," *Physics Letters A*, vol. 373, no. 12–13, pp. 1196–1200, 2009.

[174] H. Zheng, C. Shu, and Y. T. Chew, "A lattice boltzmann model for multiphase flows with large density ratio," *Journal of Computational Physics*, vol. 218, no. 1, pp. 353–371, 2006.

[175] A. R. Betz, J. Jenkins, C.-J. Kim, and D. Attinger, "Boiling heat transfer on superhydrophilic, superhydrophobic, and superbiphilic surfaces," *International Journal of Heat and Mass Transfer*, vol. 57, no. 2, pp. 733–741, 2013.

[176] X. Li, Q. Long, J. Xue, Z. Liang, B. Yan, and L. Wang, "Enhanced pool boiling heat transfer on hybrid wettability downward-facing surfaces," *Energies*, vol. 17, no. 23, p. 5849, 2024.

[177] W. Zhao, J. Liang, M. Sun, and X. Cai, "Lattice boltzmann simulations of the pool boiling curves above horizontal heaters with homogenous and heterogeneous wettability," *arXiv preprint*, 2019.

[178] S. Gong and P. Cheng, "Lattice boltzmann simulation of periodic bubble nucleation, growth and departure from a cavity in pool boiling," *International Journal of Heat and Mass Transfer*, vol. 64, pp. 122–132, 2013.

[179] C. Zhang, S. Yuan, and L. Wang, "Lattice boltzmann simulation of bubble behaviors during nucleate boiling on surfaces with different wettabilities," *International Journal of Heat and Mass Transfer*, vol. 112, pp. 279–295, 2017.

[180] C. Zhang, S. Yuan, Y. Li, and L. Wang, "Effect of surface wettability on bubble dynamics in nucleate boiling: A numerical study by lattice boltzmann method," *International Journal of Thermal Sciences*, vol. 134, pp. 56–66, 2018.

[181] S. Thutupalli, D. Geyer, R. Singh, R. Adhikari, and H. A. Stone, "Flow-induced phase separation of active particles is controlled by boundary conditions," *Proceedings of the National Academy of Sciences*, vol. 115, no. 21, pp. 5403–5408, 2018.

[182] P. Wang, L.-P. Wang, and Z. Guo, "Comparison of the lattice boltzmann equation and discrete unified gas-kinetic scheme methods for direct numerical simulation of decaying turbulent flows," *Physical Review E*, vol. 94, no. 4, p. 043304, 2016.

[183] H. Liang, B. Shi, Z. Guo, and Z. Chai, "Phase-field-based multiple-relaxation-time lattice boltzmann model for incompressible multiphase flows," *Physical Review E*, vol. 89, no. 5, p. 053320, 2014.

[184] Y. Ba, H. Liu, Q. Li, Q. Kang, and J. Sun, "Multiple-relaxation-time color-gradient lattice boltzmann model for simulating two-phase flows with high density ratio," *Physical Review E*, vol. 94, no. 2, p. 023310, 2016.

[185] M. R. Swift, E. Orlandini, W. Osborn, and J. Yeomans, "Lattice boltzmann simulations of liquid-gas and binary fluid systems," *Physical Review E*, vol. 54, no. 5, p. 5041, 1996.

[186] T. Inamuro, M. Yoshino, and F. Ogino, "A non-slip boundary condition for lattice boltzmann simulations," *Physics of fluids*, vol. 7, no. 12, pp. 2928–2930, 1995.

[187] A. Mazloomi M, S. S. Chikatamarla, and I. V. Karlin, "Entropic lattice boltzmann method for multiphase flows," *Physical review letters*, vol. 114, no. 17, p. 174502, 2015.

[188] J. W. Cahn and J. E. Hilliard, "Free energy of a nonuniform system. i. interfacial free energy," *The Journal of chemical physics*, vol. 28, no. 2, pp. 258–267, 1958.

[189] A. J. Bray, "Theory of phase-ordering kinetics," *Advances in Physics*, vol. 43, no. 3, pp. 357–459, 1994.

[190] H. Huang, D. T. Thorne Jr, M. G. Schaap, and M. C. Sukop, "Proposed approximation for contact angles in shan-and-chen-type multicomponent multiphase lattice boltzmann models," *Physical Review E—Statistical, Nonlinear, and Soft Matter Physics*, vol. 76, no. 6, p. 066701, 2007.

[191] H. Liang, J. Xu, J. Chen, H. Wang, Z. Chai, and B. Shi, "Phase-field-based lattice boltzmann modeling of large-density-ratio two-phase flows," *Physical Review E*, vol. 97, no. 3, p. 033309, 2018.

[192] D. Lycett-Brown and K. H. Luo, "Improved forcing scheme in pseudopotential lattice boltzmann methods for multiphase flow at arbitrarily high density ratios," *Physical Review E*, vol. 91, no. 2, p. 023305, 2015.

[193] Q. Li, K. Luo, Y. Gao, and Y. He, "Thermodynamic consistency of the pseudopotential lattice boltzmann model for simulating liquid–vapor flows," *Physical Review E*, vol. 87, no. 5, p. 053301, 2013.

[194] S. Gong and P. Cheng, "A lattice boltzmann method for simulation of liquid–vapor phase-change heat transfer," *International Journal of Heat and Mass Transfer*, vol. 55, no. 17, pp. 4923–4927, 2012. [Online]. Available: https://www.sciencedirect.com/science/article/pii/S0017931012002888

[195] K. Connington and T. Lee, "A review of spurious currents in the lattice boltzmann method for multiphase flows," *Journal of mechanical science and technology*, vol. 26, no. 12, pp. 3857–3863, 2012.

[196] Q. Kang, D. Zhang, and S. Chen, "Displacement of a two-dimensional immiscible droplet in a channel," *Physics of fluids*, vol. 14, no. 9, pp. 3203–3214, 2002.

[197] ——, "Displacement of a three-dimensional immiscible droplet in a duct," *Journal of Fluid Mechanics*, vol. 545, pp. 41–66, 2005.

[198] M. C. Sukop and D. Or, "Lattice boltzmann method for modeling liquid-vapor interface configurations in porous media," *Water Resources Research*, vol. 40, no. 1, 2004.

[199] L. Chen, Q. Kang, Y. Mu, Y.-L. He, and W.-Q. Tao, "A critical review of the pseudopotential multiphase lattice boltzmann model: Methods and applications," *International Journal of Heat and Mass Transfer*, vol. 76, pp. 210–236, 2014. [Online]. Available: https://www.sciencedirect.com/science/article/pii/S0017931014003378

[200] S. Li, L. Wan, N. Gui, X. Yang, J. Tu, and S. Jiang, "Thermodynamic properties of pseudopotential lattice boltzmann model for simple multiphase interfaces," *International Communications in Heat and Mass Transfer*, vol. 159, p. 108314, 2024. [Online]. Available: https://www.sciencedirect.com/science/article/pii/S0735193324010765

[201] W. Zhu, M. Wang, and H. Chen, "Study on multicomponent pseudopotential model with large density ratio and heat transfer," *International Communications in Heat and Mass Transfer*, vol. 87, pp. 183–191, 2017. [Online]. Available: https://www.sciencedirect.com/science/article/pii/S0735193317301768

[202] P.-Y. F. Robin, "Note on effective pressure," *Journal of Geophysical Research*, vol. 78, no. 14, pp. 2434–2437, 1973.

[203] A. M. Schwartz, "Capillarity-theory and practice," *Industrial & Engineering Chemistry*, vol. 61, no. 1, pp. 10–21, 1969.

[204] C. Sternling, , and L. Scriven, "Interfacial turbulence: hydrodynamic instability and the marangoni effect," *AIChE Journal*, vol. 5, no. 4, pp. 514–523, 1959.